High Resolution Active Pixel Sensor X-Ray Detectors for Digital Breast Tomosynthesis

by

Chumin Zhao

A dissertation submitted in partial fulfillment
of the requirements for the degree of
Doctor of Philosophy
(Electrical Engineering)
in the University of Michigan
2017

Doctoral Committee:

Professor Jerzy Kanicki, Chair
Professor Jeffrey A. Fessler
Professor Mitchell M. Goodsitt
Dr. Anastasios C. Konstantinidis, The Christie NHS Foundation Trust

Chumin Zhao
zhaocm@umich.edu
ORCID iD: 0000-0002-6549-2208

DEDICATION

To my parents for giving me all the wisdom, inspiration, and support.
To my wife for giving me all the patience, encouragement, and love.

ACKNOWLEDGEMENTS

I consider myself very fortunate to have Professor Jerzy Kanicki as my academic advisor for his constant guidance and advice during my master's and Ph.D. degrees. I am very grateful to him for giving me the opportunity to study in the exciting fields of solid-state devices and medical imaging. As a great educator and a friend, his attitude and passion to both research and life always inspire me. I also would like to thank my dissertation committee members: Professor Jeffrey A. Fessler, Professor Mitchell M. Goodsitt, and Dr. Anastasios C. Konstantinidis for their time and helpful suggestions.

Much of this dissertation would not have been completed without the efforts and help of other individuals. First, many appreciations to Professor Robert D. Speller, and former and current researchers at University College London: Dr. Anastasios C. Konstantinidis, Dr. Yi Zheng, and especially to Nikita Vassiljev, for kindly collecting and sharing experimental data for the advanced CMOS active pixel sensor (APS) x-ray detectors. Special thanks go to Dr. Anastasios C. Konstantinidis for teaching me the detective quantum efficiency calculation and other valuable discussions on CMOS APS detectors. Much gratitude to Dr. Mitsuru Nakata from NHK, Japan, for the collaboration on the study of amorphous In-Sn-Zn-O thin-film transistors (TFTs). I am also thankful to Mao-Hsun Cheng and Che-Lin Huang for their collaboration on the SPICE simulations for amorphous oxide TFTs and APS circuits.

I would like to express my appreciation to my past and present talented group members: Dr. Hyunsoo Kim, Dr. Eric K.-H. Yu, Aunnasha Sengupta, Rui Zhang, Linsen Bie, Che-Lin Huang, and Gokul Prakash, and the visiting scholars and students at our lab: Dr. Mitsuru Nakata (NHK), Dr. Soo Chang Kim (Samsung Display), Dr. Yongsu Lee (Samsung Display), and Mao-Hsun Cheng (National Cheng Kung University, Taiwan) for their friendship and collaborations.

Many thanks to the EECS department of University of Michigan for providing the financial support during my entire Ph.D. study.

I am also grateful to my undergraduate advisor, Professor Furong Zhu at Hong Kong Baptist University, Hong Kong, for leading me to the field of thin-film devices.

Last but not least, the deepest thanks go to my parents in China, Weijian Zhao and Jing Li, who have sacrificed so much to support and encourage me in every possible way during these years of study. I am eternally grateful to my beloved wife, Jing Li (same name as my mom), for showing me unconditional love, giving me the life I love today, and sharing all the greatest moments.

TABLE OF CONTENTS

DEDICATION ..... **ii**
ACKNOWLEDGEMENTS ..... **iii**
LIST OF FIGURES ..... **x**
LIST OF TABLES ..... **xviii**
ABSTRACT ..... **xix**
Chapter 1 Introduction **1**
1.1 Introduction to Digital Breast Tomosynthesis (DBT) 1
1.2 Description of DBT Systems 3
1.3 Passive Pixel Sensor (PPS) X-Ray Detectors 6
1.3.1 Direct conversion x-ray detectors 6
1.3.2 Indirect conversion x-ray detectors 8
1.3.3 Passive pixel sensor pixel and readout circuit 8
1.4 Active Pixel Sensor (APS) X-Ray Detectors 10
1.4.1 CMOS APS x-ray detector 10
1.4.2 TFT-based APS x-ray detectors 16
1.5 Dissertation Organization 19
Chapter 2 X-Ray Imaging Performance Evaluation and Cascaded System Analysis for APS X-Ray Detectors **21**
2.1 Empirical Imaging Performance Characterization of X-Ray Detectors 21
2.1.1 X-ray fluence 21
2.1.2 Modulation transfer function (MTF) 22
2.1.3 Noise power spectrum (NPS) 23
2.1.4 Detective quantum efficiency (DQE) 26

2.2 2D Cascaded System Analysis for Indirect CMOS APS X-Ray Detectors 26
2.2.1 2D cascaded system analysis model 28
2.2.2 Signal and noise nonlinearity 35
2.3 3D Cascaded System Analysis for Indirect CMOS APS X-Ray Detectors 36
2.3.1 3D cascaded system analysis model 36
2.3.2 Mean glandular dose (MGD) 43
2.4 Summary 44
Chapter 3 Two-Dimensional X-Ray Imaging Performance of CMOS APS X-Ray Detector for DBT 45
3.1 X-Ray Imaging Performance Evaluation for 75 μm Pixel Pitch CMOS APS X-Ray Detector 45
3.1.1 75 μm pixel pitch CMOS APS x-ray detector (Dexela 2923 MAM) .. 45
3.1.2 Experimental method and cascaded system analysis model 46
3.1.3 Experimental and modeling results 48
3.2 X-Ray Imaging Performance Evaluation for 50 μm Pixel Pitch CMOS APS X-Ray Detector 52
3.2.1 50 μm pixel pitch CMOS APS x-ray detector (DynAMITe) 52
3.2.2 Experimental method and cascaded system analysis model 54
3.2.3 Experimental and modeling results 56
3.2.4 Electrical properties of CMOS APS x-ray detector 60
3.2.5 Temporal noise of the DynAMITe SP x-ray detector 62
3.3 Summary 65
Chapter 4 Three-Dimensional X-Ray Imaging Performance of CMOS APS X-Ray Detector for DBT 66
4.1 Introduction 66
4.2 Experimental Setup 67
4.3 Angle-Dependent X-Ray Imaging Performance of the DynAMITe Detector 70
4.4 3D X-Ray Imaging Performance of the DynAMITe Detector 73
4.4.1 3D MTF, NNPS and DQE 73
4.4.2 Impact of projection angle range 76
4.4.3 Impact of mean glandular dose 77

4.4.4 Impact of focal spot size 78
4.4.5 Impact of pixelated scintillator 79
4.5 Summary 81
Chapter 5 Task-Based Modeling of a High-Resolution Medical Imaging System for DBT 83
5.1 Introduction 83
5.2 Task-Based Model 86
5.2.1 X-ray source and detector module 86
5.2.2 Object module 88
5.2.3 Display module 90
5.2.4 Observer module 93
5.2.5 Detectability index and AUC 95
5.3 Detectability Index and AUC for Various Objects 96
5.4 AUC for Small, High Contrast Objects 97
5.4.1 Object size and display pixel pitch 97
5.4.2 Detector electronic noise 99
5.5 AUC for Large, Low Contrast Objects 101
5.5.1 Number of display gray levels 101
5.5.2 DBT projection angle range 103
5.5.3 Anatomical background noise 104
5.6 Display and Ambient Luminance 105
5.7 Summary 106
Chapter 6 Fabrication and Evaluation of High Mobility Amorphous In-Sn-Zn-O Thin-Film Transistors 108
6.1 Introduction 108
6.2 High Mobility Amorphous In-Sn-Zn-O (a-ITZO) TFTs 109
6.3 Device Fabrication 110
6.4 Electrical Properties of a-ITZO TFTs 111
6.4.1 Current-voltage characteristics of a-ITZO TFTs 111
6.4.2 Field-effect mobility of a-ITZO TFTs 114
6.5 Device Optimization 120

6.5.1 Active layer thickness 120
6.5.2 Oxygen flow ratio optimization 123
6.6 Electrical Stability 125
6.7 Summary 128
Chapter 7 a-ITZO TFT APS Pixel Circuit for Indirect X-Ray Detectors 129
7.1 Chapter Overview 129
7.2 Device Fabrication 130
7.2.1 Photolithography process for a-ITZO TFTs 130
7.2.2 a-Si:H p^+-i-n^+ photodiode 130
7.3 Device Characteristics and SPICE Models 131
7.3.1 a-ITZO TFT electrical characteristics 131
7.3.2 SPICE model for a-ITZO TFT 132
7.3.3 a-Si:H p^+-i-n^+ photodiode characteristics 133
7.3.4 SPICE model for a-Si:H p^+-i-n^+ photodiode 134
7.4 a-Si:H p^+-i-n^+ Photodiode / a-ITZO TFT C-APS Circuit 135
7.4.1 C-APS circuit 135
7.4.2 SPICE simulation 137
7.5 Electrical Properties of the a-Si:H Photodiode / a-ITZO TFT C-APS Circuit 139
7.5.1 Voltage gain (A_V) and charge gain (G) 139
7.5.2 Signal linearity 140
7.5.3 Impact of field-effect mobility 141
7.5.4 Impact of a-ITZO TFT threshold voltage shift 142
7.5.5 Impact of W_{AMP} / W_{RD} ratio 144
7.6 Proposed 50 μm Pixel Circuit Layout and Fabrication Process 145
7.7 Impact of Data Line Resistance and Parasitic Capacitance 149
7.8 Noise Analysis 151
7.9 Summary 154
Chapter 8 Conclusions and Proposed Future Work 156
8.1 Conclusions of Dissertation 156
8.2 Recommendations for Future Work 159

BIBLIOGRAPHY 161

LIST OF FIGURES

Figure 1.1 Schematic of DBT system. A movable x-ray source is rotated within an angular range of ±θ and the breast is held between the compression paddle and detector. A series of projection images is reconstructed into multiple in-focus slices of images on the z-direction. (adopted from [5]) 4

Figure 1.2 Schematics of (a) direct and (b) indirect conversion detectors are shown. An a-Se photodiode and a conventional a-Si:H p-i-n photodiode are used for indirect and direct conversion detectors, respectively. 7

Figure 1.3 Schematic of pixel circuit and readout electronics of a-Si:H TFT PPS with a photodiode (PD). C_{PIX}, C_{DATA} and C_{FB} are the pixel, data line and feedback capacitance, respectively. R_{DATA} is the data line parasitic resistance. V_{READ}, V_{REF} and V_{OUT} are the TFT gate voltage, reference voltage of op-amp and output voltage, respectively. SW is the switch on the charge integrating amplifier. 9

Figure 1.4 (a) Circuit schematic of 3-T CMOS APS pixel and readout electronics with cross-sectional view of the c-Si photodiode and T_{RST} are shown. T_{RST}, T_{SF} and T_{SEL} stand for the reset transistor, source follower and row select transistor for the pixel, respectively; T_{BIAS} is the column bias transistor and C_{COL} is the storage capacitor for the column bus line. (b) Driving scheme of the 3-T CMOS APS x-ray imager based on n-MOS technology is also shown. 12

Figure 1.5 (a) Schematic of current-mode APS pixel and readout circuits. V_{IN}, V_{OUT} and I_{OUT} are the pixel input voltage, output voltage and output current, respectively. C_{FB} are the column capacitor and feedback capacitor for voltage-mode and current-mode APS, respectively. (b) Small signal circuit schematic of C-APS readout. 17

Figure 2.1 An example of (a) gain and offset corrected edge image, $Edge_{corr1}$, and (b) second order polynomial fit S(x,y) to detrend the corrected image. 23

Figure 2.2 An example of extracted (a) oversampled edge spread function, (b) averaged edge spread function, (c) line spread function and (d) modulation transfer function from corrected edge images. 24
Figure 2.3 An example of (a) gain and offset corrected flat image I(x, y) and (b) extracted 2D NPS(u, v). 25
Figure 2.4 Schematic of the signal and noise transfer for gain and spreading stages using cascaded system analysis (adopted from [47]). 27
Figure 2.5 Illustration of the 3D cascaded system analysis. Stages 0 – 9 describes the 2D cascaded system model for the APS x-ray detector. Stages 10 – 14 describes the beam obliquity, focal spot blurring effect and filtered back-projection reconstruction. 38
Figure 3.1 Schematic of the broadband x-ray and monochromatic synchrotron generation. The broadband x-ray and monochromatic synchrotron radiation spectra as a function of energy and the light output as a function of wavelength are also shown. 47
Figure 3.2 Measured and fitted MTF for Dexela 2923 MAM CMOS APS x-ray imager using a broadband x-ray radiation with a 150 μm CsI:Tl scintillator and a monochromatic synchrotron radiation with a 200 μm CsI:Tl scintillator. Results for both HFW and LFW modes are shown. 49
Figure 3.3 Experimental (symbols) and simulated (lines) data of NNPS and DQE parameters for the Dexela 2923 MAM CMOS APS x-ray imager HFW (a, b) and LFW modes (c, d) under broadband x-ray radiation of 28 kVp. 50
Figure 3.4 Experimental (symbols) and simulated (lines) data of NNPS and DQE parameters for the Dexela 2923 MAM CMOS APS x-ray imager HFW (a, b) and LFW (c, d) modes under monochromatic synchrotron radiation of 17 keV. 51
Figure 3.5 (a) Top view schematic representation of CMOS APS x-ray detector with 50 μm pixel pitch. a_{pix} and a_{pd} are the pixel pitch and effective photodiode pitch, respectively. (b) Circuit schematic of DynAMITe SP CMOS APS detector. RST, SF, RS and Bias represent the reset transistor, source follower, row select transistor and column bias transistor, respectively. C_{PD}, C_{Par} and C_{Col} are the photodiode capacitance, parasitic capacitance, and column capacitance, respectively. V_{RST} and V_{DD} are constant bias voltages. 54
Figure 3.6 Experimental setup for detector MTF, NNPS and DQE measurements. 55

Figure 3.7 Experimental (circles) and simulated (solid line) system MTF. The stage MTFs associates with scintillator blurring, FOP blurring and pixel aperture are also shown (dash lines). 56
Figure 3.8 Extracted DynAMITe CMOS APS signal S(e^-/DN) and noise N(e^-/DN) conversion gains (symbols) at detector air kerma up to 127 μGy. A second order polynomial is used to fit N(e^-/DN) (solid line). 57
Figure 3.9 Experimental (symbols) and simulated (lines) (a) nonlinear system NNPS and (b) nonlinear system DQE for detector air kerma ranging from 1.3 to 109.5 μGy. For comparison, (c) NNPS and (d) DQE data simulated using linear cascaded system analysis is also shown. 58
Figure 3.10 Experimental extracted (circles) and simulated (lines) electronic signal at the sensing node for detector air kerma up to 127 μGy. 59
Figure 3.11 Experimental (symbols) and simulated mean output signal in DN (squares) and pixel mean variance in DN^2 (circles) for detector air kerma ranging from 1.3 to 127 μGy. Signal/noise non-linearity is included. 60
Figure 3.12 Experimental (circles) and simulated (solid line) RMS pixel total noise for DynAMITe SP detector at air kerma ranging from 10^{-3} to 10^3 μGy. The detector signal-to-noise ratio (SNR_d) (dash line) is also shown. Detector full well capacity (FW), read noise and dynamic range (DR) were extracted. 61
Figure 3.13 Calculated temporal noise of CMOS APS pixel and readout circuits. 65
Figure 4.1 (a) Side-view and (b) top-view schematics of the bench-top system used to characterize the detector MTF, NNPS and DQE parameters. The detector is located on top of a rotary stage with a distance of 65 cm to the x-ray source. 68
Figure 4.2 Experimental (a) horizontal (x-direction) and (b) vertical (y-direction) MTF parameter at x-ray projection angles ranging from 0 to 30 degrees. Simulation results are not shown in this figure. 71
Figure 4.3 Experimental (symbols) and simulated (lines) horizontal x-direction (a) MTF associated with the oblique incident angles, (b) detector MTF, (c) NNPS and (d) DQE parameters at incident beam angles θ_i ranging from 0 to 30 degrees. 71
Figure 4.4 Relative errors (%) between simulated and measured MTF, NNPS and DQE parameters at x-ray beam projection angles of (a) 0°, (b) 10°, (c) 20° and (d) 30°. Spatial

frequencies from 1 to 7 mm^{-1} are chosen. 72
Figure 4.5 Calculated 3D MTF, NNPS and DQE in the (a) x-y plane: (f_x, f_y), while $f_z = 0$ and (b) x-z plane: (f_x, f_z), while $f_y = 0$. 74
Figure 4.6 (a) In-plane MTF, NNPS and DQE calculated by integrating 3D MTF, NNPS and DQE over f_z. (b) In-plane MTF, NNPS and DQE for x direction ($f_y = 0$). 75
Figure 4.7 Horizontal x-direction in-plane (a) MTF, (b) NNPS and (c) DQE for projection angle range of ±15°, ±20° and ±30° at MGD of 1.5 mGy. 77
Figure 4.8 Horizontal x-direction in-plane (a) MTF, (b) NNPS and (c) DQE for MGD ranging from 0.5 – 1.5 mGy at the projection angle range of ±20°. 78
Figure 4.9 Horizontal x-direction in-plane (a) MTF, (b) NNPS and (c) DQE for focal spot size ranging from 0 to 3 mm at the projection angle range of ±20° and MGD of 1.5 mGy. 79
Figure 4.10 Horizontal x-direction in-plane (a) MTF, (b) NNPS and (c) DQE for standard non-pixelated scintillator and 50 μm pixelated scintillators with a fill factor of unity and 0.8. The projection angle range is ±20° and the MGD is 1.5 mGy. 81
Figure 5.1 Schematic of 2 by 2 tiling of four CMOS APS sub-detectors with an active area of 12.8 × 13.1 cm^2 each. 84
Figure 5.2 Flowchart of the task-based detectability index and AUC calculation. O_{xyz} and FFT[O_{xyz}] represent a binary object in spatial and Fourier domain; μ_{obj} and μ_{bg} are the linear attenuation coefficients for the object and background materials, respectively; S_{bg} is the anatomical background noise power spectrum. 85
Figure 5.3 Calculated 2D (a) MTF, (b) NPS and DQE parameters using an x-ray tube voltage of 28 kVp and a detector air kerma of 8.57 μGy. 87
Figure 5.4 3D MTF in (a) x-y plane ($f_z = 0$) and (c) x-z plane ($f_y = 0$); 3D NPS in (b) x-y plane and (d) x-z plane. f_x, f_y and f_z are the spatial frequencies in the x, y and z directions, respectively. 88
Figure 5.5 (a) O_{xyz} (when $z = 0$) and (b) FT{O_{xyz}} (when $f_z = 0$) of a single sphere with a diameter of 150 μm in the x-y plane. (c) O_{xyz} and (b) FT{O_{xyz}} of six spheres in the x-y plane. 89
Figure 5.6 Grayscale standard display function for a medical imaging display with 10 bits (1024) gray levels and a maximum luminance of 1000 cd/m^2 [179]. 92

Figure 5.7 Calculated contrast sensitivity function for a display luminance L ranging from 1 to 1000 cd/m^2 and image angular dimension X_0 of 81.1° [177]. 95
Figure 5.8 Calculated (a) detectability index and (b) AUC for a medical imaging system based on the DynAMITe CMOS APS detector for a sphere with various diameter and mean linear attenuation coefficient. 97
Figure 5.9 Calculated AUC for detecting a single sphere with diameters of (a) 100 μm, (b) 150 μm, and (c) 200 μm at various display pixel pitch (a_{disp}) and zoom factor (λ). (d) – (f) shows the AUC to classify six spheres with the same diameters. 99
Figure 5.10 Calculated AUC for detecting six spheres with diameters of 150 μm. The electronic noise of the x-ray detector was varied as (a) 150 e^-, (b) 300 e^-, (c) 600 e^-, and (d) 1000 e^-. 100
Figure 5.11 Calculated (a) display luminance contrast and (b) AUC for detecting a large sphere with diameters of 2 mm using a display with 10 bits gray levels. (c) and (d) shows the contrast and AUC by changing the number of display gray levels to 12 bits. 102
Figure 5.12 Calculated AUC for a 2 mm sphere (mass with μ_{obj} = 0.84 cm^{-1}) using a projection range θ from ±5° to ±40°. χ of 1 and 2 were selected. 103
Figure 5.13 Calculated AUC for a 2 mm sphere (mass with μ_{obj} = 0.84 cm^{-1}) using a projection range θ from ±5° to ±40° and κ ranging from 1 × 10^{-6} to 3 × 10^{-6} mm^3. χ of 1 and 2 were selected. 104
Figure 5.14 Calculated AUC for detecting (a) six spheres (microcalcifications) with d_{sp} of 150 μm and μ_{obj} of 15.9 cm^{-1}, and (b) single sphere (masses) with d_{sp} of 2 mm and μ_{obj} = 0.84 cm^{-1} using various display maximum luminance and ambient luminance. 106
Figure 6.1 (a) Cross-sectional and (b) top views a-ITZO TFTs fabricated using mechanical mask. 111
Figure 6.2 (a) An example of output characteristics of a-ITZO TFT fabricated using mechanical mask. (b) Zoom-in output characteristics in the region of V_{DS} up to 1.0 V is also shown. The a-ITZO film thickness and O_2 gas flow ratio are 50 nm and 5%, respectively. 112
Figure 6.3 (a) An example of transfer characteristics of a-ITZO TFT in the logarithm scale. (b) Device performance in linear and saturation regions is also shown. The a-ITZO film thickness and O_2 gas flow ratio are 50 nm and 5%, respectively. 113

Figure 6.4 An example of the incremental field-effect mobility in (a) linear (V_{DS} = 0.1 V) and (b) saturation regions (V_{DS} = 10 V). The derivative of μ_{inc} ($\partial\mu_{inc}/\partial V_{GS}$) is also shown. 115
Figure 6.5 Method 1: (a) Extracted linear region (V_{DS} = 0.1 V) γ by linear fitting of $\log(I_D/I_0)$ vs. $\log((V_{GS}-V_T)/(V_0-V_T))$ at various V_T (V_0 = 5V, and I_0 = 0.58 μA). The corresponding standard error is also shown. (b) Example of the best linear fit, when the minimum error is achieved. 118
Figure 6.6 Method 2: Experimental and linear fitted $\log(\mu_{inc})$ vs. $\log(V_{GS} - V_T)$ in both linear and saturation regions. γ and K were extracted from the slope and intercept of the linear fitted data. 119
Figure 6.7 Experimental and calculated μ_{inc} (a) and I_D (b) in both linear and saturation regions using parameters extracted by Method 1 (least square linear fit method) and 2 (second order derivative method). The extracted parameters using both methods are also shown. 120
Figure 6.8 Averaged (a) threshold voltage, (b) field-effect mobility using the 10%-90% fitting method, and (c) subthreshold swing at the maximum slope point in the subthreshold region for devices with various a-ITZO thickness. The oxygen gas flow ratio for the fabricated devices is 10%. Extracted device parameters for a-IGZO TFTs (oxygen gas flow rate = 5%) with active layer thickness from 5 to 50 nm are also shown. 121
Figure 6.9 Extracted (a) threshold voltage, (b) field-effect mobility using the 10%-90% fitting method, and (c) subthreshold swing at the maximum slope point in the subthreshold region for devices fabricated using oxygen gas flow ratio from 0 to 50%. The a-ITZO film thickness is fixed at 50 nm. 124
Figure 6.10 An example of the variations of transfer characteristics of a-ITZO TFT during (a) PBTS and (b) NBTS for 10^3 seconds at stress temperature of 70 °C. 126
Figure 6.11 Variations in (a) field-effect mobility, (b) subthreshold swing, and (c) threshold voltage shift at V_{DS} = 10 V after stress time up to 10^3 seconds at 70 °C. The gate stress voltage is +10 and -10 V for PBTS and NBTS, respectively. The threshold voltage shift of a-IGZO TFT data is also shown for comparison purpose. 127
Figure 6.12 Impact of oxygen gas flow ratio on threshold voltage shift of a-ITZO TFTs with 50 nm channel thickness after 1k seconds stress time. The gate stress voltage is +10

and -10 V for PBTS and NBTS, respectively. 128
Figure 7.1 Cross-section views of (a) a-ITZO TFT and (b) a-Si:H p^+-i-n^+ photodiode. 131
Figure 7.2 Experimental and simulated (using developed SPICE model) (a) transfer characteristics (I_D vs. V_{GS}) and (b) output characteristics (I_D vs. V_{DS}) of a-ITZO TFTs. 132
Figure 7.3 (a) Measured [221] and simulated I-V characteristics for an a-Si:H p^+-i-n^+ photodiode with an active area of 40 × 40 μm^2. (b) SPICE model circuit schematic of the a-Si:H photodiode. 134
Figure 7.4 (a) Circuit illustration of the proposed a-ITZO TFT C-APS with the switched integrator readout circuit. (b) Driving scheme of the C-APS circuit. V_{RS}, V_{RD}, V_{IN} and V_{OUT} are the applied gate voltage for T_{RS}, T_{RD}, input, and output voltage, respectively; I_{ph} is the photocurrent; SW_{ER} is the external reset switch signal; t_{RS}, t_{INT}, t_{RD}, and t_{frame} are the reset, integration, readout, and frame time. 136
Figure 7.5 Waveforms of (a) the input voltage during the integration time and (b) output voltage during the readout time for I_{ph} ranging from 0 to 9 pA. 138
Figure 7.6 Absolute value of (a) ΔV_{OUT} versus ΔV_{IN} and (b) ΔQ_{OUT} versus ΔQ_{IN} for I_{ph} ranging from 0 to 9 pA. The voltage and charge gains can be extracted from the slope of these curves. 140
Figure 7.7 Absolute value of ΔV_{OUT} versus ΔV_{IN} and for I_{ph} ranging from 0 to 9 pA using TFT μ_{eff} of 31.2, 12.5 and 0.6 cm^2/Vs. 142
Figure 7.8 Extracted (a) V_{IN} and V_{OUT}, and (b) ΔV_{IN} and ΔV_{OUT} for C-APS with ΔV_T of 0, +0.54 and -0.5 V applied to T_{AMP}. 143
Figure 7.9 Extracted voltage gains for various W_{AMP}/W_{RD} ratio ranging from 63/9 to 9/63. TFT field-effect mobility of 31.2 cm^2/Vs was used. 144
Figure 7.10 A 50-μm pixel pitch layout for the proposed a-ITZO TFT C-APS. A critical dimension of 3 μm was used for the layout design. The VIA is used to connect the photodiode bottom electrode to T_{AMP} gate and T_{RS} source. V_M is the data line output voltage connected to the negative input node of the op-amp. 146
Figure 7.11 Cross-sectional view (A to A') of a-Si:H photodiode / a-ITZO TFT C-APS and illustration of photolithography steps (10 mask steps). 148
Figure 7.12 Cross-sectional view (B to B') of the fabricated data line, V_{RS} and V_M pads after mask #10. Cross-section view from C to C' shows the same structure. 149

Figure 7.13 Cross-sectional schematic of T_{RD} and the data line series resistance (R_{DATA}) and parasitic capacitances (C_{DATA}). To simplify the drawing, the regular TFT structure is shown. 150
Figure 7.14 Extracted input-output (a) voltage and (b) charge characteristics for C-APS with and without data line loadings. I_{ph} is ranging from 0 to 9 pA..... 151

LIST OF TABLES

Table 1.1 Technical specifications of clinical DBT imaging systems approved by the US FDA..... 5
Table 1.2 Comparison of PPS, V-APS and C-APS circuits. 19
Table 3.1 Key parameters used in the cascaded system model for the Dexela 2923 MAM CMOS APS x-ray detector. 48
Table 3.2 Parameters and characteristics of DynAMITe P and SP cameras..... 52
Table 3.3 Parameters used in the cascaded system model for the DynAMITe SP detector. 55
Table 6.1 Electrical properties of a-ITZO TFT fabricated using shadow mask.....114
Table 7.1 SPICE parameters for fabricated a-ITZO TFTs. 133
Table 7.2 SPICE parameters for the a-Si:H p^+-i-n^+ photodiode. 135
Table 7.3 SPICE parameters for C-APS circuit and driving scheme. 137
Table 7.4 Input referred electronic noise of a-ITZO TFT C-APS. 154

ABSTRACT

Current large area x-ray detectors for digital breast tomosynthesis (DBT) are based on the amorphous silicon (a-Si:H) passive pixel sensor (PPS) technology. However, PPS detectors suffer from a limited resolution and high electronic noise. In this dissertation, we propose high resolution large area active pixel sensor (APS) x-ray detectors based on the complementary metal-oxide-semiconductor (CMOS) and amorphous In-Sn-Zn-O (a-ITZO) thin-film transistor (TFT) technologies to improve the imager resolution and noise properties.

We evaluated the two-dimensional (2D) x-ray imaging performance as measured by the modulation transfer function (MTF), noise power spectrum (NPS) and detective quantum efficiency (DQE) for both 75 μm (Dexela 2923 MAM) and 50 μm pixel pitch (DynAMITe) CMOS APS x-ray detectors. Excellent imaging performance (DQE in the range of 0.7 – 0.3) has been achieved over the entire spatial frequency range (0 – 6.7 mm^{-1}) at low air kerma below 10 μGy using the 75 μm pixel pitch Dexela 2923 MAM detector. The 50 μm pixel pitch DyAMITe detector has further extended the spatial resolution of the detector to 10 mm^{-1} with a low electronic noise of 150 e^-. Also, a 2D cascaded system analysis model has been developed to describe the signal and noise transfer for the CMOS APS x-ray imaging systems. We also implemented three-dimensional (3D) cascaded system analysis to simulated the 3D MTF, NPS and DQE characteristics using DBT radiation conditions and acquisition geometries. The 3D cascaded system analysis for the DynAMITe detector was integrated with an object task function, a medical imaging display model, and the human eye contrast sensitivity function to calculate the detectability index and area under the ROC curve (AUC). It has been demonstrated that the display pixel pitch and zoom factor should be optimized to improve the AUC for detecting high contrast objects such as microcalcifications. Also,

detector electronic noise of smaller than 300 e^- and a high display maximum luminance (>1000 cd/cm^2) are desirable to distinguish microcalcifications of 150 μm or smaller in size. For low contrast object detection, a medical imaging display with a minimum of 12 bits gray levels is needed to realize accurate luminance levels. A wide projection angle range (≥ ±30°) combined with the image gray level magnification could improve the detectability for low contrast objects especially when the anatomical background noise is high.

CMOS APS x-ray detectors demonstrate both a high pixel resolution and low electronic noise, but are challenging to be fabricated in a large detector size greater than the wafer scale. Alternatively, current-mode APS (C-APS) based on a-ITZO TFTs was proposed for DBT due to the high gain, low noise, and capability to realize a large detector area. Specifically, we fabricated a-ITZO TFTs and achieved a high field-effect mobility of >30 cm^2/Vs. We have also evaluated the electrical performance of a 50 μm pixel pitch a-ITZO TFT C-APS combined with an a-Si:H p^+-i-n^+ photodiode using SPICE simulation. The proposed C-APS circuit demonstrates a high charge gain of 885 with data line loadings considered. A pixel circuit layout and fabrication process have also been suggested. Finally, noise analysis has been applied to the a-ITZO TFT C-APS. A low electronic noise of around 239 e^- has been established.

The research presented in this thesis indicates that APS x-ray detectors based on both CMOS and a-ITZO TFT technologies are promising for next generation DBT systems.

Chapter 1
Introduction

1.1 Introduction to Digital Breast Tomosynthesis (DBT)

Digital mammography has been the gold standard for breast cancer detection over past decades. It enables low cost and fast early breast cancer detection and diagnosis at relatively low x-ray radiation doses. However, two-dimensional (2D) mammography suffers from severe breast tissue superposition, which can limit the visibility of breast lesions [1]. To address this issue, advanced three-dimensional (3D) breast imaging technologies are needed.

As an alternative to standard mammography, digital breast tomosynthesis (DBT) has been designed to improve the visibility of the breast volume by using multiple x-ray projection views and computer algorithms to reconstruct quasi-3D images of the entire breast [2], [3]. During a typical DBT scan, around 9 to 25 projection views are captured within a narrow angular range of 15 to 50 (±7.5 to ±25) degrees to create tomographic "slices" of the breast volume with thickness of around 1 mm [4], [5]. As a result, the enhanced in-depth resolution of DBT reduces tissue overlapping and may thereby improve the diagnostic accuracy of breast cancer. The quasi-3D (i.e., the z-resolution, around 1 mm, is much worse than x-y focal plane resolution, around 100 μm) nature of DBT also enables precise lesion localization. In comparison to DBT, the 3D dedicated breast computed tomography (bCT) improves z-resolution (voxel size of about 200 μm), while sacrificing the focal plane resolution [6]–[10].

Since Niklason *et al.*'s first demonstration of DBT [2], numerous research studies have been performed to evaluate the clinical performance of DBT systems [11]–[13], optimize the acquisition geometry (incident angles, number of views and dose

distribution etc.) [14]–[17], and improve image reconstruction [18]–[22]. Today all these topics are still under active research. Clinical evaluations have demonstrated that cancer detectability on DBT is superior to digital mammography [23]. Addition of DBT to digital mammography increases diagnosis sensitivity and specificity for breast cancer, while reduces recall rates for non-cancer cases [24], [25]. Although DBT has achieved improved breast imaging in comparison to digital mammography by addressing the tissue superposition issue, several technical barriers still need to be overcome.

Similar to digital mammography, the focal-plane pixel pitch of current DBT systems is restricted to around 100 μm [4], [26]–[28], corresponding to a Nyquist frequency of 5 mm^{-1} [29]. Although smaller detector pixel pitch (70 μm) is used by the Hologic Selenia Dimensions system, 2 × 2 pixel binning is used to operate the system in the DBT mode. The reconstructed focal-plane pixel size of the Hologic DBT system is from 95 to 117 μm [30]. Image information for microcalcifications and fine details contained in higher spatial frequency region (> 5 mm^{-1}) is lost. Compared to full-field digital mammography (FFDM), DBT improves lesion detection but has not been shown to also improve microcalcification detection. Increasing the spatial resolution of DBT might result in improvement in microcalcification detection [31], [32]. To preserve the relevant diagnostic details, a high resolution DBT imager and system with focal-plane resolution corresponding to a pixel pitch of 75 μm or smaller (e.g., 50 μm) needs to be developed.

Another important issue is that, at low x-ray radiation levels for DBT, the high detector electronic noise (>1000 e^-) of existing commercial systems can induce high background image noise, which degrades the contrast-to-noise properties of lesions such as microcalcifications and masses. Hence it is also critical to reduce the detector electronic noise in DBT.

Moreover, the DBT mean glandular dose (MGD) is about 1.5 mGy for an average (4.2 cm thick) breast with 50% glandular fraction and can be as high as 3.5 mGy for thicker, denser breasts [27]. The dose of a single-view DBT exam is about one to two times that of a single-view FFDM [33]. The DBT dose level needs to be reduced.

1.2 Description of DBT Systems

Clinical DBT systems consist of a rotatable x-ray source, a compression paddle, and a digital x-ray detector on a supportive plate. Figure 1.1 shows the schematic of a complete DBT system.

During a DBT scan, a series of low exposure projection images are captured within a limited angular range of $\pm\theta$. In general, tungsten (W), molybdenum (Mo) or rhodium (Rh) can be used as the target material in combination with an aluminum (Al), Mo or Rh filter as the x-ray source [4], [5]. The x-ray source motion for tomosynthesis can be either "step-and-shoot" or "continuous" [34]. The step-and-shoot motion reduces the image blurring due to the x-ray source movement, while the continuous motion reduces the total scan time [5], [34].

The irradiated x-ray photons impinge either a direct or indirect x-ray detector and will be read by an active-matrix array typically based on the hydrogenated amorphous silicon (a-Si:H) thin-film transistor (TFT) passive pixel sensor (PPS) technology with the appropriate low noise external readout electronics [35], [36]. During image acquisition, the detector can be static or rotating (to minimize the scan angle).

Finally, the obtained projection images are reconstructed to multiple in-focus quasi-3D images with a slice thickness (or reconstruction slice gap) of around 1 mm. The most common reconstruction algorithm for DBT is the filtered back-projection (FBP). To implement FBP, multiple filters (such as ramp filter, apodization filter and slice thickness filter) are applied to the projection images before back-projection is performed [18], [37], [38]. Iterative reconstruction method such as simultaneous algebraic reconstruction technique (SART) can also be used for DBT image reconstruction [5], [39]. Both FBP and SART address the inter-plane blurring effect of conventional back-projection (BP) method and provide enhanced contrast for small and high contrast objects [20], [39]. However, noise can be amplified in the image reconstruction process, making the lesion detection challenging especially when the detector electronic noise is high. Therefore, a low noise of DBT x-ray detector is very desirable. Besides, advanced iterative reconstruction algorithms with weighted regularization have been reported to enhance lesion conspicuity and contrast-to-noise

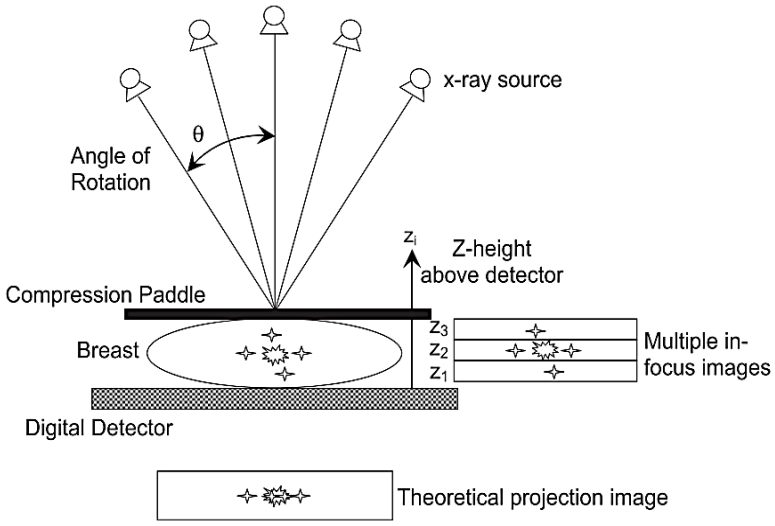

Figure 1.1 Schematic of DBT system. A movable x-ray source is rotated within an angular range of ±θ and the breast is held between the compression paddle and detector. A series of projection images is reconstructed into multiple in-focus slices of images on the z-direction. (adopted from [5])

ratio (CNR) [21], [22]. In this dissertation, the standard FBP method is used for the 3D cascaded system analysis as described in Chapter 2 and 4.

To date, three clinical DBT systems (GE SenoClaire, Hologic Selenia Dimensions, and Siemens MAMMOMAT Inspiration) have been approved by the US food and drug administration (FDA) for clinical use. Table 1.1 summarizes the technical specification of the three clinical systems produced by General Electric (GE) healthcare, Hologic and Siemens [4], [5], [26]–[28], [30].

The main difference of these three systems is the detector type. The GE SenoClaire system uses an indirect conversion detector based on a thallium-doped cesium iodide (CsI:Tl) scintillator in combination with an a-Si:H p-i-n photodiode. On the other hand, both Hologic and Siemens DBT systems implement a direct conversion detector based on the amorphous selenium (a-Se) photoconductor. Details of the direct and indirect conversion detectors are discussed in Section 1.3.

For the active-matrix array, all three systems are based on the a-Si:H TFT PPS technology. The TFT is simply used as a switch to transfer electronic signal (electrons) from the photodetector to the readout electronics. The operational principle of the PPS array will be discussed in Section 1.3.3.

The limitations of the a-Si:H TFT PPS technology include: a relatively large pixel pitch of around 100 μm, large electronic noise (greater than 1000 e^-) [40], and a slow frame rate of 1 to 4 frame per second (fps). Reducing the pixel pitch will result in higher image resolution. However, a reduction in both the digital signal and quantum noise will be observed, while the signal-to-noise ratio (SNR) is affected. Thus, the high electronic noise of PPS detectors becomes dominant, leading to noisy images. At the same time, improvement of the pixel resolution increases the readout time and total DBT scan time. Therefore, 2 × 2 pixel binning (with binned pixel pitch of 140 μm) is used by the Hologic Selenia Dimensions system to improve the image contrast-to-noise properties and speed up the readout process. In addition, the DBT dose remains to be one to two times higher than that of FFDM. It is difficult to reduce the dose due to the high electronic noise of a-Si:H TFT PPS.

	GE SenoClaire	Hologic Selenia Dimensions	Siemens MAMMOMAT
Detector type	Indirect	Direct	Direct
Detector material	CsI:Tl / a-Si:H p-i-n	a-Se	a-Se
TFT technology	a-Si:H TFT	a-Si:H TFT	a-Si:H TFT
Detector size (cm × cm)	24×30	24×29	24×30
Detector pixel pitch (μm)	100	70 (full resolution) 140 (2×2 binned)	85
Pixel resolution	2394×3062	3328×4096 (full res.) 1664×2048 (binned)	2816×3584
Focal plane pixel size (μm)	100	95-117	85
Pixel circuit	PPS	PPS	PPS
X-ray source (target/filter)	Mo/Rh	W/Al	W/Rh
X-ray tube motion	Step and shoot	Continuous	Continuous
Number of views	9	15	25
Scan time (s)	7	3.7	25
Frame rate (fps)	1.3	4.1	1.0
Total scan angle	25°	15°	50°
Detector motion	Static	Rotating	Static
Reconstruction method	Iterative	Filtered back-projection	Filtered back-projection
Dose (vs. FFDM)	100%	120%	100-200%

Table 1.1 Technical specifications of clinical DBT imaging systems approved by the US FDA.

1.3 Passive Pixel Sensor (PPS) X-Ray Detectors

1.3.1 Direct conversion x-ray detectors

For direct conversion detectors, as shown in Figure 1.2(a), x-ray photons are absorbed by semiconductors such as a-Se and directly converted to electron-hole pairs [35], [41]. The electron-hole pairs will be separated by a large electric field E (around 10 V/μm) and drifted to the anode (for holes) and cathode (for electrons) [42].

During the x-ray absorption, the quantum detection efficiency (QDE) (also known as the attenuation fraction) of a-Se is given by

$$A_Q = 1 - \exp(-\alpha L), \tag{1.1}$$

where α is the attenuation coefficient and L is the film thickness. The attenuation depth δ is defined where the beam is attenuated by 63% (i.e., $\alpha \times \delta = 1$). At the mean DBT x-ray energy of 20 keV, α is 0.02 μm^{-1} and δ is 49 μm for a-Se [35]. A thicker a-Se film will increase the QDE. However, L must be much smaller than the product of $\mu\tau E$ (i.e. the mean drift length of carriers before trapping) to ensure efficient carrier collection, where μ is the drift mobility of carriers, τ is the mean lifetime of carriers [26]. For a-Se, the electron mobility (μ_e = 0.003 – 0.006 $cm^2V^{-1}s^{-1}$) is much smaller than hole mobility (μ_h = 0.13 $cm^2V^{-1}s^{-1}$) [42]. Taking τ_e = 100 – 1000 μs and E = 10 V/μm, it is obtained that L must be smaller than 300 μm. Typically, the a-Se thickness is around 200 μm, achieving A_Q of 0.98. However, the applied voltage for direct detectors is extremely high ($V = E \times L$ = 10 V/μm × 200 μm = 2 kV) [35], which affects the TFT and array lifetime due to electrical device stressing.

The absorbed x-ray energy (E_{ab}) creates electron-hole pairs. The electron-hole pairs creation energy (ionization energy), $W_{\pm}$, is field-dependent as follows [35], [43], [44]

$$W_{\pm} = W_0 + B / E, \tag{1.2}$$

where W_0 (~6 eV at 20 keV) is the intrinsic ionization energy, B (~440 eV·V/μm) is the field-dependent parameter and E (~10 V/μm) is the electric field [35]. The calculated ionization energy for a-Se is around 50 eV. Therefore, for each x-ray photon with absorbed energy E_{ab} = 20 keV, the number of created electron-hole pairs is $E_{ab}/W_{\pm} \approx$ 400.

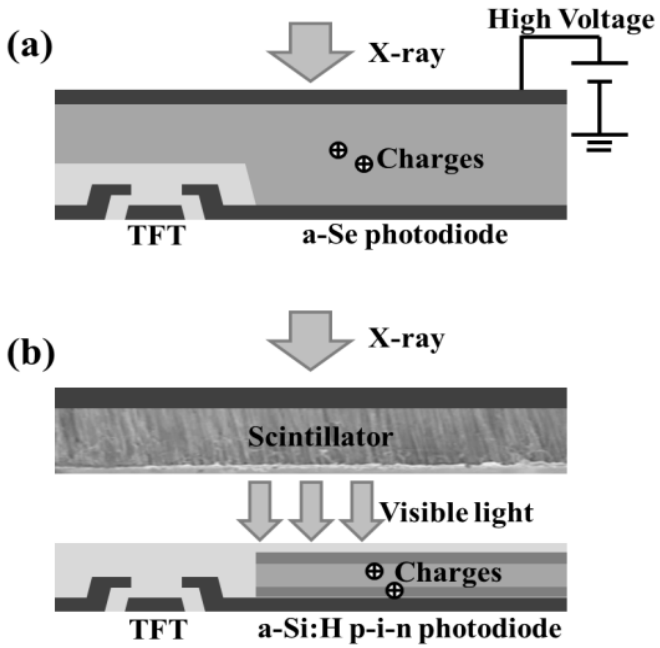

Figure 1.2 Schematics of (a) direct and (b) indirect conversion detectors are shown. An a-Se photodiode and a conventional a-Si:H p-i-n photodiode are used for indirect and direct conversion detectors, respectively.

After the separation of electron-hole pairs, electrons and holes will drift to the cathode and anode, respectively. During this process, the limiting factor is charge trapping of electrons and holes, which affects charge collection. The charge collection efficiency (η_{cc}) is given by [35], [45]

$$\eta_{cc} = x_h\left(1-\frac{1-\exp\left(-1/\Delta-1/x_h\right)}{\left[1+\left(\Delta/x_h\right)\right]\left[1-\exp\left(-1/\Delta\right)\right]}\right) + x_e\left(1-\frac{\exp\left(-1/x_e\right)-\exp\left(-1/\Delta\right)}{\left[1-\left(\Delta/x_e\right)\right]\left[1-\exp\left(-1/\Delta\right)\right]}\right), \tag{1.3}$$

where $x_h = \mu_h\tau_h E/L$, $x_e = \mu_e\tau_e E/L$ and $\Delta = \delta/L$. Although a thicker a-Se film (large L) increases the quantum efficiency A_Q, it is observed that η_{cc} is reduced for larger L. The optimized thickness of a-Se photoconductor is 200 – 300 μm by maximizing the product $A_Q \times \eta_{cc}$ (~0.95). For L > 300μm, $A_Q \times \eta_{cc}$ decreases due to the reduction of η_{cc}. This is consistent with the requirement that $\mu\tau E >> L$.

Compared with indirect conversion detectors, direct conversion detectors eliminate problems associated with the optical blurring of the scintillator, which is favorable for

high resolution DBT, while the drawbacks include required high electric field and relatively slow response due to the very low electron mobility of a-Se.

1.3.2 Indirect conversion x-ray detectors

For indirect conversion detectors, as shown in Figure 1.2(b), first x-rays are absorbed by a scintillating material and converted to photons in the visible light region. The optical photons impinge the photodiode and create electron-hole pairs, which will be separated to free carriers and collected by corresponding electrodes [46]. The conversion process from x-ray photons to electrons is indirect. Indirect x-ray detectors commonly consist of a scintillator such as CsI:Tl or terbium-doped gadolinium oxysulfide (Gd_2O_2S:Tb) and an a-Si:H p-i-n photodiode [47], [48]. The scintillators have a strong x-ray absorption properties generating $>4 \times 10^4$ photons/MeV and a fast response time in the range of microsecond to millisecond [49], [50]. Therefore, indirect conversion detectors are promising to be operated at a low dose condition and a short scan time (<4 s) for DBT. Although degradation of the modulation transfer function (MTF) at high spatial frequency region is expected due to the scintillator blurring effect, this impact can be minimized by implementation of structured phosphor such as CsI:Tl. The x-ray and optical photons can be wave-guided in the columnar structure of the CsI:Tl scintillator. Hence, the crosstalk between pixels is reduced and the image resolution can be improved. Moreover, pixelated CsI:Tl scintillator may be developed for further enhancement of spatial resolution [51], [52].

In this dissertation, we mainly focus on indirect conversion x-ray detector with the CsI:Tl scintillator. The physics of scintillator x-ray absorption, optical photon generation and propagation, optical coupling, photodiode carrier generation and collection will be discussed in Section 2.2.

1.3.3 Passive pixel sensor pixel and readout circuit

Today all the clinical approved DBT systems are based on the a-Si:H TFT PPS technology. As shown in Figure 1.3, each PPS pixel contains a photodetector (a-Si:H p-i-n photodiode or a-Se photoconductor), a pixel capacitor (C_{PIX}, which can be a combination of the photodiode capacitor and an additional storage capacitor) to store the

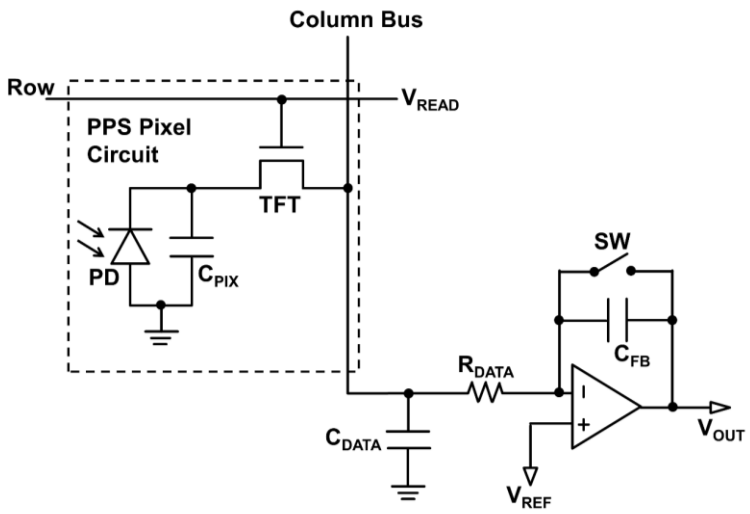

Figure 1.3 Schematic of pixel circuit and readout electronics of a-Si:H TFT PPS with a photodiode (PD). C_{PIX}, C_{DATA} and C_{FB} are the pixel, data line and feedback capacitance, respectively. R_{DATA} is the data line parasitic resistance. V_{READ}, V_{REF} and V_{OUT} are the TFT gate voltage, reference voltage of op-amp and output voltage, respectively. SW is the switch on the charge integrating amplifier.

converted electronic signal in the pixel, and an a-Si:H TFT as the switching element.

The operation of PPS circuit can be separated into three stages: integration, readout and reset.

(i) During the integration stage, the TFT gate voltage (V_{READ}) is low and the TFT is off. The TFT gate voltage is controlled by the row drivers. The photodiode is initially reversed biased at a reference voltage (V_{REF}). The x-ray pulse generates electronic charges (electrons), which are stored on C_{PIX}.

(ii) During the readout stage, V_{READ} is switched to high that turns on the TFT. The stored charge on C_{PIX} is transferred to the feedback capacitor (C_{FB}) on the preamplifier (as a charge integrator) of the external readout circuit. This will induce a change on the output voltage (V_{OUT}). The output voltage is

$$V_{OUT} = V_{REF} + \Delta Q_{IN} / C_{FB}, \tag{1.4}$$

where ΔQ_{IN} is the input charge. Since the same amount of charge is transferred from C_{PIX} to C_{FB}, the charge gain ($G = \Delta Q_{OUT}/\Delta Q_{IN}$) is unity. On the other hand, the voltage gain ($A_V = \Delta V_{OUT}/\Delta V_{IN}$) is C_{PIX}/C_{FB}. In general, C_{PIX} is around 1 pF, while C_{FB} is around 100 pF, thus $A_V << 1$.

(iii) After readout, the charge stored on C_{FB} is reset to zero by closing the switch

(SW) on the amplifier.

Although the compact PPS pixel circuit layout and simple fabrication process favor massive production for large area x-ray imagers, the main disadvantage of PPS is the high electronic noise from the external readout circuit. For a large-area active-matrix array with long column bus (data) lines, a large data line resistance (R_{DATA}) and capacitance (C_{DATA}) are connected to the input of the amplifier directly. It is known that the electronic noise of the external amplifier (σ_{amp}) is given by

$$\sigma_{amp} = \sigma_{amp0} + \gamma_{amp} C_{DATA}, \tag{1.5}$$

where σ_{amp0} is a constant (around 250 e^-) and γ_{amp} is around 15 e^-/pF [53]. The typical value for C_{DATA} is around 50 pF [41]. As a result, σ_{amp} is about 1000 e^-. Since the charge gain is unity for PPS x-ray detector, this noise is directly added to the total pixel noise, which will significantly degrade the image quality.

To minimize this impact, the input and output circuit must be separated by adding an additional amplifier in the pixel, i.e., active pixel sensor (APS).

1.4 Active Pixel Sensor (APS) X-Ray Detectors

1.4.1 CMOS APS x-ray detector

Recently, x-ray imagers based on the complementary metal-oxide-semiconductor (CMOS) APS have been considered as an alternative to a-Si:H TFT PPS x-ray detectors in bio-medical imaging applications. CMOS APS detectors overcome the drawbacks of conventional detectors by using a pixel amplifier that effectively reduces the noise floor [54], [55]. During the past few years, large area CMOS APS x-ray imagers with small pixel pitches ranging from 40 to 75 μm, low electronic noise of 50 – 165 e^-, dynamic range of 63 – 69 dB, fast frame rate of 20 – 30 fps have been developed [56]–[59].

Detector temporal performance such as lag and ghosting may cause image artifacts during the relative fast image acquisition process of DBT. Lag is the residual image charge generated in previous exposed frames that remains in electronics in subsequent frames as offset charge, while ghosting is associated with the change in x-ray sensitivity

induced by the x-ray exposure [28]. For example, for a-Se based x-ray imagers, both the lag and ghosting are caused by the charge trapping, ionization, and recombination mechanisms with the subgap bulk and interface trap states of a-Se. Zhao *et al.* have reported 4~5% image lag and ghosting using an a-Se PPS-based DBT system [28]. Unlike amorphous materials, the crystalline nature of CMOS APS x-ray detectors limits the bulk and interface traps of crystalline silicon (c-Si) to much lower values. As the result, a negligible image lag smaller than 0.1% was reported [60]. The ghosting is also expected to be minimal, which would not degrade the image. Therefore, CMOS APS x-ray detectors appear to be very promising for medical imaging technologies requiring fast frame rates (> 5 fps), such as DBT.

Specifically, the 2D projection image quality of a CMOS APS x-ray imager with a 75 μm pixel pitch (Dexela 2923 MAM) has been intensively evaluated for breast imaging applications such as mammography and DBT [59], [61]–[63]. Naday *et al* [64] and Park *et al* [63] also evaluated the DBT reconstructed images. As early indicators of breast cancer, detection of microcalcifications in sizes below 200 μm is critical but challenging for radiologists [65]. It was shown that experimentally important microcalcifications with 165 μm diameters (using a CIRS BR3D phantom) could be resolved using the Dexela 2923 MAM x-ray detector with a MGD of 2 mGy [66]. However, to distinguish smaller microcalcifications, x-ray detectors with a pixel pitch of 50 μm or smaller and low electronic noise are needed.

The Multidimensional Integrated Intelligent Imaging (MI-3) Plus consortium has developed a novel 50 μm pixel pitch CMOS APS x-ray detector (Dynamic Range Adjustable for Medical Imaging Technology), named DynAMITe. Fundamental electro-optical properties of the DynAMITe x-ray detector were previously investigated [57], [58]. Konstantinidis *et al*. show that a high contrast-to-noise ratio (CNR) and acceptable contrast-detail performance for mammography application can be achieved using the DynAMTe x-ray detector [67]. However, the x-ray imaging performance of such a high-resolution x-ray detector has not been evaluated for the low dose DBT application.

In this dissertation, both the 75 μm pixel pitch Dexela 2923 MAM [68] and 50 μm pixel pitch DynAMITe [69] CMOS APS x-ray detectors are characterized and modeled.

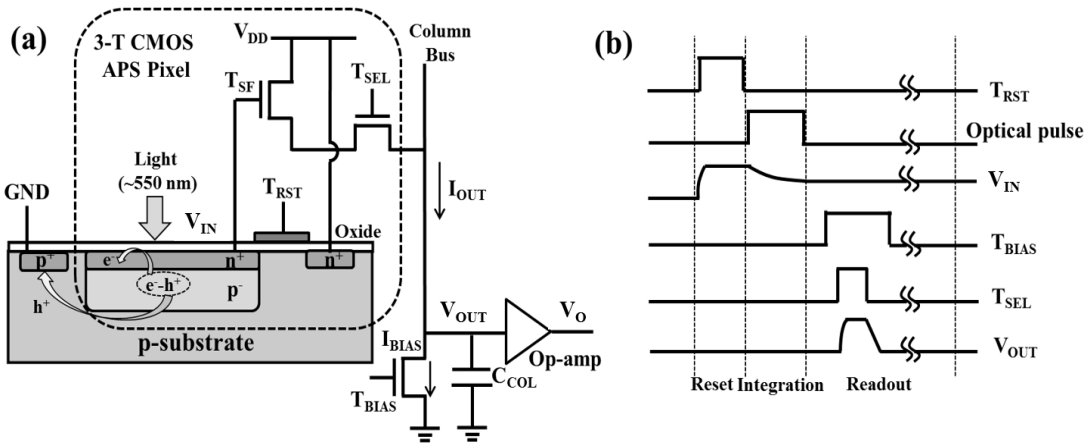

Figure 1.4 (a) Circuit schematic of 3-T CMOS APS pixel and readout electronics with cross-sectional view of the c-Si photodiode and T_{RST} are shown. T_{RST}, T_{SF} and T_{SEL} stand for the reset transistor, source follower and row select transistor for the pixel, respectively; T_{BIAS} is the column bias transistor and C_{COL} is the storage capacitor for the column bus line. (b) Driving scheme of the 3-T CMOS APS x-ray imager based on n-MOS technology is also shown.

Most of the CMOS APS x-ray detectors are based on the three-transistor (3-T) pixel design. Figure 1.4 illustrates the circuit schematic and driving scheme of the 3-T CMOS APS. In each pixel, there are a photodiode, a reset transistor (T_{RST}), a source follower (T_{SF}) and a row select transistors (T_{SEL}). Since in general voltage is used as the output signal for CMOS APS, the 3-T CMOS APS circuit can be categorized as voltage-mode APS (V-APS). The operation of APS is also separated into three stages: reset, integration and readout.

(i) ***During the reset stage***, T_{RST} is ON, while T_{SEL} is OFF. The high voltage V_{DD} is applied to the photodiode cathode (n^+-well) through the inversion channel of the T_{RST} and the input voltage V_{IN} is reset to V_{DD}. Since the photodiode p^--well is grounded, the n^+-p junction is reverse biased by V_{DD} and a depletion region is formed mainly in the p^--well. The dark current density of the n^+-p diode can be described by a combination of diffusion, thermal generation, and surface recombination current components [70]

$$J_{dark} \approx \frac{qD_n n_i^2}{L_n N_A} + \frac{qn_i W_D}{\tau_g} + \frac{1}{2} qn_i s_o, \tag{1.6}$$

where N_A is the doping concentration of the p^--well, D_n and L_n are the diffusivity and diffusion length for electrons, n_i is the intrinsic carrier density, W_D is the depletion width,

τ_g is the generation lifetime, and s_o is the surface recombination rate. The first term represents the diffusion dark current by the minority carriers across the depletion region; the second term is the thermal generation current by the space charge in depletion region; and the third term corresponds to the surface recombination current. The typical J_{dark} for CMOS APS is around 10 pA/cm^2. The low dark current level is favorable for low noise medical imaging applications such as DBT.

(ii) ***During the integration stage***, T_{RST} is OFF, while the x-ray source is ON. As shown in Figure 1.4 (b), pulsed x-ray source is used with integration time of t_{int} (around 100 ms for DBT). The x-rays generate optical photons in the scintillator. The impinging photons generate e-h pairs inside the photodiode depletion region that are separated into carriers by the electric field. Then electrons are collected in the n^+-well, while the holes are removed from p^--well through p-substrate to GND. The stored charge in the n^+-well decreases the potential V_{IN} below V_{DD}. The potential of n^+-well (V_{IN}) is given by

$$V_{IN} = V_{DD} - \frac{J_{photo} A_{PD} t_{int}}{C_{PIX}}, \tag{1.7}$$

where J_{photo} is the photocurrent density; A_{PD} is the area of photodiode; C_{PIX} is the pixel capacitance as a combination of photodiode capacitance and input node parasitic/storage capacitance.

If we neglect the dark current terms, the photocurrent density of c-Si photodiode is given by [71]

$$J_{photo} = q \cdot \frac{\Phi \cdot (1-R)}{h\nu_m} \left[1 - \frac{\exp(-\alpha W_D)}{1+\alpha L_n} \right], \tag{1.8}$$

where α is the absorption coefficient (in cm^{-1}) of c-Si, W_D is the deletion width of n^+-p junction, R is the total reflectance of the FOP/SiO_2 interface and SiO_2/Si interface, $h\nu_m$ is the mean photon energy of the optical emission spectrum, and Φ is the mean incident light intensity. Example of the driving schemes of the reset and integration stages are shown in Figure 1.4 (b).

The parameter external quantum efficiency (EQE) determines the ratio of the number of collected carriers by photodiode to the number of the incident photons, which is given by [71]

$$EQE = \frac{h\nu_m}{q} \cdot \frac{J_{photo}}{\Phi} = (1-R)\left[1 - \frac{\exp(-\alpha W_D)}{1+\alpha L_n}\right]. \quad (1.9)$$

To achieve a large EQE, the total reflectance R has to be minimized, and the product of αW_D needs to be maximized. The typical EQE value for CMOS APS x-ray detector is around 0.6 to 0.7.

(iii) ***During readout period***, both T_{SEL} and the column bias transistor T_{BIAS} are turned ON. The readout electronics can be simplified to a column storage capacitor (C_{COL}) and an operational amplifier (op-amp) [70], [72]. The output current following through T_{SF}, and T_{SEL} and charges up the column storage capacitor C_{COL}. The output voltage on the column storage capacitor (V_{OUT}) is amplified and read as the output voltage V_{OUT}. T_{BIAS} is biased such that it works in the saturation region and its drain-to-source current I_{BIAS} is given by

$$I_{BIAS} = \frac{1}{2}\left(\frac{W}{L}\right)_{BIAS} \mu_n C_{ox} (V_{G,BIAS} - V_{T,BIAS})^2, \quad (1.10)$$

where $(W/L)_{BIAS}$ is the channel width over length T_{BIAS}, μ_n is the electron mobility, C_{ox} is the oxide capacitance per unit area, $V_{G,BIAS}$ is the gate voltage and $V_{T,BIAS}$ is the threshold voltage of T_{BIAS}.

Neglecting the on-resistance of T_{SEL}, the output current of APS pixel I_{OUT} is determined by the gate-to-source voltage of T_{SF}. Since T_{SF} is operating in saturation region ($V_{DD} > V_{IN} - V_{T,RST}$), the total pixel output current can be expressed as [72]

$$I_{BIAS} + C_{COL}\frac{dV_{OUT}}{dt} = \frac{K_{SF}}{2}(V_{IN} - V_{T,SF} - V_{OUT})^2, \quad (1.11)$$

where $V_{T,SF}$ is the threshold voltage of T_{SF}, and K_{SF} is given by

$$K_{SF} = \left(\frac{W}{L}\right)_{SF} \mu_n C_{ox}, \quad (1.12)$$

where $(W/L)_{SF}$ is the transistor channel width over length of T_{SF}.

V_{OUT} as a function of readout time t is given by [72]

$$V_{OUT}(t) = V_{IN} - V_{T,SF} - k_2 \left(\frac{1 + \frac{k_1 - k_2}{k_1 + k_2} \exp\left(-\frac{k_2 K_{SF}}{C_{COL}} t \right)}{1 - \frac{k_1 - k_2}{k_1 + k_2} \exp\left(-\frac{k_2 K_{SF}}{C_{COL}} t \right)} \right), \tag{1.13}$$

where $k_1 = V_{IN} - V_{T,SF} - V_{COL}(0)$, and $k_2 = \sqrt{2I_{BIAS} / K_{SF}}$. For sufficient long readout time, V_{OUT} is saturated at ($V_{IN} - V_{T,SF} - k_2$). Therefore, in the ideal case, the voltage gain of CMOS APS is $A_V = \Delta V_{OUT}/\Delta V_{IN} = 1$. In reality, A_V of around 0.8 is typical for CMOS APS circuits.

The charge gain of CMOS APS, as the ratio of output and input charge variation, is given by.

$$G = \frac{\Delta Q_{OUT}}{\Delta Q_{IN}} = \frac{C_{COL}}{C_{PIX}}. \tag{1.14}$$

Since in general $C_{COL} >> C_{PIX}$, this will result in a substantial G. The large charge gain is expected to minimize the input-referred electronic noise.

If we consider the voltage gain (A_{amp}) of the external readout amplifier, the amplified output voltage (V_O) is presented as $V_O = A_{amp} V_{OUT} = A_{amp} (V_{IN} - V_{T,SF} - k_2)$.

The conversion gain (in volts/electron) of the APS pixel and readout electronics is given by the derivative of V_O to the total number of input charges (Q_{IN}/q):

$$CG = \frac{\Delta V_O}{\Delta Q_{IN} / q} = \frac{A_{amp} q}{C_{PIX}} \frac{\Delta V_{OUT}}{\Delta V_{IN}} = \frac{A_{amp} q}{C_{PIX}}. \tag{1.15}$$

C_{PIX} is a dominated by the photodiode capacitance (C_{PD}) and is also contributed by the pixel storage (C_{ST}) and/or the parasitic capacitance (C_{PAR}) at the input node. Therefore, to achieve a large conversion gain, the photodiode capacitance needs to be reduced. But when reducing the C_{PD}, the number of collected carrier is also be reduced. Hence, we need to reach a compromise between C_{PD} and photodiode area. In reality, C_{PD} is not a constant but dependent on V_{IN}. Therefore, CG is also a function of V_{PD}, which will result in signal nonlinearity.

Finally, an analog-to-digital converter (ADC) is used to convert the signal in volts to a digital number (DN). It should be noticed that for CMOS APS x-ray imager, the real signal is obtained by subtracting the average dark signal over a number (e.g. 32) of dark frames.

In this dissertation, both the 75 μm (Dexela 2923 MAM) and 50 μm pixel pitch (DynAMITe) x-ray detectors characterized for DBT application are based on the 3-T CMOS APS. CMOS APS x-ray detectors achieve both high resolution and ultra-low electronic noise (due to the high gain) at the same time. These properties are very promising for next generation DBT application, but the fabrication of large area CMOS APS x-ray detector is complicated and expensive. Sub-detector tiling is also needed to realize a CMOS APS detector active area (e.g., 25.6 × 26.2 cm^2) suitable for DBT.

Alternatively, due to the mature and cost-effective fabrication process of TFT array over large area, TFT-based APS x-ray detectors can also be introduced to medical imaging applications such as DBT.

1.4.2 TFT-based APS x-ray detectors

In the past decade, TFT-based APS circuits have been studied [53], [73], [74]. V-APS circuit similar to CMOS APS may be used for TFT APS. However, it has been reported that the readout speed for TFT-based V-APS is slow, with a rise time of around 250 to 700 μs for a-Si:H TFT V-APS [58]. This readout speed is not sufficient for large area DBT x-ray imagers.

Karim *et al.* introduced the a-Si:H TFT current-mode APS (C-APS) circuit by implementing a charge integrating amplifier (adopted from PPS) as the readout circuit [53], [73], [74], [77]. Although the pixel circuit remains the same as V-APS, the readout method is different for C-APS. An example circuit schematic of C-APS with readout electronics is shown in Figure 1.5 (a). The C-APS circuit has also been investigated for polysilicon (poly-Si) TFT APS x-ray detectors [78]–[82]. In this dissertation, among others we will focus on developing amorphous oxide semiconductor TFT-based C-APS for DBT to realize a high-resolution, high charge gain and low electronic noise [76], [83]–[85].

(i) During the reset and (ii) integration stages, the C-APS circuit operation is the same as that of CMOS V-APS.

(iii) During the readout stage, in the ideal case, if we neglect the on-resistance (R_{ON}) of the readout TFT (T_{RD}), the source voltage of the amplifying TFT (T_{AMP}) is fixed at ground (GND). Therefore, a constant current (I_{OUT}), which is the

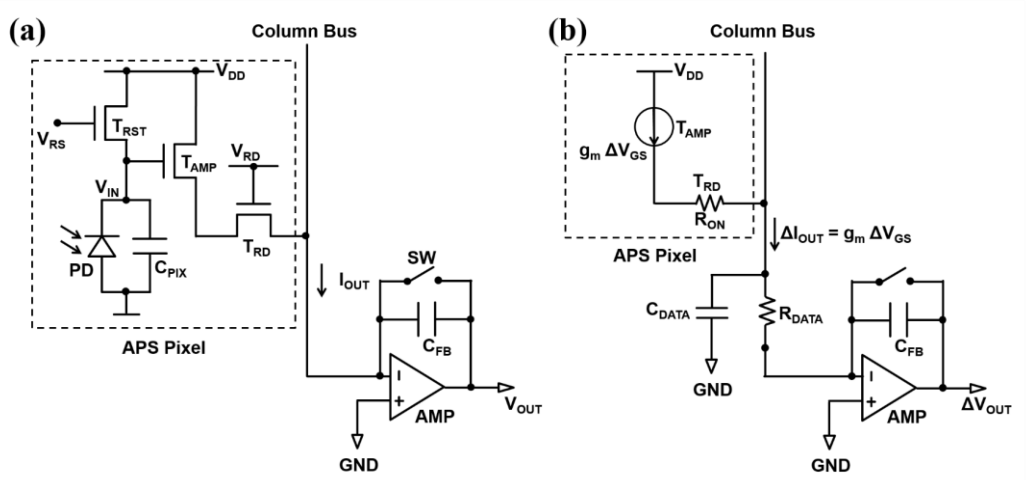

Figure 1.5 (a) Schematic of current-mode APS pixel and readout circuits. V_{IN}, V_{OUT} and I_{OUT} are the pixel input voltage, output voltage and output current, respectively. C_{FB} are the column capacitor and feedback capacitor for voltage-mode and current-mode APS, respectively. (b) Small signal circuit schematic of C-APS readout.

drain-to-source current of T_{AMP}, is used to charge up the C_{FB} on the charge integrating amplifier. Therefore, the output charge and voltage are determined by the pixel current. This circuit is called "current-mode" APS, where I_{OUT} is dependent on the T_{AMP} gate voltage (V_{IN}).

Detailed driving scheme of the TFT-based C-APS will be discussed in Chapter 7.

In reality, both R_{ON} and the data line resistance (R_{DATA}) could degrade the circuit performance. Figure 1.5 (b) shows the C-APS readout circuit schematic for a small signal analysis. Specifically, a small input voltage change ΔV_{IN} will lead to an output current change ΔI_{OUT}, which is given by

$$\Delta I_{OUT} = g_m \times \Delta V_{GS}, \tag{1.16}$$

where g_m is the transconductance of T_{AMP} and ΔV_{GS} is the gate-to-source voltage change of T_{AMP}. For C-APS operating in the saturation region,

$$g_m = \mu_{eff} \frac{W_{AMP}}{L} C_{ox} \left(V_{GS} - V_T\right), \tag{1.17}$$

where μ_{eff} represents the field-effect mobility of TFT, W_{AMP} and L are the channel width and length of T_{AMP}, C_{ox} is the gate insulator capacitance, and V_T is the threshold voltage of T_{AMP}.

The input voltage change ΔV_{IN} can be expressed as the sum of ΔV_{GS} and voltage

drop on R_{ON} and R_{DATA}, i.e.,

$$\Delta V_{IN} = \Delta V_{GS} + \Delta I_{OUT}\left(R_{ON} + R_{DATA}\right). \tag{1.18}$$

The on-resistance of T_{RD} can be described by

$$R_{ON} = \frac{L}{\mu_{eff} W_{RD} C_{ox}\left(V_{GS,RD} - V_T\right)}, \tag{1.19}$$

where W_{RD} is the channel width of T_{RD}, $V_{GS,RD}$ is the gate-to-source voltage of T_{RD}.

Overall, the readout circuit behaves like a degenerated source follower. Solving Equation 1.16 and 1.18, the charge gain of TFT-based C-APS is given by [53]

$$G = \left|\frac{\Delta Q_{OUT}}{\Delta Q_{IN}}\right| = \left|\frac{\Delta I_{OUT}}{\Delta V_{IN}}\right| \frac{t_{RD}}{C_{PIX}} = \frac{g_m}{1 + g_m \cdot (R_{ON} + R_{DATA})} \cdot \frac{t_{RD}}{C_{PIX}}, \tag{1.20}$$

where t_{RD} is the readout time (around 20 μs).

The voltage gain of C-APS simply follows

$$A_V = \left|\frac{\Delta V_{OUT}}{\Delta V_{IN}}\right| = \frac{C_{PIX}}{C_{FB}} G = \frac{g_m}{1 + g_m \cdot (R_{ON} + R_{DATA})} \cdot \frac{t_{RD}}{C_{FB}}. \tag{1.21}$$

To increase the charge or voltage gains of C-APS, it is critical to improve g_m and μ_{eff} of TFTs. The μ_{eff} of a-Si:H TFT is below 1 $cm^2V^{-1}s^{-1}$, which limits the C-APS performance. At the same time, R_{ON} and R_{DATA} must be minimized.

Among the candidates of high-mobility TFT technologies, amorphous In-Ga-Zn-O (a-IGZO) TFTs are widely considered as the next generation TFT technology for active-matrix flat-panel displays (AM-FPDs) and imagers (AM-FPIs) due to their high μ_{eff} of around 10 $cm^2\ V^{-1}s^{-1}$, low leakage current (I_{OFF} <10^{-13} A), improved electrical stability and high spatial uniformity [86]–[90]. Recently amorphous In-Sn-Zn-O (a-ITZO) with even higher μ_{eff} of around 30 $cm^2V^{-1}s^{-1}$ have also been studied [89], [91]–[94]. In this dissertation, device characteristics of a-ITZO TFTs are characterized in Chapter 6. a-ITZO TFT-based C-APS pixel circuit are designed and evaluated using SPICE simulation in Chapter 7.

Table 1.2 shows the comparison of PPS, V-APS and C-APS circuits. Both V-APS and C-APS circuits can achieve a high charge gain to reduce the electronic noise. Advanced CMOS technology should be used for V-APS due to the slow readout speed of TFT-based V-APS. High-mobility amorphous oxide semiconductor TFTs are

favorable to C-APS achieving both a high charge gain and fast readout.

	PPS	V-APS	C-APS
Transistor technology	TFT	CMOS or TFT	TFT
Output signal	charge	voltage	current
Voltage gain (A_V)	C_{PIX}/C_{FB} << 1	1	$\frac{g_m}{1+g_m\cdot(R_{ON}+R_{DATA})}\cdot\frac{t_{read}}{C_{FB}}$
Charge gain (G)	1	C_{COL}/C_{PIX} >>1	$\frac{g_m}{1+g_m\cdot(R_{ON}+R_{DATA})}\cdot\frac{t_{read}}{C_{PIX}}\gg 1$
Electronic noise	high	low	Low
Readout speed	fast	CMOS - fast TFT - slow	fast

Table 1.2 Comparison of PPS, V-APS and C-APS circuits.

1.5 Dissertation Organization

This dissertation presents the electrical, optical and x-ray imaging performance of high-resolution x-ray detectors based on CMOS (Chapters 2 – 5) and amorphous oxide semiconductor TFT (Chapters 6 and 7) APS technologies.

- **Chapter 2** discusses the experimental methods and cascaded system analysis to characterize and model the x-ray imaging properties (i.e., modulation transfer function (MTF), noise power spectrum (NPS), and detective quantum efficiency (DQE)) of CMOS APS x-ray detectors. This chapter is partially based on [68], [69], [84].
- **Chapter 3** presents the measured and simulated (based on 2D cascaded system analysis) detector imaging characteristics (2D MTF, NPS and DQE) for both a 75 μm pixel pitch (Dexela 2923 MAM) and a 50 μm pixel pitch (DynAMITe) CMOS APS detectors. This chapter is based on [68], [69].
- **Chapter 4** discusses the 3D and in-plane MTF, NPS and DQE parameters of the DynAMITe detector using the 3D cascaded system analysis model. This chapter is based on [95].

- **Chapter 5** proposes a task-based model in combination with the 3D cascaded system analysis to simulate the detectability index (*d'*) and area under the receiver operating characteristic (ROC) curve, i.e., AUC, for multiple imaging tasks using the DynAMITe detector. This chapter is based on [96].
- **Chapter 6** evaluates the device characteristics and stability of DC sputtered a-ITZO TFTs. This chapter is based on [97].
- **Chapter 7** discusses the SPICE simulation, pixel layout design, fabrication, and electronic noise of a-ITZO TFT C-APS circuits for DBT application. This chapter is partially based on [85], [98], [99].
- **Chapter 8** summarizes this dissertation work. Future research directions are also recommended.

Chapter 2

X-Ray Imaging Performance Evaluation and Cascaded System Analysis for APS X-Ray Detectors

2.1 Empirical Imaging Performance Characterization of X-Ray Detectors

This section discusses the experimental methods used to characterize the x-ray detector x-ray imaging performance parameters: MTF, NPS and DQE in the spatial frequency domain. Specifically, the MTF measures the detector signal resolution; the NPS describes a combination of x-ray quantum and detector electronic noise; and the DQE combines both the signal (in MTF) and noise (in NPS) indicating the detector 2D projection imaging performance.

The experimental methods were used to characterize the detector performance of a 75 μm pixel pitch Dexela 2923 MAM [68] and a 50 μm pixel pitch DynAMITe [69] CMOS APS x-ray detector that are discussed in Chapter 3.

2.1.1 X-ray fluence

For an x-ray spectrum, the mean x-ray fluence ($\overline{q_0}$), defined by the number of incident x-ray quanta per unit area, changes as a function of the detector air kerma (K_a). The mean x-ray fluence per air kerma ($\overline{q_0}/K_a$) in x-rays mm^{-2} μGy^{-1} is given by [100]

$$\overline{q_0}/K_a = \int_0^{E_{\max}} \Phi_{0,norm}(E)\left(\frac{q_0}{K_a}(E)\right)dE = \int_0^{E_{\max}} \Phi_{0,norm}(E)\frac{W\cdot Q}{(\mu_{en}(E)/\rho)_{air}\cdot E\cdot q\cdot 10^8}dE, \quad (2.1)$$

where $\Phi_{0,\text{norm}}$ is the normalized x-ray spectrum (sum up to unity), (q_0/K_a) is the x-ray

fluence per air kerma at each energy E, W is the air work function (33.97 eV), Q is the charge liberated in air by one Roentgen (1 R = 8.76 mGy), q is the electron charge and $(\mu_{en}(E)/\rho)_{air}$ is the mass energy absorption coefficient of air.

2.1.2 Modulation transfer function (MTF)

The MTF measures the change in signal amplitude through an imaging system in the spatial frequency domain. The tilted edge technique was used to measure the MTF of CMOS APS detectors [101]. An x-ray opaque, polished edge plate (e.g., W foil, 1 mm thick, 99.95 % pure) was placed in front of the detector at a small tilted angle (1.5 - 3°) with respect to the detector rows and columns. A number of raw edge images (e.g. N = 20 to reduce the random noise) was captured when placing the edge horizontally and vertically. A standard gain and offset correction algorithm was applied to remove the fixed pattern noise (FPN) by capturing additional 10 frames of flat and dark images without the edge sample [102]. The corrected edge images can be extracted by [102], [103]

$$\overline{Edge_{corr1}}(x,y)=\left[\overline{Edge}(x,y)-\overline{Dark}(x,y)\right]\cdot\frac{\overline{\overline{Flat}(x,y)-\overline{Dark}(x,y)}}{\overline{Flat}(x,y)-\overline{Dark}(x,y)} \tag{2.2}$$

where $\overline{Edge}(x,y)$, $\overline{Flat}(x,y)$, and $\overline{Dark}(x,y)$ are the mean edge, flat and dark images over n frames. $\overline{\overline{Flat}(x,y)-\overline{Dark}(x,y)}$ is a scaling factor (a constant) as the mean pixel value of an offset-corrected flat image. Figure 2.1 (a) shows a gain and offset corrected edge image $\overline{Edge_{corr1}}(x,y)$.

After that, a second order polynomial fit ($S(x, y)$) correction was applied to the gain and offset corrected images to remove the low spatial frequency trends caused by the x-ray field non-uniformity [102], [104]. The detrended edge image is given by

$$\overline{Edge_{corr2}}(x,y)=\frac{\overline{Edge_{corr1}}(x,y)}{S(x,y)}\cdot\overline{S(x,y)} \tag{2.3}$$

where $\overline{S(x,y)}$ is the mean value of the second order polynomial fit $S(x,y)$. Figure 2.1 (b) shows an example of $S(x,y)$ taking into account the x-ray field nonuniformity.

The corrected pixel values of several consecutive lines across the edge were used to

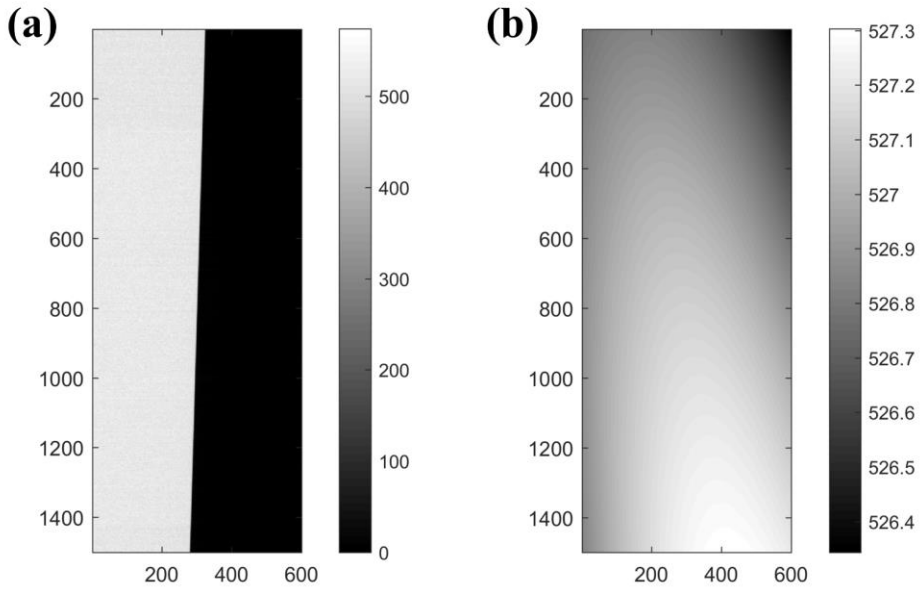

Figure 2.1 An example of (a) gain and offset corrected edge image, $Edge_{corr1}$, and (b) second order polynomial fit $S(x,y)$ to detrend the corrected image.

generate the oversampled edge spread function (ESF) curves. These ESF curves were laterally shifted to the same position and combined (averaged) to reduce the statistical noise. The averaged ESF was differentiated to obtain the oversampled line spread function (LSF). Finally, a Fourier transform (FT) of the LSF gives the MTF (normalized to 1) in the spatial frequency domain corresponding to either spatial x or y direction [62]. The process of MTF extraction is summarized by the following expression and shown in Figure 2.2.

$$MTF(u) = \left| FT\left\{ LSF(x) \right\} \right| = \left| FT\left\{ \frac{d}{dx}\left[ESF(x) \right] \right\} \right|. \tag{2.4}$$

2.1.3 Noise power spectrum (NPS)

The NPS describes the change in signal variance through an imaging system in the spatial frequency domain. A subtraction algorithm was applied for gain and offset correction. The corrected flat image $I(x, y)$ using the modified gain and offset correction algorithm reported by Konstantinidis *et al*. [103]

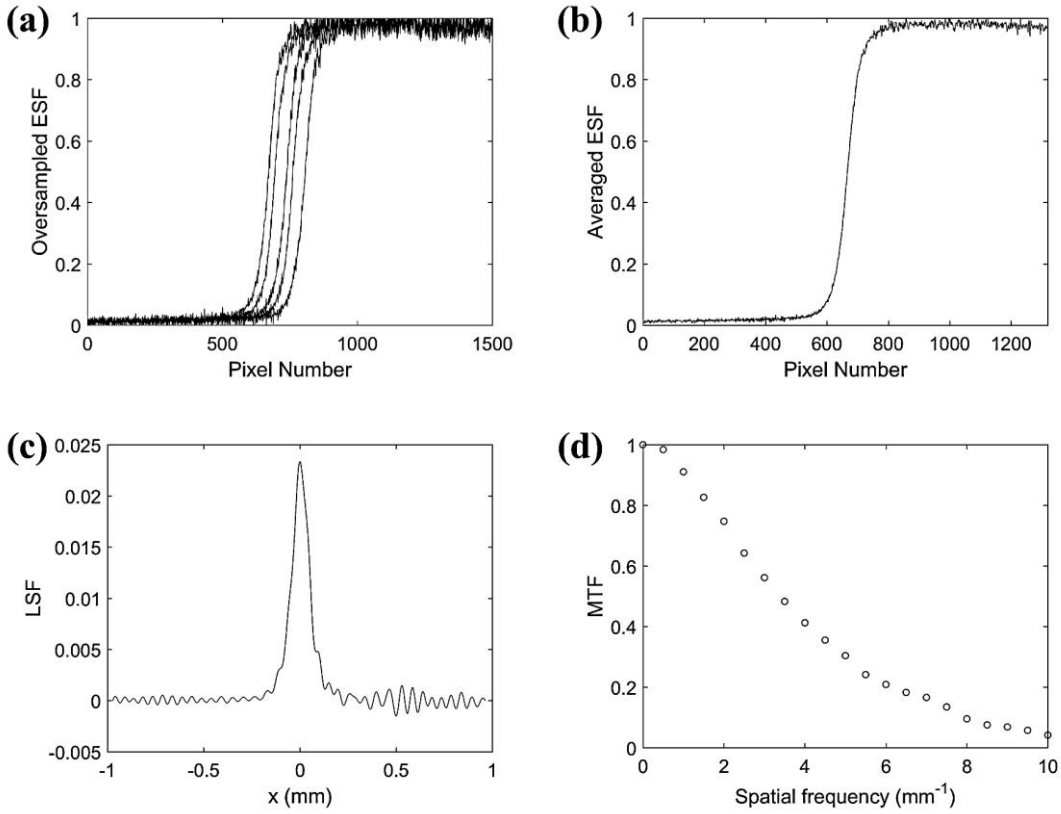

Figure 2.2 An example of extracted (a) oversampled edge spread function, (b) averaged edge spread function, (c) line spread function and (d) modulation transfer function from corrected edge images.

$$I(x,y) = \frac{Flat_1(x,y) - Flat_2(x,y)}{\sqrt{2}} + \overline{\overline{Flat}(x,y) - \overline{Dark}(x,y)}, \qquad (2.5)$$

where $Flat_1(x,y)$ and $Flat_2(x,y)$ are two frames of the raw flat image. Figure 2.3 (a) shows an example of the gain and offset corrected flat image.

The NPS was measured based on the IEC standard [104]. First, overlapping regions of interest (ROI) of 256 × 256 pixels were selected from a central area (1280 × 1280 pixels) of the gain and offset corrected flat image. Then a second order polynomial fit ($S(x,y)$) was performed to the corrected flat-field image ($I(x,y)$) to remove the low frequency (background) trends. The 2D NPS profile can be calculated from the sum of Fourier transforms of ($I(x,y)$-$S(x,y)$) for all the ROIs.

$$NPS(u,v) = \frac{\Delta x \cdot \Delta y}{N_{ROI} \cdot N_x \cdot N_y} \sum_{i=1}^{M} \left| FT\left[I(x_i, y_i) - S(x_i, y_i) \right] \right|^2 \qquad (2.6)$$

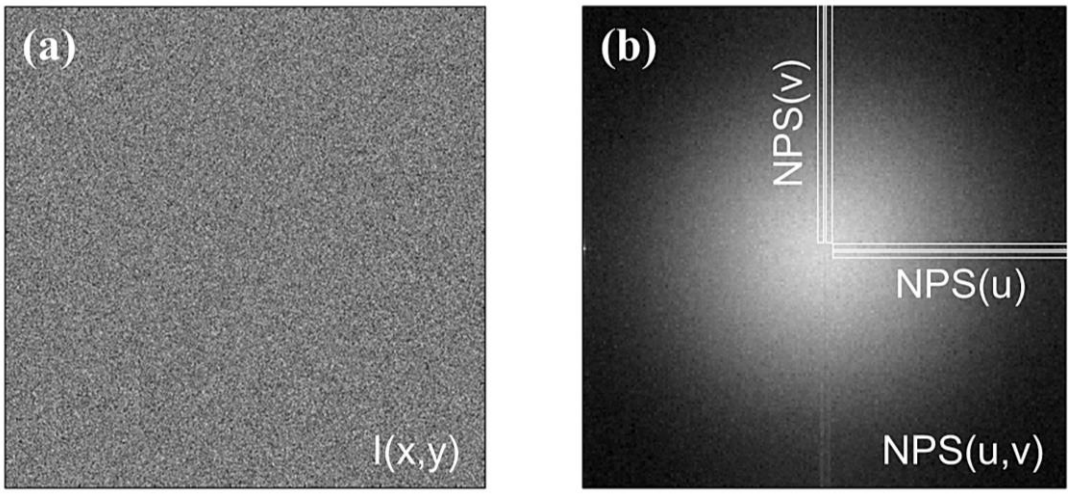

Figure 2.3 An example of (a) gain and offset corrected flat image $I(x, y)$ and (b) extracted 2D NPS(u, v).

where Δx and Δy are the pixel pitches in x and y directions, N_{ROI} is the number of ROIs, N_x and N_y gives the number of rows and columns in each ROI ($N_x = N_y = 256$). We selected three frames of corrected images with 1280 × 1280 pixels each to realize more than four million independent pixels to get an accuracy of 5% on the NPS results that corresponds to 10% accuracy on the DQE values [104]. In each frame, several (i.e., 9 by 9) ROIs of 256 × 256 pixels each were selected with a shift of 128 pixels (half-overlapping ROIs according to the IEC 62220-1-2 standard). Therefore, $N_{ROI} = 9 \times 9 \times 3 = 243$.

Figure 2.3 (b) presents an example of extracted 2D NPS(u, v). Data from seven rows and columns on both sides of the zero-spatial frequency (a total of 14 lines) was extracted and averaged, resulting in the horizontal and vertical 1D NPS. The 1D normalized NPS (NNPS) was calculated by $NNPS(u) = NPS(u) / d(DN)^2$, where $d(DN)$ is the mean large area output signal in digital number. The above steps were repeated to extract 1D NNPS for various x-ray exposure levels.

The mean signal d(DN) and mean variance σ^2(DN^2) were also experimentally determined from the flat field images captured for NNPS calculation using the following expressions [105], [106]

$$d(DN) = \frac{1}{MN}\sum_{i,j}\overline{d_{i,j}}, \quad \text{where } \overline{d_{i,j}} = \frac{1}{L}\sum_{k} d_{i,j,k} \tag{2.7}$$

and

$$\sigma^2(DN^2) = \frac{1}{MN}\sum_{i,j}\overline{\sigma_{i,j}^2}, \text{ where } \overline{\sigma_{i,j}^2} = \frac{1}{L}\sum_{k} d_{i,j,k}^2 - \left(\overline{d_{i,j}}\right)^2. \quad (2.8)$$

where M and N are the pixel numbers in x and y directions, L (= 10) is the number of flat field images, $\overline{d_{i,j}}$ and $(\overline{\sigma_{i,j}})^2$ are the mean signal and variance at position (i, j) over L frames, respectively.

2.1.4 Detective quantum efficiency (DQE)

DQE is the ratio between the square of output $(SNR_{out})^2$ and input signal-to-noise ratio $(SNR_{in})^2$. Since $(SNR_{in})^2$ is the x-ray fluence $(\overline{q_0})$ multiplied by the pixel area $(a_{pix})^2$, DQE indicates the dose efficiency. The 1D DQE (e.g., horizontal, at x or u direction) can be calculated by [104]

$$DQE(u) = \frac{(SNR_{out})^2}{(SNR_{in})^2} = \frac{d(DN)^2 \cdot MTF^2(u)}{\overline{q_0} \cdot NPS(u)} = \frac{MTF^2(u)}{\overline{q_0} \cdot NNPS(u)}. \quad (2.9)$$

2.2 2D Cascaded System Analysis for Indirect CMOS APS X-Ray Detectors

To investigate detector key parameters such as the MTF, NPS and DQE, cascaded system analysis is a very useful tool. This technique has been widely used to examine the 2D imaging performance of x-ray detectors [46], [47], [107], [108]. In such analysis, the signal and noise propagation and blurring within the x-ray imaging system are divided into a series of gain and spreading stages.

In this dissertation, the 2D cascaded system analysis is used to characterize the detector 2D x-ray imaging performance of both the Dexela 2923 MAM (75 μm pixel pitch) and DynAMITe (50 μm pixel pitch) CMOS APS x-ray detectors.

Figure 2.4 shows the scheme illustration of signal and noise transfer for gain and spreading stages [47]. The signal and noise transfer for a gain stage can be described by [47]

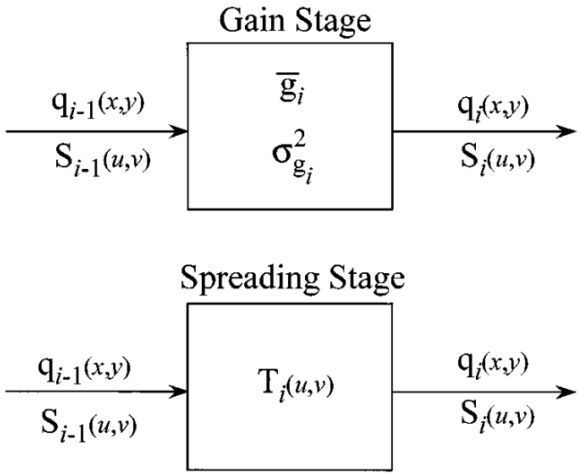

Figure 2.4 Schematic of the signal and noise transfer for gain and spreading stages using cascaded system analysis (adopted from [47]).

$$\begin{aligned} &\bar{q}_i = \bar{g}_i \bar{q}_{i-1}, \\ &S_i(u,v) = \bar{g}_i^2 S_{i-1}(u,v) + \sigma_{g_i}^2 \bar{q}_{i-1} + S_{add}, \end{aligned} \qquad \text{(gain stage)} \qquad (2.10)$$

where $\bar{q}_i$ and $\bar{g}_i$ are the mean signal and gain of stage *i*. S_i and σ_{gi} are the noise power spectrum and gain variance of stage *i*. *u* and *v* stand for the spatial frequencies in x and y directions, respectively. S_{add} is the additive noise power spectrum such as the detector electronic noise.

The spreading stages can be categorized into "stochastic" or "deterministic" spreading stages. A stochastic spreading stage can distribute an x-ray or optical quanta randomly with a distance described by the point spread function (PSF) in the spatial domain (or a transfer function $T_i(u,v)$ in the spatial frequency domain). Examples of stochastic spreading stages are scintillator and fiber optic plate (FOP) blurring. On the other hand, a deterministic spreading stage describes sampling of an optical quanta by a pixel aperture. The noise power spectra of stochastic and deterministic spreading stages are given by [47]

$$\begin{aligned} &S_i(u,v) = \left[S_{i-1}(u,v) - \bar{q}_{i-1} \right] T_i^2(u,v) + \bar{q}_{i-1}, && \text{(stochastic spreading stage)} \\ &S_i(u,v) = S_{i-1}(u,v) T_i^2(u,v). && \text{(deterministic spreading stage)} \end{aligned} \qquad (2.11)$$

Based on the above theory, a 9-stage 2D cascaded system analysis model is

developed as follows.

2.2.1 2D cascaded system analysis model

Stage 0: Incident x-ray quanta. The input x-ray signal (mean x-ray fluence, $\bar{q}_0$) is proportional to the input air kerma (K_a) at detector surface. The mean x-ray fluence per input air kerma, $\bar{q}_0 / K_a$ (in x-rays/mm^2 per μGy) can be obtained using the incident x-ray spectrum ($\Phi(E)$) and the mass energy-absorption coefficient of dry air $(\mu_{en}/\rho)_{air}$ in cm^2/g as a function of x-ray energy E (Equation 2.1).

Stage 1: X-ray absorption by CsI:Tl scintillator (gain stage). The first gain stage of the system describes the mean x-ray absorption by the scintillator ($\bar{g}_1$). For cascaded system, $\bar{g}_1$ is generally determined by the quantum detection efficiency (QDE), representing the mean number of absorbed x-rays per incident x-ray quanta [47], [109]. However, as the scintillator is an energy integrator rather than a photon counter [110], the energy absorption efficiency (EAE), defined by the mean energy absorbed per incident unit of energy, gives a better estimation of the maximum detectability of the system for x-ray energies below the K-absorption edge of iodine at 33.2 keV [59]. Hence, we used EAE to calculate the x-ray absorption by scintillator. $\bar{g}_1$ is given by

$$\bar{g}_1 = EAE = \frac{\int_0^{E_{\max}} \Phi_0(E) \cdot T_0(E) \cdot E \cdot \left(\frac{\mu_{en}(E)}{\mu(E)} \right) \cdot \left(1 - e^{-\mu(E)t}\right) \cdot dE}{\int_0^{E_{\max}} \Phi_0(E) \cdot E \cdot dE}, \quad (2.12)$$

where $\Phi_0(E)$ is the x-ray energy spectrum as a function of x-ray photon energy (E), $T_0(E)$ is the transmission (0.85 – 0.95) of the scintillator protection layer, t is the scintillator thickness (150 – 200 μm for CsI:Tl scintillator used for CMOS APS x-ray detector), $\mu(E)$ and $\mu_{en}(E)$ are the linear attenuation and energy absorption coefficients of the scintillator, respectively [110].

In general, EAE is scintillator thickness dependent, i.e., a thicker CsI:Tl layer produces a higher EAE. However, at the same time, the long optical path in the scintillating material degrades the MTF and DQE at high spatial frequencies due to the light scattering effect.

Stage 2: Optical photon generation and emission in scintillator (gain stage). The absorbed x-rays are converted into optical photons in the scintillator. The conversion process can be divided into three consecutive stages: a) the excitation of electrons in the atomic inner shell, and relaxation and creation of a large number of electron-hole (e-h) pairs through an avalanche process; b) carrier migration and further relaxation leading to formation of excitons, having an energy smaller than the bandgap; and c) e-h recombination and light emission (photoluminescence) [111], [112]. In general, to create an e-h pairs, an average energy (E_{eh}) greater than compound's bandgap (E_{g}) is required. The number of optical photons generated inside the scintillator by an absorbed x-ray photon with energy E is given by [111], [112]

$$N_{ph}(E) = N_{eh}(E) \cdot S \cdot Q = \frac{E}{E_{eh}} \cdot S \cdot Q, \tag{2.13}$$

where $N_{\text{eh}}(E)$ is the number of e-h pairs generated by a single x-ray photon with energy E, S is the transfer efficiency of the e-h pair energy to the luminescent center inside the bandgap, Q is the luminecense quantum efficiency, and E_{eh} is the average energy required to create one e-h pair. The optical yield (in photons/keV), the number of optical photons generated by a single x-ray photon per unit x-ray energy, is given by

$$\eta_{opt} = \frac{N_{ph}(E)}{E} = \frac{1}{E_{eh}} \cdot S \cdot Q. \tag{2.14}$$

For CsI:Tl, E_{eh} is around $2.5E_{\text{g}}$ and E_{g} is 6.4 eV [49]. S and Q are dependent on the material manufacturing technology. Assuming S and Q are equal to 1 (ideal case), the calculated maximum η_{opt} of CsI:Tl is 62 photons/keV, which is within the range of reported experimental values ranging from 52 to 66 photons/keV [112], [113].

In the cascaded system analysis, η_{opt} of 55 – 58 photons/keV was used.

The fraction of generated photons that can escape from the scintillator ($\eta_{\text{esc}}(z)$) is associated with the vertical distance z to the bottom interface between the scintillator and a fiber optic plate (FOP) as the substrate [114]. The light output in number of escaped optical photons per absorbed x-ray quanta of energy E at position z is given by $g_2(E,z) = \eta_{\text{opt}} \times E \times \eta_{\text{esc}}(z)$. The mean light output (number of optical photons) per absorbed x-ray by a scintillator with thickness t is given by [109]

$$\overline{g_2} = \frac{\int_0^{E_{\max}} \sum_z \Phi_0(E)\left(e^{-\mu(E)(t-z)}\right)\left(1-e^{-\mu(E)\Delta z}\right) g_2(E,z)dE}{\int_0^{E_{\max}} \Phi_0(E)T_0(E)\left(1-e^{-\mu(E)t}\right)dE}. \quad (2.15)$$

The Poisson excess (ε_{g2}) describes the gain variance of $\overline{g_2}$, which is given by

$$\varepsilon_{g2} = \overline{g_2}\left(\frac{1}{I_S}-1\right)-1, \quad (2.16)$$

where I_S is the Swank factor quantifying the noise associated with x-ray to photon conversion process [46], [115].

Stage 3: Scintillator scattering (stochastic blurring stage). The lateral scattering of optical photons in the scintillator can introduce optical cross-coupling between imager pixels leading to image blur and degradation of image quality. This is the first blurring stage that spatial frequency is included in the cascaded system. In this dissertation, we propose two methods to extract the transfer function of this stage (T_3).

Method 1: The scintillator scattering can be approximated by a Lorentzian fit to the experimental data [47]

$$T_3(u,v) \approx \left(1+H_3{}^2\left(u^2+v^2\right)\right)^{-1}, \quad (2.17)$$

where H_3 can be obtained by fitting the experimental MTF data, u and v are the spatial frequencies in x and y direction, respectively.

It is known that CsI:Tl forms needle-shaped crystal columns that prevent the optical cross-coupling. Sharma *et al*. studied the impacts of CsI:Tl structure and optical properties of the scintillator MTF (T_3) through Monte Carlo simulations [116]. It was observed that the scintillator MTF would increase with a larger bulk absorption coefficient, reduced surface roughness, smaller inter-column distance and suppressed columnar wall crossover in the first monolayer of the scintillator in contact with the FOP. In this work, all these effects are simplified to a factor H_3, i.e., a smaller H_3 value will lead to an improved T_3(u,v).

This method was used to extract T_3 for the DynAMITe x-ray detector to be discussed in Section 3.2 [69].

Method 2: An alternative approach that we applied to extract T_3(u,v) was using an

exponential decay function to fit the measured system one dimensional (1D) MTF [68]

$$MTF(u) = A \times \exp(-u / B) + C, \tag{2.18}$$

where A, B and C are fitting parameters. Then the combined scintillator (Stage 3) and the FOP (Stage 5) blurring function ($T_3 \times T_5$) can be calculated by dividing the fitted system MTF by the transfer function of the pixel aperture T_7(u,v) as described in Stage 7. Note that this method extract the product of T_3 and T_5, thus Stage 5 can be neglected if the exponential decay function is used.

This method was used in the cascaded system analysis for the Dexela 2923 MAM CMOS APS x-ray detector (Section 3.1) [68].

Stage 4: Optical coupling of the fiber optic plate (gain stage). In general, the CsI:Tl scintillator is attached to the CMOS image sensor by a FOP. The optical photons that escape from the scintillator impinge the FOP. The optical coupling efficiency ($\overline{g_4}$) defined by the fraction of photons transmitted through the FOP is given by [117]

$$\overline{g_4} = NA^2 T_F (1 - L_R) F_C, \tag{2.19}$$

where NA (~1) is the numerical aperture of a fiber optic, T_F (0.65 – 0.8) is the transmittance of fiber optic core, L_R (~0.1) is the Fresnel reflection optical loss at the surface and F_C (~0.75) is the fill factor of the fiber optic core [117], [118]. Calculated $\overline{g_4}$ of 0.44 – 0.55 was used for the cascaded system analysis.

Taking the above stages into consideration, the NPS at stage 4 is given by [47]

$$S_4(u,v) = \overline{q_0 g_1 g_2 g_4}\left[1 + \overline{g_4}(\overline{g_2} + \varepsilon_{g2}) T_3^2(u,v)\right], \tag{2.20}$$

Stage 5: Image blurring by the fiber optic plate (stochastic blurring stage). In addition to the scintillator, the FOP also blurs the image [118]. Equation 2.17 can be also used to model the FOP blurring ($T_5(u,v)$) by changing H_3 to H_5 of around 0.06 to fit the data from Jain *et al* [118]. Since the FOP blurring is a stochastic spreading stage [107], the NPS at stage 5 can be written as

$$\begin{aligned} S_5(u,v) &= (S_4(u,v) - \overline{q_0 g_1 g_2 g_4}) T_5^2(u,v) + \overline{q_0 g_1 g_2 g_4} \\ &= \overline{q_0 g_1 g_2 g_4}\left[1 + \overline{g_4}(\overline{g_2} + \varepsilon_{g2}) T_3^2(u,v) T_5^2(u,v)\right], \end{aligned} \tag{2.21}$$

Note: This stage may be skipped if Method 2 is used at Stage 3.

Stage 6: Photon absorption and electron generation by photodiode (gain stage). For CMOS APS x-ray detectors, the optical photons that escaped from the FOP are absorbed by the c-Si photodiode. Photo-induced carriers are generated in the depletion region and electrons are captured by the N^+ well. The gain of this stage ($\overline{g_6}$) represents the number of electrons collected per incident photon, i.e., the external quantum efficiency (EQE) of photodiode (Equation 1.9). The NPS at this stage is

$$S_6(u,v) = S_5(u,v)\overline{g_6}^2 + \overline{q_0 g_1 g_2 g_4 g_6}(1-\overline{g_6}), \tag{2.22}$$

Stage 7: Pixel presampling and blurring (deterministic blurring stage). The imager pixel blurring associated with the photodiode active area is expressed as [47], [119]

$$T_7(u,v) = \left|\mathrm{sinc}(\pi a_{pd} u)\cdot \mathrm{sinc}(\pi a_{pd} v)\right|, \tag{2.23}$$

where a_{pd} is the effective pitch of the photodiode. We assume that the photodiode active area is square. Then a_{pd} is given by

$$a_{pd} = a_{pix}\sqrt{FF}, \tag{2.24}$$

where a_{pix} is the pixel pitch and FF is the pixel fill factor (area ratio of the photodiode and entire pixel). A smaller a_{pd} will lead to a greater T_7(u,v) and thus MTF(u,v) at high spatial frequencies. Therefore, a high-resolution detector (e.g. 50 – 75 μm pixel pitch) is needed for DBT to distinguish fine details (such as microcalcifications) associated with high spatial frequencies.

As this spreading stage is deterministic, the NPS of stage 7 is given by

$$S_7(u,v) = a_{pd}^4 S_6(u,v) T_7(u,v). \tag{2.25}$$

Up to this stage, all the spreading stages have been described. The system presampling MTF can be written as

$$MTF(u,v) = T_3(u,v)T_5(u,v)T_7(u,v). \tag{2.26}$$

$d(e^-) = (a_{\mathrm{pd}})^2\overline{q_0 g_1 g_2 g_4 g_6}$ gives the electrical signal in electrons on the sensing node (gate of T_{SF} for CMOS V-APS or T_{AMP} for TFT-based C-APS).

Stage 8: NPS aliasing. The limiting spatial frequency (Nyquist frequency, f_{Nyq}) is given by $1/(2a_{\mathrm{pix}})$ because of aliasing. The f_{Nyq} for 75 and 50 μm pixel pitch is 6.7 and 10 mm^{-1}, respectively. This stage represents the NPS aliasing of the detector. The NPS after aliasing is given by [46], [108], [119]

$$S_8(u,v) = S_7(u,v) ** III_8(u,v) = \sum_{m,n=-\infty}^{+\infty} S_7(u - \frac{m}{a_{pix}}, v - \frac{n}{a_{pix}}), \qquad (2.27)$$

where m and n are integers, and $III_8(u,v)$ is a Fourier transform of the sampling grid (i.e., a 2D comb function) [108].

Stage 9: APS conversion gain and read noise: For CMOS APS x-ray detectors, the last stage of the 2D cascaded system describes the electron-to-DN conversion process and includes additional read noise for CMOS APS. The conversion gain (CG) in DN/e^- of CMOS APS is defined as the ratio between the variations in output (in DN) and input signals (in e^-). The mean variance (MV) analysis method is widely used to extract CG and σ_{R} for CMOS image sensors [57], [62], [106]. The total variance of the digital signal (σ_{S}^2) as a function of output digital signal d(DN) is given by

$$\sigma_S^2(DN^2) = CG(DN/e^-)d(DN) + \sigma_R^2(DN^2), \qquad (2.28)$$

where the conversion gain CG(DN/e^-) and the read noise σ_{R}(DN) can be extracted from the slope and intercept of the mean variance curve. Note that this method is commonly used with the optical illumination, thus the detector is tested using a light source without scintillator. The input referred read noise in electrons (at N^+-well of photodiode) is simply $\sigma_{\mathrm{R}}(e^-) = \sigma_{\mathrm{R}}(\mathrm{DN})/CG(\mathrm{DN}/e^-)$.

The above analysis only holds for linear signal and noise responses. Cascaded system analysis also requires that the x-ray imaging system has a linear response [47]. However, it has been reported that signal and noise response of CMOS APS detectors are nonlinear mainly due to the detector nonlinear sensitivity (V/e^-) [106], [120]. Thus, the extracted CG(DN/e^-) and cascaded system analysis could result in error [106]. This issue can be addressed by applying the nonlinear compensation method described in Section 2.2.2 [106], [121]. A signal conversion gain (S(e^-/DN)) and a noise conversion gain (N(e^-/DN)) are extracted and adapted to the cascaded system analysis separately. Both S(e^-/DN) and N(e^-/DN) are signal-dependent. The NPS of the final stage is given

by

$$NPS(u,v) = \left(S_8(u,v) + a_{pix}^2\sigma_R^2\right)g_{9,N}^2 + \left(a_{pd}^4\overline{q_0 g_1 g_2 g_4 g_6}\right)\sigma_{g9,N}^2, \qquad (2.29)$$

where $g_{9,N}$(DN/e$^-$) = 1/N(e$^-$/DN) is the noise conversion gain in DN/e$^-$ and $(\sigma_{g9,N})^2$ is the variance of $g_{9,N}$. For the DynAMITe detector, $\sigma_{g9,N} = 0.35\times g_{9,N}$ was obtained from previous work [58]. In general, σ_R for CMOS APS x-ray detectors is in the range of 100 to 350 e$^-$.

The mean variance can be extracted by the following integral [119]

$$\sigma^2(DN^2) = \int\int_{u,v=-f_{Nyq}}^{f_{Nyq}} NPS(u,v)dudv. \qquad (2.30)$$

Note that σ^2(DN^2) is the mean variance of signal under x-ray exposure, while σ_S^2(DN^2) in Equation 2.28 is the mean variance of signal under light illumination.

The final stage digital output in DN is given by

$$d(DN) = a_{pd}^2\overline{q_0 g_1 g_2 g_4 g_6}g_{9,S}, \qquad (2.31)$$

where $g_{9,S}$(DN/e$^-$) = 1/S(e$^-$/DN) is the signal conversion gain in DN/e$^-$.

The normalized noise power spectrum, $NNPS$(u,v), is given by

$$\begin{aligned} NNPS(u,v) &= \frac{NPS(u,v)}{d^2(DN)} \\ &= \frac{\left(S_8(u,v) + a_{pix}^2\sigma_R^2\right)g_{9,N}^2 + \left(a_{pd}^4\overline{q_0 g_1 g_2 g_4 g_6}\right)\sigma_{g9,N}^2}{a_{pd}^4\left(\overline{q_0 g_1 g_2 g_4 g_6}g_{9,S}\right)^2}. \end{aligned} \qquad (2.32)$$

If the signal and noise nonlinearity is ignored (i.e. $g_{9,S} = g_{9,N}$ and $\sigma_{g9,N} = 0$), the NNPS can be simplified as

$$NNPS(u,v) = \frac{S_8(u,v) + a_{pix}^2\sigma_R^2}{a_{pd}^4\left(\overline{q_0 g_1 g_2 g_4 g_6}\right)^2} = \frac{S_8(u,v) + a_{pix}^2\sigma_R^2}{d(e^-)^2}. \qquad (2.33)$$

Hence, the DQE is calculated by Equation 2.9 as shown previously

$$DQE(u) = \frac{MTF^2(u)}{\overline{q_0}\cdot NNPS(u)}. \qquad (2.9)$$

At the same time, the detector output SNR (SNR_d) is given by

$$SNR_d = d/\sigma. \qquad (2.34)$$

The 2D cascaded system analysis model will be used to simulate the MTF, NNPS

and DQE of CMOS APS x-ray detectors (in Chapter 3).

2.2.2 Signal and noise nonlinearity

In cascaded system analysis, it is assumed that the signal and noise propagations are linear, which is valid for PPS based detectors. However, for CMOS APS x-ray detectors, the detector performance is affected by the signal and noise nonlinearity [106]. Therefore, the cascaded linear system analysis must be modified to address the nonlinearity issue for CMOS APS x-ray detectors.

The signal nonlinearity originates from both the sensitivity (V/e^-) nonlinearity at the sensing node and the voltage gain (V/V) nonlinearity [121]. Now we neglected the V/V nonlinearity and only considered the V/e^- nonlinearity, as it has a very small impact for CMOS V-APS detectors based on Equation 1.13.

Since the photodiode capacitance (C_{PD}) varies under different reverse bias, V/e^- nonlinearity is expected. C_{PD} at a low signal ($d(e^-) \approx 0$) is expressed as

$$C_{PD}(0) = a_{pd}^2 \left(\frac{2}{q\varepsilon_S N_A} \left(V_{bi} + V_{RST} \right) \right)^{-1/2}, \tag{2.35}$$

where ε_S is the dielectric constant of silicon, N_A is the doping concentration of the P^- epitaxial layer, V_{bi} is the built-in voltage of the p^--n^+ junction, V_{RST} is the reset voltage. The total capacitance at the input sensing node (i.e. C_{PIX}) is the sum of C_{PD} and a constant parasitic capacitor (C_{Par}) and/or storage capacitor (C_{ST}). Therefore, C_{PIX} as a function of $d(e^-)$ can be estimated by

$$\begin{aligned} C_{PIX}\left(d(e^-)\right) &= C_{PD}\left(d(e^-)\right) + C_{Par} \\ &= a_{pd}^2 \left(\frac{2}{q\varepsilon_S N_A} \left(V_{bi} + V_{RST} - \frac{q d(e^-)}{C_{PD}(0)} \right) \right)^{-1/2} + C_{Par}. \end{aligned} \tag{2.36}$$

It is well known that the conversion gain of CMOS image sensors is proportional to $q/C_{PIX}(d(e^-))$. Thus the signal conversion gain $g_{9,S}(DN/e^-)$ can be extracted by $g_{9,S}(0) \times (C_{PIX}(0) / C_{PIX}(d(e^-)))$, where $g_{9,S}(0)$ can be obtained using the MV analysis at very low signal region.

The method to extract the noise gain is described as follows [106], [121]: It is assumed that the signal and noise gain are equal at low optical illumination or low x-ray

exposure, i.e. $S(e^-/DN) = N(e^-/DN)$. We extracted the conversion gain for the DynAMITe x-ray detector at low illumination $S_1(e^-/DN)$ by linear fitting of the MV curve adopted from Ref. [57]. The signal at the sensing node at the lowest exposure level is $d_1(e^-) = d_1(DN) \times S_1(e^-/DN)$. Since signal nonlinearity only occurs at the CMOS APS level, linear response is expected for $d(e^-)$. Hence, the electron signal at x-ray exposure level n ($d_n(e^-)$) is proportional to the x-ray exposure, i.e. $d_n(e^-) = d_1(e^-) \times (K_{a,n}/K_{a,1})$.

The noise gain is given by

$$N_n(e^-/DN) = \frac{\sqrt{d_n(e^-)}}{\sigma_{shot,n}(DN)}, \tag{2.37}$$

where $\sigma_{shot,n}(DN)$ is the corresponding optical shot noise for the x-ray exposure level n. The variance $(\sigma_{shot,n}(DN))^2$ can be obtained from the MV graph [57] by $(\sigma_{S,n}(DN))^2 - (\sigma_R(DN))^2$ based on Equation 2.28.

We can also get the signal gain $S_n(e^-/DN)$ by

$$S_n(e^-/DN) = d_n(e^-)/d_n(DN). \tag{2.38}$$

Finally, second order polynomial fits can be applied to the discrete $S_n(e^-/DN)$ and $N_n(e^-/DN)$ to realize continuous $S(e^-/DN)$ and $N(e^-/DN)$. Then $g_{9,S}(DN/e^-)$ and $g_{9,N}(DN/e^-)$ (as shown in Equation 2.29) are $1/S(e^-/DN)$ and $1/N(e^-/DN)$, respectively.

2.3 3D Cascaded System Analysis for Indirect CMOS APS X-Ray Detectors

2.3.1 3D cascaded system analysis model

Since DBT is a quasi-3D imaging technology, the DBT image quality is influenced by the system geometry and reconstruction algorithms [4], [122]. Therefore, the 3D imaging performance should be evaluated for the CMOS APS detectors. However, to empirically investigate the 3D imaging performance, proper DBT x-ray source and phantom studies are required. To deal with this issue, the 3D cascaded system analysis was developed and is presented in this dissertation.

Previously, 3D cascaded system analysis models have been developed and validated for both cone-beam computed tomography (CT) and DBT [37], [38], [119], [123]–[125]. In this section, the developed 2D cascaded system model as discussed in Section 2.2 is extended to the 3D spatial frequency space. To implement the 3D cascaded system analysis, first the 2D MTF, NPS and DQE characteristics are measured and simulated at various projection angles (θ_i) ranging from 0 to 30°. This angle range covers the typical projection angles currently used for DBT systems. We used the FBP reconstruction method to convert the 2D MTF, NPS and DQE at each θ_i to the 3D spatial frequency domain (f_x, f_y, f_z). The FBP is a standard image reconstruction method currently used for clinically approved Hologic Selenia Dimensions and Siemens MAMMOMAT Inspiration DBT commercial systems [4]. The implemented 3D cascaded system model is used to investigate the impacts of projection angle range, MGD, fiber optic plate optical coupling efficiency, focal spot blurring effect, pixel size and scintillator pixilation on the 3D imaging performance of a CMOS APS detector.

In this dissertation, the validated 3D cascaded system analysis model developed by Zhao *et al*. [37] in combination with the 9-stage 2D cascaded system analysis model [69] as discussed in Section 2.2 is used to simulate the 3D MTF, NNPS and DQE parameters of CMOS APS x-ray detector. A complete flowchart of the 14-stage 3D cascaded system analysis model is described in Figure 2.5. Specifically, the beam obliquity (stage 10), focal spot blurring (stage 11), reconstruction filters (stage 12) and 3D sampling (stage 13 and 14) are added.

Detailed illustration of stages 0 to 9 were described in Section 2.2.1 assuming the projection angle is perpendicular to the detector surface (i.e., $\theta_i = 0$). Considering various θ_i values used for DBT, stages 0 to 2 should be modified. At an oblique angle θ_i, the x-ray fluence is modified as $\bar{q}_0(\theta_i) = \bar{q}_0 \cdot \cos(\theta_i)$. The scintillator x-ray energy absorption efficiency ($\bar{g}_1$) at θ_i can be derived by modifying Equation 2.12,

$$\bar{g}_1(\theta_i) = \frac{\int_0^{E_{max}} \Phi_0(E) \cdot T_0(E) \cdot E \cdot \left(\frac{\mu_{en}(E)}{\mu(E)} \right) \cdot \left(1 - e^{-\mu(E)t/\cos\theta_i}\right) \cdot dE}{\int_0^{E_{max}} \Phi_0(E) \cdot E \cdot dE}, \quad (2.39)$$

where $t/\cos(\theta_i)$ is the optical path in the scintillator with a thickness of t.

The mean light output (number of optical photons) per absorbed x-ray photon ($\bar{g}_2$)

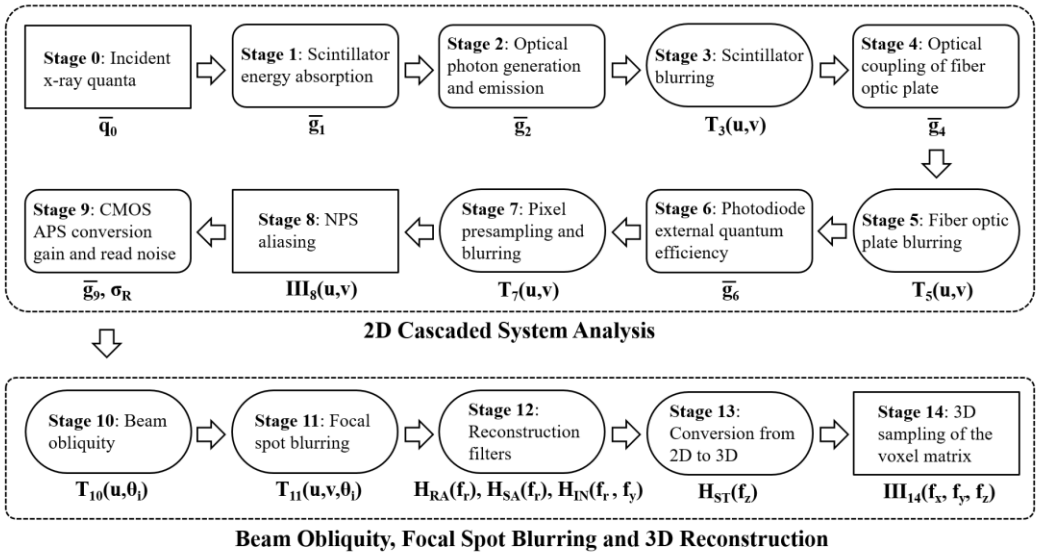

Figure 2.5 Illustration of the 3D cascaded system analysis. Stages 0 – 9 describes the 2D cascaded system model for the APS x-ray detector. Stages 10 – 14 describes the beam obliquity, focal spot blurring effect and filtered back-projection reconstruction.

at θ_i can be described by modifying Equation 2.15,

$$\overline{g_2}(\theta_i) = \frac{\int_0^{E_{\max}} \sum_z \Phi_0(E) \cdot \left(e^{-\mu(E)(t-z)/\cos\theta_i}\right) \cdot \left(1 - e^{-\mu(E)\Delta z/\cos\theta_i}\right) g_2(E,z) dE}{\int_0^{E_{\max}} \Phi_0(E) \cdot T_0(E) \cdot \left(1 - e^{-\mu(E)t/\cos\theta_i}\right) dE}. \quad (2.40)$$

We assume that the oblique incident angles will not influence the stages that follows, since the optical path and moving direction of the optical photons escaped from the scintillator is random.

Stage 10: Beam obliquity. The impact of oblique incident angles (θ_i) on MTF is included in this stage to describe the MTF blurring ($T_{10}(u,\theta_i)$). It should be noted that $T_{10}(u,\theta_i)$ only affects the MTF on the direction of rotation (x or u direction). The transfer function of the oblique incident angle blurring stage can be calculated by integrating the Fourier domain optical transfer function over the spectrum [126],

$$T_{10}(u,\theta_i) = \frac{\left| \int E \frac{1 - \exp\left(-\mu(E)t/\cos\theta_i - i2\pi u t \tan\theta_i\right)}{1 + i2\pi u \sin\theta_i / \mu(E)} \Phi_0(E) dE \right|}{\int E \left[1 - \exp\left(-\frac{\mu(E)t}{\cos\theta_i}\right)\right] \Phi_0(E) dE}. \quad (2.41)$$

The angle-dependent detector 2D MTF is given by MTF(u,v,θ_i) = MTF(u,v) × $T_{10}(u,\theta_i)$. Experimentally $T_{10}(u,\theta_i)$, also known as the MTF associated with the oblique incident angle (MTF_{ob}), can be measured by

$$MTF_{ob}(u,\theta_i) = T_{10}(u,\theta_i) = MTF(u,\theta_i)/MTF(u,0), \tag{2.42}$$

where MTF(u,θ_i) and MTF(u,0) are the measured MTF(u) using projection angles of θ_i and 0 degrees, respectively.

The signal and noise power spectra are $\Psi_{10}(u,v,\theta_i)$ = MTF(u,v,θ_i) and $S_{10}(u,v,\theta_i)$ = NNPS(u,v,θ_i), respectively. The log-normalization has been taken into account during the normalization of NPS [119].

Stage 11: Focal spot blurring. It was reported that the focal spot blurring can be the dominant system blurring factor for x-ray detectors with a pixel pitch smaller than 100 μm operated in the DBT mode [28]. In general, there are two focal spot blurring components that need to be considered: the focal spot size (a_f) and the focal spot travel distance during a single x-ray projection. Since the CMOS APS detector is operated in a step-and-shoot tube motion mode, the focal spot travel distance can be neglected. Only the focal spot size is considered in this study. The focal spot size blurring transfer function can be determined by [127]

$$T_{11}(u,v,\theta_i) = \left|\text{sinc}\,(a_f(\theta_i)\cdot u)\times\text{sinc}\,(a_f(\theta_i)\cdot v)\right|, \tag{2.43}$$

where the focal spot size projected on the detector surface at projection angle θ_i is given by

$$a_f(\theta_i) = a_{fs}\cdot d_2/(d_1\cdot\cos\theta_i), \tag{2.44}$$

where a_{fs} is the source output focal spot size, d_1 is the distance of x-ray source to the center of rotation, d_2 is the distance of detector to the center of rotation at θ_i = 0. We used d_1 = 61 cm and d_2 = 4 cm in the 3D cascaded system analysis. For focal planes located at different d_2 values the effective a_f should be adjusted, i.e., reduced focal spot blurring for smaller d_2.

The signal and noise power spectra at stage 11 are given by

$$\psi_{11}(u,v,\theta_i) = \psi_{10}(u,v,\theta_i)\times T_{11}(u,v,\theta_i), \tag{2.45}$$

$$S_{11}(u,v,\theta_i) = S_{10}(u,v,\theta_i). \tag{2.46}$$

As the focal spot blurring only affects the signal spectrum (MTF) without any impact on the NPS [37], it would be expected to have a significant influence on DQE.

Stage 12: Reconstruction filters. This stage includes the ramp (H_{RA}), spectrum apodization (H_{SA}) and interpolation filters (H_{IN}) that are used for FBP. Before applying the filters to the signal and noise power spectra, $\Psi_{11}(u,v,\theta_i)$ and $S_{11}(u,v,\theta_i)$ should be converted to the 3D space coordinated by (f_r, f_y, θ_i). The coordinates (f_r, f_y, θ_i) represents the tilted plane at θ_i perpendicular to the projection x-ray beam, while (u,v) gives the detector surface plane. The coordinates (f_r, θ_i) define the DBT system rotational plane. The relationship between (f_r, f_y, θ_i) and (u,v,θ_i) is described as $f_r = u/\cos(\theta_i) \approx u$ and $f_y = v$. In this dissertation, f_r can be approximated by u, since those large f_r values at wide θ_i will be filtered by the slice thickness filter to be discussed in Stage 13.

The ramp filter is a high-pass filter with the amplitude proportional to $|f_r|$. It is used to compensate the non-uniform spoke density at each f_r given by N / ($\theta \cdot f_r$), where N (= 21 views) is the number of projection views and θ is the total angle range (e.g. θ = 40° for an incident angle range of ±20°). Without the ramp filter, it was found that the 3D MTF drops rapidly because of the normalization by the spoke density [37]. The ramp filter is only applied to the f_r direction [37]

$$H_{RA}(f_r) = 2\tan(\theta)\frac{|f_r|}{f_{r,Nyq}}, \quad |f_r| \le f_{r,Nyq} \tag{2.47}$$

where $f_{r,Nyq}$ is the Nyquist frequency on the f_r direction. For examples, the DynAMITe detector with a 50 μm pixel pitch will lead to $f_{r,Nyq}$ of 10 mm^{-1}.

The spectrum apodization filter is a smoothing low-pass filter to eliminate the high frequency noise given by [17], [37]

$$H_{SA}(f_r) = 0.5\left[1+\cos\left(\frac{\pi f_r}{A f_{r,Nyq}}\right)\right], \quad |f_r| \le f_{r,Nyq} \tag{2.48}$$

where A defines the window width. A = 1.5 is used in the calculation for the DynAMITe detector [37], which will result in H_{SA} = 0.25 at $f_r = f_{r,Nyq}$ = 10 mm^{-1}. $H_{RA}(f_r)$ and $H_{SA}(f_r)$ duplicate at $f_r \pm n \cdot 2f_{r,Nyq}$ (n is an integer), if $|f_r| > f_{r,Nyq}$.

The 2D interpolation filter is used to approximate a continuous image, where the projection signal is located at the center of a pixel [119]:

$$H_{IN}(f_r, f_y) = \mathrm{sinc}(a_{pix} f_r)^2 \mathrm{sinc}(a_{pix} f_y)^2. \quad (2.49)$$

The signal and noise power spectra at stage 12 are given by [37], [119]

$$\psi_{12}(f_r, f_y, \theta_i) = \psi_{11}(f_r, f_y, \theta_i) \times H_{RA}(f_r) \times H_{SA}(f_r) \times H_{IN}(f_r, f_y), \quad (2.50)$$

$$S_{12}(f_r, f_y, \theta_i) = S_{11}(f_r, f_y, \theta_i) \times \left[H_{RA}(f_r) \times H_{SA}(f_r) \times H_{IN}(f_r, f_y) \right]^2. \quad (2.51)$$

Stage 13: Conversion from 2D to 3D. Using the FBP reconstruction method, the filtered Ψ_{12} and S_{12} planes at each θ_i will be reconstructed to the 3D frequency domain with the Cartesian coordinates of (f_x, f_y, f_z), where the (f_x, f_y) spatial frequency planes are parallel to the detector surface (u, v) and f_z is perpendicular to the detector. The typical reconstruction slice thickness (d_z) is around 1mm for DBT corresponding to $f_{z,Nyq} = 1/(2d_z) = 0.5$ mm^{-1}. As discussed in stage 14, the z-direction 3D NPS aliasing (occurs at $f_z = n \cdot 2f_{z,Nyq}$) will dramatically increase the NPS at high f_r and f_y values. To prevent this effect, a slice thickness filter ($H_{ST}(f_z)$) should be added to limit the z-direction aliasing. H_{ST} is given by [37]

$$H_{ST}(f_z) = \begin{cases} 0.5\left[1 + \cos\left(\dfrac{\pi f_z}{B f_{r,Nyq}}\right)\right], & |f_z| \le B f_{r,Nyq} \text{ and } |f_z| \le \tan(\theta) f_{r,Nyq} \\ 0 & \text{elsewhere} \end{cases} \quad (2.52)$$

where B is a parameter controling the width of the filter. In the calculation, $B = 0.05$ is used such that $B \cdot f_{r,Nyq} = f_{z,Nyq} = 0.5$ mm^{-1}. In other words, MTF and NPS components at z-frequencies $f_z > f_{z,Nyq}$ are removed. Hence, the z-direction NPS aliasing will not affect the 3D imaging performance.

The 3D signal spectrum and NPS are given by [37]

$$\psi_{13}(f_r, f_y, \theta_i) = \frac{N}{\theta f_r} \times \psi_{12}(f_r, f_y, \theta_i) \times H_{ST}(f_z), \quad (2.53)$$

$$S_{13}(f_r, f_y, \theta_i) = \frac{N}{\theta f_r} \times S_{12}(f_r, f_y, \theta_i) \times H_{ST}^2(f_z). \quad (2.54)$$

where $N / (\theta \times f_r)$ is the spoke density and $f_z = f_r \times \sin(\theta_i)$. Then the calculated Ψ_{13} and S_{13} should be mapped from the (f_r, f_y, θ_i) to the (f_x, f_y, f_z) coordinates:

$$\begin{cases} \psi_{13}(f_x, f_y, f_z) = \psi_{13}(f_r, f_y, \theta_i) \\ S_{13}(f_x, f_y, f_z) = S_{13}(f_r, f_y, \theta_i) \end{cases}, \text{ where } \begin{cases} f_x = f_r \cos(\theta_i) \\ f_z = f_r \sin(\theta_i) \end{cases} \quad (2.55)$$

Stage 14: 3D sampling of the voxel matrix. The final stage describes the 3D sampling and NPS aliasing effect associated with the reconstructed voxel dimensions of $d_x = d_y = a_{pix}$ and $d_z = 1$ mm. Considering a typical tomographic reconstructed slice at about 4 cm above detector, this should lead to an insignificant geometric magnification $M = (1 + d_2/d_1) = 1 + 4/65 = 1.07$, where d_1 is the detector to focal plane distance and d_2 is the source to detector distance. Since the spatial frequency axes are not scaled down by this magnification value (≈1), the geometric magnification should not greatly affect the spatial resolution. In this study, the magnification factor was ignored. The aliased 3D NPS is given by [37], [119], [125]

$$\begin{aligned} S_{14}(f_x, f_y, f_z) &= S_{13}(f_x, f_y, f_z) *** \mathrm{III}(f_x, f_y, f_z) \\ &= \sum_{i,j,k} S_{14}(f_x, f_y, f_z)\delta\left(f_x - \frac{i}{d_x}, f_y - \frac{j}{d_y}, f_z - \frac{k}{d_z}\right), \end{aligned} \tag{2.56}$$

where i, j and k are integers and $\mathrm{III}(f_x, f_y, f_z)$ is a 3D sampling function. Since the slice thickness filter was applied to the reconstruction, the impact of z-direction NPS aliasing is eliminated in this study. The signal spectrum does not change during this process, $\Psi_{14}(f_x, f_y, f_z) = \Psi_{13}(f_x, f_y, f_z)$.

The 3D MTF and NNPS and DQE are given by

$$MTF(f_x, f_y, f_z) = \mathrm{Norm}\left[\psi_{14}(f_x, f_y, f_z)\right], \tag{2.57}$$

$$NNPS(f_x, f_y, f_z) = S_{14}(f_x, f_y, f_z), \tag{2.58}$$

$$DQE(f_x, f_y, f_z) = \frac{\theta f_r}{N\overline{q_0}} \cdot \frac{\psi_{14}^2(f_x, f_y, f_z)}{S_{14}(f_x, f_y, f_z)}, \tag{2.59}$$

where the Ψ_{14} is normalized to unity as the 3D MTF and the term $\theta f_r/N$ is used to normalize the spoke density for the 3D DQE calculation [119].

For DBT, one slice of the reconstructed tomographic image contains information of f_z ranging from $-f_{z,Nyq}$ to $+f_{z,Nyq}$. Therefore, we evaluate the in-plane MTF, NNPS and DQE by integrating the 3D parameters over f_z [37]

$$MTF_{ip}(f_x, f_y) = \mathrm{Norm}\left[\int_{-f_{z,Nyq}}^{+f_{z,Nyq}} MTF(f_x, f_y, f_z)df_z\right], \tag{2.60}$$

$$NNPS_{ip}(f_x, f_y) = \int_{-f_{z,Nyq}}^{+f_{z,Nyq}} NNPS(f_x, f_y, f_z)df_z, \tag{2.61}$$

$$DQE_{ip}(f_x, f_y) = d_z \int_{-f_{z,Nyq}}^{+f_{z,Nyq}} DQE(f_x, f_y, f_z) df_z, \tag{2.62}$$

where the d_z (= 1 mm) term is used to normalize the in-plane DQE as $d_z = 1/(2f_{z,Nyq})$. The in-plane DQE is considered as an average of the 3D DQE over f_z.

The integrated in-plane MTF, NNPS and DQE are used to evaluate the CMOS APS detector 3D imaging performance for DBT as discussed in Chapter 4.

2.3.2 Mean glandular dose (MGD)

The MGD calculation for DBT can be also included in the cascaded system analysis [128]–[132]. Sechopoulos *et al.* reported the MGD for a complete DBT scan as [132]

$$MGD = X \cdot D_g N_0 \cdot \sum_{\theta_i} RGD(\theta_i), \tag{2.63}$$

where X is the breast surface exposure in roentgen (R) per projection, D_gN_0 is the normalized glandular dose in mGy/R for the zero-degree projection ($\theta_i = 0$), and $RGD(\theta_i)$ is the relative glandular dose coefficient at each projection angle.

The breast surface exposure is calculated from the detector surface air kerma by

$$\frac{X}{K_a} = \frac{\int_0^{E_{max}} \Phi(E) \cdot \xi(E)^{-1} \cdot dE}{0.00876 \times \int_0^{E_{max}} \Phi(E) \cdot \xi(E)^{-1} \cdot \exp\left[-(\mu/\rho)_b \rho_b t_b\right] \cdot dE}, \tag{2.64}$$

where $\xi(E)^{-1}$ is the exposure per x-ray fluence [110], and t_b is the thickness of the compressed breast. The factor 0.00876 was used to convert the x-ray exposure unit from gray to roentgen. To simplify the calculation, we fixed the incident x-ray spectrum Φ(E) at 28 kVp. In the clinical use, the tube voltage may vary for different breast thickness.

The normalized glandular dose for mammography and tomosynthesis has been reported for specific x-ray spectra for various anode/filtration [129]–[131]. Boone reported the D_gN_0 values can be extracted from any arbitrary x-ray spectrum by the following expression [128]

$$D_g N_0 = \frac{\int_0^{E_{max}} \Phi(E) \cdot \xi(E)^{-1} \cdot D_g N(E) \cdot dE}{\int_0^{E_{max}} \Phi(E) \cdot \xi(E)^{-1} \cdot dE}, \tag{2.65}$$

where $D_gN(E)$ stands for the mono-energetic normalized glandular dose. In this work, $D_gN(E)$ and thus D_gN_0 can be calculated using the parameters tabulated by Boone [128].

At each projection angle θ_i, $RGD(\theta_i)$ for a cranio-caudal (CC) view was computed using the parameters provided by Sechopoulos *et al* [132]. The MGD for a medio-lateral oblique (MLO) view is not evaluated in this work.

The MGD calculation will be considered for 3D cascaded system analysis in Chapter 4. The impact of MGD on detector 3D imaging performance will be discussed in Section 4.4.3.

2.4 Summary

This chapter presented the experimental methods to evaluate the 2D x-ray imaging performance (MTF, NNPS and DQE) of CMOS APS x-ray detectors. The 2D MTF, NNPS and DQE parameters can also be simulated using 2D cascaded system analysis. The experimental and simulation method will be used to evaluate the CMOS APS x-ray detector performance in Chapter 3. We will use the 3D cascaded system analysis (as an extension of the 2D model) to simulate the 3D x-ray imaging performance and impacts of various x-ray source, acquisition, and detector parameters in Chapter 4.

Chapter 3
Two-Dimensional X-Ray Imaging Performance of CMOS APS X-Ray Detector for DBT

3.1 X-Ray Imaging Performance Evaluation for 75 μm Pixel Pitch CMOS APS X-Ray Detector

In this section, the 2D x-ray imaging performance of a large area (29×23 cm^2) CMOS APS x-ray detector (Dexela 2923 MAM (Perkin-Elmer, London)) with a pixel pitch of 75 μm is characterized and modeled. We have developed a cascaded system model for CMOS APS x-ray detectors using both a broadband x-ray radiation and monochromatic synchrotron radiation. The experimental data including MTF, NNPS and DQE will be compared with simulated results using the cascaded system analysis model. Both a high full well (HFW) and low full well (LFW) modes of the Dexela 2923 MAM CMOS APS x-ray imager will be characterized and modeled.

3.1.1 75 μm pixel pitch CMOS APS x-ray detector (Dexela 2923 MAM)

The Dexela 2923 MAM CMOS APS x-ray detector used in this work is based on a 3-T CMOS V-APS technology. Detailed technical description of this x-ray imager (such as the transistor dimension and pixel layout) is not provided in open literature.

It is known that the Dexela 2923 MAM x-ray detector offers an option to switch between the HFW and LFW modes [59], [62], [63]. The full well capacity is defined as the maximum number of electrons that can be stored on the sensing node. The HFW mode is designed to achieve a high full well capacity ($N_{HFW} \sim 1.6 \times 10^6$ electrons) and

high dynamic range (~73 dB), but at the expense of higher electronic noise (360 e^-) [59], [62]. In comparison, the LFW mode has a relatively lower full well capacity (N_{LFW} ~ 0.5 × 10^6 electrons), smaller dynamic range (69 dB), and lower electronic noise (165 e^-) [59], [62]. The LFW is more sensitive to small signal, but is limited in dynamic range. In general, switching between HFW and LFW modes can be achieved by adding an additional input storage capacitor (C_{ST}) to the photodiode capacitance (C_{PD}). If we consider C_{PD} is approximately constant under various reverse bias, the full well capacity can be described as $N_{HFW} = (C_{ST}+C_{PD})\times V_{DD}/q$ and $N_{LFW} = C_{PD}\times V_{DD}/q$ for HFW and LFW modes, respectively. Assuming that V_{DD} is in the range of 1~3 V, the corresponding total input capacitance for HFW ($C_{ST}+C_{PD}$) and LFW (C_{PD}) modes of Dexela 2923 MAM CMOS APS x-ray imager can be calculated to be 85~255 fF and 27~81 fF, respectively. For the LFW mode, the small C_{PD} will result in a larger conversion gain; reported values in the literatures are 8.4×10^{-3} digital numbers per electron (DN/e^-), and 0.026 DN/e^- for HFW and LFW modes, respectively [62].

3.1.2 Experimental method and cascaded system analysis model

The MTF, NPS and DQE parameters were measured using both broadband (by Patel *et al*. [63]) and monochromatic synchrotron radiations (by Konstantinidis *et al*. [59]). Figure 3.1 shows the schematics of broadband [63] and a monochromatic synchrotron radiations [59]. In both cases, the IEC standard recommendations were followed for measurements of MTF, NPS and DQE parameters [104].

The x-ray source for the broadband radiation is a W anode with Be exit window filtration of 0.76 mm thickness, and an external Rh filter of 0.05 mm thickness [63]. An additional 1.4 mm Al filtration was added to match the half value layer (HVL) of 0.75 mm Al specified in IEC 62220-1-2 for mammography [104]. The x-ray tube voltage was set at 28 kVp.

The x-ray beams of monochromatic synchrotron radiation were generated from one of the bending magnets of the storage ring (Figure 3.1). The x-ray photon energy (17 keV) was selected using a double-crystal Si monochromator [59].

The experimental methods for MTF, NNPS and DQE measurement were described in Section 2.1. The detector was tested using both a broadband x-ray radiation with a

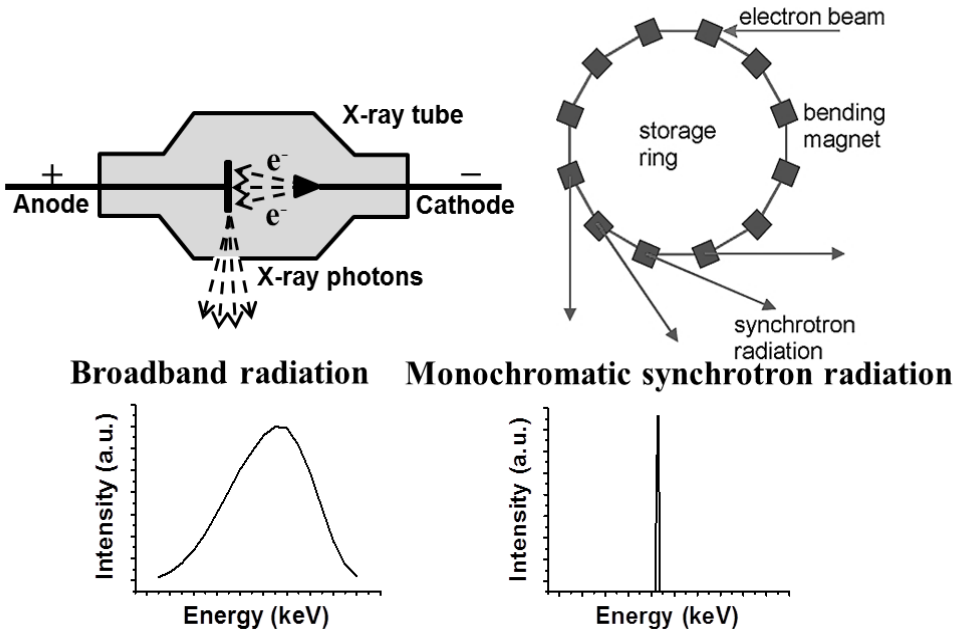

Figure 3.1 Schematic of the broadband x-ray and monochromatic synchrotron generation. The broadband x-ray and monochromatic synchrotron radiation spectra as a function of energy and the light output as a function of wavelength are also shown.

150 μm CsI:Tl scintillator and a monochromatic synchrotron radiation with a 200 μm CsI:Tl scintillator [59], [63]. The key parameters used in the cascaded system analysis for the Dexela 2923 MAM CMOS APS x-ray detector are listed in Table 3.1. At Stage 3, the exponential decay function (Method 2) was used to fit the experimental MTF data for both the broadband and monochromatic cases. For cascaded system analysis, the NNPS and DQE parameters can be calculated using Equation 2.33 and 2.9, respectively.

Signal nonlinearity is considered in both cases. However, to utilize the signal and noise nonlinearity model discussed in Section 2.2.2, detailed mean variance analysis for the Dexela 2923 MAM detector needed. In this section, a simplified method is proposed. To compensate for the signal nonlinearity, a signal nonlinearity factor f (from 0 to 1) as a function of K_a can be extracted from the derivative of signal response curve [47]. The NNPS is thereby modified to

$$NNPS(u,v)=\frac{\left[1+\overline{g_4g_6}f(\overline{g_2}f+\varepsilon_{g2})T_3^2(u,v)\right]T_7^2(u,v)^{**}III_8(u,v)}{\overline{q_0g_1g_2g_4g_6}f}+\frac{a_{pix}^2\sigma_R^2}{a_{pd}^4(\overline{q_0g_1g_2g_4g_6}f)^2}. \quad (3.1)$$

Parameters	Value (Broadband, 28 kVp)	Value (Monochromatic, 17 keV)	Description
$\overline{q_0}/K_a$	5975 x-rays/mm^2/μGy	4083 x-rays/mm^2/μGy	Mean fluence/Air Kerma
$\bar{g}_1$	0.72	0.89	Mean x-ray absorption
$\bar{g}_2$	612	543	Scintillator quantum gain
I_S	0.91	0.90	Swank factor
ε_{g2}	59.5	59.3	Scintillator Poisson excess
A	0.97	1.05	Fitting parameter A forMTF
B	3.10	4.50	Fitting parameter B for MTF
C	0.03	-0.05	Fitting parameter C for MTF
$\bar{g}_4$	0.55	0.55	FOP coupling efficiency
$\bar{g}_6$	0.60	0.60	Photodiode EQE
a_{pix}	75 μm	75 μm	Pixel pitch
a_{pd}	68.7 μm	68.7 μm	Effective photodiode pitch
FF	0.84	0.84	Pixel fill factor
σ_R	360 e$^-$ (HFW) 165 e$^-$ (LFW)	360 e$^-$ (HFW) 165 e$^-$ (LFW)	Additive electronic noise

Table 3.1 Key parameters used in the cascaded system model for the Dexela 2923 MAM CMOS APS x-ray detector.

3.1.3 Experimental and modeling results

Figure 3.2 shows the experimental and simulated data of system MTF for Dexela 2923 MAM CMOS APS x-ray imager (HFW and LFW modes) using a broadband x-ray radiation with a 150 μm CsI:Tl scintillator and a monochromatic synchrotron radiation with a 200 μm CsI:Tl scintillator. The exponential decay function provides a good fit to measured system MTF within the Nyquist frequency region (<6.7 lp/mm^{-1}). The broadband x-ray radiation shows a lower MTF curve in comparison to the monochromatic synchrotron radiation, although the CsI:Tl thickness is thinner (150 μm). Konstantinidis *et al.* demonstrated using monochromatic synchrotron radiation that MTF changes as a function of energy, when the used x-ray energy is below the CsI:Tl K-absorption edge (33.2 keV for I and 36 keV for Cs) [59]. The difference in MTF is

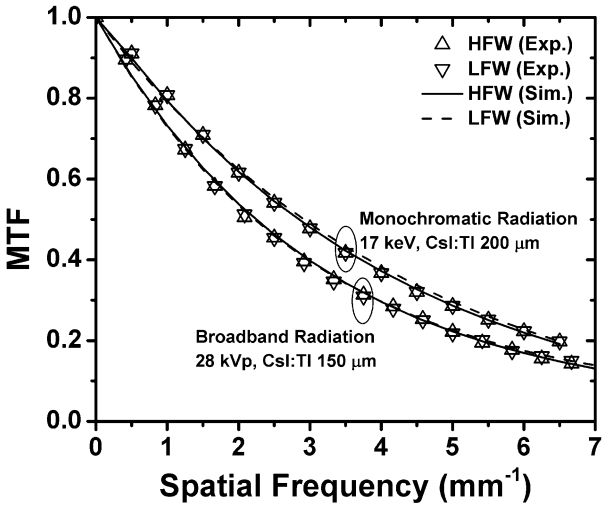

Figure 3.2 Measured and fitted MTF for Dexela 2923 MAM CMOS APS x-ray imager using a broadband x-ray radiation with a 150 μm CsI:Tl scintillator and a monochromatic synchrotron radiation with a 200 μm CsI:Tl scintillator. Results for both HFW and LFW modes are shown.

due to different CsI:Tl scintillators used for monochromatic and broadband radiations.

Figure 3.3 show the experimental data [63] and simulated data of NNPS and DQE parameters for the Dexela 2923 MAM CMOS APS x-ray imager using a clinical broadband x-ray radiation of 28 kVp for HFW (a, b) and LFW (c, d) modes, respectively. In both cases, a DQE of greater than 0.7 and ~0.3 can be achieved at a low spatial frequency of 0.5 mm^{-1} (DQE(0.5)) and Nyquist frequency of 6.7 mm^{-1} (DQE(f_{Nyq})), respectively.

Without signal nonlinearity, the simulated DQE (for both HFW and LFW modes) at zero spatial frequency (DQE(0)) saturates at a value of ~0.65 at K_a > 60 μGy, which is lower than the experimental results (>0.7). On the other hand, the simulated DQE with signal nonlinearity fits well the experimental data at low spatial frequencies (< 3 mm^{-1}). The small variation is mainly due to the measurement errors. At the same time, we recognize there is a deviation of ~19% between experimental and simulated DQE at spatial frequencies >6 lp/mm. This deviation can originate from underestimated electronic noise and neglected FOP blurring stage in the simulation. The simulation best match the experimental results at low K_a (<10 μGy). The deviation at higher K_a values may result from nonlinear signal and noise properties.

The evaluated K_a for the HFW mode (from 1.69 to 118.9 μGy) covers a wide range;

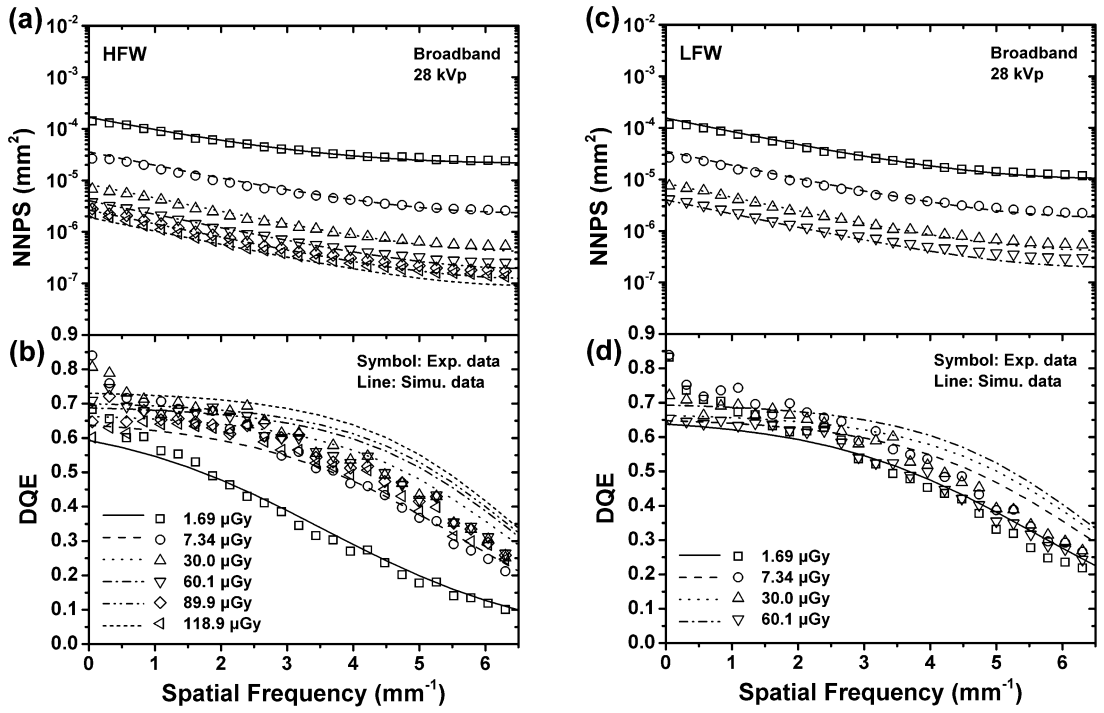

Figure 3.3 Experimental (symbols) and simulated (lines) data of NNPS and DQE parameters for the Dexela 2923 MAM CMOS APS x-ray imager HFW (a, b) and LFW modes (c, d) under broadband x-ray radiation of 28 kVp.

this is possible due to a high full well capacity (1.6×10^6 e^-) and a high dynamic range (73 decibels (dB)). However, at DBT K_a levels (1.69 and 7.34 uGy) the DQE values for HFW mode are low, due to the high electronic noise (360 e^-). Even though the dynamic range of LFW mode is lower (69 dB), higher DQE values can be achieved for K_a from 1.69 to 60.1 μGy, which is suitable for DBT application. Therefore, based on this study, we suggest that the LFW mode should be used for low dose clinical applications such as DBT, while the HFW mode is suitable for digital mammography, since it can detect larger signals.

Figure 3.4 show the experimental data adopted from a previous study [59] and simulated data of NNPS and DQE parameters for the Dexela 2923 MAM CMOS APS x-ray imager using monochromatic synchrotron radiation of 17 keV under HFW (a, b) and LFW (c, d) modes, respectively. K_a levels from 29.7 to 227.1 μGy and from 12.8 to 60.6 μGy were used for HFW and LFW modes, respectively, which corresponds to digital mammography. The DQE at low frequencies increases as a function of K_a, which

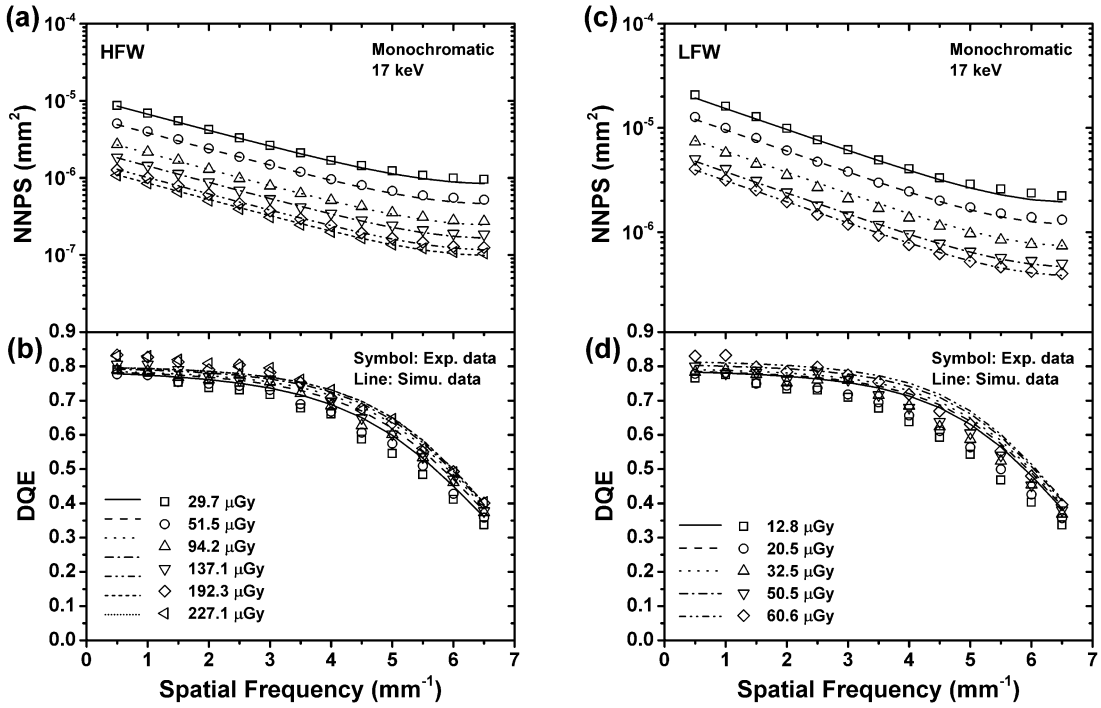

Figure 3.4 Experimental (symbols) and simulated (lines) data of NNPS and DQE parameters for the Dexela 2923 MAM CMOS APS x-ray imager HFW (a, b) and LFW (c, d) modes under monochromatic synchrotron radiation of 17 keV.

indicates existence of signal nonlinearity.

Considering the signal nonlinearity, a negligible deviation (around 5%) between simulated and experimental measured DQE at spatial frequencies <1 mm^{-1} was achieved. We still observed a deviation of about 10% for at high spatial frequencies (>5 mm^{-1}) region. The results show that DQE(0.5) and DQE(f_{Nyq}) are ~0.8 and ~0.4, respectively.

In summary, the 75 μm pixel pitch Dexela 2923 MAM CMOS APS x-ray detector demonstrates a high DQE of 0.2 to 0.65 at a very low air kerma of 1.69 μGy (using a broadband x-ray radiation with a tube voltage of at 28 kVp). The Nyquist frequency was limited at 6.67 mm^{-1}. To resolve small objects such as microcalcifications smaller than 150 μm, the detector spatial resolution needs to be further improved. Therefore, a high-resolution CMOS APS x-ray detector with a 50 μm pixel pitch and low electronic noise is very desirable for DBT application.

3.2 X-Ray Imaging Performance Evaluation for 50 µm Pixel Pitch CMOS APS X-Ray Detector

3.2.1 50 µm pixel pitch CMOS APS x-ray detector (DynAMITe)

The wafer scale (12.8 × 13.1 cm^2) DynAMITe (Dynamic Range Adjustable for Medical Imaging Technology) CMOS APS x-ray detector was fabricated using the standard 0.35 µm CMOS technology [133]. Since the detector is two-side buttable, a 2 × 2 tiling of sub-detectors can cover a large area of 25.6 × 26.2 cm^2 suitable for DBT application [57].

The studied DynAMITe detector is dynamic range (DR) adjustable and can operate in either a) high DR, full pixel mode (P mode, 100 µm pixel pitch), or b) a high resolution, subpixel mode (SP mode, 50 µm pixel pitch). This is realized by activating either a pixel photodiode (P diode) in a 100 × 100 μm^2 full pixel area or a subpixel photodiode (SP diodes) in a 50 × 50 μm^2 subpixel area [57]. The characteristics of DynAMITe P and SP modes are summarized in Table 3.2 [57], [58].

	P mode	SP mode
Pixel pitch (µm)	100	50
Pixel resolution	1280 × 1312	2560 × 2624
Full well capacity (e^-)	~1.9×10^6	~2.8×10^5
Conversion gain (DN/e^-)	3.4×10^{-3}	0.02
Read noise (e^-)	780	~150
Dynamic range	~2435, (68 dB)	~1867, (65 dB)
External quantum efficiency (%)	54	64
Pixel fill factor	0.7	0.7
Maximum full frame rate (fps)	90	30

Table 3.2 Parameters and characteristics of DynAMITe P and SP cameras.

The switch between P and SP modes is not dynamic, i.e., either P or SP mode can be selected before an x-ray exposure. This will allow to switch between 100 and 50 µm pixel pitch. The SP mode achieves a small pixel pitch of 50 µm, large conversion gain of around 0.02 DN/e^-, low σ_R of around 150 e^- and frame rate of 30 fps [57], [58]. These properties make the SP mode very promising for low dose applications such as DBT.

Although not being characterized here, the existence of P mode offers the detector a possibility of being used to achieve high DR (68 dB) and fast frame rate (90 fps), that could be required for applications such as x-ray diffraction measurements [134].

In this work, we focus exclusively on the DynAMITe detector working in the SP mode with a pixel pitch of 50 μm. A 150 μm thick CsI:Tl scintillator with FOP was integrated on top of the DynAMITe sensor.

Figure 3.5(a) shows a top view schematic representation of a CMOS APS x-ray detector. The entire pixel area consists of a photodiode active area and an area containing all the electronics such as transistors and bias lines. For DynAMITe SP detector, the pixel pitch (a_{pix}) is 50 μm giving a total pixel area of 2500 μm^2, while the fill factor (FF = 0.7) is the ratio of photodiode active area (1750 μm^2) to the total pixel area. In the cascaded system analysis, we assume that the photodiode active area is square. Hence, an effective photodiode pitch (a_{pd}) of 41.8 μm is defined such that a_{pd}^2 equals to the photodiode area.

The DynAMITe SP detector is also based on the standard 3-T CMOS APS technology. Figure 3.5(b) shows the circuit schematic of conventional 3-T CMOS APS with readout electronics [55]. RST, SF, RS and Bias represent the reset transistor, source follower, row select transistor in each pixel and bias transistor in the column circuit, respectively. The operation of CMOS V-APS was discussed in Section 1.4.

The readout of DynAMITe detector is based on the rolling shutter method [135]: the rows of pixels are reset and read in a sequence. After the reset of row N, the readout process of row 1 begins. The integration time (around 0.2 s for DBT) is determined by the time gap between reset and readout for a row. Correlated double sampling (CDS) is not used for DynAMITe SP detector.

The DynAMITe detector has been designed according to the radiation hardness-by-design methodology. All the in-pixel transistors have been designed with source and drain physically enclosed using an Enforced Layout Geometry (ELG) to reduce the edge leakage, which is generated in the transition area between thin gate oxide and the thick field oxide [136], [137]. The radiation hardness of this detector has been evaluated through x-ray radiation damage testing and shows a damage threshold of 204 Gy(Si), which is acceptable for medical imaging applications [138].

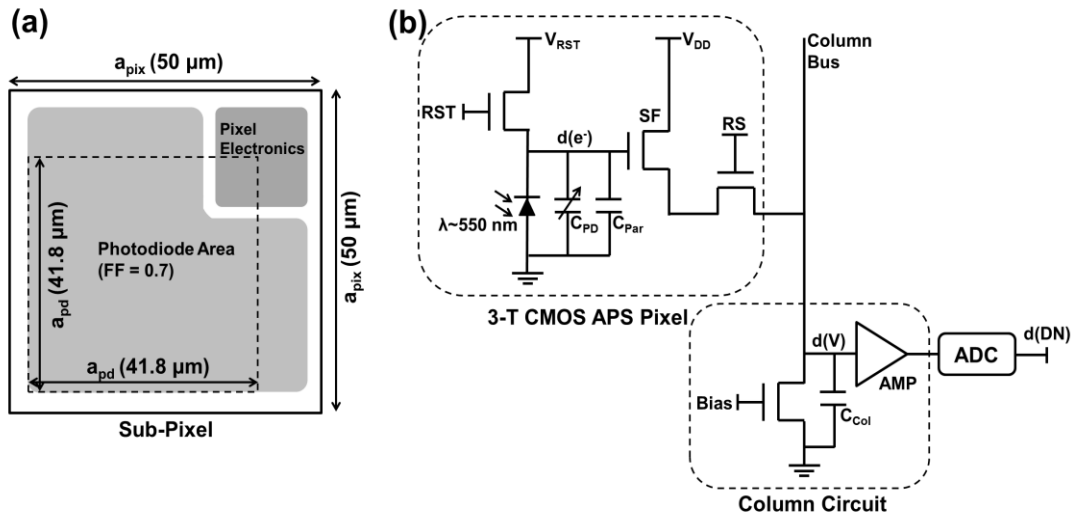

Figure 3.5 (a) Top view schematic representation of CMOS APS x-ray detector with 50 µm pixel pitch. a_{pix} and a_{pd} are the pixel pitch and effective photodiode pitch, respectively. (b) Circuit schematic of DynAMITe SP CMOS APS detector. RST, SF, RS and Bias represent the reset transistor, source follower, row select transistor and column bias transistor, respectively. C_{PD}, C_{Par} and C_{Col} are the photodiode capacitance, parasitic capacitance, and column capacitance, respectively. V_{RST} and V_{DD} are constant bias voltages.

3.2.2 Experimental method and cascaded system analysis model

The DynAMITe SP x-ray detector was characterized by measuring the MTF, NNPS and DQE at various air kerma levels. Figure 3.6 shows the experimental setup used for such measurements. A W anode x-ray tube with an inherent Al filtration of 1.4 mm was used as the x-ray source. An external filtration of 1.1 mm Al was added to reach a total filtration of 2.5 mm Al for MTF, NNPS and DQE measurement and simulation. According to the IEC standard for mammography [104], the tube voltage was set at 28 kVp and the HVL was measured as ~0.83 mm Al using the Raysafe Xi dosimeter, which contains Al filtration internally and calculates automatically the HVL. The DynAMITe SP x-ray detector was placed at 60.5 cm from the x-ray source. The source to detector distance is similar to those DBT systems in clinical use (~65 cm) [4]. In this experiment, both the x-ray source and detector were in stationary positions.

The x-ray fluence per air kerma ($\bar{q}_0/K_a$) is 7009 x-rays mm^{-2} µGy^{-1}, which was used in the cascaded system analysis. This number was calculated using the SPEKTR software [139] for the W/Al x-ray source with 28 kVp tube voltage. Briefly, this

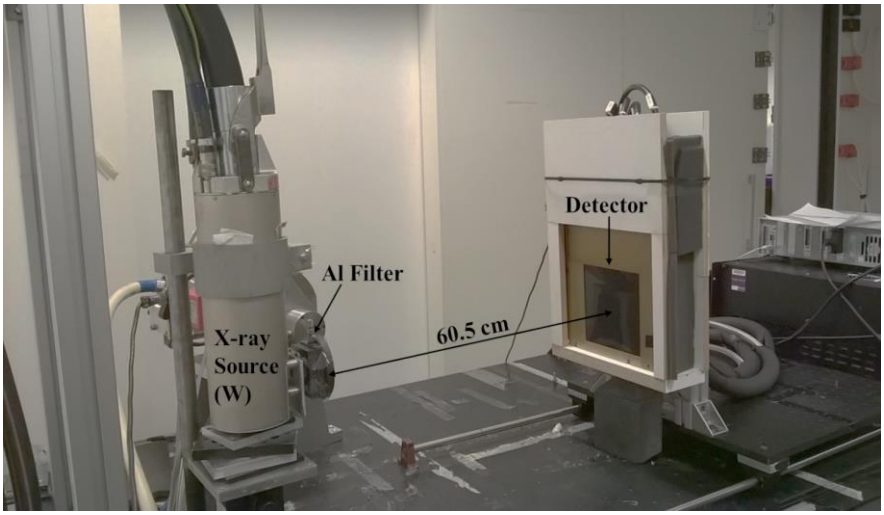

Figure 3.6 Experimental setup for detector MTF, NNPS and DQE measurements.

software simulates the normalized x-ray spectrum with the added filtration ($\Phi_{0,norm}$ in Equation 2.1); then (q_0/K_a) at each energy E is calculated. Finally the $\bar{q}_0/K_a$ is calculated by integrating (q_0/K_a) over $\Phi_{0,norm}$. The HVL was also calculated by SPEKTR to be 0.824 mm Al, which is consistent with the measured value for the x-ray source used. By replacing the detector with a dosimeter (Raysafe Xi), K_a values for various exposure conditions were measured.

Parameter	Value	Description
$\bar{q}_0/K_a$	7009 x-rays/mm^2/μGy	Mean x-ray fluence/air kerma
$\bar{g}_1$	0.55	Mean x-ray absorption
$\bar{g}_2$	580	Scintillator mean quantum gain
I_S	0.87	Swank factor
ε_{g2}	85.7	Scintillator Poisson excess
H_3	0.29	Scintillator blurring fitting parameter
$\bar{g}_4$	0.44	FOP optical coupling efficiency
H_5	0.06	FOP blurring fitting parameter
$\bar{g}_6$	0.64	Photodiode EQE
FF	0.7	Pixel fill factor
a_{pix}	50 μm	Pixel pitch
a_{pd}	41.8 μm	Effective photodiode pitch
$g_{9,S}$	0.024 – 0.023 DN/e$^-$	Signal conversion gain of CMOS APS
$g_{9,N}$	0.025 – 0.022 DN/e$^-$	Noise conversion gain of CMOS APS
σ_R	145 e$^-$	Additive read noise

Table 3.3 Parameters used in the cascaded system model for the DynAMITe SP detector.

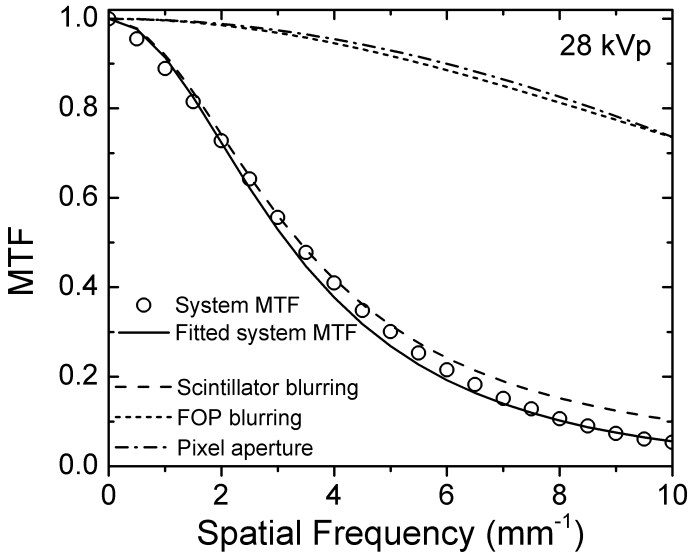

Figure 3.7 Experimental (circles) and simulated (solid line) system MTF. The stage MTFs associates with scintillator blurring, FOP blurring and pixel aperture are also shown (dash lines).

The experimental methods used for MTF, NNPS and DQE measurement were discussed in Section 2.1. Also the 9-stage cascaded system analysis model discussed in Section 2.2.1 was used to calculate the MTF, NNPS and DQE parameters. At stage 3, the Lorentzian fit method (Method 1) was used to simulate the scintillator blurring effect. In addition, the signal and noise nonlinearity (Section 3.2.2) was characterized and included in the cascaded system model. All the parameters extracted and used for the cascaded system analysis are summarized in Table 3.3.

3.2.3 Experimental and modeling results

Figure 3.7 illustrates the experimental and simulated MTFs up to f_{Nyq} of 10 mm^{-1} at x-ray tube voltage 28 kVp. Simulated MTFs representing the scintillator spreading (T_3(u,v)), FOP blurring (T_5(u,v)) and pixel sampling (T_7(u,v)) based on cascaded system analysis are also shown. Thanks to the pixel pitch of 50 μm, the f_{Nyq} achieved for DynAMITe SP detector is doubled in comparison to current clinical systems with pixel pitches of ~100 μm (f_{Nyq} of ~ 5 mm^{-1}) [4]. It can be seen that for such a high-resolution x-ray imager, the limiting factor for spatial resolution (i.e. system presampling MTF) is the scintillator scattering rather than the pixel blurring. Therefore, from this work, we

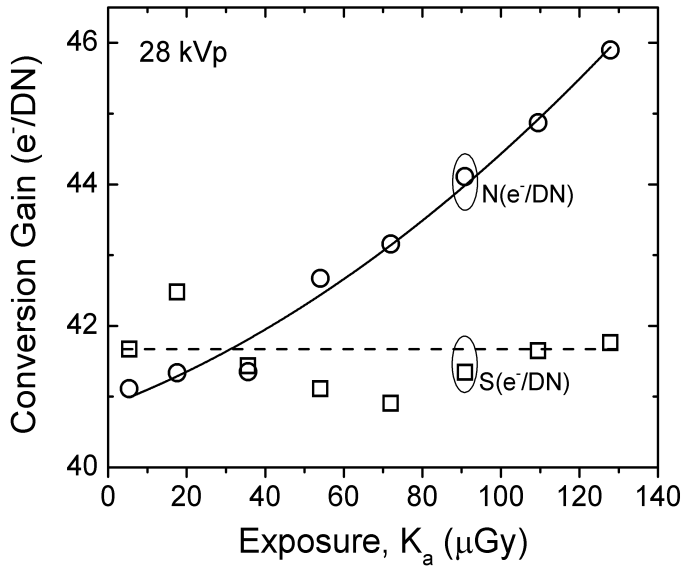

Figure 3.8 Extracted DynAMITe CMOS APS signal $S(e^-/DN)$ and noise $N(e^-/DN)$ conversion gains (symbols) at detector air kerma up to 127 μGy. A second order polynomial is used to fit $N(e^-/DN)$ (solid line).

can conclude that for imagers with higher resolution, the signal transfer property of CsI:Tl or any other scintillator needs to be improved. Impact of using pixelated scintillator to improve detector spatial resolution was evaluated and discussed in Section 4.4.5.

As discussed in Section 2.2.2, signal and noise nonlinearity should be included in cascaded system analysis to accurately model the detector NNPS and DQE parameters. Figure 3.8 shows the extracted signal and noise gain ($S(e^-/DN)$ and $N(e^-/DN)$, Equation 2.37 and 2.38) using the DynAMITe x-ray detector at detector exposure up to 127 μGy. It can be seen that the noise gain $N(e^-/DN)$ increases at large x-ray exposure, while the signal gain $S(e^-/DN)$ remains approximately constant. A second order polynomial fit was applied for $N(e^-/DN)$ and $g_{9,N}(DN/e^-)$ was calculated as $1/ N(e^-/DN)$. At low x-ray exposure, $g_{9,N}(DN/e^-) \approx g_{9,S}(DN/e^-)$. At large x-ray exposure, $g_{9,N}(DN/e^-) < g_{9,S}(DN/e^-)$, i.e., a lower output noise but a larger output signal. As a result, the signal-to-noise property should be enhanced and an improved maximum DQE is expected.

The measured and simulated (a) 1D NNPS and (b) DQE at a wide K_a range from 1.3 to 109.5 μGy are shown in Figure 3.9. Signal and noise non-linearity was included.

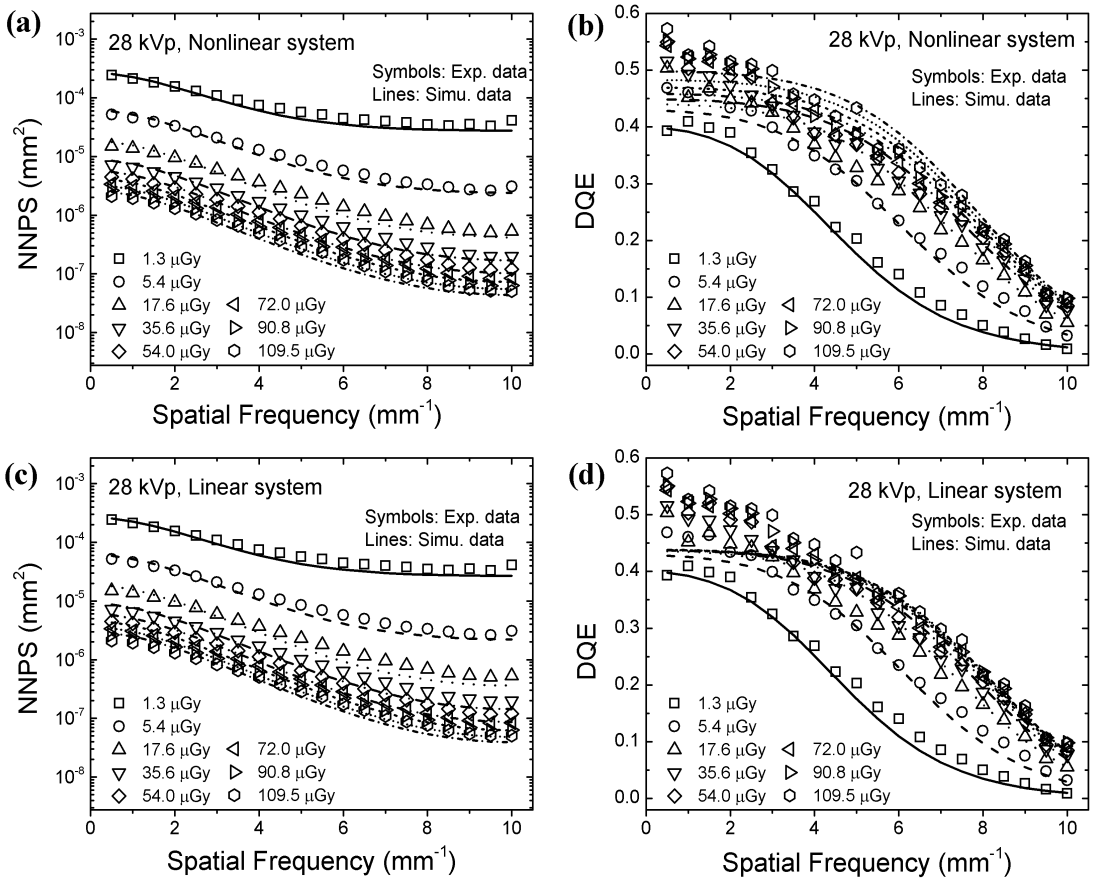

Figure 3.9 Experimental (symbols) and simulated (lines) (a) nonlinear system NNPS and (b) nonlinear system DQE for detector air kerma ranging from 1.3 to 109.5 μGy. For comparison, (c) NNPS and (d) DQE data simulated using linear cascaded system analysis is also shown.

For typical DBT detector exposures (K_a >17.6 μGy), the DynAMITe SP x-ray detector achieves a DQE of >0.5 and around 0.1 at low spatial frequencies (<1 mm^{-1}) and f_{Nyq} = 10 mm^{-1}, respectively. The DQE at low spatial frequencies (DQE ≈ 0.5) is similar to a prototype Siemens direct conversion DBT system [140], while the maximum spatial resolution (f_{Nyq}) is extended from ~5 to 10 mm^{-1}. The DQE at the f_{Nyq} = 10 mm^{-1} does not vanish, demonstrating that the studied imager is capable to distinguish microcalcifications in the dimension of 100 μm.

At low x-ray exposures (K_a <5.4 μGy), the DQE drops especially in the high spatial frequency region (>5 mm^{-1}). It was found that the drop in DQE at low exposure levels is due to the electronic noise because in these levels the detector system is not quantum-limited.

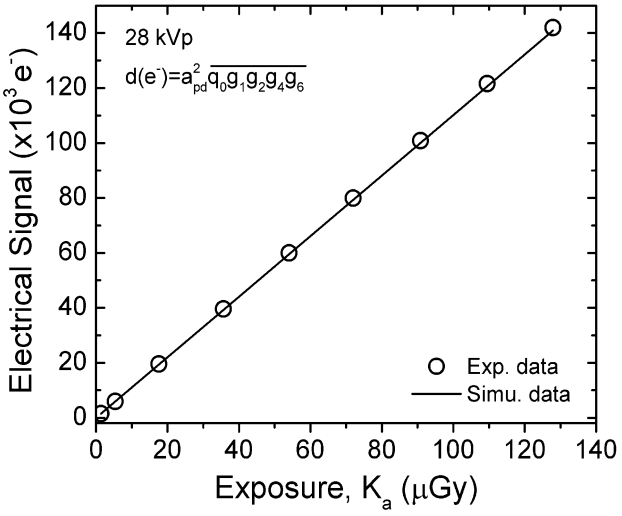

Figure 3.10 Experimental extracted (circles) and simulated (lines) electronic signal at the sensing node for detector air kerma up to 127 μGy.

For comparison purpose, we also simulated the NNPS and DQE using linear cascaded system analysis. As shown in Figure 3.9 (c) and (d), if both the signal and noise are considered linear, the DQE at low spatial frequency saturates at a value (~0.45) smaller than the experimental results, when a high exposure (>17.6 μGy) is used. At K_a = 109.5 μGy and spatial frequency of 0.5 lp/mm, the NNPS and DQE differences between linear and nonlinear cascaded system analysis are 14% and 12%, respectively. Although not obvious in Figure 3.9, the NNPS variation is nontrivial leading to clearly visible DQE drop at spatial frequencies close to zero. Hence, signal and noise non-linearity should be included in the cascaded system analysis (especially for higher K_a) to precisely describe the NNPS and DQE variations as a function of the spatial frequency.

Unlike the conventional PPS x-ray detectors [46], [108], in which the signal and noise response is linear, the DQE of DynAMITe SP CMOS APS x-ray imager does not saturate at high exposure values. Instead, the DQE increases with K_a for the entire spatial frequency range. This increase can be addressed by introducing the CMOS APS signal ($g_{9,S}$(DN/e$^-$) = 1/S(e$^-$/DN)) and noise gains ($g_{9,N}$(DN/e$^-$)=1/N(e$^-$/DN)) to the cascaded system analysis. After the detector nonlinearity compensation is considered, both simulated NNPS and DQE fit well the experimental data.

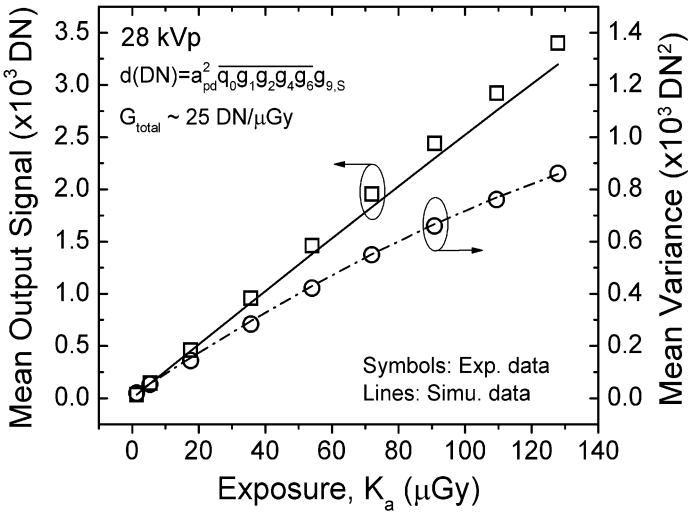

Figure 3.11 Experimental (symbols) and simulated mean output signal in DN (squares) and pixel mean variance in DN^2 (circles) for detector air kerma ranging from 1.3 to 127 μGy. Signal/noise non-linearity is included.

We extracted the experimental input referred electrical signal ($d(e^-)$) at the sensing node by $d(DN) \times S(e^-/DN)$. As shown in Figure 3.10, the simulated $d(e^-)$, given by $(a_{pd})^2 \overline{q_0 g_1 g_2 g_4 g_6}$, is consistent with experimentally extracted data for K_a up to 127 μGy. Therefore, the gain parameters used in the simulation are validated. In addition, linear signal response is observed up to stage 6 of the cascaded system. The signal nonlinearity only occurs on the CMOS APS level (stage 9).

Figure 3.11 shows the measured and simulated mean output signal $d(DN)$ and mean variance $\sigma^2(DN^2)$ at various x-ray exposure levels. In comparison to signal (R-value ≈ 0.9993), mean variance nonlinearity over K_a is observed (R-value ≈ 0.997). This finding is consistent with the large variation in $N(e^-/DN)$ as shown in Figure 3.8. The mean signal and variance extracted experimentally and theoretically are consistent with each other. Hence, we demonstrated that the nonlinear compensation operated in cascaded system analysis is necessary and results in reliable analysis. The total system gain (G_{total}) of ~25 DN/μGy was extracted from the slope of $d(DN)$ vs. K_a curve.

3.2.4 Electrical properties of CMOS APS x-ray detector

In general, linear cascaded system analysis is applied to simulate the x-ray imaging

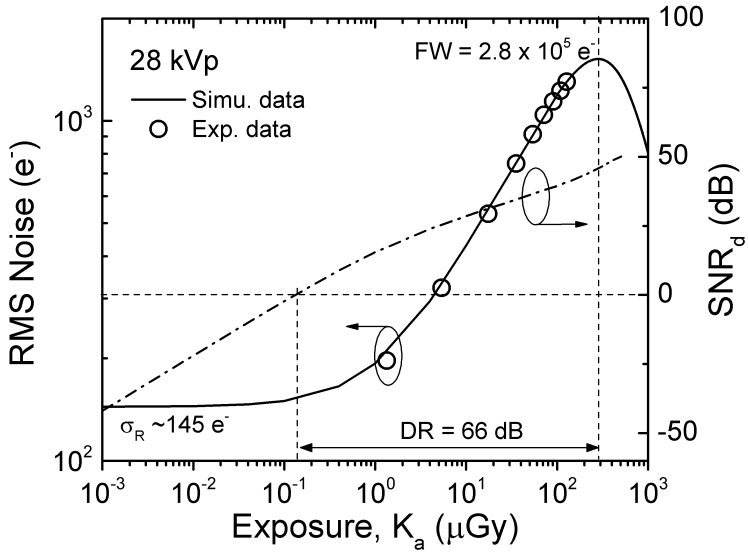

Figure 3.12 Experimental (circles) and simulated (solid line) RMS pixel total noise for DynAMITe SP detector at air kerma ranging from 10^{-3} to 10^{3} μGy. The detector signal-to-noise ratio (SNR_d) (dash line) is also shown. Detector full well capacity (FW), read noise and dynamic range (DR) were extracted.

performance of flat-panel x-ray detectors, while the electrical properties such as full well capacity (FW), DR and read noise of x-ray detectors are not evaluated. In this study, the nonlinear cascaded system analysis enables direct extraction of the electrical properties without additional optical or electrical measurements.

Figure 3.12 shows the total noise in RMS electrons at K_a from 1 nGy to 1 mGy. $\sigma(e^-)$ is extracted by $\sigma(DN) \times K(e^-/DN)$. At a very large K_a (>285 μGy), the CMOS APS x-ray detector is saturated and $\sigma(DN)$ drops as $(g_{9,N}(DN/e^-))^2$ decreases fast with K_a. $\sigma(DN)$ data for K_a > 285 μGy should not be considered. Here to extract the FW and DR, a constant conversion gain (K = 0.024 e^-/DN) was used, so that $\sigma(e^-)$ is proportional to $\sigma(DN)$.

The full well capacity of a CMOS image sensor is given by $FW(e^-) = K(e^-/DN) \times d_{max}(DN) = d_{max}(e^-)$, where $d_{max}(e^-)$ is determined when $\sigma(DN)$ (i.e. $\sigma(e^-)$) reaches the maximum. At $K_{a,max}$ = 285 μGy, $d_{max}(DN)$ = 6667 DN, hence the FW of 2.8×10^5 e^- was obtained..

The dynamic range is defined by the ratio of maximum ($K_{a,max}$) and minimum input signal ($K_{a,min}$). $K_{a,min}$ is normally defined when the SNR_d reaches zero decibel, i.e. signal

equal to noise. As shown in Figure 3.12, the SNR_d were calculated by Equation 2.24 and we got $K_{a,min}$ = 0.14 μGy. Thus $DR = 20 \log(K_{a,max}/K_{a,min})$ = 66 dB was extracted. Since the signal conversion from K_a to $d(e^-)$ is linear, the DR can also be calculated by $DR = 20 \log(FW(e^-)/\sigma_R(e^-))$ = 66 dB.

The electronic read noise ($\sigma_R \sim 145\ e^-$) can be directly acquired from the noise floor at low exposure ($K_a < 0.1$ μGy) levels.

The extracted FW, DR and σ_R values from the nonlinear cascaded system analysis are consistent with the experimental and published results obtained by MV analysis ($2.8 \times 10^5\ e^-$, 66 dB, ~150 e^-, respectively) [57], [58]. Therefore, we demonstrated that the proposed cascaded system analysis in combination with signal/noise nonlinearity can be used as an efficient tool to evaluate the electrical properties of 50 μm pixel pitch CMOS APS x-ray detectors.

3.2.5 Temporal noise of the DynAMITe SP x-ray detector

For low dose DBT application, when K_a < 10 μGy, the temporal noise (read noise) of CMOS APS x-ray imager can be the limiting factor for imaging performance. Thereby, to further improve the detector performance, the temporal noise of DynAMITe SP detector needs to be evaluated. In general, the total temporal noise of CMOS APS pixel circuit (σ_{pixel}) consists of reset noise (σ_{reset}), dark current shot noise (σ_{dark}), thermal noise for SF ($\sigma_{th,SF}$), RS ($\sigma_{th,RS}$) and Bias transistors ($\sigma_{th,Bias}$), and transistor flicker noise for RST ($\sigma_{fl,RST}$), SF ($\sigma_{fl,SF}$) and RS ($\sigma_{fl,RS}$) [141]:

$$\sigma_{pixel}^2 = \sigma_{reset}^2 + \sigma_{dark}^2 + \sigma_{th,SF}^2 + \sigma_{th,RS}^2 + \sigma_{th,Bias}^2 + \sigma_{fl,RST}^2 + \sigma_{fl,SF}^2 + \sigma_{fl,RS}^2, \quad (3.2)$$

where all the temporal noise components are in electrons and input referred to the sensing node.

The reset noise is described as

$$\sigma_{reset} = \sqrt{2kTC_{PIX}}/q, \quad (3.3)$$

where k is the Boltzmann constant, T is the temperature, C_{PIX} (~40 fF) is the total input capacitance. In general, reset noise is given by $(kTC_{PIX})^{1/2}/q$. However, since the double sampling technique currently used for DynAMITe detector is uncorrelated (i.e. two separate frames are used to capture the dark and x-ray images), the reset noise variance

should be doubled [53]. To reduce or eliminate the reset noise, 4-T CMOS APS with a pinned photodiode in combination with correlated double sampling (CDS) should be developed [142].

The dark current shot noise is given by

$$\sigma_{dark} = \sqrt{J_{dark} a_{pd}^2 t_{\text{int}} / q}, \tag{3.4}$$

where J_{dark} (~10 pA/cm^2) is the dark current density of c-Si photodiode, $(a_{\text{pd}})^2$ is the photodiode area, and t_{int} is the integration time (~0.15 s).

The thermal noise of SF, RS and Bias transistors was reported [120]. The input referred thermal noise for these transistors can be written as

$$\sigma_{th,SF} = \frac{C_{PIX}}{qA_V}\left(\frac{2}{3}\frac{kT}{C_{Col}}\frac{1}{1+\left(g_{m,SF}/g_{d,RS}\right)}\right)^{1/2}, \tag{3.5}$$

$$\sigma_{th,RS} = \frac{C_{PIX}}{qA_V}\left(\frac{kT}{C_{Col}}\frac{1}{g_{d,RS}\left(1/g_{d,RS}+1/g_{m,SF}\right)}\right)^{1/2}, \tag{3.6}$$

$$\sigma_{th,Bias} = \frac{C_{PIX}}{qA_V}\left(\frac{kT}{C_{Col}} g_{m,Bias}\left(\frac{1}{g_{d,RS}}+\frac{1}{g_{m,SF}}\right)\right)^{1/2}, \tag{3.7}$$

where A_{V} is the voltage gain (in V/V) of the SF (~0.8), C_{Col} is the transistor in the column line, $g_{\text{m,SF}}$, $g_{\text{d,RS}}$ and $g_{\text{m,Bias}}$ represent the transconductance of SF, channel conductance of RS and transconductance of Bias transistor, respectively.

The flicker noise ($\sigma_{\text{fl,RST}}$, $\sigma_{\text{fl,SF}}$ and $\sigma_{\text{fl,RS}}$) was calculated by adopting the non-stationary time domain model [143]:

$$\sigma_{fl,RST}^2 = \left(\frac{C_{IN}}{WLC_{ox}}\right)^2 \frac{1}{(t_{rst}+\delta)^2}\int_0^{t_{rst}}\int_0^{t_{rst}}\int_{\lambda_L}^{\lambda_H} C_\lambda(t_1,|t_2-t_1|)g(\lambda)d\lambda dt_1 dt_2, \tag{3.8}$$

$$\sigma_{fl,SF}^2 = \left(\frac{g_{m,SF}C_{IN}}{A_V WLC_{ox}}\right)^2 \frac{e^{-\frac{2g_{m,SF}}{C_{M2}}t_r}}{C_{M2}^2}\int_0^{t_r}\int_0^{t_r}\int_{\lambda_L}^{\lambda_H} C_\lambda(t_1,|t_2-t_1|)g(\lambda)e^{\frac{g_{m,SF}}{C_{M2}}(t_1+t_2)}d\lambda dt_1 dt_2, \tag{3.9}$$

$$\sigma_{fl,RS}^2 = \left(\frac{g_{m,RS}C_{IN}}{A_V WLC_{ox}}\right)^2 \frac{e^{-\frac{2g_{d,RS}}{C_{M3}}t_r}}{C_{M3}^2}\int_0^{t_r}\int_0^{t_r}\int_{\lambda_L}^{\lambda_H} C_\lambda(t_1,|t_2-t_1|)g(\lambda)e^{\frac{g_{d,RS}}{C_{M3}}(t_1+t_2)}d\lambda dt_1 dt_2, \tag{3.10}$$

where W and L are the transistor channel width and length, C_{ox} is the gate oxide capacitance per unit area, t_{rst} is the reset time, t_{r} is the readout time, δ is the thermal time,

λ stands for the transition rate for an electron to occupy a trap state, λ_H and λ_L are the highest and lowest transition rate respectively, $g_{m,RS}$ is the transconductance of RS, $C_{M2} = (1+g_{m,SF}/g_{d,RS})C_{Col}$, $C_{M3} = (1+g_{d,RS}/g_{m,SF})C_{Col}$, $C_\lambda(t,\tau)$ represents the auto-covariance function of the trap electron number $N(t)$, and $g(\lambda)$ is the distribution of λ, C_λ and $g(\lambda)$ are given by [143]

$$C_\lambda(t,\tau) = \frac{1}{4} e^{-2\lambda\tau}\left(1-e^{-4\lambda t}\right), \tag{3.11}$$

$$g(\lambda) = \frac{4kTWLt_{ox}N_t}{\lambda \ln\left(\lambda_H / \lambda_L\right)}, \tag{3.12}$$

where t_{ox} is the thickness of transistor gate oxide, N_t is the gate oxide trap density. Taking standard parameters for 0.35 μm CMOS technology, the flicker noise of RST, SF and RS were calculated.

All the temporal noise elements of CMOS APS pixel circuit are shown in Figure 3.13. After adding up all the components, σ_{pixel} of 116 e^- is obtained. The 50 μm pixel pitch CMOS APS pixel noise is mainly due to the reset kTC noise, σ_{reset} ~ 114 e^-, while dark current shot noise, thermal and flicker noise show negligible contributions to the total noise. The calculated σ_{pixel} deviates from the previously extracted read noise σ_R of ~145 e^-. The difference indicates the presence of a large readout circuit noise of ~87 e^- in the system. The FPN was removed by the image correction algorithm during the evaluation of imaging performance and excluded from the temporal noise analysis; hence it will not contribute to the extracted total read noise. Most likely, the reset noise (114 e^-) and noise from external readout circuit electronics (87 e^-) contribute the most to the extracted σ_R of ~145 e^-.

If in the future, the external readout circuit noise can be reduced by better circuit design, the temporal noise is still limited by σ_{reset}. To minimize σ_{reset}, CDS has been widely used in CMOS image sensor industry [55], [144]. To realize real CDS, 4-T CMOS APS pixel design in combination with a pinned photodiode (PPD) should be used [145]. Within a single frame, CDS will read both a reset (dark) and an x-ray photon induced signal row by row (or column by column). The integration time of CDS with 4-T CMOS APS is determined by the time period between the PPD reset stage and carrier transfer stage in each row (or column), when the detector is irradiated [55].

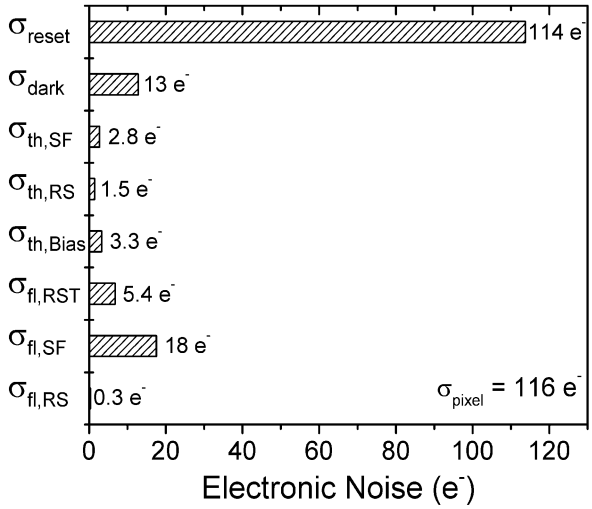

Figure 3.13 Calculated temporal noise of CMOS APS pixel and readout circuits.

Therefore, to implement such x-ray imaging technology, an extended (but not necessarily continuous) x-ray pulse width (including both the integration and readout times) is required, because the integration stage shifts during the readout process in each row (or column). A much lower σ_{read} of around 50 - 100 e^- is expected using such technology.

3.3 Summary

The 50 μm pixel pitch DynAMITe CMOS APS x-ray detector achieves both a high spatial resolution (f_{Nyq}) up to 10 mm^{-1} and a low electronic noise of around 150 e^-. Maximum DQE of around 0.55 has been demonstrated at a low DBT K_a of ~10 μGy. In addition, the 2D cascaded system analysis model has been validated by simulating both the x-ray imaging performance and detector electrical properties. The noise properties of the DynAMITe detector have also been studied.

So far, CMOS APS x-ray detectors show very high 2D x-ray imaging performance as measured by the 2D MTF, NNPS and DQE. In the next chapter, the 3D DBT imaging performance of the DynAMITe CMOS APS x-ray detector will be evaluated using the 3D cascaded system analysis.

Chapter 4
Three-Dimensional X-Ray Imaging Performance of CMOS APS X-Ray Detector for DBT

4.1 Introduction

The 2D x-ray imaging performance of the DynAMITe CMOS APS x-ray detector has been measured and evaluated using cascaded system analysis in Chapter 3. Since DBT is a quasi-3D imaging technology, the DBT image quality is influenced by the system geometry and reconstruction algorithms [4], [122]. Therefore, the 3D imaging performance should be evaluated for the CMOS APS detectors. 3D cascaded system analysis for CMOS APS detectors was developed and is presented in this Chapter.

Previously, 3D cascaded system analysis models have been developed and validated for both cone-beam CT and DBT [37], [38], [119], [123]–[125], [146]. In this study, the previously developed 2D cascaded system model for the DynAMITe detector is extended to the 3D spatial frequency space. To implement the 3D cascaded system analysis, first the 2D MTF, NPS and DQE characteristics of the DynAMITe detector are measured and simulated at various projection angles (θ_i) ranging from 0 to 30°. This angle range covers the typical projection angles currently used for DBT systems [4]. We used the FBP reconstruction to convert the 2D MTF, NPS and DQE at each θ_i to the 3D spatial frequency domain (f_x, f_y, f_z). The implemented 3D cascaded system model is used to investigate the impacts of projection angle range, MGD, fiber optic plate optical coupling efficiency, focal spot blurring effect, pixel size and scintillator pixilation on the 3D imaging performance of the CMOS APS detector.

4.2 Experimental Setup

During a DBT scan, multiple projection images are collected at oblique projection angles. Oblique incident of x-ray photons on the detector will lead to resolution loss (MTF degradation at high spatial frequencies) [126]. It was also established that the off-axis incident x-ray beams do not affect the NPS [147]. Thus, DQE will be degraded by the square of MTF term. Therefore, it is important to evaluate experimentally the detector 2D MTF, NPS and DQE at oblique incident angles.

The angle-dependent 2D imaging performance of the DynAMITe detector was characterized by measuring the MTF, NPS and DQE parameters at oblique x-ray incident angles. As shown in Figure 4.1, a tomosynthesis bench-top system with a rotary stage was used to rotate the detector from 0 to 30° (incident x-ray beam is perpendicular to the detector at 0°). The detector is angulated together with the rotary stage, while the x-ray source is stationary. The x-ray source to detector distance is 65 cm and the center of rotation is located at the detector surface. This setup is empirically equivalent to a typical DBT system with a rotating x-ray source and fixed detector.

The used x-ray source was a tungsten (W) anode with an inherent aluminum (Al) filtration of 1.4 mm and a focal spot size of 3 mm. This focal spot size is larger than that of clinical DBT systems (typically 0.3 mm). However, since the tilted edge plate for MTF measurement was placed directly on top of the CMOS APS x-ray detector, the large focal spot size should not affect the measured MTF results. An external filtration of 1.1 mm Al was added to reach a total filtration of 2.5 mm Al and half value layer of around 0.83 mm Al according to the IEC standard for mammography [104]. A tube voltage of 28 kVp with a mean x-ray fluence per air kerma ratio ($\bar{q}_0/K_a$) of 7009 x-rays mm^{-2} μGy^{-1} was used [69]. The air kerma was fixed at K_a = 20 μGy for all projection angles. A sufficient large K_a value was used here to enhance the impact of oblique incident angles on the 2D detector performance.

The tilted edge technique was used to measure the 1D (horizontal and vertical) MTF of the DynAMITe detector at each projection angle θ_i [101]. A polished W edge plate was attached to the detector surface at a small tilted angle (1.5 - 3°) with respect to the detector rows or columns [59], [69]. At oblique projection angles, partial

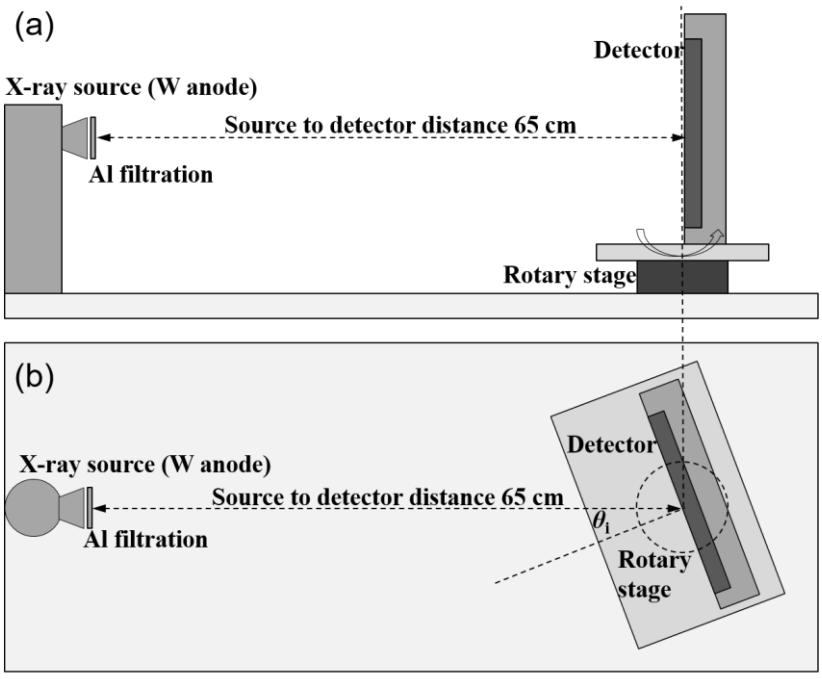

Figure 4.1 (a) Side-view and (b) top-view schematics of the bench-top system used to characterize the detector MTF, NNPS and DQE parameters. The detector is located on top of a rotary stage with a distance of 65 cm to the x-ray source.

transmission of x-ray photons through the edge may affect the MTF. This is considered as a source of uncertainty in this study. At each projection angle, a number of raw edge images (N_{edge} = 20) and flat field images (N_{flat} = 10) were captured at fixed K_a = 20 μGy (measured at zero degree projection angle) to reduce the random noise. Additional 10 frames of dark images (N_{dark} = 10) were also collected for offset correction. At each θ_i, the MTF extraction follows the discussion in Section 2.1.2. The 1D presampling MTF in either x (horizontal MTF(u)) or y direction (vertical MTF(v)) was calculated from the fast FFT of the oversampled LSF as the derivative of ESF [59], [69], [148]. The horizontal presampling MTF at θ_i is given by

$$MTF(u,\theta_i) = \left|FT\left\{LSF(x,\theta_i)\right\}\right| = \left|FT\left\{\frac{\partial}{\partial x}\left[ESF(x,\theta_i)\right]\right\}\right|. \qquad (4.1)$$

After that, the same process was repeated to measure the vertical presampling MTF at each θ_i, i.e. MTF(v, θ_i) by rotating the tilted edge by 90°. The rotatory plane is parallel to the x direction (i.e. the detector rotated horizontally).

The MTF component associated with the beam obliquity is given by

$$MTF_{ob}(u,\theta_i) = MTF(u,\theta_i)/MTF(u,0). \quad (4.2)$$

The NPS was measured from the gain and offset corrected flat-field images following the IEC standard [104] (as previous discussed in Section 2.1.3). The 2D NPS profile at each θ_i can be calculated by

$$NPS(u,v,\theta_i) = \frac{\Delta x \cdot \Delta y}{M \cdot N_x \cdot N_y} \sum_{j=1}^{M} \left| FFT\left[I(x_j, y_j, \theta_i) - S(x_j, y_j, \theta_i) \right] \right|^2, \quad (4.3)$$

where $I(x_j, y_j, \theta_i)$ is the corrected flat-field image at θ_i within a 256 × 256 region of interest (ROI), $S(x_j, y_j, \theta_i)$ is a 2D second order polynomial fit for $I(x_j, y_j, \theta_i)$ to remove the low frequency trends, Δx and Δy are the pixel pitches in x and y directions ($\Delta x = \Delta y$ = 50 μm), M is the number of ROIs (M = 243 to reach at least three million independent pixels [104]), N_x and N_y are the number of columns and rows in each ROI ($N_x = N_y$ = 256) [59], [69], [104]. The 1D horizontal (NPS(u)) and vertical NPS (NPS(v)) were extracted and averaged from seven lines on either side of zero spatial frequency.

The horizontal NNPS was calculated by $NNPS(u, \theta_i) = NPS(u, \theta_i) / d^2$, where d is the mean pixel signal in digital number (DN). The same process was used for vertical NNPS(v, θ_i).

The 1D DQE at each θ_i was calculated using the measured MTF and NNPS data. For instance, the horizontal DQE at θ_i is given by

$$DQE(u,\theta_i) = \frac{MTF^2(u,\theta_i)}{\overline{q_0} \cdot NNPS(u,\theta_i)}, \quad (4.4)$$

where $\overline{q_0}$ is the mean x-ray fluence measured at θ_i = 0 ($\overline{q_0}$= 7009 x-rays mm^{-2} μGy × 20 μGy = 1.402 × 10^5 x-rays mm^{-2}). Taking into account the fact that $\overline{q_0}$ is angular dependent, calculated zero frequency DQE(0) at θ_i is expected to be reduced by a factor of cos(θ_i). Although q_0 is spatial variant, we consider that the mean value of $\overline{q_0}$ over a large area is approximately constant.

The angle-dependent 2D MTF, NNPS and DQE parameters were used for the 3D cascaded system analysis as described in details in Section 2.3.

4.3 Angle-Dependent X-Ray Imaging Performance of the DynAMITe Detector

The 2D MTF, NNPS and DQE parameters for the 50 μm pixel pitch DynAMITe CMOS APS detector at oblique incident angles ranging from 0 to 30° were measured and simulated. Both the horizontal (parallel to the rotary plane) and vertical (parallel to the rotary axis) MTF parameters were extracted. In Figure 4.2, it is observed that beam obliquity only blurs the horizontal MTF (x or u direction in this study). The vertical MTF is not affected by oblique projection angles (x-ray source moving on the horizontal direction).

Figure 4.3 (a) shows the horizontal MTF component associated with the beam obliquity, i.e., $MTF_{ob}(u,\theta_i)$, extracted from measured MTF data by Equation 4.2 and cascaded system analysis by Equation 2.41. A scintillator thickness t of 150 μm was used in the calculation, which agrees with the scintillator thickness used in the prototype CMOS APS detector. The result demonstrates that a wide x-ray projection angle (e.g., $\theta_i > 20°$) will reduce the MTF by more than 40% especially at high spatial frequencies greater than 5 mm^{-1}. Therefore, for a 50 μm pixel pitch CMOS APS detector with a Nyquist frequency of 10 mm^{-1}, it is necessary to characterize the 2D angle-dependent detector response and include it in the 3D cascaded system analysis.

As shown in Figure 4.3 (b), since $MTF(u,\theta_i) = MTF_{ob}(u,\theta_i) \times MTF(u,0)$, the detector spatial resolution, $MTF(u,\theta_i)$, is degraded by the beam obliquity. On the other hand, both the experimental and simulation results (Figure 4.3 (c)) indicate that the $NNPS(u,\theta_i)$ is not greatly influenced by θ_i. As a result, based on Equation 4.4, the angle-dependent $DQE(u,\theta_i)$ at high spatial frequency range is degraded by the $MTF^2(u,\theta_i)$. Also we expect that $DQE(u,\theta_i)$ at zero spatial frequency, i.e., $DQE(0,\theta_i)$, will be reduced by a factor of $\cos(\theta_i)$ due to the reduction of x-ray fluence at θ_i. The modeled angle-dependent 2D MTF and NNPS data were used as the input at stage 11 for the 3D cascaded system analysis.

Previously, the 2D angle-invariant cascaded system analysis model was validated for the DynAMITe detector [69]. Specifically, the gain stages and detector nonlinearity were verified through mean signal and variance measurements and simulations; the

zero-degree MTF, NNPS and DQE at various air kerma values were also validated.

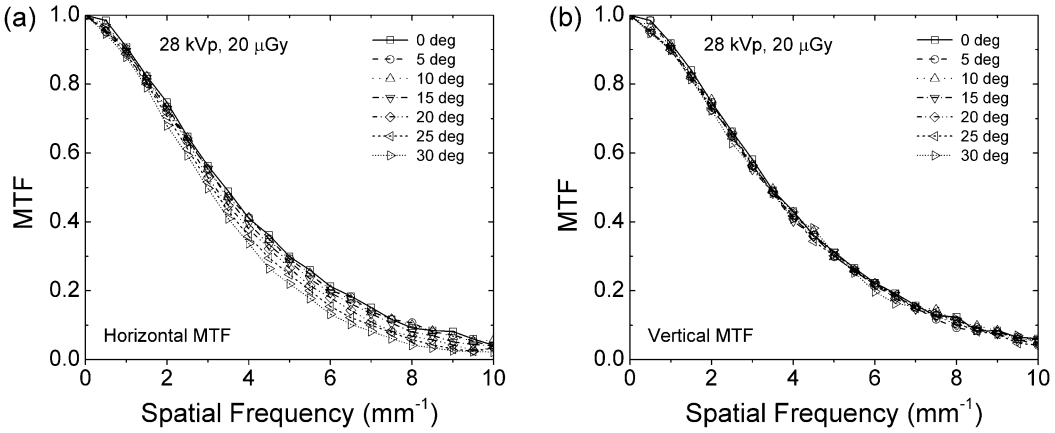

Figure 4.2 Experimental (a) horizontal (x-direction) and (b) vertical (y-direction) MTF parameter at x-ray projection angles ranging from 0 to 30 degrees. Simulation results are not shown in this figure.

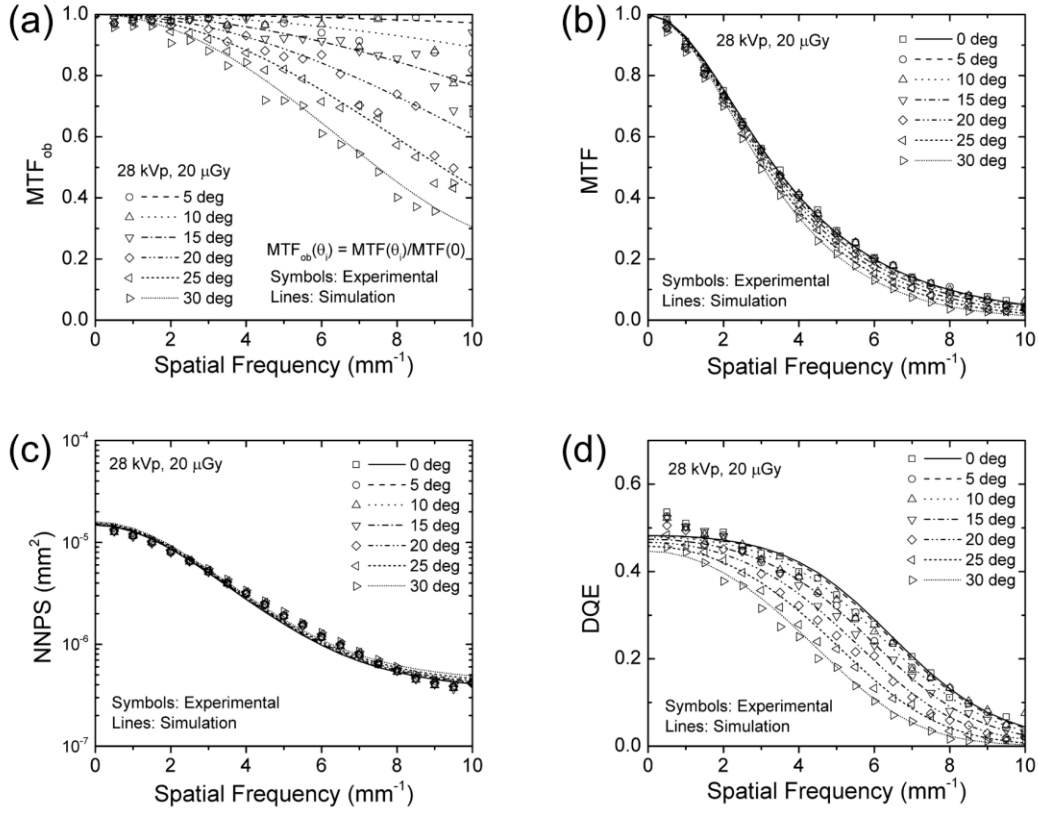

Figure 4.3 Experimental (symbols) and simulated (lines) horizontal x-direction (a) MTF associated with the oblique incident angles, (b) detector MTF, (c) NNPS and (d) DQE parameters at incident beam angles θ_i ranging from 0 to 30 degrees.

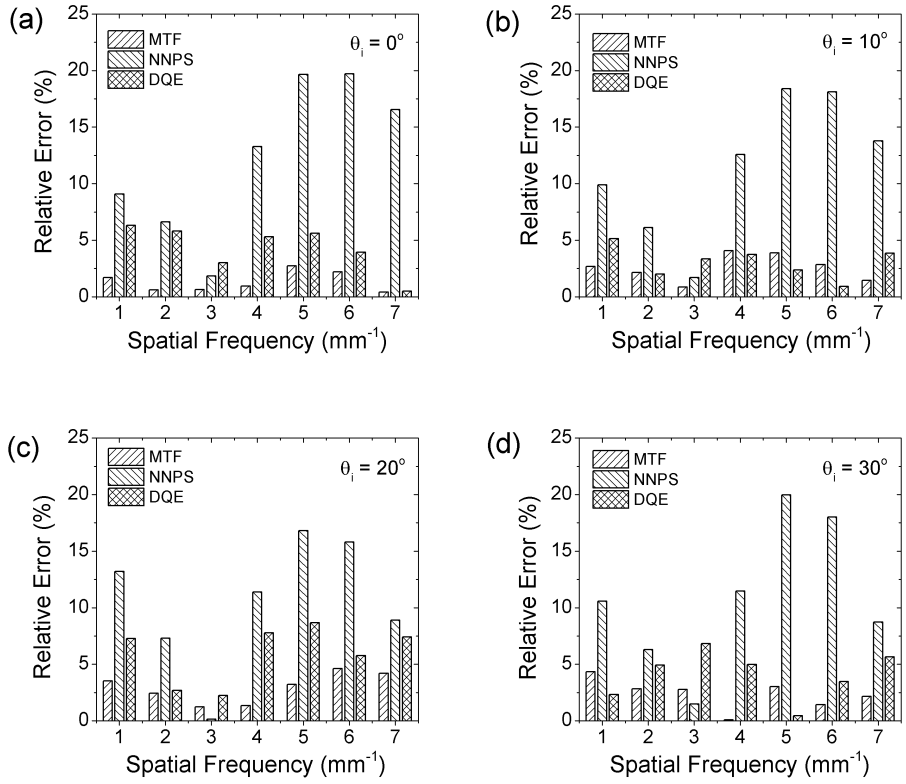

Figure 4.4 Relative errors (%) between simulated and measured MTF, NNPS and DQE parameters at x-ray beam projection angles of (a) 0°, (b) 10°, (c) 20° and (d) 30°. Spatial frequencies from 1 to 7 mm^{-1} are chosen.

Before implementation of cascaded system analysis to the 3D spatial frequency domain, it is critical to verify the 2D angle-dependent model. The maximum absolute errors ($\Delta x = |x_{sim} - x_{exp}|$) between the simulated and experimental MTF and DQE values (within entire spatial frequency range for all projection angles) are 0.04 and 0.05 (mean absolute errors are 0.011 and 0.015 for MTF and DQE), respectively. The maximum absolute errors occur at low spatial frequencies (<1 mm^{-1}). This is mainly due to the non-ideal MTF Lorentz fitting (stage 3) at low frequencies. We believe that the absolute errors are small and should not affect the results presented in this paper.

The relative errors ($\sigma_{error} = |x_{sim} - x_{exp}| / x_{sim}$) between the experimental and simulated MTF, NNPS and DQE results at x-ray projection angles of 0, 10, 20 and 30 degrees are shown in Figure 4.4. At higher spatial frequencies (8 – 10 mm^{-1}), due to the very small MTF values, a negligible absolute error (e.g., 0.01) will lead to a large relative error. Hence, spatial frequencies greater than 8 mm^{-1} (corresponding to MTF

smaller than 0.1) are omitted in Figure 4.4. The relative error of the MTF parameter is <4.6%. The NNPS parameter shows a relative error of <20%. In the cascaded system analysis, NNPS was calculated by multiplication of the square of several transfer functions ($T^2(u,v)$). Thus, the errors in MTF simulation is accumulated and amplified as the NNPS error. The NNPS deviation trend for cascaded system analysis was also observed in other studies [46], [109]. Since the MTF and NNPS errors in the cascaded system analysis are correlated, the DQE error can be reduced (proportional to $MTF^2/NNPS$). The relative errors of the DQE parameter are <8.7% under various angles and spatial frequencies. The DQE errors are within the accepted precision (10%) based on the IEC standard [104]. Hence, the angle-dependent cascaded system analysis demonstrates acceptable agreement with the experimental results. The verified angle-dependent 2D cascaded system analysis will be used as the input for the 3D cascaded system analysis.

4.4 3D X-Ray Imaging Performance of the DynAMITe Detector

4.4.1 3D MTF, NNPS and DQE

As described in Section 2.3, the 3D MTF, NNPS and DQE in the (f_x, f_y, f_z) space was calculated in combination with the FBP reconstruction. A typical DBT x-ray tube voltage of 28 kVp was used. The detector air kerma (DAK) was 8.57 μGy to realize a MGD of 1.5 mGy. If a 4.5 cm breast tissue with 50% glandularity is considered, this will lead to an entrance surface air kerma (ESAK) of 0.24 mGy and a MGD of 1.5 mGy for 21 projection views. The MGD calculation was described previously elsewhere [68], [69]. Focal spot size of 0.3 mm is used for 3D cascaded system analysis. The impact of focal spot size will be discussed in Section 4.4.4.

Figure 4.5 shows the simulated 3D MTF, NNPS and DQE (Equations 2.57 – 2.59) in the (a) x-y plane (f_x, f_y), while $f_z = 0$ and (b) x-z plane (f_x, f_z), while $f_y = 0$. Although these 3D parameters have not been empirically measured in this study, the adopted 3D

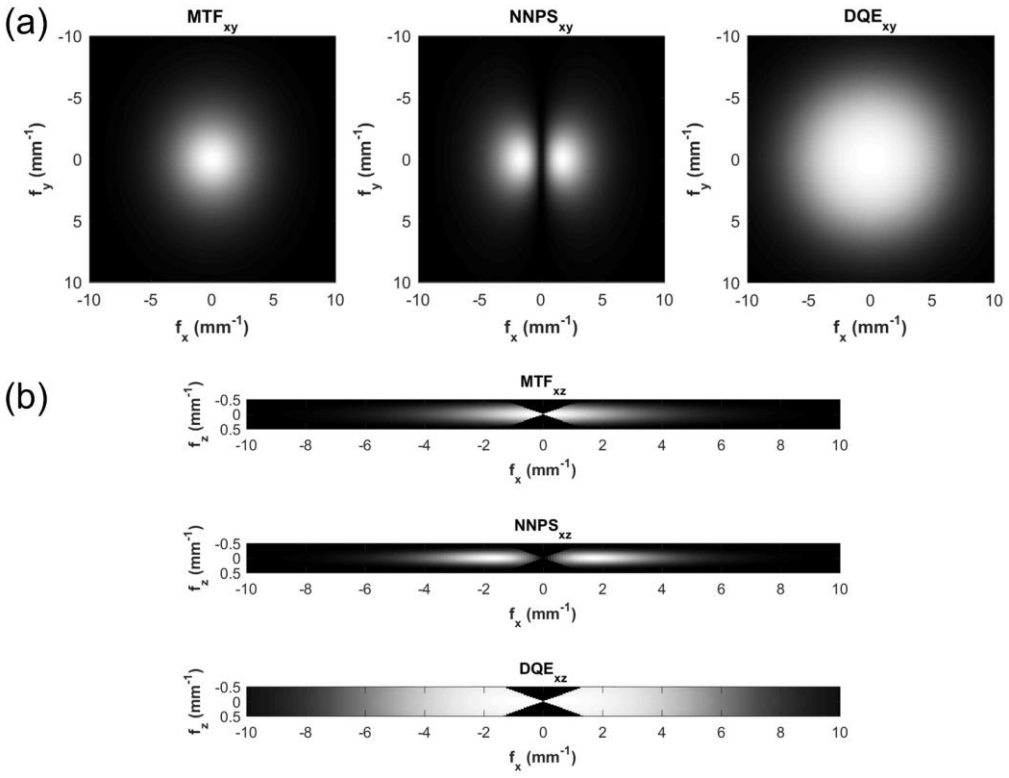

Figure 4.5 Calculated 3D MTF, NNPS and DQE in the (a) x-y plane: (f_x, f_y), while $f_z = 0$ and (b) x-z plane: (f_x, f_z), while $f_y = 0$.

cascaded system analysis model based on FBP reconstruction method have been validated previously by others with a good agreement between calculated and experimental results [38]. Therefore, the 3D MTF, NNPS and DQE presented in this work should be reliable. The obtained result demonstrates that a high spatial resolution of around 8 mm^{-1} in the x-y plane can be achieved. The x-z plane MTF, NNPS and DQE vanishes at low spatial frequencies with angles greater than the maximum projection angle. This is associated with the acquisition geometry (limited projection angle range) of DBT and will lead to poor image quality at low spatial frequencies. The impact of projection angle range on the 3D imaging performance will be discussed in section 4.4.2. In addition, modified ramp filters may be used to preserve some of the information at low spatial frequencies [127] and reduce aliasing artifacts [149].

Figure 4.6 (a) shows the calculated in-plane MTF(f_x, f_y), NNPS(f_x, f_y) and DQE(f_x, f_y) by integrating the 3D MTF, NNPS and DQE over f_z (Equations 2.57 - 2.59). The

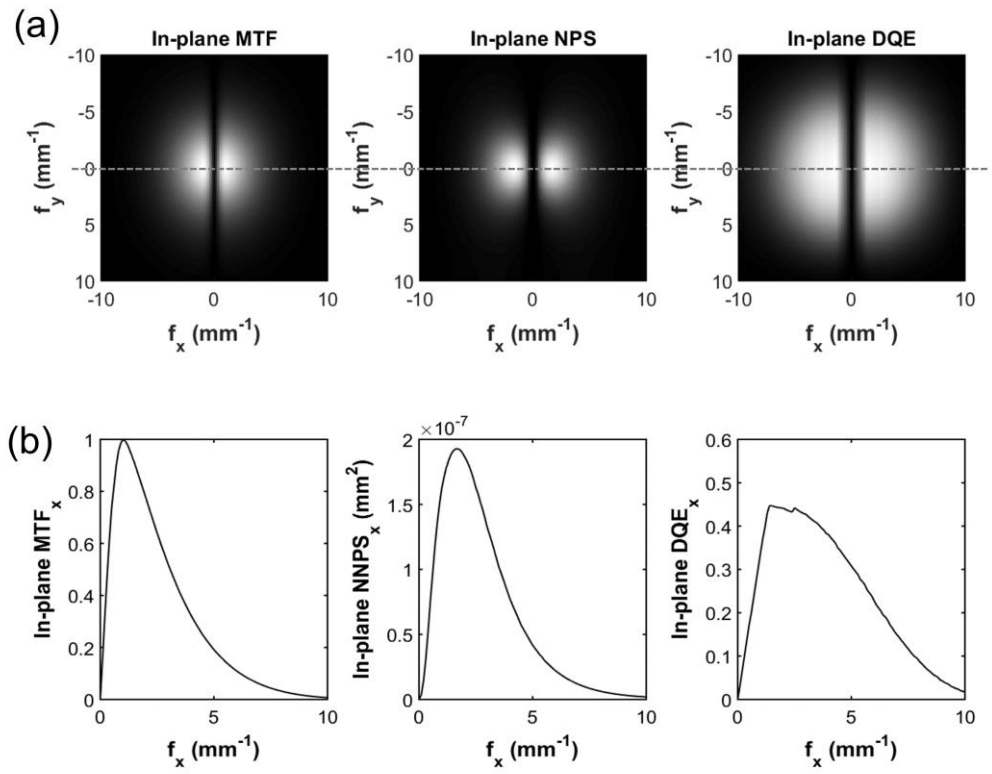

Figure 4.6 (a) In-plane MTF, NNPS and DQE calculated by integrating 3D MTF, NNPS and DQE over f_z. (b) In-plane MTF, NNPS and DQE for x direction ($f_y = 0$).

in-plane MTF, NNPS and DQE are considered as the figure of merits to characterize the 3D detector performance for DBT. The horizontal in-plane MTF, NNPS and DQE (Figure 4.6 (b)) are extracted from Figure 4.6 (a) by taking $f_y = 0$. In the following sections, only the in-plane MTF, NNPS and DQE are shown (to simplify the complexity of the presented figures) as the figure of merits to describe the 3D imaging performance of the DynAMITe CMOS APS detector.

Although the 2D detector MTF and DQE is degraded by the oblique incident angles at high spatial frequencies, it does not affect the 3D imaging performance significantly. This is because f_z is limited within a narrow range from -0.5 to 0.5 mm^{-1}. As a result, as shown in Figure 4.5 (b), the impact of wide angle, high frequency regions are eliminated. The maximum in-plane DQE achieved by the DynAMITe CMOS APS detector is close to 0.5; this value is mainly limited by the scintillator absorption ($\bar{g_1}(\theta_i = 0)$ that is around 0.56). The maximum in-plane DQE is comparable to the 2D DQE of

the Siemens MAMMOMAT a-Se direct conversion DBT system [28]. To improve the in-plane DQE, a thicker scintillator could be considered. However, such thicker scintillator could increase the scintillator blurring effect and affect the image resolution. Another possible solution will be proposed in Section 4.4.5. It is also shown that the horizontal in-plane DQE is proportional to f_x in the low spatial frequency region (< 2 mm^{-1}), which is associated with the limited projection angle range for DBT.

4.4.2 Impact of projection angle range

The impact of projection angle range (from ±15° to ±30°) on 3D MTF, NNPS and DQE are evaluated. The 28 kVp tube voltage, 21 projection views and 1.5 mGy MGD are kept constant. Based on the simulation results (not shown), a wider blank gap (e.g. Figure 4.6 (a)) appears in the middle of the in-plane MTF, NNPS and DQE and a wider "triangular" blank region (e.g. Figure 4.5 (b)) can be observed at low f_x values of the x-z plane MTF, NNPS and DQE, if a narrower projection angle range (e.g. ±15°) is used. The blank regions indicate loss of image information in the low spatial frequency region, which can be associated with large, low contrast mass detection in DBT [38]. As shown in Figure 4.7, increase of the projection angle range will shift the peak of in-plane MTF to lower frequencies and improve the in-plane DQE at low frequency region. This is consistent with the experimental and cascaded system modeling results reported by Zhao *et al* (2009). Based on our simulation results, we can confirm that a wider DBT projection angle range will result in better detection of low contrast objects such as masses [15], [38]. However, more projection views will result in a higher MGD, which is not desirable from the patient point-of-view. A possible solution to address this problem would be to have non-uniform dose distribution at different projection angles. It was also reported that a modified ramp filter with a non-zero flat transfer function (H_{RA}) at low frequencies can be used to improve the low-frequency reconstructed image quality [127]. The evaluation of the reconstruction filters impact is not considered in this study. In the following sections, the projection angle range is fixed at ±20° for consistency.

Also, shown in Figure 4.7, the in-plane DQE at high spatial frequency region almost overlaps the 2D detector DQE. Therefore, it is demonstrated that the projection

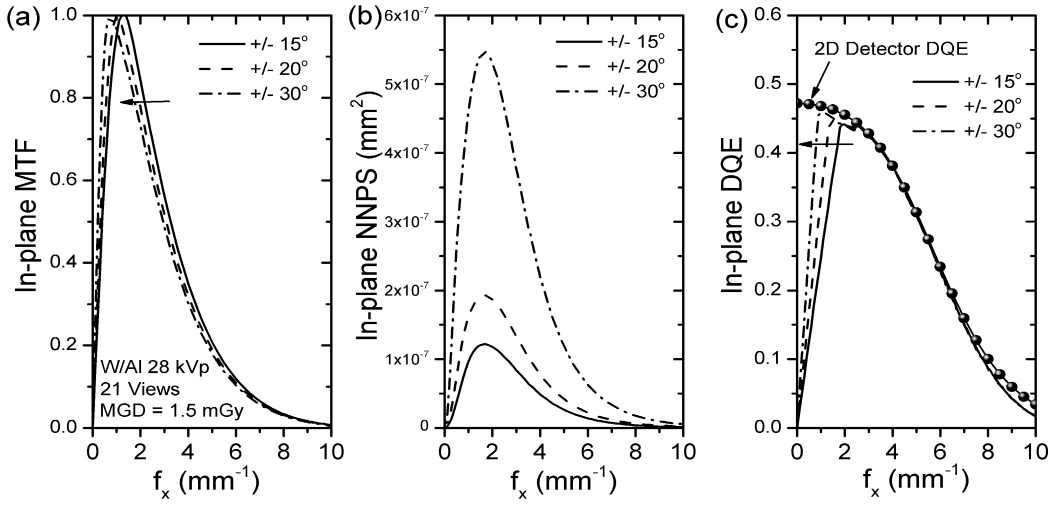

Figure 4.7 Horizontal x-direction in-plane (a) MTF, (b) NNPS and (c) DQE for projection angle range of ±15°, ±20° and ±30° at MGD of 1.5 mGy.

angle range and the FBP image reconstruction method will not affect the 3D imaging performance of a CMOS APS detector at high spatial frequencies, which is desirable for subtle microcalcification detection. Hence, we can conclude that to detect small features, the DBT detector requires to have both a high resolution and low noise characteristics. This can be realized, for example, using the CMOS or amorphous oxide TFT-based APS technology [83]–[85].

4.4.3 Impact of mean glandular dose

The current MGD used for DBT is around 1.5 mGy for an average breast with 50% glandularity [27], [132], [150]. In this study, the impact of dose on the 3D imaging performance is evaluated by varying the calculated MGD values from 0.5 to 1.5 mGy (Figure 4.8). As expected, dose does not change the in-plane MTF, but is inversely proportional to the normalized NPS. It can be observed that the in-plane DQE only decreases slightly, by about 5 and 15% averaged over the entire spatial frequency range, if MGD is reduced from 1.5 mGy to 1.0 and 0.5 mGy, respectively. This result indicates that the 3D imaging performance of the detector under investigation does not decrease significantly at very low dose. Therefore, possible dose reduction could be achieved using the 50 μm pixel pitch CMOS APS x-ray detector, because the low electronic noise

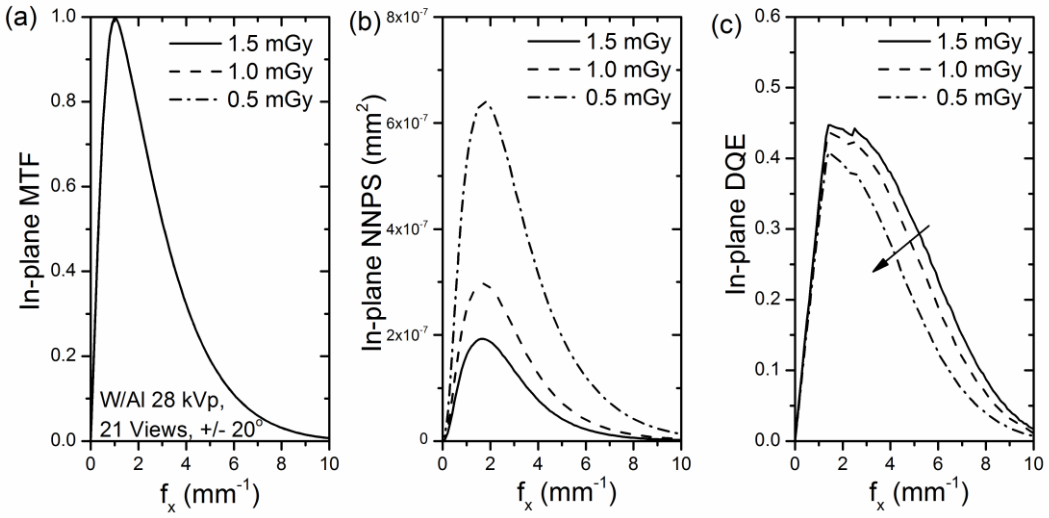

Figure 4.8 Horizontal x-direction in-plane (a) MTF, (b) NNPS and (c) DQE for MGD ranging from 0.5 – 1.5 mGy at the projection angle range of ±20°.

of this detector (σ_R ~ 150 e^-) is not the dominant noise component at low dose exposures. The noise at low doses (i.e., 0.5 – 1.5 mGy) is quantum noise limited. Under this condition, we expect the image quality to be approximately proportional to the square root of the x-ray fluence (i.e. dose). On the other hand, if the electronic noise is high (e.g., a-Si:H TFT PPS detectors with σ_R > 1000 e^-), the imager noise at low exposure is dominated by the electronic noise floor. Thus, image signal-to-noise ratio (SNR) decreases rapidly, if a very low dose is used. Hence, a high-resolution CMOS APS detector is a very promising technology for next generation low dose DBT system.

4.4.4 Impact of focal spot size

In DBT, the impact of focal spot blurring effect should be considered. Figure 4.9 shows a comparison between the calculated in-plane and x-z plane MTF, NNPS and DQE with a source focal spot size (a_{fs} in Equation 2.44) ranging from 0 to 3 mm. As described in Equation 2.43, a large a_{fs} will lead to a large effective focal spot size on the detector (a_f) that blurs the MTF laterally. Since the focal spot size will not affect the NNPS, the in-plane DQE is decreased by the square of MTF over the entire spatial frequency range, if a_{fs} is greater than 1 mm. To maintain a good image quality, an x-ray tube focal spot size of 0.3 mm or smaller should be used. This conclusion is consistent

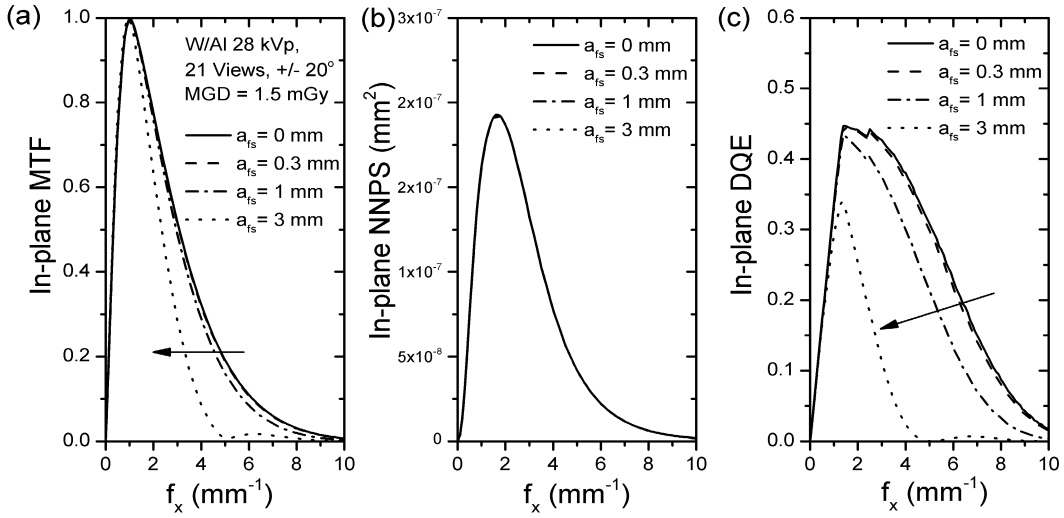

Figure 4.9 Horizontal x-direction in-plane (a) MTF, (b) NNPS and (c) DQE for focal spot size ranging from 0 to 3 mm at the projection angle range of ±20° and MGD of 1.5 mGy.

with the DBT industry practice using a focal spot size of 0.3 mm [151].

Another type of focal spot blurring is due to the focal spot motion during an x-ray pulse. This effect, evaluated by Zhao and Zhao (2008), shows reduction in DQE on the f_x direction. In this study, the focal spot motion blurring effect is eliminated by using the standard step-and-shoot x-ray tube motion. Such tube motion provides better visibility of microcalcifications due to the improved MTF at high spatial frequencies [34].

4.4.5 Impact of pixelated scintillator

The maximum in-plane DQE achieved using the DynAMITe detector in combination with the 150 µm CsI:Tl scintillator is around 0.5. It is well-known that the maximum DQE is associated with the scintillator thickness. In general, a thicker scintillator can improve the quantum detection efficiency and thus the zero-frequency DQE. On the other hand, the MTF at high spatial frequencies would be degraded due to the optical signal cross-talk between adjacent pixels [115]. The ideal scintillator should achieve both a high x-ray absorption with minimum blurring.

To prevent the scintillator optical blurring, pixelated scintillators have been proposed and evaluated [152]–[155]. Pixelated scintillators can be fabricated by (a) patterning a pre-deposited CsI:Tl film [152], (b) thermal evaporation CsI:Tl on a

pre-patterned pixelated substrate [51], [156] or (c) filling scintillating phosphors in pixelated molds (2D wells) [157]. It has been reported by different groups that pixelated scintillators improve the MTF and DQE at high spatial frequencies [51], [52], [152], [155]–[157]. In this work, the impact of scintillator pixelation on the 3D imaging performance is evaluated.

In the 3D cascaded system analysis for non-pixelated scintillator having thickness of 150 μm, a Loreantz fit was used to simulate the 2D transfer function associated with scintillator blurring effect ($T_3(u, v)$). To describe the signal transfer of pixelated scintillator, $T_3(u, v)$ is modified as $T_3(u, v) = \mathrm{sinc}(a_{sc} \cdot u) \times \mathrm{sinc}(a_{sc} \cdot v)$, where a_{sc} is the scintillator pixel pitch [52]. It should be noted that we assume that the optical cross-talk between adjacent pixels is completely removed (ideal case) by the scintillator pixelation. This could be realized by using the 2D mold or fill the gap with reflective oxides [152], [153], [157]. In addition, a scintillator performance correction factor (γ_{sc}) is multiplied by the scintillator absorption ($\bar{g}_1$); γ_{sc} may include the combined impacts of scintillator fill factor (defined by the active scintillator area over the entire scintillator pixel area) and/or the reduction in scintillator absorption. In this study, we consider a scintillator pixel pitch $a_{sc} = a_{pix} = 50$ μm and a γ_{sc} in the range of 0.8 to 1.

Figure 4.10 shows the in-plane and x-z plane MTF, NNPS and DQE for the 50 μm pixel pitch DynAMITe CMOS APS detector with a standard non-pixelated scintillator as the reference and a 150 μm thick pixelated scintillator having $a_{sc} = 50$ μm and $\gamma_{sc} = 1$. It is obvious that the 3D MTF, NNPS and DQE expand over both f_x and f_y directions. As shown in Figure 4.10, the in-plane MTF and DQE of detector with the pixelated scintillator improves significantly (by more than 0.2) in the high spatial frequency range ($f_x > 5$ mm^{-1}). Therefore, the spatial resolution of the reconstructed images is expected to be improved, which is a promising feature for microcalcification detection. On the other hand, a limited γ_{sc} (e.g., 0.8) will reduce the in-plane DQE (Figure 4.10 (a)) without affecting the in-plane MTF (Figure 4.10 (a)). Thereby, it is critical that the scintillator has a high fill factor and x-ray absorption to maintain a high DQE. Hence, using a thicker pixelated scintillator would be desirable, since no degradation in spatial resolution is expected in such case. From the cascaded system model, it is indicated that a 250 μm thick scintillator can increase the scintillator x-ray absorption by 18% ($\bar{g}_1$~

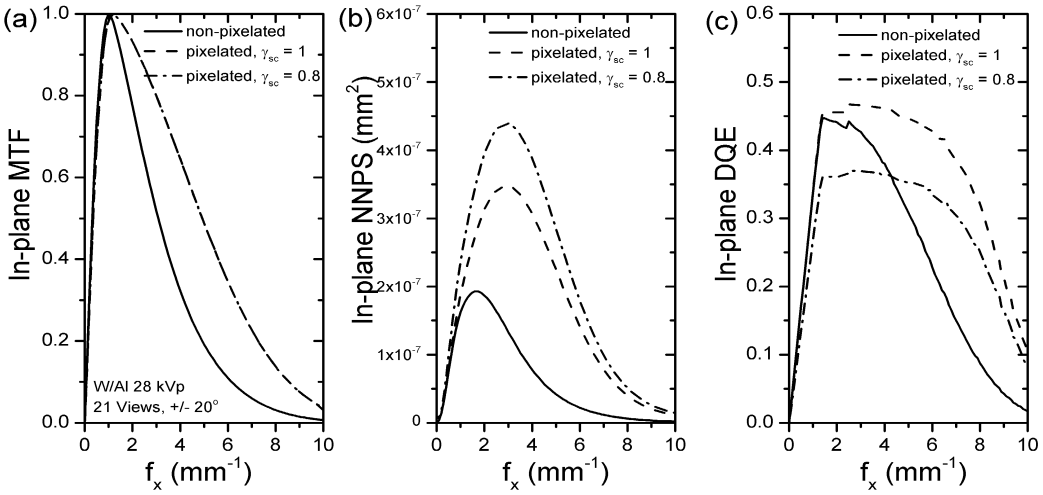

Figure 4.10 Horizontal x-direction in-plane (a) MTF, (b) NNPS and (c) DQE for standard non-pixelated scintillator and 50 μm pixelated scintillators with a fill factor of unity and 0.8. The projection angle range is ±20° and the MGD is 1.5 mGy.

0.66) in comparison to the 150 μm thick scintillator. We believe that the pixelated scintillator in combination with the low-noise CMOS APS detector should be suitable for microcalcification detection with sizes ranging from 100 to 150 μm. Also a DBT system based on the CMOS APS detector will allow radiologists to better visualize the shape of microcalcifications with the image information contained in the high spatial frequency range for observer studies. Another suggested approach to improve the spatial resolution is to use the direct conversion amorphous selenium (a-Se) photodetector in combination with the CMOS APS backplane [142], [158].

4.5 Summary

This chapter implemented the 3D cascaded system analysis to evaluate the 3D x-ray imaging performance of the CMOS APS x-ray detector. The detector demonstrates both high in-plane resolution up to around 8 mm^{-1} and in-plane DQE of around 0.5. The impacts of projection angle range, mean glandular dose, and focal spot size were evaluated. Pixelated scintillator is recommended to further improve the spatial resolution of the CMOS APS x-ray detector.

In Chapter 5, the developed 3D cascaded system analysis described above is integrated with the task-based modeling and detectability index calculation by introducing various task functions [119], [123], [125], [146], [159], [160] to evaluate the detectability of imaging tasks.

Chapter 5
Task-Based Modeling of a High-Resolution Medical Imaging System for DBT

5.1 Introduction

Although promising imaging performance has been achieved by CMOS APS x-ray detectors, system level observer studies using these detectors are very limited [66], [161]. This is due to the non-existence of a fully integrated CMOS APS prototype medical imaging system, immature DBT image reconstruction algorithms for the high-resolution detector, and insufficient human observer studies.

Task-based image quality assessments with mathematical model observers enable development, evaluation, and optimization of medical imaging systems without costly prototypes and time consuming human observer studies [162]–[167]. Cascaded system analysis in combination with the Fourier domain representation of imaging tasks and observer models provides a framework for task-based modeling used for various medical imaging applications [119], [123], [125], [146], [160], [168], [169].

Various observer models such as channelized Hoteling model, prewhitening (PW) model, PW model with eye filter and internal noise (PWEi), non-prewhitening (NPW) model, NPW model with eye filter (NPWE), and NPW model with eye filter and internal noise (NPWEi), have been evaluated and compared for task based modeling [125], [170]–[173]. Gang *et al*. and Richard *et al*. studies show a reasonable agreement with human observer performance using the NPWEi as model observers for both tomosynthesis and CT, while the simple PW model seems to overestimate the observer performance [125], [169]. Cockmartin *et al*. demonstrated good correlation between

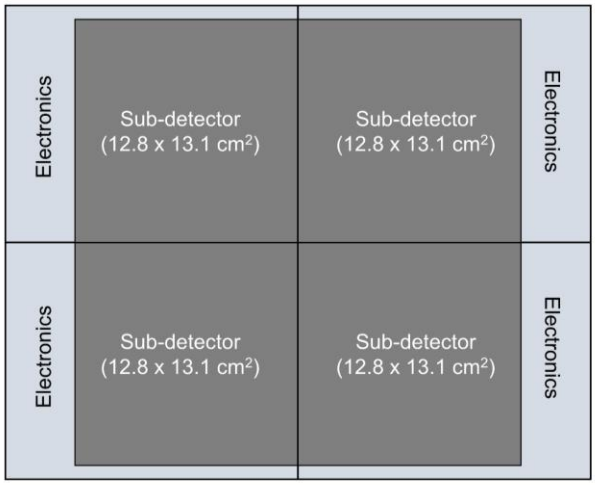

Figure 5.1 Schematic of 2 by 2 tiling of four CMOS APS sub-detectors with an active area of 12.8 × 13.1 cm^2 each.

NPWE model observer and detectability index for microcalcifications in DBT images of patients [174]. Castella *et al*. also reported good match with human observer data for mass detection in tomosynthesis using the NPWEi model [175].

In this chapter, the NPWEi model is adopted to evaluate the task-based image quality assessments of the 50 μm pixel pitch DynAMITe CMOS APS detector for DBT application. However, human observer studies are needed in the future to determine the best observer model for DBT. In Chapters 2 – 4, we have measured and modeled the 2D and 3D MTF, NPS and DQE characteristics of the DynAMITe detector [69], [95]. The detector has demonstrated an in-plane spatial resolution of around 8 mm^{-1} (at DQE of around 0.1) with low electronic noise of around 150 e^-. A 2 by 2 tiling of four sub-detectors will cover a large active area of 25.6 × 26.2 cm^2 with an ultra-high (5120 × 5248) detector resolution as shown in Figure 5.1. It was reported that distributed row drivers and dedicated edge pixel design allow a butting gap of less than 70 μm for CMOS APS x-ray detectors [176]. The butting gap (70 μm) is slightly wider than the pixel pitch of the DynAMITe detector (50 μm). We believe the narrow butting gap (around one pixel) would not affect the image quality significantly. Alternatively, amorphous oxide semiconductor TFT APS active matrix array can be used to realize a large detector active area suitable for DBT without sub-detector tiling. The proposed amorphous oxide semiconductor TFT and APS circuit will be discussed in Chapter 6

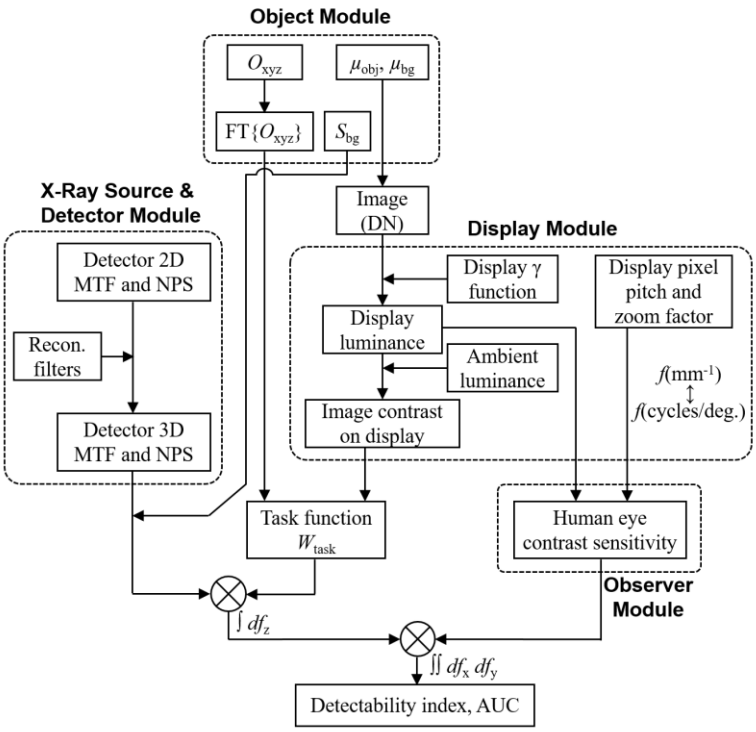

Figure 5.2 Flowchart of the task-based detectability index and AUC calculation. O_{xyz} and FFT[O_{xyz}] represent a binary object in spatial and Fourier domain; μ_{obj} and μ_{bg} are the linear attenuation coefficients for the object and background materials, respectively; S_{bg} is the anatomical background noise power spectrum.

and 7.

To fully utilize the detector resolution (5k-resolution), a compatible 5k ultra-high definition (UHD) medical imaging monitor needs to be developed in the future. Today's DBT medical imaging displays (e.g., Barco MDMG-5221) have a resolution of 2048 x 2560 and a DICOM calibrated maximum luminance of 1000 cd/m^2. Since medical imaging displays are used as the intermediate device between reconstructed DBT digital images and observers, their impacts on the task-based object detectability should be studied. In addition, the human eye contrast sensitivity as a function of display luminance should be also considered [177].

The task-based model for the DynAMITe CMOS APS detector in combination with a medical imaging display module and model observers is used to evaluate image tasks of detecting subtle, high contrast objects (such as microcalcifications) and large, low contrast objects (such as masses) for DBT application. The impacts of various parameters associated with the x-ray radiation, object size and contrast, x-ray detector,

medical imaging display, and human eye contrast sensitivity are evaluated using the task-based model.

5.2 Task-Based Model

The task-based model developed in this study consists of four modules: A) an x-ray source and detector module, B) an object module, C) a display module, and D) an observer module. Figure 5.2 shows the flowchart of the task-based detectability index (*d*') and area under the receiver operating characteristic (ROC) curve (i.e., AUC) calculation. The following provides a detailed description of each module.

5.2.1 X-ray source and detector module

The x-ray source and detector module describes the 2D and 3D imaging performance (i.e., MTF and NPS) of the DynAMITe CMOS APS detector. The detector's 2D MTF, NPS and DQE parameters were characterized at various x-ray projection angles (up to ±30°) using an x-ray source with a W anode and a total filtration of 2.5 mm Al at 28 kVp based on the IEC standard for mammography [104] in Chapter 3 [69], [95]. In Chapter 3, we have also developed a 2D cascaded system analysis model for the DynAMITe CMOS APS detector presenting a good agreement with experimental results [69]. Figure 5.3 shows an example of the calculated 2D (a) MTF, (b) NNPS and (c) DQE characteristics. A focal spot size of 0.3 mm is included. The studied 50 μm pixel pitch DynAMITe detector demonstrated a high Nyquist frequency of 10 mm^{-1} and a maximum DQE of around 0.5 at a low detector air kerma of 8.57 μGy.

Taking into account the x-ray beam obliquity [126] and reconstruction filters for FBP method [37], [119], a 14-stage 3D cascaded system analysis model was developed to calculate the 3D MTF, NPS and DQE of the DynAMITe detector in Chapter 4 [95].

It should be noted that in this chapter, the 3D MTF, and NPS are unnormalized to ensure consistency between signal and noise power for detectability index calculation.

The unnormalized 3D MTF was calculated by [37]

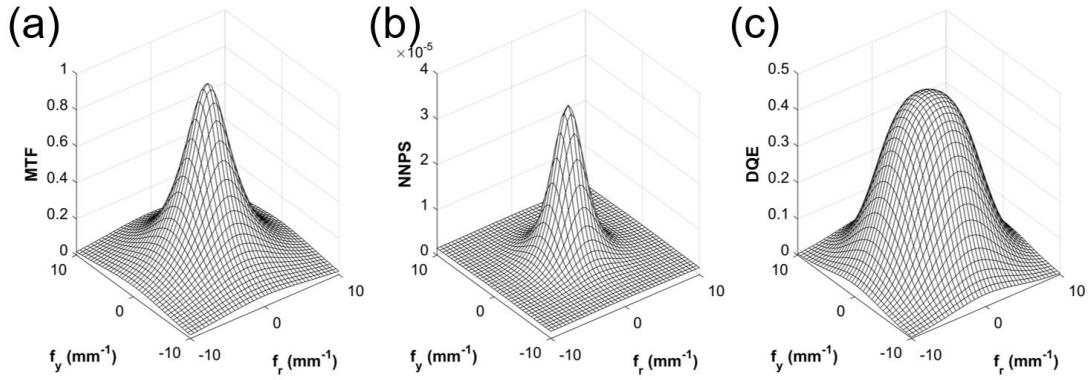

Figure 5.3 Calculated 2D (a) MTF, (b) NPS and DQE parameters using an x-ray tube voltage of 28 kVp and a detector air kerma of 8.57 μGy.

$$MTF(f_x, f_y, f_z) = \frac{N}{\theta f_r} \cdot MTF(u,v) \cdot T_{10}(u,\theta_i) \cdot T_{11}(u,v,\theta_i) \cdot H_{RA}(f_r) \cdot H_{SA}(f_r) \cdot H_{IN}(f_r, f_y) \cdot H_{ST}(f_z), \tag{5.1}$$

where $MTF(u,v) = T_3 \cdot T_5 \cdot T_7$ is the 2D MTF up to stage 9, (u, v) defines the spatial frequencies of the CMOS APS detector, (f_r, f_y) defines the spatial frequency plane perpendicular to the incident beam for each projection, $f_r = f_x/\cos\theta_i = f_z/\sin\theta_i$, and $N/(\theta f_r)$ is the spoke density at f_r.

The 3D NPS is given by [37]

$$NPS(f_x, f_y, f_z) = \frac{N}{\theta f_r} \cdot NPS(u,v,\theta_i) \cdot H_{RA}^2(f_r) \cdot H_{SA}^2(f_r) \cdot H_{IN}^2(f_r, f_y) \cdot H_{ST}{}^2(f_z) *** \mathrm{III}_{14}(f_x, f_y, f_z), \tag{5.2}$$

where $NPS(u,v,\theta_i)$ is the 2D NPS cascaded through a series of gain and spreading stages 0 to 9, III_{14} is a 3D sampling function for the reconstructed voxel matrix. Details of the 2D and 3D cascaded system analysis for the DynAMITe detector were discussed in Chapter 2 and 4.

Figure 5.4 shows the calculated 3D MTF in (a) horizontal x-y plane (MTF_{xy}) and (c) vertical x-z plane (MTF_{xz}) and NPS in (b) horizontal x-y plane (NPS_{xy}) and (d) vertical x-z plane (NPS_{xz}). An x-ray tube voltage of 28 kVp and a detector air kerma of 8.57 μGy were chosen to realize a total mean glandular dose (MGD) of 1.5 mGy for 21 projection views within an angular range of ±20°. The reconstructed voxel size is 50 μm

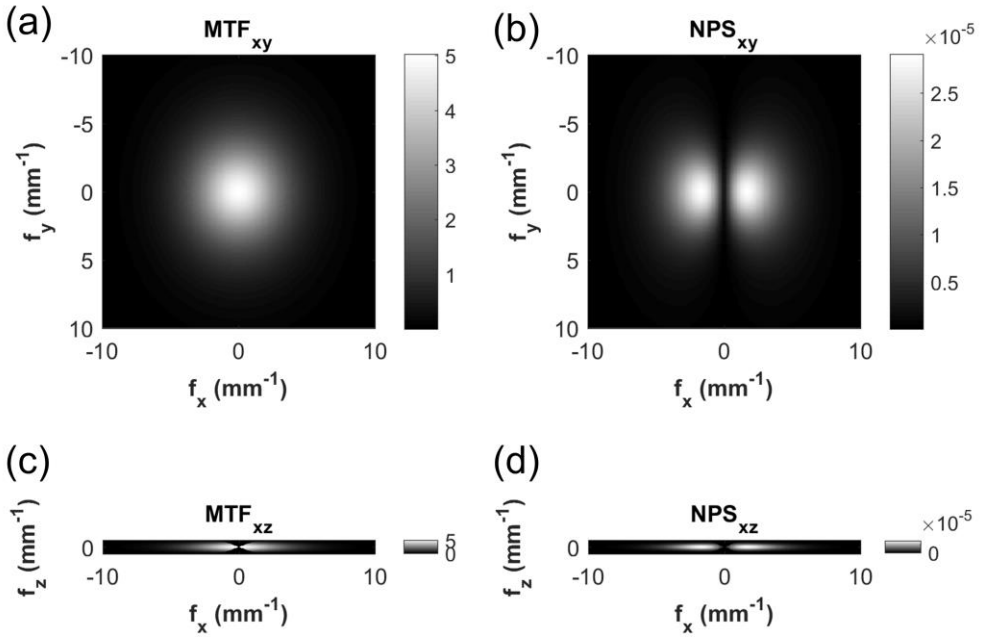

Figure 5.4 3D MTF in (a) x-y plane ($f_z = 0$) and (c) x-z plane ($f_y = 0$); 3D NPS in (b) x-y plane and (d) x-z plane. f_x, f_y and f_z are the spatial frequencies in the x, y and z directions, respectively.

× 50 μm × 1 mm. Maximum spatial frequencies of 10 mm^{-1} and 0.5 mm^{-1} have been achieved in the f_x (and f_y), and f_z directions, respectively. The empty triangular regions at low f_x values are due to the limited projection angle range for DBT. Without further notation, the above radiation and acquisition conditions were used in the task-based modeling discussed in Section 5.3 and 5.4.

The 3D MTF and NPS characteristics were weighted by a 3D task function (W_{task}) describing imaging tasks for detecting an object (i.e., lesion of interest). The 3D NPS parameter contains both the quantum noise (S_Q) of the imaging system and the electronic noise (S_E) of the detector (i.e., NPS = $S_Q + S_E$). In addition, the 3D anatomical background (structural) noise of the object (S_{bg}) is added to the 3D NPS as discussed in Section 5.2.2.

5.2.2 Object module

The detection task describes the ability of a medical imaging system to distinguish between two binary hypotheses: $h_1(x, y, z)$ denotes the "existence" of an object at a

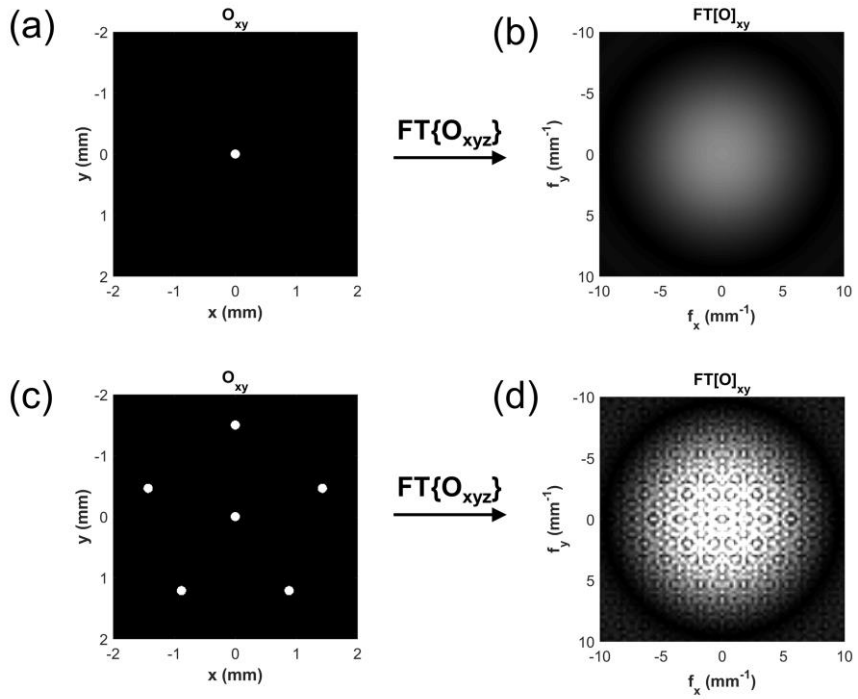

Figure 5.5 (a) O_{xyz} (when z = 0) and (b) FT{O_{xyz}} (when f_z = 0) of a single sphere with a diameter of 150 μm in the x-y plane. (c) O_{xyz} and (b) FT{O_{xyz}} of six spheres in the x-y plane.

certain location in the spatial domain, while $h_2(x, y, z)$ denotes the "absence" of the object. The task function is a combination of object function (O_{xyz}) in the spatial frequency domain and the object contrast (C). It should be noted that this is all for the "signal known exactly" (SKE, i.e., known shape, location, and amplitude) evaluation.

The object function O_{xyz} in the spatial domain can be expressed as $O_{xyz} = h_1(x, y, z) - h_2(x, y, z)$ [167], [169]. The Fourier transform (FT) of O_{xyz}, i.e. FT{O_{xyz}}, represents the distribution of an object (lesion of interest) in the spatial frequency domain. In this study, binary spheres with various dimensions are chosen as O_{xyz} indicating detection of spheres on uncluttered background [125]. Figure 5.5 demonstrate (a) an example of the O_{xyz} (i.e., a single sphere with a diameter of d_{obj} = 150 μm) shown in the x-y plane and (b) FT{O_{xyz}} in the (f_x, f_y), assuming a sharp sphere boundary; Figure 5.5 (c) and (d) show O_{xyz} the FT{O_{xyz}} of six uniformly distributed spheres as shown in Figure 5.5 (a). A smaller sphere in the spatial domain will result in a broader distribution in the spatial frequency domain. Further discussion of sphere dimensions can be found in Section 5.3.

The object contrast C for human or model observers is commonly defined by the

difference between the linear attenuation coefficients of object (μ_{obj}) and background (μ_{bg}) materials [125], [178], i.e., C is proportional to $\Delta\mu = |\mu_{obj} - \mu_{bg}|$. This is valid only if the conversion from the linear attenuation coefficient to the display luminance is linear. Although the digital image (in digital numbers, DNs) is considered linear to μ for tomosynthesis, the relationship between image DNs and display luminance levels is nonlinear for medical imaging displays [179]. Therefore, to accurately model the observer performance, a display module is included in this study. The conversion from the linear attenuation coefficients (μ_{obj} and μ_{bg}) to display luminance levels (L_{obj} and L_{bg}) will be discussed in Section 5.2.3.

In addition to the signal and contrast of the object, the anatomical background noise of breast tissue should also be included in the model. It has been reported that the 3D S_{bg} can be described by a power law spectrum [125], [180]:

$$S_{bg} = \frac{\kappa}{(\alpha f)^{\beta}}, \tag{5.3}$$

where κ denotes the magnitude of breast tissue variation (associated with glandularity) and β (typically ~3) is the degree of correlation, $f = (f_x^2 + f_y^2 + f_z^2)^{1/2}$ is the spatial frequency in the 3D Fourier domain, and α is 1 mm to maintain unit of the equation. In this study, $\beta = 2.76$ was chosen based on experimental results by Gang et al [125]. The impact of S_{bg} magnitude (κ) will be studied in Section 5.5. Without further notation, κ is assumed to be 10^{-6} mm^3 in this dissertation [181].

For the NPWEi model, S_{bg} is weighted by the 3D MTF and added to the 3D NPS of the CMOS APS imaging system. Hence the total equivalent 3D NPS of the system is given by

$$S_{total} = NPS + MTF \cdot S_{bg} = S_Q + S_E + MTF \cdot S_{bg}. \tag{5.4}$$

5.2.3 Display module

For CT and tomosynthesis, it is assumed that the digital signal of reconstructed images is proportional to the tissue's linear attenuation coefficient. However, for medical imaging displays, digital numbers (DNs) of the reconstructed DBT images are transferred to display luminance by a nonlinear DICOM grayscale standard display function (commonly known as the display gamma (γ) function for regular monitors)

[179]. Since the human eye contrast sensitivity is associated with the object luminance, the grayscale standard display function is included in the task-based model.

The grayscale standard display function was derived from Barten's human visual contrast sensitivity model [179], [182], [183]. Specifically, Barten's model (also discussed in Section 5.2.4) determines the just-noticeable luminance difference (JND) as the threshold modulation that is just visible to human eyes between two adjacent luminance levels (L_j and L_{j+1}), i.e., JND = $(L_{j+1} - L_j)/(L_{j+1} + L_j)$ [179]. Therefore, the luminance at each gray level can be iteratively extracted by

$$L_{j+1} = L_j \cdot \frac{1 + JND}{1 - JND}. \tag{5.5}$$

In this work, the display gray level for a material with a linear attenuation coefficient of μ is determined by $j = 2^N \cdot (\mu/\mu_{max})$, where N is the number of bits in gray codes, μ_{max} is the corresponding maximum linear attenuation coefficient. In this work, μ_{max} is fixed at 15.9 cm^{-1} referring to the linear attenuation coefficient of microcalcifications ($CaCO_3$) at a mean x-ray energy of about 20 keV [184]. At each gray level, the luminance L_j was scaled by the maximum luminance of display (L_{max}). In addition, the ambient luminance (L_{amb}) is added to the total luminance.

Figure 5.6 shows the grayscale standard display function for a medical imaging display with 10 bits (2^{10} = 1024) gray levels, L_{max} of 1000 cd/m^2 and L_{amb} = 0. A nonlinear relationship between display gray levels and display luminance is clearly shown. The impacts of display gray levels, display maximum, and ambient luminance will be discussed later in this chapter.

The object luminance contrast shown on a display is

$$C = \left| \frac{L_{obj} - L_{bg}}{L_{obj} + L_{bg}} \right|, \tag{5.6}$$

where L_{obj} and L_{bg} are the display luminance for lesion and background materials, respectively. L_{obj} and L_{bg} are given by

$$\begin{aligned} L_{obj} &= L_{j=2^N \cdot (\mu_{obj}/\mu_{max})} + L_{amb}, \\ L_{bg} &= L_{j=2^N \cdot (\mu_{bg}/\mu_{max})} + L_{amb}. \end{aligned} \tag{5.7}$$

The task function is a combination of $FT\{O_{xyz}\}$ with the object contrast for human

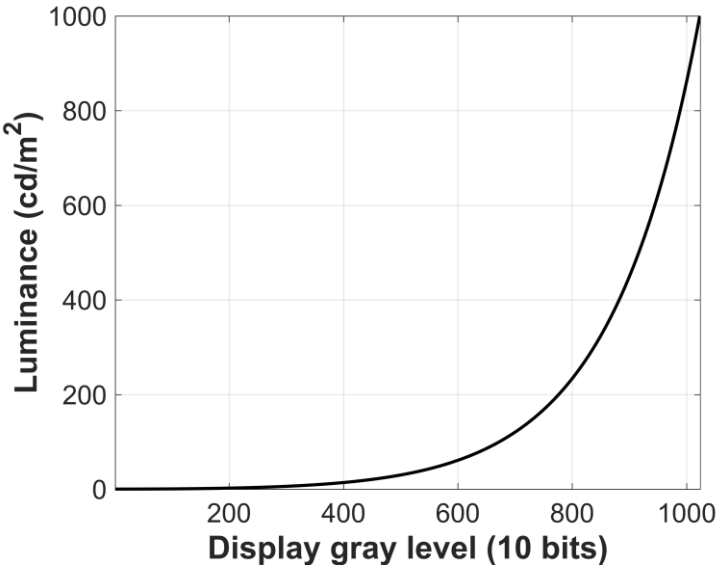

Figure 5.6 Grayscale standard display function for a medical imaging display with 10 bits (1024) gray levels and a maximum luminance of 1000 cd/m^2 [179].

or model observers [178]:

$$W_{task} = \left| C \cdot \mathrm{FT}\left\{ O_{xyz} \right\} \right|. \tag{5.8}$$

To accommodate the detector high resolution (5120 × 5248), we assume in this study the same resolution for the display to explore the image quality for future medical imaging displays, although such a high resolution medical imaging display is not currently available. The display total area (A_{disp}) is given by

$$A_{disp} = N \cdot M \cdot a_{disp}^2, \tag{5.9}$$

where $N{\cdot}M$ represents the display resolution (5120 × 5248) and a_{disp} is the display pixel pitch. Without further notation, a_{disp} is assumed to be 165 μm, which is compatible with a high definition Barco MDMG-5221 mammo tomosynthesis monitor. The display pixel pitch is also associated with the angular spatial frequency (f_{deg}) in cycles per degree for observers as discussed in Section 5.2.4.

It should be emphasized that the detector resolution, display resolution and display size are beyond the standard of available systems/products on the market. The aim of this work is not to evaluate an existed medical imaging system, but to explore possible implementation and requirements for ultra-high-resolution CMOS APS x-ray detectors and medical imaging displays for future DBT application. The proposed display module

is not currently validated, since 5k-resolution medical imaging displays are currently not available.

5.2.4 Observer module

The observer module of the developed task-based model takes outputs of L_{obj}, a_{disp} and A_{disp} from the display module and generates a contrast sensitivity function as model observers. The contrast sensitivity of human eye is defined as the inverse of the threshold modulation of a sinusoidal luminance pattern, when the tested pattern reaches 50% probability of detection. The Barten's contrast sensitivity model depends on a large number of physical quantities such as MTF, quantum efficiency, signal-to-noise ratio, and integration time of the eye; angular size and luminance of the image; and neural noise [177], [182], [183]. A mathematical approximation of the complicated physical model has been reported by Barten and demonstrated reasonable agreement with published measurement results [177]. The mathematical contrast sensitivity expression is given by [177]

$$E = \frac{5200\exp\left[-0.0016 f_{\text{deg}}^2 \left(1+100/L\right)^{0.08}\right]}{\sqrt{\left(1+\frac{144}{X_0^2}+0.64 f_{\text{deg}}^2\right)\left(\frac{63}{L^{0.83}}+\frac{1}{1-\exp\left(-0.02 f_{\text{deg}}^2\right)}\right)}}, \tag{5.10}$$

where f_{deg} is the angular spatial frequency in cycles per degree of visual angle, L is the mean luminance of the image averaged by the image areas of object and background, and X_0^2 is the angular size of the image.

The mean luminance of an image over the entire display area is presented by

$$L = L_{obj}\frac{A_{obj}}{A_{disp}} + L_{bg}\left(1-\frac{A_{obj}}{A_{disp}}\right), \tag{5.11}$$

where A_{obj} is the object area on the display.

The image angular dimension or viewing angle X_0 in degrees is given by

$$X_0 = 2\tan^{-1}\left(\frac{\sqrt{A_{disp}}}{2\cdot d_{view}}\right), \tag{5.12}$$

where d_{view} is the viewing distance (50 cm). X_0 for a very large scale (84.5 cm × 86.6 cm)

medical imaging display with a 5120 × 5248 resolution and pixel pitch of 165 μm is 81.1°. This angular size is large because of the very large display dimensions used in the evaluation. It should be noted that we are evaluating properties for advanced medical imaging display that is not available for clinical practice. Although the image angular size of 81.1° is wider than the typical values using standard medical imaging displays, the increase in the contrast sensitivity function E is negligible based on Barten's results, when X_0 is greater than 10° [177].

Figure 5.7 shows the contrast sensitivity function (E as a function of f_{deg}) of human eye at L ranging from 1 to 1000 cd/m^2 and X_0 = 81.1°. It is demonstrated that human visual system is most sensitive to angular frequencies ranging from 1 to 10 cycles/degree. Besides, the contrast sensitivity increases at higher L indicating better sensitivity for brighter (high contrast) objects.

To be consistent with the 3D cascaded system analysis and the object module, the angular frequency f_{deg} (in cycles per degree) in Barten's model should be converted to f_{x} and f_{y} (in mm^{-1}). The conversion from f_{deg} to f_{x} and f_{y} can be expressed as

$$f_{x,y} = f_{\text{deg}} \cdot \tan^{-1}\left(1\ \text{mm}/d_{view}\right) \cdot \left(a_{disp}\lambda / a_{pix}\right), \tag{5.13}$$

where d_{view} is the viewing distance in mm, a_{disp} is the display pixel pitch, a_{pix} is the detector pixel pitch and λ is a display zoom factor (default 1) describing the zoom-in feature of displays when viewing subtle lesions. The term $\tan^{-1}(1\ \text{mm}/d_{\text{view}})$ converts cycles/degree to mm^{-1}, and $(a_{\text{disp}}\lambda/a_{\text{pix}})$ is a scaling factor to map display spatial frequencies to the reconstructed slice image's spatial frequencies f_{x} and f_{y}.

The zoom factor is equivalent to a multiplication of the display pixel pitch (i.e., display $\lambda \times \lambda$ pixel binning) without changing the total display size A_{disp}. The effective display resolution is $(5120/\lambda \times 5248/\lambda)$. For simplicity, image interpolation is not considered here. Also, the impact of image zoom-in on image sharpness and noise is not evaluated.

It should be noted that the contrast sensitivity function E was applied to the reconstructed slices. Therefore, 3D MTF, NPS and W_{task} should be integrated over f_{z} before multiplication of $E(f_{\text{x}}, f_{\text{y}})$.

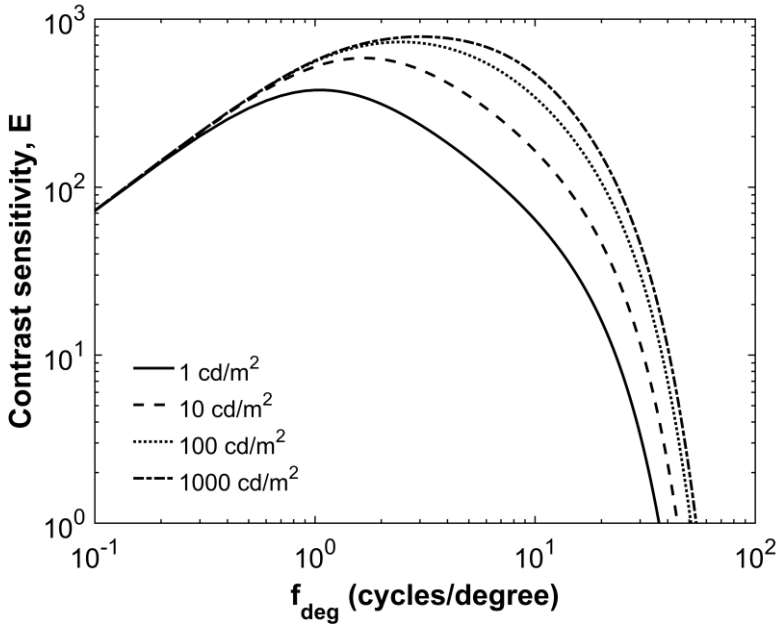

Figure 5.7 Calculated contrast sensitivity function for a display luminance L ranging from 1 to 1000 cd/m^2 and image angular dimension X_0 of 81.1° [177].

5.2.5 Detectability index and AUC

The detectability index provides a task-based performance that combines the noise equivalent quanta (NEQ = MTF^2/NPS) and W_{task}. The simplest observer model is described by a pre-whitening (PW) model that decorrelates the image noise [125]. Among various observer models studied, the NPWEi model agreed best with observer studies at various x-ray radiation conditions [125], [169]. The NPWEi model does not decorrelate the image noise. In addition, human eye contrast sensitivity function E and internal noise (N_{i}) are added. The detectability index of the NPWEi model is described as [164]:

$$d'^2 = \frac{\left[\iint E^2 \left(\int MTF \cdot W_{task} df_z\right)^2 df_x df_y\right]^2}{\iint \left[\left(E^4 \int S_{total} df_z\right) \cdot \left(\int MTF \cdot W_{task} df_z\right)^2 + N_i\right] df_x df_y}, \qquad (5.14)$$

where MTF and S_{total} are the 3D MTF and total NPS with anatomical background noise, W_{task} is the task function describing the object size and luminance contrast, E is a 2D human eye contrast sensitivity function, N_{i} is the internal uncorrelated white noise, which is proportional to the zero-frequency S_{total} [164]

$$N_i = 0.02\left(\frac{d_{view}}{100}\right)^2 S_{total}(0,0). \quad (5.15)$$

In addition, the task-based detectability index *d*' can be related to the area under the ROC curve (AUC) as [125], [162], [169]

$$AUC = \frac{1}{2}\left(1+\frac{2}{\sqrt{\pi}}\int_0^{d'/2}\exp(-x^2)dx\right) = \frac{1}{2}\left(1+erf\left(\frac{d'}{2}\right)\right). \quad (5.16)$$

The AUC describes the probability that a classifier will rank a random chosen positive test higher than a randomly chosen negative one. As shown in Equation 5.16, AUC is ranging from 0.5 (a very poor test or pure guessing) to 1 (a perfect test or completely obvious for observers) [125]. Therefore, in this work, AUC was used to score the task-based assessments.

5.3 Detectability Index and AUC for Various Objects

The calculated *d'* and AUC are determined by a large number of parameters associated with x-ray radiation, object, detector, and display performance. First, imaging tasks should be specified for DBT. Figure 5.8 shows the calculated *d'* and AUC using the DynAMITe CMOS APS x-ray detector (NPWEi model) in combination with a high resolution medical imaging display for detecting a single sphere with various sphere diameters (d_{sp}) and linear attenuation coefficients (μ_{obj}). The linear attenuation coefficient of the breast tissue is fixed at μ_{bg} = 0.7 cm^{-1} considering a mean x-ray energy of 20 keV. μ_{obj} above or below μ_{bg} will result in increased *d'* and AUC. The x-ray radiation and acquisition conditions were fixed at W/Al anode/filtration at 28 kVp, 21 projection views within ±20°, and MGD = 1.5 mGy. The focal spot size used in simulation is 0.3 mm. We observed that using a simple PW model [125] to repeat the simulation (data not shown) leads to both higher d' and AUC for all imaging tasks. The finding is consistent with Gang *et al*. data [125].

d' and AUC demonstrate the same trend with higher values appear at large d_{sp} and high μ_{obj}. As expected, high AUC can be achieved for large and high contrast objects. However, detection of small (d_{sp} < 0.5 mm) and/or low contrast objects (μ_{obj} < 1 cm^{-1}) is

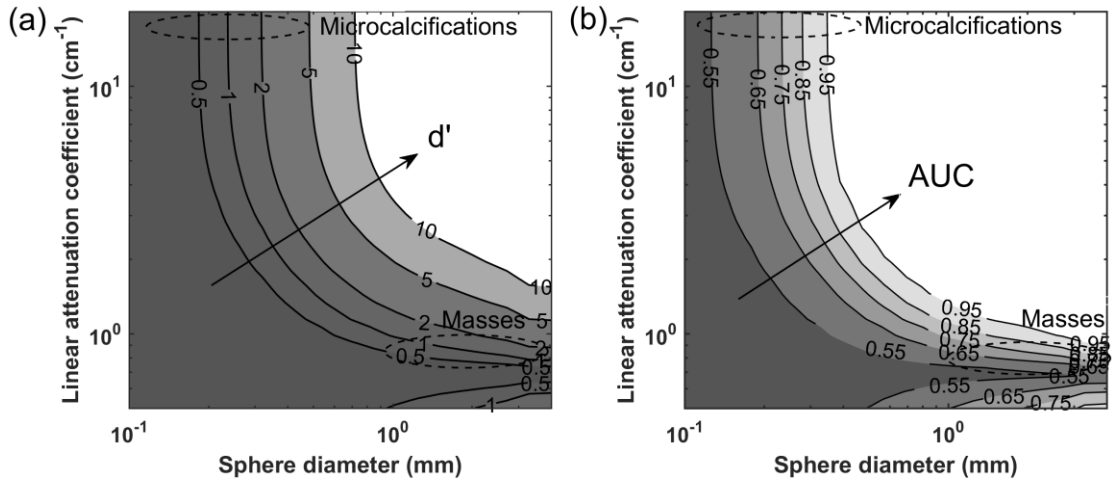

Figure 5.8 Calculated (a) detectability index and (b) AUC for a medical imaging system based on the DynAMITe CMOS APS detector for a sphere with various diameter and mean linear attenuation coefficient.

challenging. These imaging tasks include lesions of interest such as microcalcifications (small, high contrast objects) and masses (soft lesions) for DBT as labeled on Figure 5.8. In the following sections, AUC for both small, high contrast objects and large, low contrast objects are calculated. On the other hand, *d'* shares very similar information as AUC, which is neglected below.

5.4 AUC for Small, High Contrast Objects

5.4.1 Object size and display pixel pitch

The ability to detect small, high contrast objects is determined by the object dimension (d_{sp}), luminance contrast associated with μ_{obj}, and display zoom factor (λ). High contrast (μ_{obj} = 15.9 cm^{-1} and C = 0.99) microcalcifications with different dimensions (d_{sp} ranging from 100 to 200 μm) were evaluated. Besides, AUC of detecting a single sphere and a cluster of six spheres as shown in Figure 5.5 were compared.

Since human eyes are sensitive to a narrow range of angular frequencies (f_{deg} from 1 to 10 cycles/degree), the displayed image size should be carefully modulated to reach

maximum detectability. As shown in Equation 5.13 and discussed in Section 5.2.4, this can be controlled by changing the display pixel pitch (a_{disp}) and λ. In general, to enhance the image quality of such small objects, the displayed images should be zoomed in, which will result in a part of the image displayed on the monitor.

Figure 5.9 (a) – (c) shows calculated AUC for a single sphere with dimension from 100 to 200 μm using a_{disp} ranging from 50 (same as the DynAMITe detector) to 250 μm (to explore the impact of display pixel pitch on AUC) and a display zoom factor λ of 1 to 40. The maximum AUCs achieved for distinguishing single 100, 150 and 200 μm spheres are 0.58, 0.72 and 0.85, respectively. At the same time, AUC increases when using larger a_{disp} and λ. Figure 5.9 (d) – (e) repeated the calculation of (a) – (c) by replacing the single sphere to a group of six spheres (as shown in Figure 5.5). It is clearly shown that the AUC values for detecting a group of microcalcifications are higher than that of viewing a single object. The high-resolution imaging system demonstrates a satisfactory image quality (AUC > 0.9) for detecting clusters of microcalcifications greater than 150 μm using a_{disp} of 165 μm and $\lambda > 10$. a_{disp} values smaller than 100 μm will not help improve the image quality due to the limited sensitivity of human eye at high spatial frequencies [182].

On the other hand, AUC of 0.68 is achieved to detect 100 μm microcalcifications. To further improve the detectability for such small objects without increasing the MGD, the CsI:Tl scintillator may be replaced by a pixelated thicker scintillator (e.g., 250 μm). The thicker pixelated scintillator is expected to enhance both the x-ray absorption and reduce the scintillator blurring and optical cross-talk between adjacent pixels [52], [95], [155]. Calculated AUC (not shown) can be improved to 0.72 with the pixelated scintillator. Another possible option to further improve image resolution for subtle object detection is to combine CMOS APS x-ray detector with direct conversion detectors such as a-Se or mercury iodide (HgI_2) [142], [158], [185]. But in such case the uniform coverage of direct conversion photoconductors over the butting gap between sub-detectors (Figure 5.1) can be a problem. Alternatively, direct conversion detector in combination with amorphous oxide semiconductor TFT APS arrays can be used without the tiling issue. Further studies will be needed to establish the best solution to address this important issue.

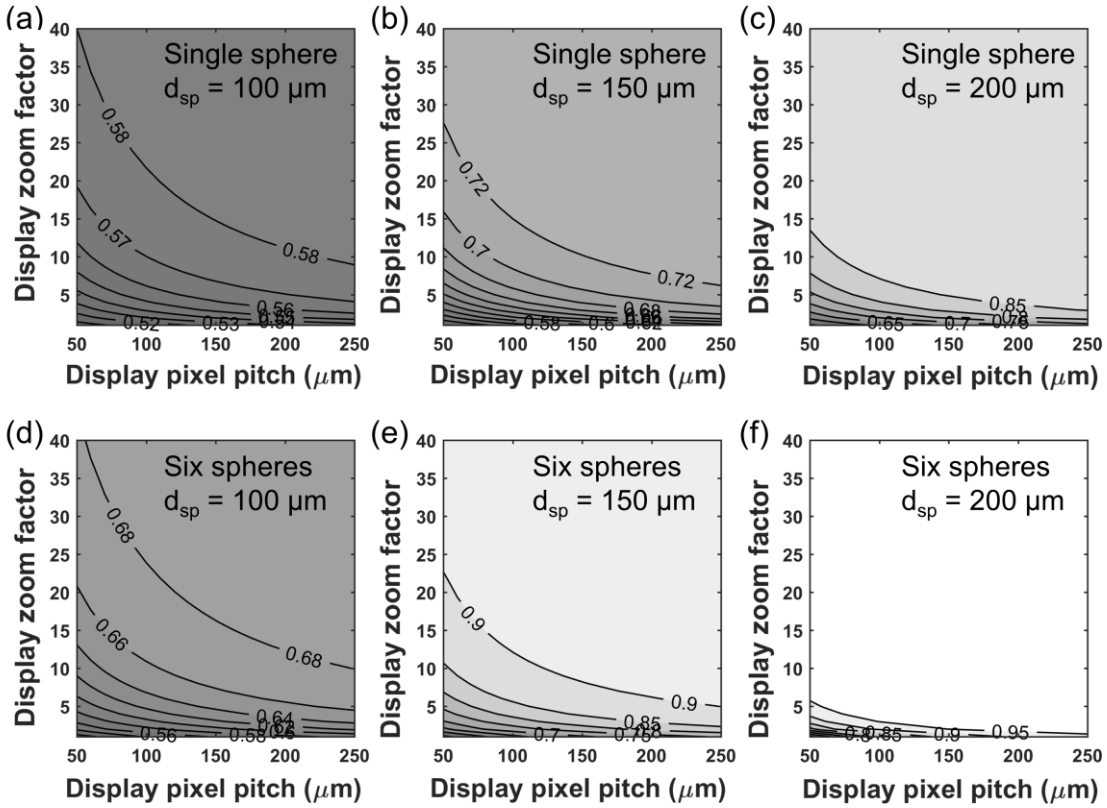

Figure 5.9 Calculated AUC for detecting a single sphere with diameters of (a) 100 µm, (b) 150 µm, and (c) 200 µm at various display pixel pitch (a_{disp}) and zoom factor (λ). (d) – (f) shows the AUC to classify six spheres with the same diameters.

5.4.2 Detector electronic noise

The main advantage of CMOS APS x-ray detectors over conventional PPS detectors is its low electronic noise. Figure 5.10 shows the calculated AUC for detecting six spheres (simulated microcalcifications) with 150 µm in size using detectors with various electronic noise (σ_{read}) ranging from 150 to 1000 e^-. It is shown that the maximum AUC value drops from 0.9 to 0.74 by increasing σ_{read} to 1000 e^-. Michell *et al.* reported AUC for microcalcifications of about 0.79 using a Hologic PPS system with MGD ranging from 1.66 to 1.90 mGy for a standard breast [186]. This AUC value is close to the estimation for an x-ray detector with high electronic noise (AUC ≈ 0.74 for σ_{read} = 1000 e^-). The detector electronic noise of around 300 e^- or smaller is desirable to achieve high AUC values. Zoom-in of the displayed image will not improve the

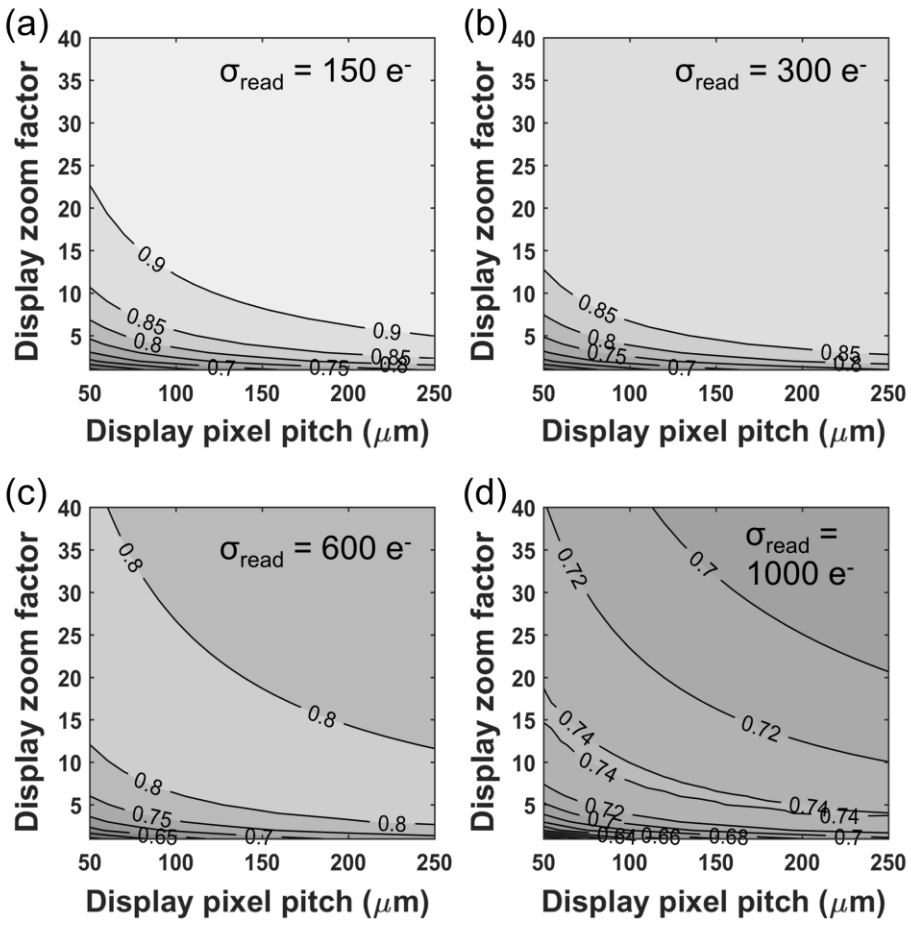

Figure 5.10 Calculated AUC for detecting six spheres with diameters of 150 μm. The electronic noise of the x-ray detector was varied as (a) 150 e^-, (b) 300 e^-, (c) 600 e^-, and (d) 1000 e^-.

detectability index significantly for a detector with high electronic noise (e.g., 1000 e^-). The spatial noise due to the fluctuation of display luminance is neglected in the task-based model. The impact of anatomical background noise (S_{bg}) on AUC will be discussed later.

For DBT application with a 50 μm pixel pitch detector, $\sigma_{read} < 300$ e^- is sufficient to detect small (e.g., 150 μm) microcalcifications. Such low noise level could be achieved by CMOS APS x-ray detectors [68], [158], [187], [188] or APS detectors based on amorphous oxide TFTs [84], [85]. The electronic noise of amorphous oxide TFT APS x-ray detectors need to be further studied using fabricated prototype imager.

The low electronic noise of the DynAMITe CMOS APS detector also features possible dose reduction for DBT. In this study, we considered a detector surface air

kerma of 8.57 μGy, which is corresponding to a MGD of 1.5 mGy considering a 4.5 cm thick breast with 50% glandularity. The MGD calculation was discussed in a previous work [68]. To evaluate the impact of MGD, we reduced the detector air kerma to 5.71 and 2.86 μGy (corresponding to MGD of 1.0 and 0.5 mGy) and calculated AUC for high contrast objects (e.g., microcalcifications) with 150 μm diameter using the DynAMITe detector. The calculated maximum AUC values are 0.85 and 0.76 using σ_{read} of 150 e^- and MGDs of 1.0 and 0.5 mGy, respectively. Hence, this study indicates that possible dose reduction (to 1.0 mGy) can be achieved using the low noise CMOS APS x-ray detector without a significant degradation of AUC (a reduction of 0.05).

5.5 AUC for Large, Low Contrast Objects

Based on the task-based analysis, the high resolution medical imaging system has demonstrated good reconstructed image quality (as measured by the detectability index and AUC) for small, high contrast microcalcifications. Another lesion of interest for breast cancer detection is the large (in comparison to small microcalcifications), low contrast mass (e.g., C <0.1). It should be noted that mass size can be ranging from 1 mm to several centimeters [189]. We selected the lower end (2 mm) as a challenging imaging task. Simulation result (not shown) shows that AUC increases (by about 0.05) for larger sphere size (e.g., d_{sp} of 4 mm). In this section, AUC for detecting large, low contrast objects is evaluated. Object linear attenuation coefficients μ_{obj} ranging from 0.6 to 0.85 were considered, while the background material's (breast tissue) linear attenuation coefficient μ_{bg} was fixed at around 0.7 cm^{-1}. The mean attenuation coefficient for low contrast objects is around 0.84 cm^{-1} corresponding to that of masses at a mean x-ray energy of 20 keV [190].

5.5.1 Number of display gray levels

For viewing low contrast objects, the display gray levels' window width may be modulated to enhanced the object contrast. In general, a narrower window width leads

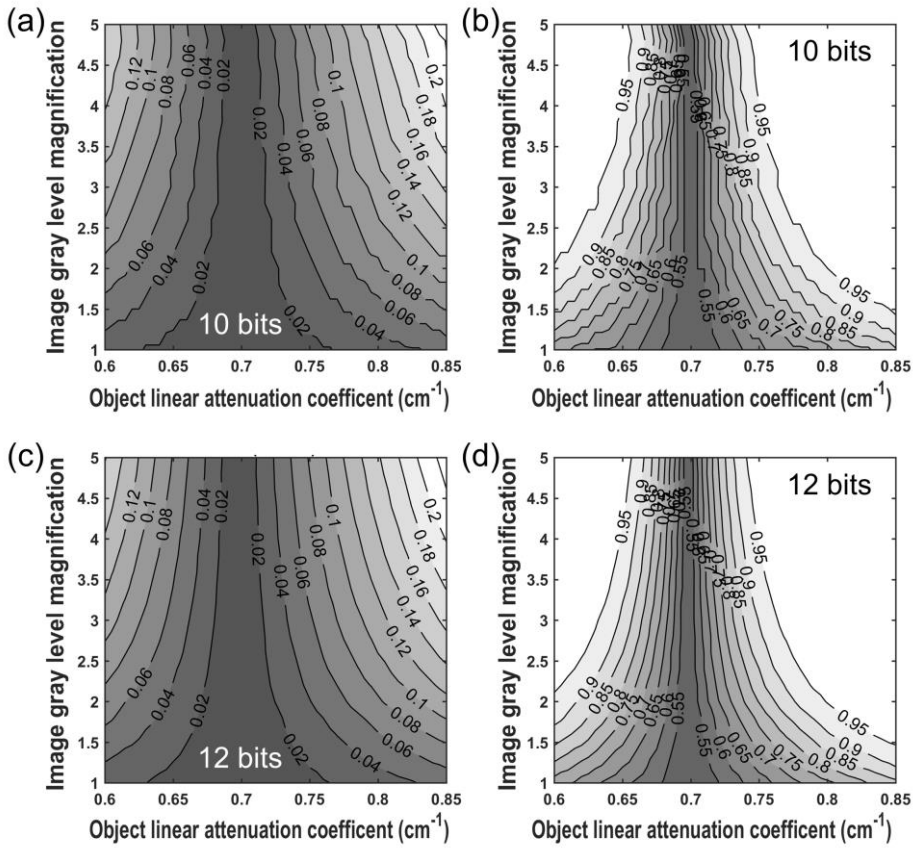

Figure 5.11 Calculated (a) display luminance contrast and (b) AUC for detecting a large sphere with diameters of 2 mm using a display with 10 bits gray levels. (c) and (d) shows the contrast and AUC by changing the number of display gray levels to 12 bits.

to more display gray levels distributed within the low image DN range, while the maximum displayable image DN is reduced. This can be realized by magnifying the image gray codes by a factor χ. Since we assumed that the image gray levels are proportional to the linear attenuation coefficients, it is equivalent to change μ_{obj} and μ_{bg} to $\chi\mu_{obj}$ and $\chi\mu_{bg}$, respectively.

Figure 5.11 shows the calculated (a) display luminance contrast (C) and (b) AUC for a 2 mm single sphere with μ_{obj} ranging from 0.6 to 0.85 cm^{-1} and image gray level magnification χ of 1 to 5. The total number of display gray levels is 10 bits (or 1024). A projection angle range of ±20° and MGD of 1.5 mGy were used. Without gray level magnification (χ = 1), an AUC value of 0.81 can be achieved for masses with μ_{obj} of 0.84 cm^{-1}. The AUC can be further improved to 0.95, if χ >2 and C > 0.08.

However, fluctuation of the contour boundaries can be observed in Figure 5.11 (a) and (b) due to the limited number of display gray levels (10 bits), which could lead to

inaccurate display luminance. Most of current DBT medical imaging displays (e.g., Barco MDMG-5221) have a gray level of 10 bits, which may not be sufficient to realize accurate image luminance especially for low contrast objects. On the other hand, the output signal (DNs) of the DynAMITe detector is 14 bits. To accommodate display gray levels, the 14 bits signal levels has to be truncated to 10 bits for the display. This will result in luminance inaccuracy and error in contrast especially for low contrast objects (when the luminance is low).

To address this issue, 12 bits (e.g., EIZO LCD GS521-CL-BK mammography display) or higher medical imaging displays would be preferred. Figure 5.11 (c) and (d) shows the *C* and AUC results using 12 bits gray codes. Smooth contour boundaries can be realized indicating accurate display luminance levels for low contrast object detection.

5.5.2 DBT projection angle range

Another important parameter for detecting low contrast objects is the geometrical x-ray projection angle range θ. In previous discussion, θ was fixed at ±20° for 21 evenly distributed projection views (MGD = 1.5 mGy). As shown in Figure 5.4 and also described in Chapter 4 [95], a limited θ will result in image information lost in the low

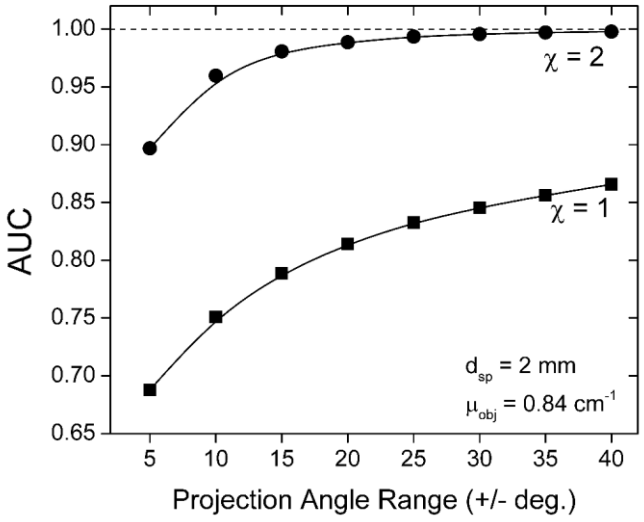

Figure 5.12 Calculated AUC for a 2 mm sphere (mass with μ_{obj} = 0.84 cm^{-1}) using a projection range θ from ±5° to ±40°. χ of 1 and 2 were selected.

spatial frequency range (<1 mm^{-1}), which is associated with the W_{task} for detecting large spheres.

Figure 5.12 shows the calculated AUC parameters for detecting a 2 mm sphere with μ_{obj} of 0.84 cm^{-1} using θ ranging from ±5° to ±40°. Image gray level magnification factors χ of 1 and 2 were chosen. Regardless of χ, AUC values increase with the θ. To maximize the AUC, θ of ±30° or greater is preferred for mass detection. This finding is consistent with the contrast-detail test using a CIRS DBT phantom [15]. At θ = ±30°, AUC values of 0.85 and 0.99 were achieved with χ of 1 and 2, respectively. Image gray level magnification could increase AUC by around 0.15 to 0.2 at all projection angle ranges.

5.5.3 Anatomical background noise

It should be noted that the anatomical background noise (S_{bg}) of the object could also affect the detectability and AUC. In previous sections, β = 2.76 and κ = 10^{-6} mm^3 were used. Determination of β and κ requires empirical measurements of S_{bg} for a specific object or phantom [181]. In this study, κ as the magnitude of S_{bg} was varied from 10^{-6} to 3 × 10^{-6} mm^3 to explore the impact of S_{bg} on AUC for large, low contrast sphere detection.

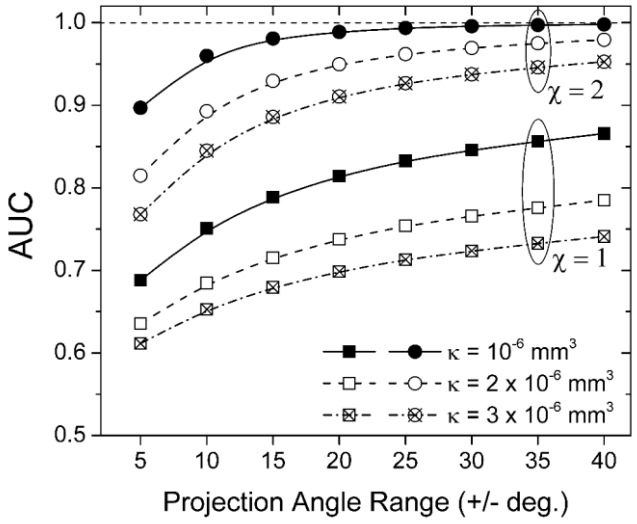

Figure 5.13 Calculated AUC for a 2 mm sphere (mass with μ_{obj} = 0.84 cm^{-1}) using a projection range θ from ±5° to ±40° and κ ranging from 1 × 10^{-6} to 3 × 10^{-6} mm^3. χ of 1 and 2 were selected.

It is shown in Figure 5.13 that the calculated AUC values for a large κ of 3×10^{-6} mm^3 at $\theta = \pm 30°$ drops to around 0.72 and 0.94, when χ of 1 and 2 were used, respectively. A large S_{bg} may refer to breasts with a higher density or glandularity. The findings indicate potential difficulties in detecting low contrast lesions such as masses in breasts with high anatomical background noise (i.e., high glandularity). Using a wider projection range (e.g., ±40°) could help improve the detectability for low contrast objects in noisy backgrounds as shown in Figure 5.13.

5.6 Display and Ambient Luminance

Finally, the display maximum (L_{max}) and ambient luminance (L_{amb}) levels could influence the detectability for both small, high contrast and large, low contrast objects. The typical L_{max} and L_{amb} values are around 1000 cd/m^2 (Barco MDMG-5221) and below 50 cd/m^2 (typical radiology room), respectively.

As shown in Figure 5.14 (a), we calculated the AUC values for detecting six spheres (microcalcifications) with d_{sp} of 150 μm and μ_{obj} of 15.9 cm^{-1}. The display pixel pitch (a_{disp}) and zoom factor (λ) were fixed to 165 μm and 10, respectively. As expected, AUC will reach its maximum value (>0.9) under large L_{max} (>1000 cd/m^2) and small L_{amb} (<50 cd/m^2) values. AUC for high contrast microcalcification detection is more sensitive to L_{max}, because increasing L_{max} would increase the human eye contrast sensitivity.

On the other hand, if large and low contrast objects such as masses (d_{sp} = 2 mm and μ_{obj} = 0.84 cm^{-1}) are considered. The L_{amb} has to be controlled as low as possible as presented in Figure 5.14 (b). χ of 2 was used to enhance the image contrast. Since the contrast for masses are low, high L_{amb} (>5 cd/m^2) could lead to further degradation of the object luminance contrast and AUC. This finding is consistent with the study by Pollard *et al* [191] and requirements for the ambient luminance (<10 cd/m^2) for mammography radiology room based on the European protocol [192].

Briefly, a high L_{max} (>1000 cd/m^2) is promising for microcalcification detection, while a low L_{amb} (<5 cd/m^2) is more important for low contrast mass detection. The

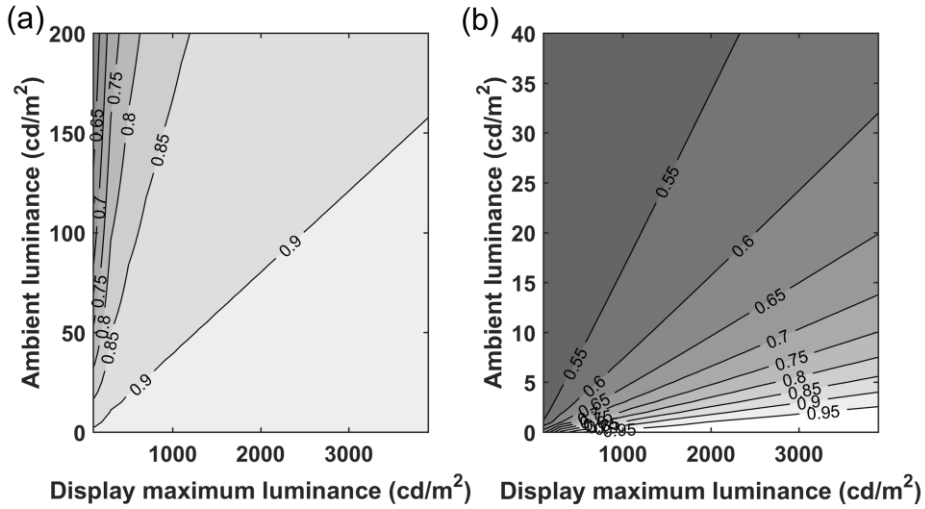

Figure 5.14 Calculated AUC for detecting (a) six spheres (microcalcifications) with d_{sp} of 150 μm and μ_{obj} of 15.9 cm^{-1}, and (b) single sphere (masses) with d_{sp} of 2 mm and μ_{obj} = 0.84 cm^{-1} using various display maximum luminance and ambient luminance.

required L_{max} is higher than current DBT medical imaging display (e.g., Barco MDMG-5221). Also, it is suggested that a dark ambient condition should be used, when imaging low contrast objects.

5.7 Summary

This chapter evaluated the detectability for various imaging tasks using the high-resolution CMOS APS x-ray detector and medical imaging display. High AUC values (>0.9) for both high contrast (such as microcalcifications) and low contrast (such as masses) objects have been demonstrated with optimized detector noise and display zoom factor and luminance properties.

So far, the electrical properties, 2D and 3D x-ray imaging performance, and task-based detectability of high-resolution CMOS APS x-ray detectors have been evaluated. Up to date, there is no doubt that CMOS APS detectors achieve the highest detector resolution and lowest electronic noise compared with other active-matrix backplane technologies.

To realize a large detector area (e.g., about 24 cm × 30 cm) for DBT using CMOS

APS detectors, it is possible to tile several wafer-scale (e.g., about 12 cm × 13 cm) sub-detectors. Fabrication multiple sub-detectors is required with increased fabrication cost. The detector tiling may have detrimental impact on the imaging performance without dedicated edge pixel design allowing a narrow butting gap comparable to the pixel pitch. Alternative large area, high-resolution, low noise x-ray detectors can also be considered for DBT.

Chapter 6
Fabrication and Evaluation of High Mobility Amorphous In-Sn-Zn-O Thin-Film Transistors

6.1 Introduction

Amorphous oxide semiconductor TFTs, as the next generation TFT technology, are being used in the flat-panel display (e.g., TVs) industry to replace the old a-Si:H TFT arrays. The high field-effect mobility (>10 cm^2/Vs), low leakage current (<10^{-13} A), good electrical stability and fast response properties make them very desirable for APS circuits. In addition, low cost, low temperature, large area panel fabrication process has been developed. Therefore, indirect or direct x-ray imagers based on amorphous oxide semiconductor TFT APS are very promising for DBT, if a pixel pitch (<75 μm) and electronic noise (<300 e^-) comparable to CMOS APS can be demonstrated.

Conventional a-Si:H TFTs enjoyed great success on both active-matrix flat-panel displays (AMFPDs) and imagers (AMFPIs) over past decades. However, the field-effect mobility of a-Si:H TFT is low (typical μ_{eff} of 0.5 to 1 cm^2/Vs). This is because the hybridized sp^3 orbitals of Si atoms form covalent bonds that are very sensitive to the bond angle variations. The atomic structure disorder and bond angle / length fluctuation of about 3 to 10% create both band tail states and deep trap states associated with the Si defects. These trap states significantly affect carrier (electrons and holes) transport in the amorphous material [193]. Such a low mobility is not sufficient for future high resolution AMFPDs or APS x-ray detectors for DBT.

On the other hand, for amorphous oxide semiconductor semiconductors, the delocalized ns orbitals (n is the principle quantum number or shell number) of heavy

metal cations (such as In, Ga, Sn or Zn) are isotropic. The sphere shaped isotropic metal ns orbitals do not greatly affect the carrier transport between a) the metal ns and oxygen 2p orbitals and b) the metal ns and metal ns orbitals, in the amorphous phase [88]. As a result, μ_{eff} in the order of 10 cm^2/Vs or higher can be achieved by amorphous oxide semiconductors.

Among various amorphous oxide semiconductors, amorphous In-Ga-Zn-O (a-IGZO) TFTs have been intensively studied and being considered for high-resolution displays [87]–[89], [99], [194]–[206] and x-ray imagers [76], [84], [207]. a-IGZO TFTs have demonstrated μ_{eff} ranging from 5 to 20 cm^2/Vs, a low leakage current of $<10^{-13}$ A, and good electrical stability [87], [194], [198], [199]. These properties are very promising for DBT APS x-ray detectors [84].

Based on Equation 1.20, to develop the TFT-based C-APS circuit with a large charge gain, TFTs μ_{eff} and g_m (proportional to μ_{eff}, Equation 1.17) should be further improved. A large device channel width over length ratio (W_{AMP}/L) for the amplifying TFT, a small on-resistance of the readout TFT (R_{ON}), and a low data line series resistance (R_{DATA}) are also desirable to achieve a high charge gain. At the same time, stable electrical properties with low threshold voltage shift (e.g., $|\Delta V_T| < 1V$) must be demonstrated under constant bias stress.

In this chapter, to fulfill the requirement for high performance TFT-based C-APS, amorphous In-Sn-Zn-O (a-ITZO) TFTs with even higher field-effect mobility of around 30 cm^2/Vs are proposed, fabricated and evaluated. These TFTs will be used to investigate the C-APS circuit to be discussed in Chapter 7.

6.2 High Mobility Amorphous In-Sn-Zn-O (a-ITZO) TFTs

Recently, a-ITZO TFTs with a boosted μ_{eff} of ~30 cm^2/Vs, V_T of ~1 V, and *SS* of smaller than 0.3 V/dec have attracted much attention as an alternative to a-IGZO TFTs [203], [206], [208], [209]. Ryu *et al* reported that the device properties such as V_T and *SS* are highly related to the Sn/(In+Sn+Zn) ratio, while improved device stability was achieved by increasing the Sn/Zn ratio [210], [211]. It was also reported that the

electron effective mass (m_e^*) in a-ITZO varies from 0.23 to 0.28 m_e by changing the ratio of (In+Sn)/(In+Sn+Zn) [212]. The obtained a-ITZO m_e^* is smaller than that of a-IGZO (0.34 m_e) [199], indicating increased field-effect mobility. In addition, the average interatomic distance between the In/Sn atoms in a-ITZO was found to be around 3.59 Å at (In+Sn)/(In+Sn+Zn) = 67%, which is smaller than the In atom interatomic distance in a-IGZO (4.35 Å, In/(In+Ga+Zn) = 33%) [212]. The closer In/Sn interatomic distance is expected to enhance the overlaps between In-5s and Sn-5s atomic orbitals resulting in increased conduction band mobility. The impacts of process conditions on device parameters and electrical instability should also be investigated.

We fabricated DC sputtered a-ITZO TFTs and optimized the process conditions. The normalized weight ratio of our a-ITZO target is In_2O_3 : ZnO : SnO_2 = 1 : 2.67 : 1.24. The voltage-dependent field-effect mobility of a-ITZO TFTs were investigated with parameters extracted using two different analytical methods. We also studied the impacts of channel thickness and oxygen gas flow ratio on device performance. Finally, the electrical stability of a-ITZO TFTs under positive and negative BTS was evaluated and compared with that of a-IGZO TFTs.

6.3 Device Fabrication

Figure 6.1 shows the cross-sectional and top views of the fabricated a-ITZO TFT by shadow masks to avoid influence of the photolithography steps on a-ITZO channel optimization. We used highly doped (p^{++}) silicon wafers with a 100 nm thermal oxide (SiO_2) layer as the substrate. The highly-doped silicon and thermal oxide acted as the gate electrode and gate insulator, respectively. The a-ITZO film was deposited on the substrate by DC sputtering in a mixture of Ar / O_2 gases at a pressure of 0.53 Pa and a DC power density of 3.1 W/cm^2. The O_2 gas flow ratio (O_2 gas flow rate / (Ar gas flow rate + O_2 gas flow rate) × 100%) was varied from 0 to 50%, while the pressure was kept constant. After the a-ITZO deposition, the a-ITZO film was annealed at 350 ˚C for 30 min. Then molybdenum (Mo) was DC sputtered as the source/drain (S/D) electrodes. Shadow masks were used to pattern the a-ITZO channel and S/D electrodes. Finally,

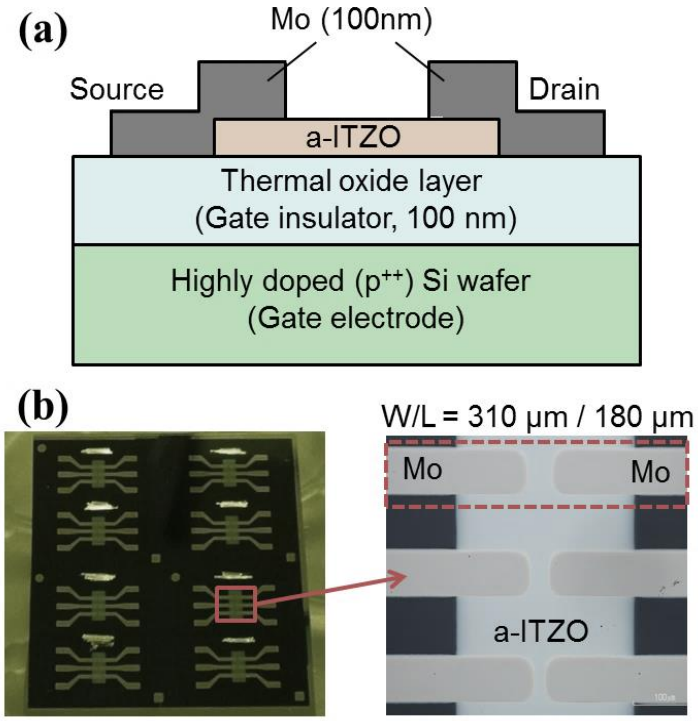

Figure 6.1 (a) Cross-sectional and (b) top views a-ITZO TFTs fabricated using mechanical mask.

fabricated TFTs were annealed again at 300 ˚C for 30 min. The channel width (W) and length (L) of the shadow mask TFTs were measured to be 310 and 180 μm, respectively. No passivation layer was used to the device structure.

6.4 Electrical Properties of a-ITZO TFTs

6.4.1 Current-voltage characteristics of a-ITZO TFTs

Figure 6.2 (a) shows the output characteristics of a-ITZO TFT under various gate-to-source voltages (V_{GS}) ranging from 0 to 20 V. The O_2 gas flow ratio and a-ITZO thickness were 5% and 50 nm, respectively. A clear distinction between linear and saturation regions was observed. Figure 6.2 (b) represents the detail of the output characteristics for small drain-to-source voltage (V_{DS}) ranging from 0 to 1.0 V. To evaluate the a-ITZO / Mo S/D contact properties, the derivative of the output characteristics ($\partial I_D/\partial V_{DS}$) is also shown. The result represents linear output

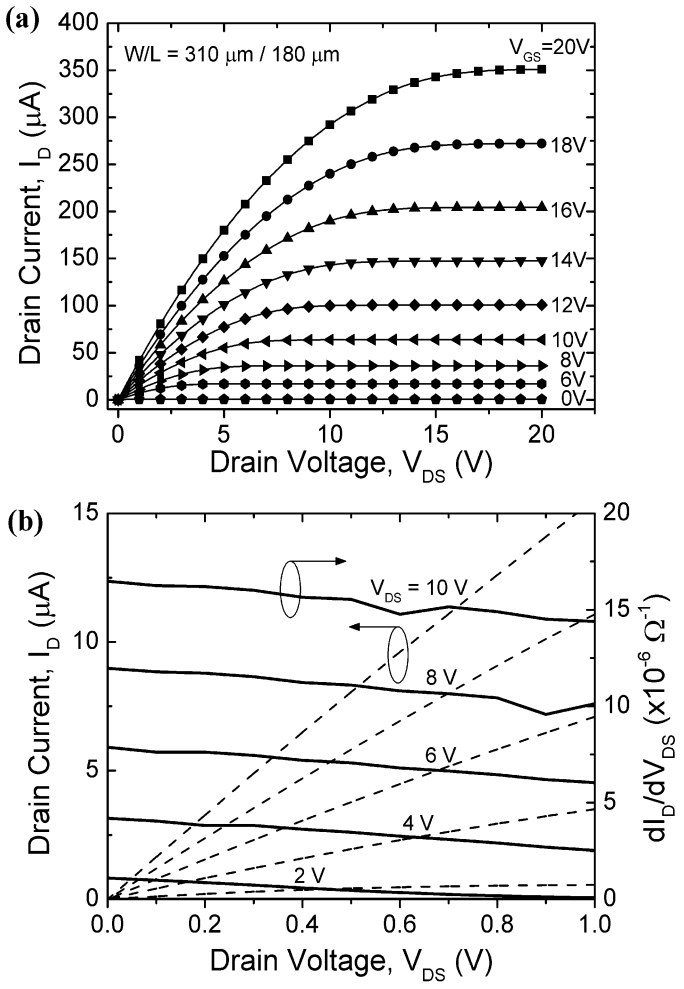

Figure 6.2 (a) An example of output characteristics of a-ITZO TFT fabricated using mechanical mask. (b) Zoom-in output characteristics in the region of V_{DS} up to 1.0 V is also shown. The a-ITZO film thickness and O_2 gas flow ratio are 50 nm and 5%, respectively.

characteristics at small V_{DS}, which indicates that ohmic contacts are formed between a-ITZO and Mo S/D electrodes.

Figure 6.3 (a) shows the transfer characteristics of a-ITZO TFTs at V_{DS} = 0.1 and 10 V. The gate current is sufficiently low demonstrating proper device operation. Lower off-current (I_{off}) is expected for TFTs patterned by photolithography. We initially extracted the device parameters such as the V_T and μ_{eff} using standard MOSFET equations in the linear (V_{DS} = 0.1 V) and saturation regions (V_{DS} = 10 V):

$$I_{D,lin} = \frac{W}{L}\mu_{eff}C_{ox}(V_{GS} - V_T)V_{DS}, \tag{6.1}$$

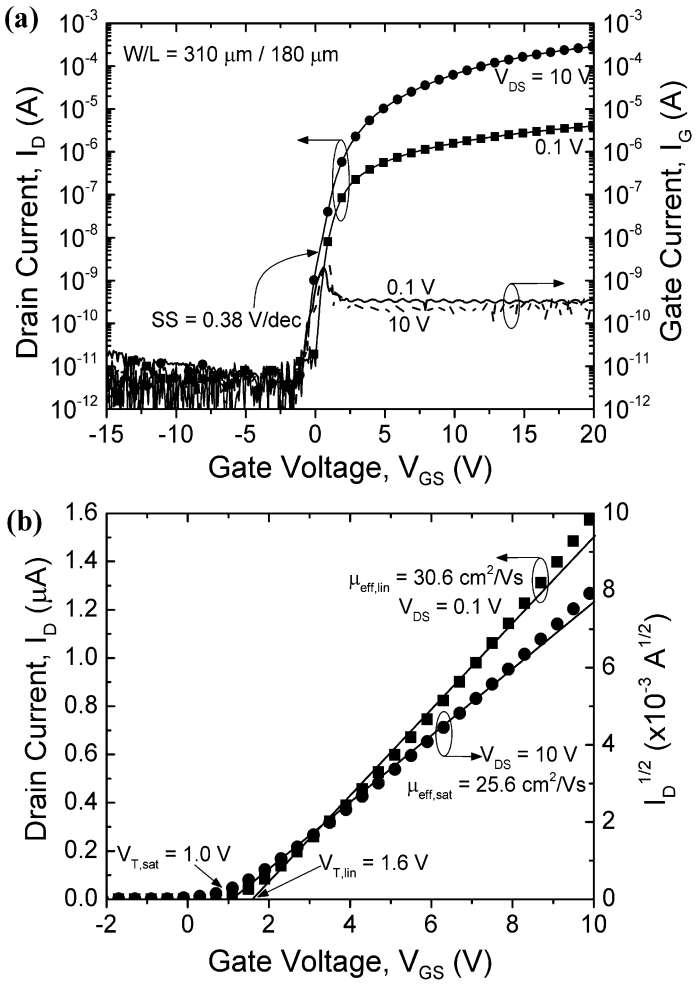

Figure 6.3 (a) An example of transfer characteristics of a-ITZO TFT in the logarithm scale. (b) Device performance in linear and saturation regions is also shown. The a-ITZO film thickness and O_2 gas flow ratio are 50 nm and 5%, respectively.

$$I_{D,sat} = \frac{W}{2L}\mu_{eff}C_{ox}(V_{GS} - V_T)^2, \tag{6.2}$$

where W and L are channel width and length, and C_{ox} is the gate capacitance per unit area (~35.4 nF/cm^2).

Figure 6.3 (b) shows the I_D-V_{GS} and $I_D^{1/2}$-V_{GS} relationships in the linear and saturation regions, respectively. The linear fitting method based on 10%-90% of maximum I_D was used for initial extraction of V_T and μ_{eff}. More accurate models for field-effect mobility extraction will be discussed in Section 6.4.2. The *SS* was extracted

at the maximum slope point from the subthreshold region from Figure 6. 3 (a) using $SS = \{\mathrm{Max}[d\log(I_D)/dV_{GS}]\}^{-1}$. The electrical parameters for the a-ITZO TFTs extracted by this approach are summarized in Table 6.1. The extracted field-effect mobility in the linear and saturation regions are 30.6 and 25.6 cm^2/Vs, respectively. These values are about three times higher than that of typical a-IGZO TFTs (~10 cm^2/Vs).

Parameters	Linear region (V_{DS} = 0.1 V)	Saturation region (V_{DS} = 10 V)
V_T (V)	1.6	1.0
μ_{eff} (cm^2/Vs)	30.6	25.6
SS (V/dec)	0.38	0.39

Table 6.1 Electrical properties of a-ITZO TFT fabricated using shadow mask

6.4.2 Field-effect mobility of a-ITZO TFTs

The μ_{eff} extracted using the 10%-90% linear fitting method (Table 6.1) neglected the gate voltage dependence. Thus these values are considered as average values over the TFT operation region. However, it can be seen in Figure 6.3 (b) that the I_D-V_{GS} (V_{DS} = 0.1 V) and $I_D^{1/2}$-V_{GS} (V_{DS} = 10 V) curves are not perfectly linear, indicating that the slope of this curve or field-effect mobility is gate voltage dependent; i.e. $\mu_{eff}(V_{GS})$. The $\mu_{eff}(V_{GS})$ is associated with the conduction band tail states trapping a portion of electrons in the channel [199]. As V_{GS} increases (Fermi level increases), more of these states are filled. Thereby, an increased number of free electrons can contribute into drain current leading to an increased μ_{eff}. For a-ITZO TFTs, a more accurate field-effect mobility model taking the gate voltage dependence into consideration needs to be developed.

First, as shown in Figure 6.4, we extracted the incremental field-effect mobility (μ_{inc}) as a function of V_G in (a) linear and (b) saturation regions using the following equations:

$$\mu_{inc,lin}(V_{GS}) = \left(\frac{\partial I_{D,lin}}{\partial V_{GS}}\right)\left(\frac{L}{WC_{ox}V_{DS}}\right), \tag{6.3}$$

$$\mu_{inc,sat}(V_{GS}) = \left(\frac{\partial I_{D,sat}^{1/2}}{\partial V_{GS}}\right)^2\left(\frac{2L}{WC_{ox}}\right). \tag{6.4}$$

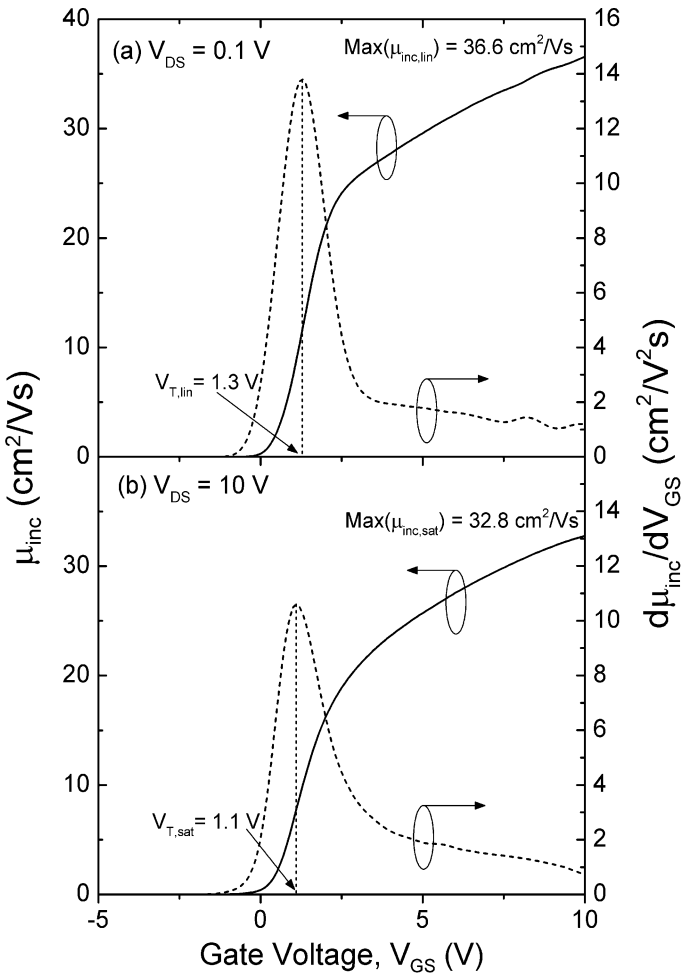

Figure 6.4 An example of the incremental field-effect mobility in (a) linear (V_{DS} = 0.1 V) and (b) saturation regions (V_{DS} = 10 V). The derivative of μ_{inc} ($\partial\mu_{inc}/\partial V_{GS}$) is also shown.

The μ_{inc} of a-ITZO TFT increases with V_{GS}, which is in agreement with a nonlinear I_D-V_{GS} behavior. Similar behavior was also observed for a-IGZO TFTs in previous work [87]. The maximum μ_{inc} (Max(μ_{inc})) for the linear and saturation regions are 36.6 and 32.8 cm^2/Vs. As expected, the Max(μ_{inc}) values are greater than the average μ_{eff} values in Table 6.1.

Taking the $\mu_{eff}(V_{GS})$ into consideration, in the linear and saturation region, Equation 6.1 and 6.2 can be respectively written as

$$I_{D,lin} = \frac{W}{L} \cdot \mu_{eff}(V_{GS}) \cdot C_{ox} \cdot (V_{GS} - V_T) \cdot V_{DS}, \tag{6.5}$$

$$I_{D,sat} = \frac{W}{2L} \cdot \mu_{eff}(V_{GS}) \cdot C_{ox} \cdot (V_{GS} - V_T)^2, \quad (6.6)$$

and the field-effect mobility $\mu_{eff}(V_{GS})$ can be expressed as

$$\mu_{eff}(V_{GS}) = \mu_0 \left(\frac{V_{GS} - V_T}{V_C} \right)^{\gamma - 1} = K(V_{GS} - V_T)^{\gamma - 1}, \quad (6.7)$$

where γ is a power law mobility coefficient describing the dependence of μ_{eff} on ($V_{GS} - V_T$) as an indicator of conduction band tail states density, and K (in the unit of $cm^2 V^{-\gamma} s^{-1}$) is a material dependence parameter [199]. The parameter K is dependent on the a-ITZO intrinsic band mobility (μ_0), critical voltage (V_C), and γ ($K = \mu_0 \times V_C^{1-\gamma}$) [87]. Considering a μ_0 of 50 cm^2/Vs, γ of ~1.15, V_C of 1627 V, and K of 16.5 $cm^2 V^{-\gamma} s^{-1}$ were extracted through SPICE parameters extraction for a-ITZO TFTs fabricated by photolithography.

Substituting Equation 6.7 to Equation 6.5 and 6.6, we have

$$I_{D,lin} = KC_{ox} \left(\frac{W}{L} \right) (V_{GS} - V_T)^{\gamma} V_{DS}, \quad (6.8)$$

$$I_{D,sat} = KC_{ox} \left(\frac{W}{2L} \right) (V_{GS} - V_T)^{\gamma + 1}. \quad (6.9)$$

From Equation 6.3, 6.4, 6.8 and 6.9, the incremental field-effect mobility in the linear ($\mu_{inc,lin}$) and saturation ($\mu_{inc,sat}$) regions can be described as

$$\mu_{inc,lin}(V_{GS}) = K\gamma(V_{GS} - V_T)^{\gamma - 1}, \quad (6.10)$$

$$\mu_{inc,sat}(V_{GS}) = K\left(\frac{\gamma + 1}{2} \right)^2 (V_{GS} - V_T)^{\gamma - 1}, \quad (6.11)$$

In the ideal case, $\gamma = 1$, thus the field-effect mobility is a constant K, i.e. $\mu_{eff} = \mu_{inc,lin} = \mu_{inc,sat} = \mu_0 = K$. In the linear region, $\partial\mu_{inc}/\partial V_{GS} = K\gamma(\gamma - 1)(V_{GS} - V_T)^{\gamma-2}$. Assume $1 < \gamma < 2$, then $(\gamma - 2) < 0$, thus the maximum of $\partial\mu_{inc}/\partial V_{GS}$ is obtained when ($V_{GS} - V_T$) approaches zero. Hence, V_T in the linear region can be extracted, when $\partial\mu_{inc}/\partial V_{GS}$ reaches the maximum. This approach also works for the saturation region. The extracted V_T values in the linear and saturation regions are 1.3 and 1.1 V, respectively. These V_T values will also be used to extract K and γ.

In this study, we propose two methods to extract V_T, K, and γ in the linear and saturation regions. The first method (Method 1) is based on the least square linear fit to

the logarithm of drain current ratio by changing the V_T value [87], [213].

In the linear region, from Equation 6.8, the method can be described as

$$\log\left(\frac{I_{D,lin}}{I_0}\right) = \gamma \log\left(\frac{V_{GS} - V_T}{V_0 - V_T}\right), \tag{6.12}$$

where I_0 is a sufficiently large reference drain current at $V_{GS} = V_0$, i.e. $I_0 = I_D(V_{GS} = V_0)$. We chose V_0 = 5V with I_0 = 0.58 μA. For a specific V_T value, γ can be extracted from the slope of linearly fitted $\log(I_D/I_0)$ vs. $\log((V_{GS}-V_T)/(V_0-V_T))$. By varying the V_T value, the optimum V_T and thus γ were determined, when the RMS standard error of the linear fitting reached the minimum. Figure 6.5 (a) shows an example of extracted linear region γ and corresponding linear fitting RMS standard error for selected V_T ranging from 0.5 to 1.3 V. When the standard error reached the minimum, V_T of 0.9 V and γ of 1.27 were obtained for the linear region. Then K = 15.9 $cm^2 V^{-\gamma} s^{-1}$ can be obtained by operating another linear fitting to Equation 6.8.

In the saturation region, Equation 6.9 can be modified to

$$\log\left(\frac{I_{D,sat}}{I_0}\right) = (\gamma + 1)\log\left(\frac{V_{GS} - V_T}{V_0 - V_T}\right). \tag{6.13}$$

By applying the same linear fitting to $\log(I_D/I_0)$ vs. $\log((V_{GS}-V_T)/(V_0-V_T))$, we extracted the saturation region V_T, γ, and K of 0.7 V, 1.32, and 11.9 $cm^2 V^{-\gamma} s^{-1}$, respectively.

The second method (Method 2) first extracts V_T from the maximum of $\partial\mu_{inc}/\partial V_{GS}$ (i.e. the second order derivative of I_D vs. V_{GS}) [87], [214]. We assume that $\partial\mu_{inc}/\partial V_{GS}$ increases in the subthreshold region and decreases in the threshold region due to the difference properties of deep gap and band tail states in a-ITZO films [92]. Based on this method, as shown in Figure 6.4, V_T = 1.3 V and 1.1 V were obtained for the linear and saturation regions, respectively.

Equation 6.10 and 6.11 can be modified as

$$\log(\mu_{inc,lin}) = \log(K\gamma) + (\gamma - 1)\log(V_{GS} - V_T), \tag{6.14}$$

$$\log(\mu_{inc,sat}) = \log(K) + 2\log\left(\frac{\gamma + 1}{2}\right) + (\gamma - 1)\log(V_{GS} - V_T). \tag{6.15}$$

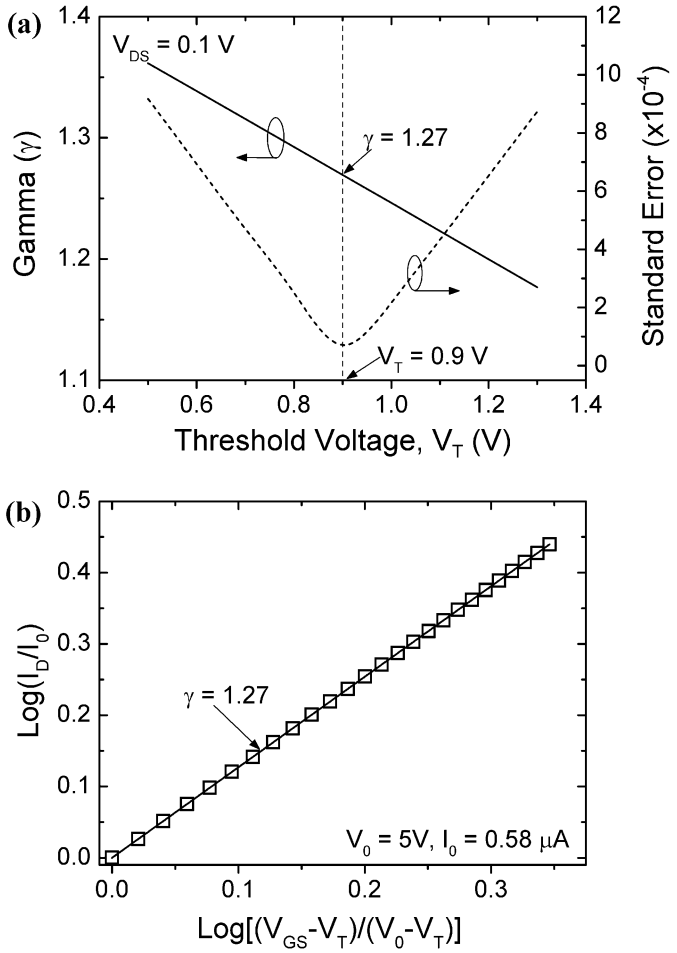

Figure 6.5 Method 1: (a) Extracted linear region (V_{DS} = 0.1 V) γ by linear fitting of log(I_D/I_0) vs. log((V_{GS}-V_T)/(V_0-V_T)) at various V_T (V_0 = 5V, and I_0 = 0.58 μA). The corresponding standard error is also shown. (b) Example of the best linear fit, when the minimum error is achieved.

By linear fitting of log(μ_{inc}) vs. log($V_{GS} - V_T$), ($\gamma - 1$) and K can be extracted from the slope and intercept of the plot, respectively. As shown in Figure 6.6, using this second order derivative method (Method 2), V_T = 1.3 V, γ = 1.22 and K = 18.3 cm^2 V$^{-\gamma}$ s^{-1} were extracted in the linear region. In the saturation region, we acquired V_T = 1.1 V, γ = 1.33 and K = 12.0 cm^2 V$^{-\gamma}$ s^{-1}.

Figure 6.7 shows the experimental and calculated μ_{inc} and I_D by substituting V_T, γ, and K extracted by two different methods. Calculated curves using both methods fit the experimental data in the linear and saturation regions. Parameters extracted using both methods are listed in the Table in Figure 6.7. In comparison to the parameters extracted previously for a-IGZO TFTs (γ ~1.5, K ~1.8) [87], a smaller γ and a greater K were

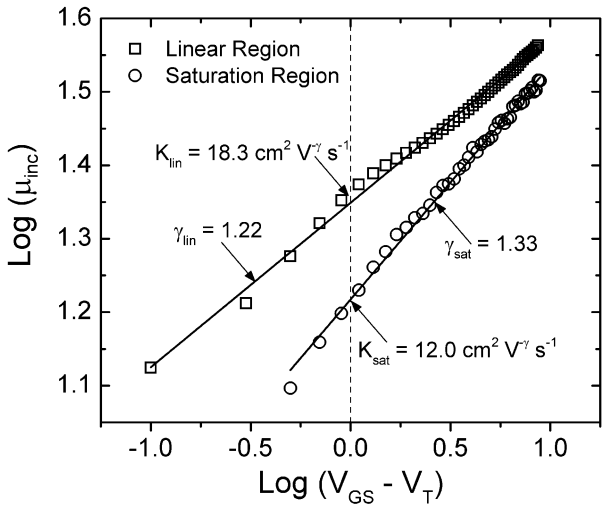

Figure 6.6 Method 2: Experimental and linear fitted log(μ_{inc}) vs. log($V_{GS} - V_T$) in both linear and saturation regions. γ and K were extracted from the slope and intercept of the linear fitted data.

obtained for a-ITZO TFTs. The smaller γ demonstrates suppressed μ_{eff} dependence on V_{GS} and a reduction in the conduction band tail states, while the large K indicates increased a-ITZO band mobility in comparison to a-IGZO.

However, it was observed that V_T extracted using the second derivative method (Method 2) is greater than the experimental data. We believe the V_T deviation can be induced by the neglected series resistance of source/drain contacts ($R_{S/D}$) during the parameter extraction. The $R_{S/D}$ will induce a negative threshold voltage shift ($\Delta V_T = I_D \times R_{S/D}$) to the experimental data, while this shift is neglected for the calculated data. Moreover, a greater I_D in the saturation region will result in a smaller V_T and a reduced $\mu_{inc,sat}$ in compassion to that of the linear region as shown in the table of Figure 6.7 (b). In other words, the μ_{inc} in the saturation region can be expressed as

$$\mu_{inc,sat}(V_{GS}) = K\left(\frac{\gamma+1}{2}\right)^2 (V_{GS} - V_T - I_D R_{S/D})^{\gamma-1}. \quad (6.16)$$

The greater V_T extracted by Method 2 will lead to a smaller calculated I_D as shown in Figure 6.7 (b). For the least square linear fit method (Method 1), the impact of $R_{S/D}$ on V_T was suppressed by dividing (V_{GS}-V_T) by (V_0-V_T). Therefore, Method 1 is suggested for $\mu_{eff}(V_{GS})$ and V_T extraction to minimize the impact of $R_{S/D}$. Compare V_T extracted using Method 1 and 2, a ΔV_T of 0.4 V is expected for both the linear and

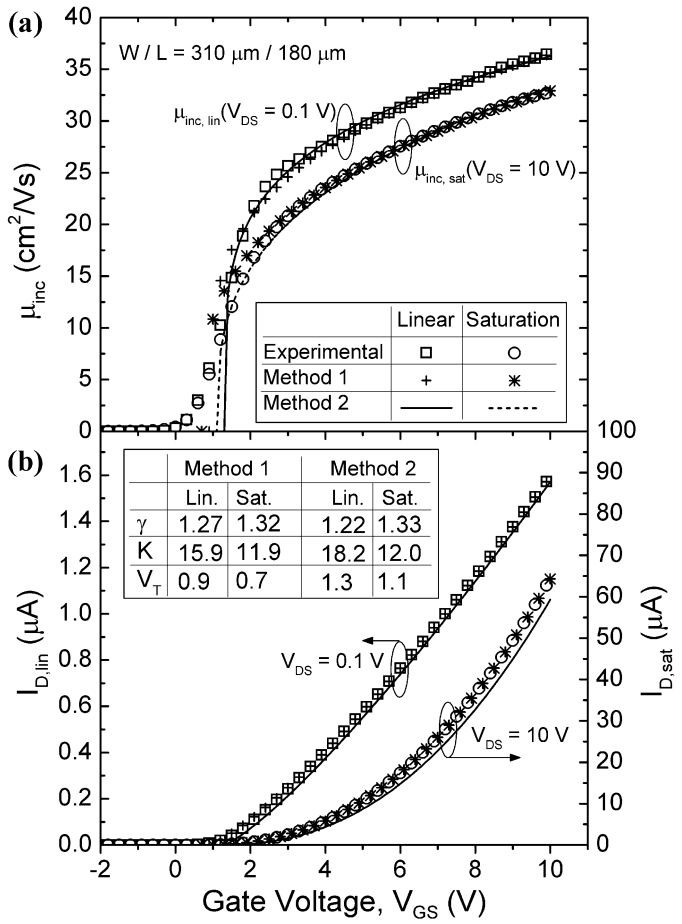

Figure 6.7 Experimental and calculated μ_{inc} (a) and I_D (b) in both linear and saturation regions using parameters extracted by Method 1 (least square linear fit method) and 2 (second order derivative method). The extracted parameters using both methods are also shown.

saturation regions. Taking I_D of 8.2×10^{-8} to 2.6×10^{-8} A at V_T ranging from 1.1 to 1.3 V, $R_{S/D}$ of 4.9 to 15 MΩ is obtained.

6.5 Device Optimization

6.5.1 Active layer thickness

To optimize the a-ITZO TFT device performance, the impacts of a-ITZO thickness on device electrical properties were evaluated. We fabricated a-ITZO TFTs with a-ITZO channel thickness ranging from 15 to 100 nm. As shown in Figure 6.8, V_T, and μ_{eff} for

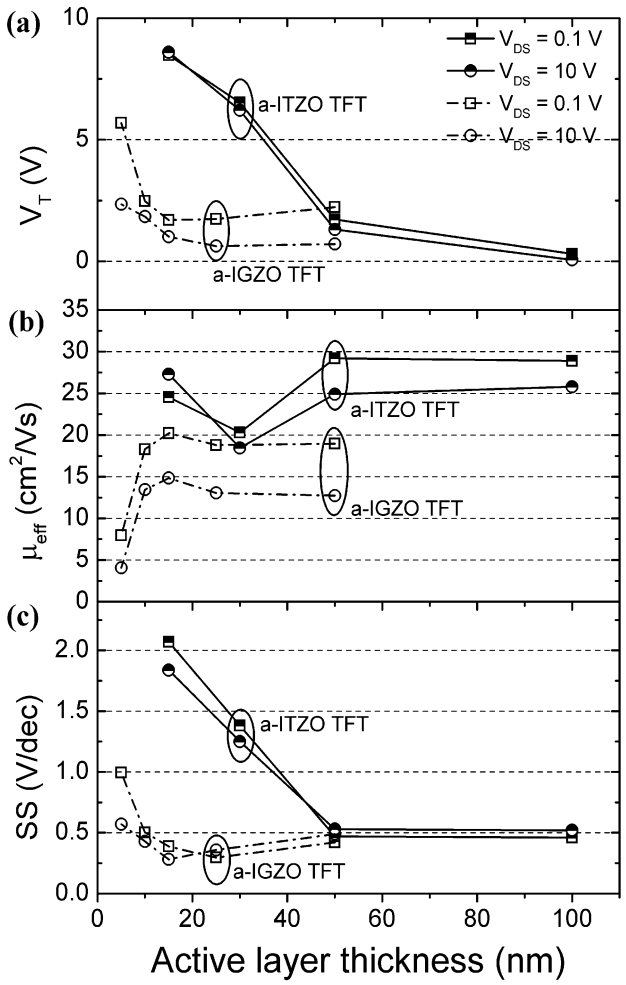

Figure 6.8 Averaged (a) threshold voltage, (b) field-effect mobility using the 10%-90% fitting method, and (c) subthreshold swing at the maximum slope point in the subthreshold region for devices with various a-ITZO thickness. The oxygen gas flow ratio for the fabricated devices is 10%. Extracted device parameters for a-IGZO TFTs (oxygen gas flow rate = 5%) with active layer thickness from 5 to 50 nm are also shown.

devices with various channel thickness (at O_2 gas flow rate of 10%) were extracted using the 10%-90% fitting method, while *SS* was extracted at the maximum slope point in the subthreshold region. To minimize the statistical error, averaged V_T, μ_{eff} and *SS* over multiple samples are shown. It is observed that V_T and *SS* decrease with increase of the a-ITZO thickness that is consistent with the results of a-IGZO TFTs (also shown in Figure 6.8). V_T, μ_{eff} and *SS* saturate at a-ITZO thickness larger than 50 nm.

The *SS* is generally considered as an indicator of the sum of the deep bulk states (N_{BS}, in cm^{-3}/eV) and gate insulator-semiconductor interface trap states (N_{SS}, in cm^{-2}/eV)

[87], [215]. Here we consider an effective maximum area density of states (N_{eff}, in cm^{-2}/eV), including both N_{BS} and N_{SS}, given by [208], [216]

$$N_{eff} = \left(\frac{SS \log(e)}{kT/q} - 1 \right) \frac{C_{ox}}{q}, \tag{6.17}$$

where k is the Boltzmann constant, T is the temperature, and q is the electron charge.

Taking the *SS* values in the linear region (V_{DS} = 0.1 V), the N_{eff} were calculated to be 8.5×10^{12}, 4.9×10^{12}, 1.5×10^{12}, and 1.5×10^{12} cm^{-3}/eV for channel thicknesses of 15, 30, 50 and 100 nm, respectively.

The trend of V_T variation with channel thickness is highly correlated with changes of *SS*. The reduction in N_{eff} will increase the free carriers in the channel. Therefore, the V_T is decreasing for thicker a-ITZO films. Similar result was observed for a-IGZO TFTs with channel thickness from 5 to 50 nm (Figure 6.8). Therefore, to achieve a small threshold voltage, low *SS*, and high field-effect mobility, a-ITZO films of at least 50 nm should be deposited.

The observed high N_{eff} (i.e. increase in V_T and *SS*) for a-ITZO TFTs with thin active layers (e.g. 15 and 30 nm) is likely to induce smaller μ_{eff} values due to electron trapping. This is consistent with our observations for a-IGZO TFTs (Figure 2.17). However, an abnormally high μ_{eff} was observed for the 15 nm a-ITZO TFT.

It is possible to explain the high μ_{eff} for the 15 nm a-ITZO TFT by the gate-bias induced back-channel current. Since the devices were not passivated, hydrogen (H) atoms from the atmosphere (e.g. H_2O) could possibly diffuse into the a-ITZO back-channel and form donor-like trap states [217], [218]. These states would not be ionized and remain inactive (neutral) for thick a-ITZO films (i.e. the back-channel is not depleted). However, for very thin films (e.g. 15 nm), the donor-like states on the backchannel will overlap with the front channel region and be ionized by the positive gate bias generating H^+ ions. During this process, additional electrons are provided to the overlapped channel region, increasing the operational current of the TFT. This behavior is similar to having a dual-gate TFT with both the front and back-channel currents contribute to I_{DS} [194]. As a result, higher field-effect mobility will be extracted for the ultra-thin 15 nm a-ITZO TFT.

We also checked the impact of contact resistance (r_c) on μ_{eff}. The extracted γ values

using Method 1 were 0.83 and 0.85 for 15 nm and 30 nm channel thicknesses, respectively. We also found that $\mu_{inc,lin}$ decreases with V_{GS} indicating $\gamma < 1$. This is a unique feature for TFTs with a large r_c [199]. For thin a-ITZO films with thickness < 30 nm, the large *SS* and V_T indicate a large number of trap states and limited free electrons. We expect that the Fermi level will be deeper within the bandgap. As the result, the a-ITZO (< 30 nm) / Mo source and drain contacts can be considered as Schottky junctions with a large r_c rather than ideal ohmic contacts. Therefore, we expect that the high μ_{eff} for 15 nm a-ITZO TFT should not be due to a low r_c.

6.5.2 Oxygen flow ratio optimization

To optimize the O_2 gas flow ratio (P_{O2}) during a-ITZO sputtering, we fabricated a-ITZO TFTs with 50 nm channel thickness using various P_{O2} from 0 to 50%. The extracted device parameters such as V_T, μ_{eff} and *SS* using the 10%-90% fitting method are shown in Figure 6.9. In general, when P_{O2} is increased from 0 to 5%, V_T and *SS* are decreasing while μ_{eff} is increasing. Further increase of P_{O2} (> 5%) leads an increase of V_T and *SS* with a reduction in μ_{eff}. The P_{O2} effects on a-ITZO TFT device properties are very similar to our previous observations on a-IGZO TFTs [90].

For P_{O2} increased from 5 to 50 %, V_T and *SS* increase, while μ_{eff} decreases. The P_{O2} is possibly related to the acceptor-like deep states, which can be considered as weakly bonded excess oxygen states (O^0 or O^-) [90], [219]. Our previous study on a-IGZO TFTs shows that, for higher P_{O2}, the peak of acceptor-like states (excess oxygen states) increases. At the same time, the mean energy position of acceptor-like states shifts to the conduction band [90]. Both the peak increment and mean energy position shift will trap more electrons in the channel to form ionized stable O^{2-} states. As a result, both V_T and *SS* increase, while μ_{eff} reduces with increasing P_{O2}.

Alternatively, the reduction of μ_{eff} with increasing P_{O2} could also be associated with the increase of acceptor-like conduction band tail states. Based on our previous numerical simulation results, if this is the case, γ must increase for higher P_{O2} [199]. However, the γ values in the linear region extracted using Method 1 are 1.27 and 1.17 for P_{O2} of 5 and 50%, respectively. Therefore, this assumption is not valid. It is most likely that the increase of V_T, *SS* and the reduction of μ_{eff} is according to the increase of

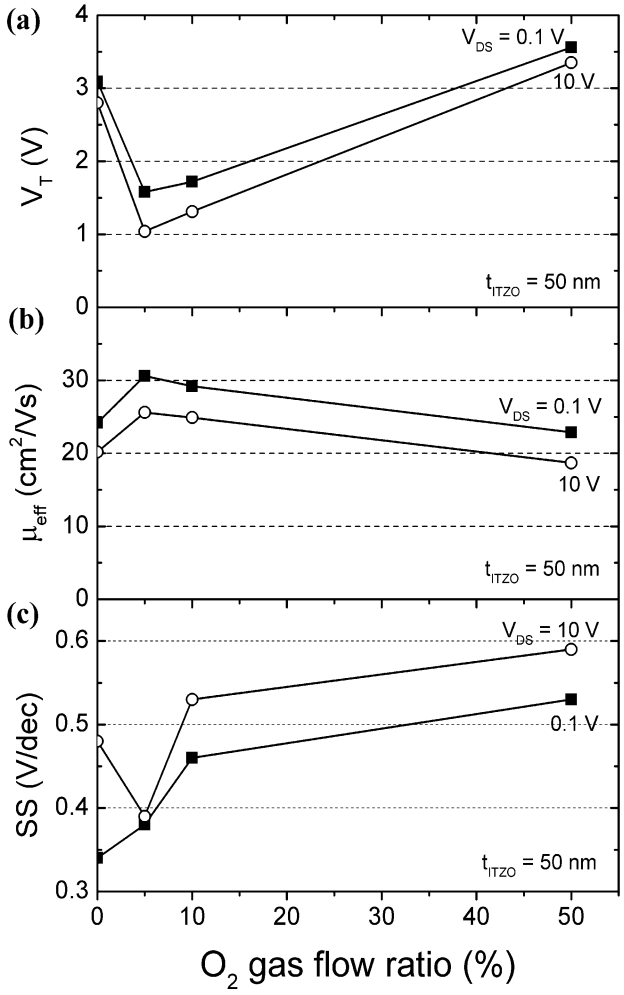

Figure 6.9 Extracted (a) threshold voltage, (b) field-effect mobility using the 10%-90% fitting method, and (c) subthreshold swing at the maximum slope point in the subthreshold region for devices fabricated using oxygen gas flow ratio from 0 to 50%. The a-ITZO film thickness is fixed at 50 nm.

acceptor-like deep states (O^0 or O^-) instead of conduction band tail states for higher P_{O2}.

For P_{O2} of 0% in comparison to 5%, a higher V_T, *SS*, and a lower μ_{eff} are observed. The γ in the linear region (γ = 1.29) for P_{O2} = 0% extracted using Method 1 is slightly higher that of P_{O2} = 5% (1.27). The authors expect that at very low P_{O2} (0%), i.e. high Ar gas flow ratio, the deposited a-ITZO film microscopic quality is reduced because of the damages caused by high energy Ar plasma bombardments. The conduction band tail states should increase resulting in a larger γ, a low μ_{eff} and a high V_T and *SS* [90], [199]. The discontinuity of *SS* at P_{O2} = 0% may originate from the experimental error. A

relatively large *SS* fluctuation was observed, when a relatively large V_{GS} increment (0.5 V) was used during the measurement. As shown in Figure 6.9, the optimal P_{O2} for a-ITZO TFT fabrication is 5% for a-ITZO channel thickness of 50 nm.

6.6 Electrical Stability

It is critical to evaluate the electrical stability of a-ITZO TFTs for industrial mass production. Figure 6.10 shows the variation of transfer characteristics of a-ITZO TFTs (50 nm a-ITZO thickness, 5% O_2 gas flow ratio) in the saturation region (V_{DS} = 10 V) during (a) positive bias-temperature stress (PBTS) and (b) negative bias-temperature stress (NBTS) at stress temperature of 70 °C. During PBTS, a positive DC gate bias of $V_{G,stress}$ = +10 V was applied to the gate, while the S/D contacts were grounded. After a stress time of 10^3 seconds, a positive threshold voltage shift of ΔV_T = +0.54 V, a field-effect mobility drop of $\Delta\mu_{eff}$ = -1.4 cm^2/Vs (5.1%), and a slightly *SS* increase of +0.04 V/dec (13%) were observed (Figure 6.11). The threshold voltage was extracted as the V_{GS} when $I_D = 10^{-7}$ A (constant drain current method); the 10%-90% linear fitting method was used to extract μ_{eff}; and the *SS* was extracted by the maximum inverse of the log(I_D)-V_{GS} slope in the subthreshold region. During NBTS, a negative DC gate bias of $V_{G,stress}$ = -10 V was applied to the gate. As shown in Figure 6.11, a negative threshold voltage shift of ΔV_T = -0.50 V, a field-effect mobility increase of $\Delta\mu_{eff}$ = +4.9 cm^2/Vs (18%), and a *SS* increase of +0.1 V/dec (34%). It should be noticed that no passivation layer was used in the device structure.

We also compared the ΔV_T of a-ITZO TFTs with that of a-IGZO TFTs (without passivation layer) in Figure 6.11 (c). The ΔV_T for a-IGZO TFT is +2.6 and -1.6 for PBTS and NBTS, respectively. It is clear that a-ITZO TFTs can achieve better electrical stability (i.e. reduced ΔV_T) in comparison to a-IGZO TFTs. The improved electrical stability of a-ITZO TFT is very promising for APS x-ray imager application, where the TFTs are continuously bias-stressed.

Lee *et al* reported that the positive ΔV_T for a-IGZO TFTs during PBTS increases with increasing P_{O2} [90]. Similar results have been observed for a-ITZO TFTs as shown

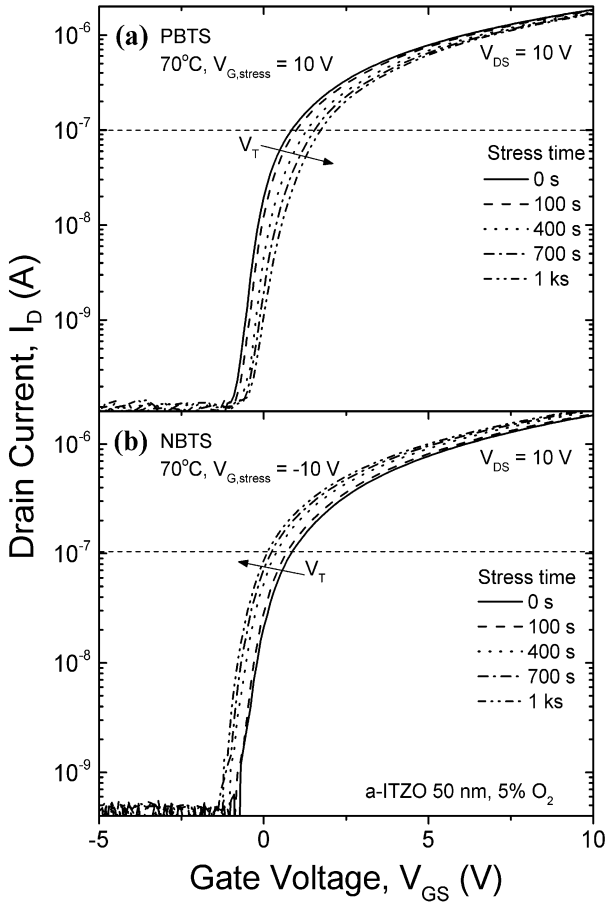

Figure 6.10 An example of the variations of transfer characteristics of a-ITZO TFT during (a) PBTS and (b) NBTS for 10^3 seconds at stress temperature of 70 °C.

in Figure 6.12. For P_{O2} from 5 to 50%, ΔV_T of a-ITZO TFTs during PBTS keeps increasing. This finding indicates that ΔV_T during PBTS is oxygen-related, which can be associated with the acceptor-like excess oxygen states (O^0 or O^-). We expect that, during PBTS, O_2 or H_2O in the ambient atmosphere can diffuse into the channel layer and form weakly bonded O^0 or O^- states. These acceptor-like states can possibly trap electrons in the channel layer and form more stable O^{2-} states. The generation of negatively charged sites in the a-ITZO channel will lead to a positive shift of V_T. This effect is enhanced when P_{O2} is increased (i.e. ΔV_T increases with the increase of P_{O2}). It is likely that a large PBTS ΔV_T for P_{O2} = 0% is due to larger number of conduction band tail states induced by Ar plasma bombardment of the channel layer during the film growth [90].

On the contrary, we did not observe ΔV_T variation with P_{O2} for NBTS. Thereby, the

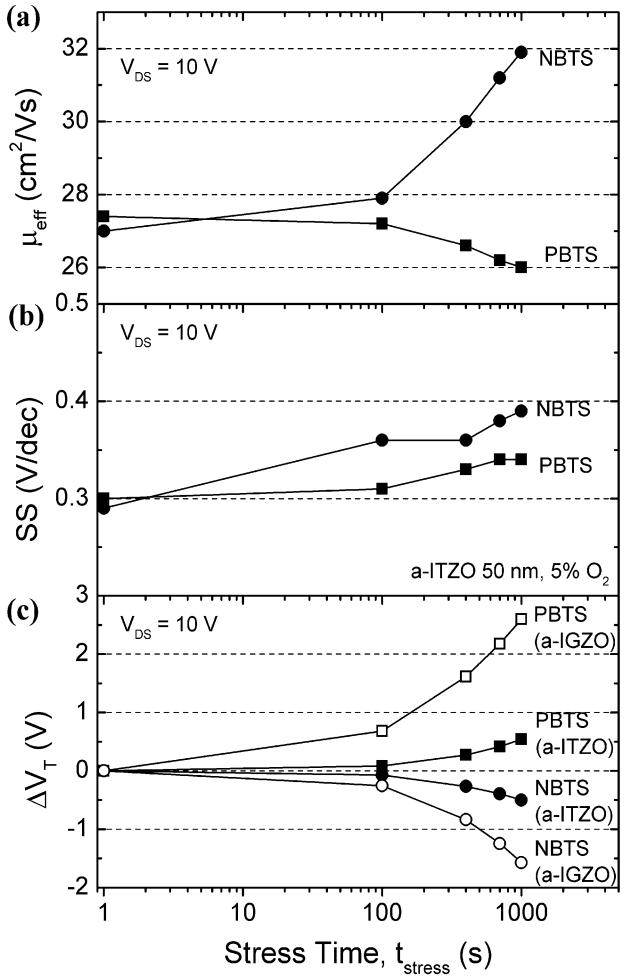

Figure 6.11 Variations in (a) field-effect mobility, (b) subthreshold swing, and (c) threshold voltage shift at V_{DS} = 10 V after stress time up to 10^3 seconds at 70 °C. The gate stress voltage is +10 and -10 V for PBTS and NBTS, respectively. The threshold voltage shift of a-IGZO TFT data is also shown for comparison purpose.

negative ΔV_T for a-ITZO TFTs during NBTS is not related to oxygen gas. A simple mechanism to explain this effect is H^+ doping to the a-ITZO film from H_2O molecules in the ambient air [217], [218]. The H^+ ion can be attracted (diffuse or drifted) into the a-ITZO film, when V_{GS} is negative. The positive charge sites in the active layer will induce a negative shift of V_T.

It is also shown in Figure 6.12 that the experimental window as defined by O_2 flow ratio is very narrow (5 – 10%) to achieve electrically stable a-ITZO TFTs. The optimized O_2 flow ratio is 5% taking into account both the device characteristics (V_T, μ_{eff} and *SS*) and electrical stability.

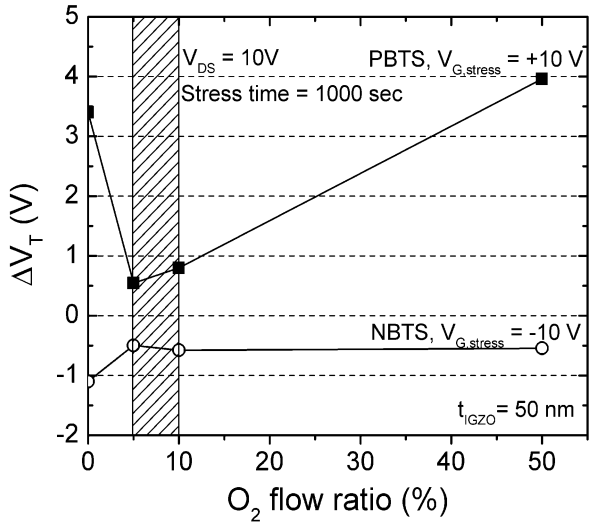

Figure 6.12 Impact of oxygen gas flow ratio on threshold voltage shift of a-ITZO TFTs with 50 nm channel thickness after 1k seconds stress time. The gate stress voltage is +10 and -10 V for PBTS and NBTS, respectively.

6.7 Summary

This chapter discussed the device fabrication, electrical properties, process optimization, and stability of a-ITZO TFTs. a-ITZO TFTs have demonstrated both high field-effect mobility (>30 cm^2/Vs) and good electrical stability, which are promising for APS. Oxygen flow ratio of 5% and a-ITZO active layer of 50 nm are recommended for device fabrication. Based on the device characteristics, in Chapter 7, we will propose a-ITZO TFT C-APS circuits for DBT. The circuit performance will be evaluated using SPICE simulation.

Chapter 7
a-ITZO TFT APS Pixel Circuit for Indirect X-Ray Detectors

7.1 Chapter Overview

The objective of this chapter is to evaluate the electrical properties of C-APS circuits based on the high mobility a-ITZO TFTs. To realize comparable imaging performance of the a-ITZO TFT C-APS with CMOS APS, we need to investigate the properties of such pixel circuit.

The C-APS circuits are based on a combination of a B-doped – intrinsic – P-doped (p^+-i-n^+) a-Si:H photodiode and a-ITZO TFTs. Section 7.2 discusses the photolithography fabrication process of the a-ITZO TFTs and the a-Si:H p^+-i-n^+ photodiode. Device characteristics and SPICE models of the a-ITZO TFTs and a-Si:H p^+-i-n^+ photodiodes are presented in Section 7.3. Based on the devices characteristics, a SPICE model for the a-Si:H photodiode / a-ITZO TFT C-APS are developed and investigated in Section 7.4. Next, Section 7.5 discusses the electrical properties of the proposed C-APS circuit. Voltage gain, charge gain, signal linearity, and the impact of the a-ITZO TFT threshold voltage shifts on C-APS are evaluated. A layout for a pixel pitch of 50 μm and an associated fabrication process are suggested in Section 7.6. Data line loadings for 4k-resolution x-rays imagers are computed and taken into consideration to study their impact on circuit performances as discussed in Section 7.7. Finally, in Section 7.8, noise analysis is performed.

7.2 Device Fabrication

7.2.1 Photolithography process for a-ITZO TFTs

The fabrication process of the back-channel-etched (BCE) a-ITZO TFT have been discussed and published by Nakata *et al*. [220]. First, a gate electrode (Mo) was sputtered on a glass substrate. After patterning the gate electrode, a 470-nm-thick amorphous silicon oxide (a-SiO_x) as a gate insulator were deposited using the plasma-enhanced chemical vapor deposition (PECVD). Next, the a-ITZO film was deposited by DC sputtering with an O_2 flow ratio of 5% (O_2 flow ratio optimized in Chapter 6), subsequently patterned by a wet etching process, and then annealed at 300 °C. Afterward, the S/D electrodes (Mo) were deposited by sputtering and patterned by the phosphoric acid, acetic acid, and nitric acid (PAN) etchant. A second annealing process at 200 °C were applied in ambient air. Finally, an organic or inorganic film acting as a passivation layer is deposited over the a-ITZO TFT [220]. Figure 7.1 (a) shows the cross-section view of the fabricated a-ITZO TFT.

7.2.2 a-Si:H p^+-i-n^+ photodiode

The fabrication process of the a-Si:H p^+-i-n^+ photodiode was described in [221], [222]. Mo was used as the bottom cathode electrode. Using PECVD, a 50-nm-thick heavily P-doped (n^+) layer, a 1-μm-thick undoped/intrinsic a-Si layer, and a 50-nm-thick heavily B-doped (p^+) layer were sequentially deposited. Next, indium-tin-oxide (ITO), a transparent anode electrode, was deposited on the top of the p^+ layer. Then, the a-Si:H p^+-i-n^+ photodiode was annealed at 150 °C to suppress the excess current coming from extrinsic defect generation. The a-Si:H p^+-i-n^+ photodiode is top-illuminated through the transparent ITO anode. This photodiode structure is adopted to realize a low dark current under reverse bias and high quantum efficiency. Figure 7.1 (b) shows the cross-section view of the a-Si:H photodiode.

To realize 50 μm pixel pitch C-APS circuit with a high pixel fill factor, the stacked structure is proposed for a-ITZO TFT C-APS. The cross-sectional view of the stacked a-Si:H photodiode / a-ITZO TFT C-APS is shown later in Figure 7.11. In such a

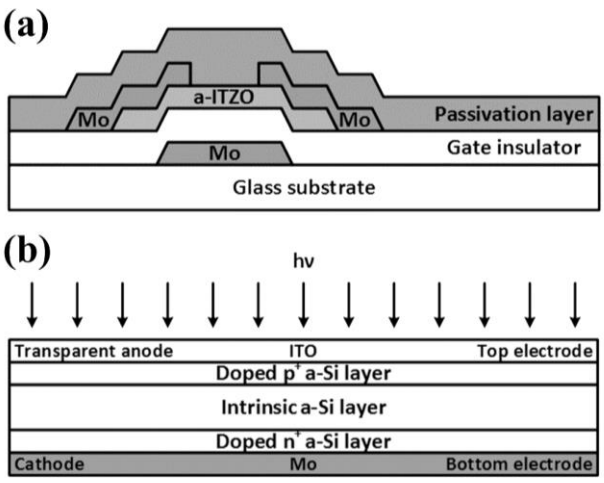

Figure 7.1 Cross-section views of (a) a-ITZO TFT and (b) a-Si:H p^+-i-n^+ photodiode.

structure, the a-Si:H p^+-i-n^+ photodiode is fabricated on top of the TFT APS array. The complete pixel layout and fabrication process will be discussed in Section 7.6.

7.3 Device Characteristics and SPICE Models

7.3.1 a-ITZO TFT electrical characteristics

Figure 7.2 (a) and (b) (symbols) show the measured transfer (I_D vs. V_{GS}) and output (I_D vs. V_{DS}) characteristics of the a-ITZO TFT with channel width / length (W/L) equals to 35 μm/15 μm. The transfer characteristic was obtained by sweeping V_{GS} from -20 V to 20 V for V_{DS} at 0.1 V (linear region) and 20 V (saturation region). On the other hand, the output characteristic was acquired by sweeping V_{DS} from 0 V to 20 V, while V_{GS} was fixed at 0, 5, 10, 15 and 20 V.

As described in Chapter 6, the incremental field-effect mobility as a function of V_{GS} in linear (μ_{inc_lin}) region and in saturation region (μ_{inc_sat}) can be calculated by Equation 6.3 and 6.4, respectively. Extracted values of μ_{inc_lin} and μ_{inc_sat} are 27.6 and 31.2 cm^2/Vs at V_{GS} = 10 V. The device mobility is gate voltage dependent with extracted γ of around 1.15. The minimum subthreshold swing is 153 mV/dec. Fabricated device also achieved a I_{OFF} lower than 10^{-14} A. Using the linear fitting method based on 10% to 90% of maximum I_D of transfer characteristics in linear scale, the extracted initial V_T is -0.93 V.

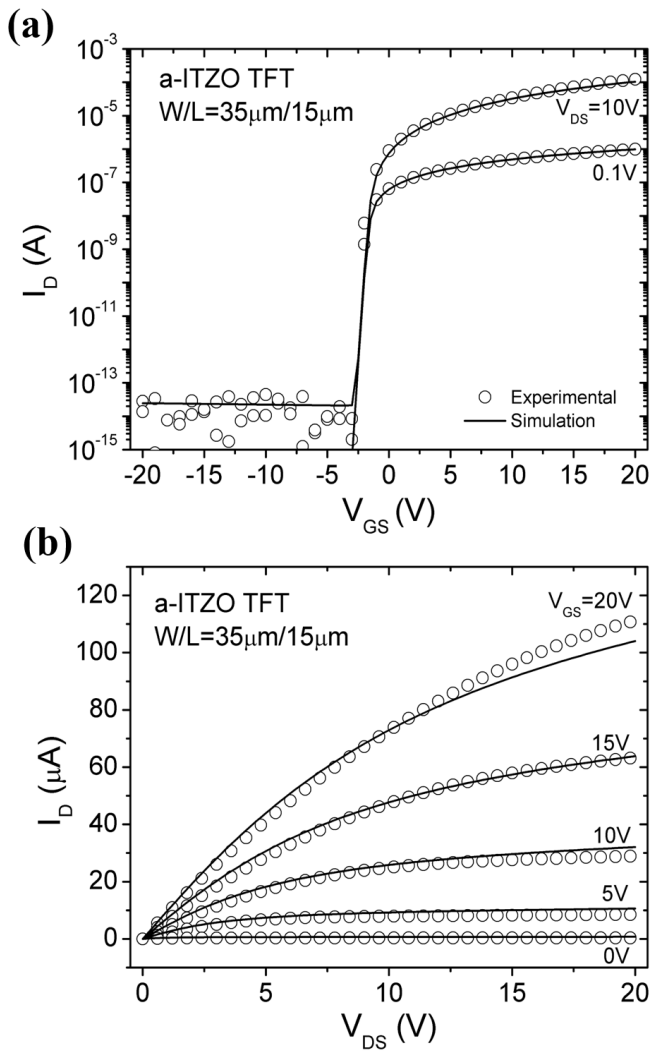

Figure 7.2 Experimental and simulated (using developed SPICE model) (a) transfer characteristics (I_D vs. V_{GS}) and (b) output characteristics (I_D vs. V_{DS}) of a-ITZO TFTs.

7.3.2 SPICE model for a-ITZO TFT

We developed an a-ITZO TFT SPICE model by modifying the Rensselaer Polytechnic Institute (RPI) a-Si:H TFT model (LEVEL = 35) [223]. All the extracted SPICE parameters for the a-ITZO TFTs are listed and described in Table 7.1.

The field-effect mobility model described in Section 6.4.2 can be used to extract the most important parameters above threshold such as VTO, GAMMA, and VAA. Specifically, based on Equation 6.7,

$$\mu_{eff}(V_{GS}) = \mu_0 \left(\frac{V_{GS} - V_T}{V_C} \right)^{\gamma - 1} = MUBAND \left(\frac{V_{GS} - VTO}{VAA} \right)^{GAMMA}, \qquad (7.1)$$

where MUBAND = μ_0, VTO = V_T, VAA = V_C, and GAMMA = $\gamma - 1$.

The simulated transfer and output characteristics of the a-ITZO TFT using the Silvaco SmartSpice software are also shown in Figure 7.2 (solid lines). It has been demonstrated that a good fit between the experimental data and simulated curves can be achieved in this study.

	Parameter	Description	Value
Above threshold region	VTO	Zero-bias threshold voltage	-2 V
	GAMMA	Power low mobility parameter (i.e., $\gamma - 1$)	0.151
	VAA	Characteristic voltage for field-effect mobility	1.62×10^3 V
	ALPHASAT	Saturation modulation parameter	0.526
	LAMBDA	Channel modulation parameter	6.9×10^{-3} V^{-1}
	M	Knee shape parameter	1.59
	MUBAND	Electron band mobility	50 cm^2/Vs
	DELTA	Transition width parameter	5
	VMIN	Convergency parameter	0.05 V
Sub-threshold region	VFB	Flat-band voltage	-5 V
	V0	Characteristic voltage of deep states	0.399 V
	GMIN	Mid-gap density of states	4.96×10^{14} $cm^{-3}eV^{-1}$
	DEF0	Dark Fermi level position	1.5 eV
	NC	Effective conduction band density of states	5×10^{18} cm^{-3}
Leakage region	IOL	Zero-bas leakage current	10^{-12} A
	VDSL	Hole leakage current drain voltage parameter	10^3 V
	VGSL	Hole leakage current gate voltage parameter	10^2
	SIGMA0	Minimum leakage current	10^{-18} A
Others	EPSI	Relative permittivity of gate insulator	3.9
	EPS	Relative permittivity of a-ITZO	10
	TOX	Gate oxide thickness	470 nm

Table 7.1 SPICE parameters for fabricated a-ITZO TFTs.

7.3.3 a-Si:H p^+-i-n^+ photodiode characteristics

Figure 7.3 (a) shows the measured dark I-V characteristics (symbols) of an a-Si:H

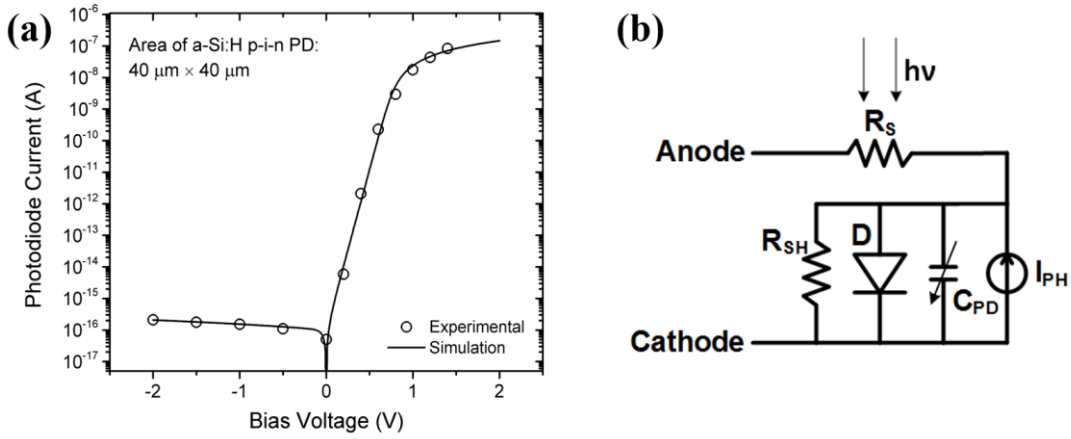

Figure 7.3 (a) Measured [221] and simulated I-V characteristics for an a-Si:H p^+-i-n^+ photodiode with an active area of 40 × 40 µm^2. (b) SPICE model circuit schematic of the a-Si:H photodiode.

p^+-i-n^+ photodiode adopted from [221], normalized to an active area of 40 × 40 µm^2 that is suitable for proposed pixel circuit. Considering a 50 µm pixel pitch, this will lead to a fill factor of 0.64, which can be realize using the stacked structure (a-Si:H photodiode on top of the passivated TFT APS array). A very low dark current of around 2 × 10^{-16} A can be achieved using the a-Si:H photodiode. Such a low dark current is very promising to realize a low electronic noise for APS x-ray imagers as described Section 7.8. It should be noted that the proposed a-Si:H photodiode was scaled down from a larger fabricated device.

7.3.4 SPICE model for a-Si:H p^+-i-n^+ photodiode

We have also developed a SPICE model (Figure 7.3 (b)) for the a-Si:H p^+-i-n^+ photodiode using a basic diode (D) model (Level = 1) in combination with the series (R_S) and shunt resistances (R_{sh}), photodiode capacitance (C_{PD}), and current source to simulate the photocurrent (I_{ph}). Table 7.2 lists all the SPICE parameters for the a-Si:H photodiode model. The simulated (scaled down) photodiode (active area: 40 × 40 µm^2) I-V characteristics using SmartSpice is consistent with the experimental results obtained by Weisfield *et al*. that was also scaled down to a 40 × 40 µm^2 photodiode active area [221].

Parameter	Description	Value
J_S	Saturation current density	6.25 pA/cm^2
N	Ideality factor	165
R_S	Series resistance	120 Ω cm^2
R_{sh}	Shunt resistance	304 GΩ cm^2
I_{ph}	Photocurrent	0 – 9 pA
C_{PD}	Photodiode capacitance	0.12 pF

Table 7.2 SPICE parameters for the a-Si:H p$^+$-i-n$^+$ photodiode.

7.4 a-Si:H p$^+$-i-n$^+$ Photodiode / a-ITZO TFT C-APS Circuit

7.4.1 C-APS circuit

A SPICE model for the C-APS circuit has been developed by combining the a-ITZO TFT and a-Si:H photodiode devices models. As discussed in Section 1.4.2, the C-APS readout circuit is chosen due to the fast readout speed and high charge gain in comparison to V-APS.

Figure 7.4 (a) shows the circuit schematics for the C-APS circuit using three a-ITZO TFTs (reset: T_{RS}, amplifying: T_{AMP}, and readout: T_{RD}) and a top-anode a-Si:H p$^+$-i-n$^+$ photodiode. The pixel capacitance ($C_{PIX} \approx 0.14$ pF) is a combination of the C_{PD} (0.12 pF) and all pixel input parasitic capacitance of around 0.019 pF. I_{ph} is a current source simulating the photocurrent. V_{DD} (10 V) and V_{PD} (5V) are dc voltage supplies.

The operation principle of TFT-based C-APS was described in Section 1.4.2. Briefly, T_{RS} resets the input charge stored on the pixel capacitance during the reset period. Photodiode detects photo signals and stores collected carriers during the integration period. T_{AMP} amplifies detected photo-induced signals and acts as a constant current source (I_{OUT}) whose value is controlled by its gate voltage (V_{IN}) during the readout period. T_{RD} is treated like an access controlling the connection between APS and the external readout circuit.

The readout circuit is based on the switched integrator including an operational amplifier (op-amp), a feedback capacitor (C_{FB}), and an external reset switch (SW_{ER}). The op-amp provides a high gain to sustain the virtual short between its positive (grounded) and negative inputs. C_{FB} integrates $Q_{OUT} = I_{OUT}\, t_{RD}$ to produce readout

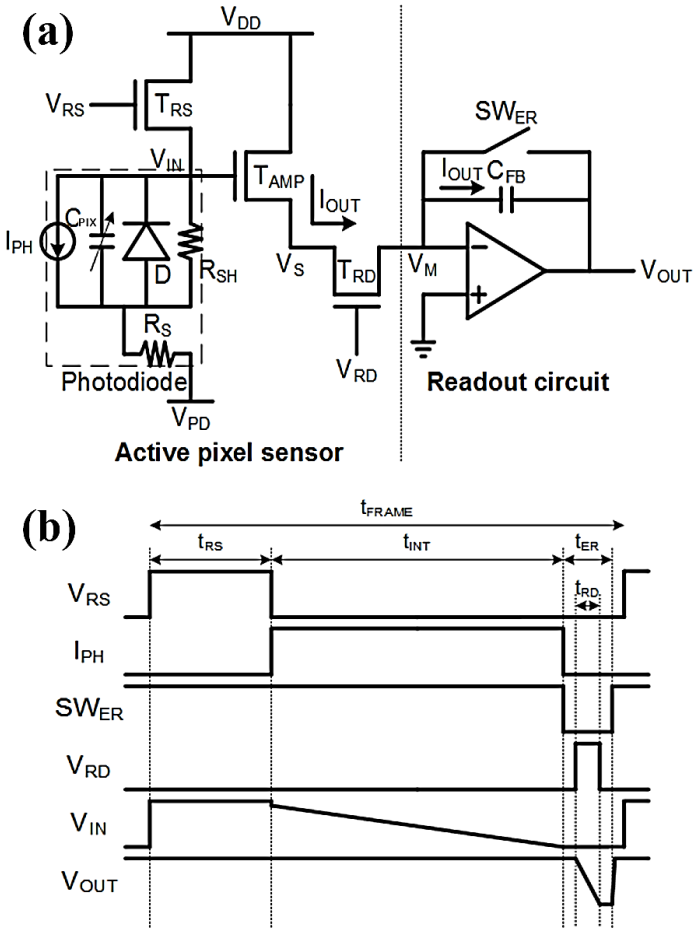

Figure 7.4 (a) Circuit illustration of the proposed a-ITZO TFT C-APS with the switched integrator readout circuit. (b) Driving scheme of the C-APS circuit. V_{RS}, V_{RD}, V_{IN} and V_{OUT} are the applied gate voltage for T_{RS}, T_{RD}, input, and output voltage, respectively; I_{ph} is the photocurrent; SW_{ER} is the external reset switch signal; t_{RS}, t_{INT}, t_{RD}, and t_{frame} are the reset, integration, readout, and frame time.

voltages ($V_{OUT} = Q_{OUT}/C_{FB}$) used for reconstructing x-ray images by the back-end signal processing. The SW_{ER} was used to reset V_{OUT}. In this work, the PSpice model of the commercial ACF2101 (Texas Instruments) switched integrator was adopted for the C-APS simulation [224]. The maximum and minimum output voltages for the op-amp are 15 V and -15 V, respectively. With this wide output voltage range, a large C_{FB} is unnecessary to prevent V_{OUT} from reaching saturation easily.

Figure 7.4 (b) sketches an example driving scheme for the C-APS circuit. V_{RS} and V_{RD} are the gate voltage pulse for T_{RS} and T_{RD}, respectively. t_{RS}, t_{INT}, t_{RD}, and t_{frame} are the, integration, readout time, and frame period respectively. t_{ER} is the time when SW_{ER}

is open. When I_{ph} pulse is applied, the photocurrent decreases V_{IN} during t_{INT}. A V_{IN} shift will vary the gate voltage of T_{AMP} and change I_{OUT} and V_{OUT} consequently.

7.4.2 SPICE simulation

Silvaco SmartSpice software was used to evaluate C-APS circuit. In the SPICE simulation, V_{DD} was set higher than V_{PD} by 5V to ensure that the photodiode is reverse biased. The gate OFF/ON voltages were chosen to be -5V / 10V for T_{RS} and T_{RD}. During APS operation, since V_{DD} is greater than $V_{IN} - V_T$, T_{AMP} works in the saturation region. The TFT channel widths (W's) and length (L = 3 μm) were determined based on a 50 μm × 50 μm pixel area. The pixel layout and fabrication process will be proposed in Section 7.6. A 100 pF C_{FB} was used to store the readout charges. An integration time of 100 ms was chosen, which is consistent with the current DBT system. A very short readout time (t_{RD} = 20 μs) is sufficient to gain a high output voltage. In the simulation, only a single row operation is simulated. The frame time for the SPICE simulation is t_{frame} = 100.2 ms. Considering a 4k by 4k imager resolution for DBT, the total frame time is estimated to be around 200 ms, which is similar to current DBT systems on the market [4]. Table 7.3 lists circuit parameters used for the C-APS SPICE simulation.

Parameter	Description	Value
V_{DD}	DC voltage supply	10 V
V_{PD}	DC voltage supply to photodiode anode	5 V
V_{RS}	T_{RS} gate voltage (OFF/ON)	-5 V / 10 V
V_{RD}	T_{RD} gate voltage (OFF/ON)	-5 V / 10 V
W_{RS}	Chanel width of T_{RS}	10 μm
W_{AMP}	Chanel width of T_{AMP}	36 μm
W_{RD}	Chanel width of T_{RD}	36 μm
L	Channel length	3 μm
C_{FB}	Feedback capacitor	100 pF
t_{RS}	Reset time	100 μs
t_{INT}	Integration time	100 ms
t_{RD}	Readout time	20 μs
t_{ER}	SW_{ER} holding time	40 μs
t_{frame}	Frame time / period	100.2 ms

Table 7.3 SPICE parameters for C-APS circuit and driving scheme.

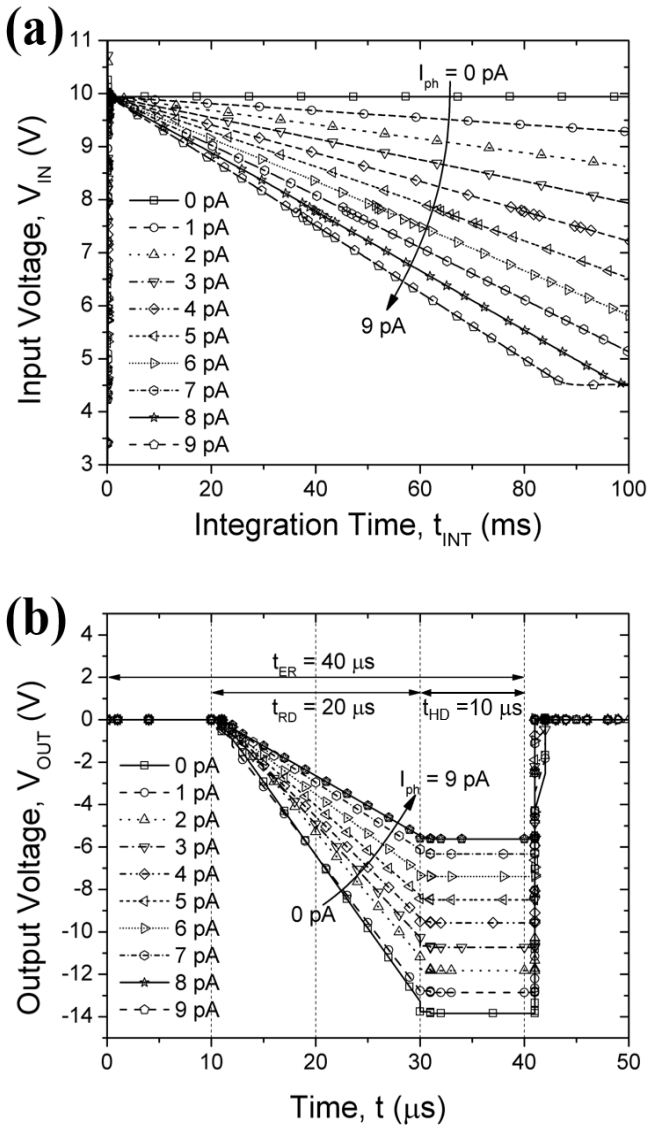

Figure 7.5 Waveforms of (a) the input voltage during the integration time and (b) output voltage during the readout time for I_{ph} ranging from 0 to 9 pA.

Figure 7.5 shows the waveforms of (a) the input voltage (V_{IN}) during the integration time (t_{INT} = 100 ms) and (b) the output voltage (V_{OUT}) during the readout time for I_{ph} ranging from 0 to 9 pA. During t_{INT}, the photocurrent will discharge C_{PIX}. Therefore, V_{IN} decreases. A higher I_{ph} will result in further reduced V_{IN} (V_{IN} saturates at I_{ph} = 7.8 pA) and thus I_{OUT}. As a result, the absolute value of V_{OUT} ($|V_{OUT}| = |I_{OUT}|\ t_{RD}/C_{FB}$) is also reduced.

7.5 Electrical Properties of the a-Si:H Photodiode / a-ITZO TFT C-APS Circuit

7.5.1 Voltage gain (A_V) and charge gain (G)

Similar to CMOS V-APS, the input and output signals for a-ITZO C-APS are measured by the voltage difference under illuminated (I_{ph}) and dark ($I_{ph} = 0$) conditions, i.e., $\Delta V_{IN} = V_{IN}(I_{ph}) - V_{IN}(I_{ph}=0)$ and $\Delta V_{OUT} = V_{OUT}(I_{ph}) - V_{OUT}(I_{ph}=0)$. Both V_{IN} and V_{OUT} (dark and illuminated conditions) were extracted during the readout holding time (t_{HD} = 10 μs as shown in Figure 7.5 (b)).

Figure 7.6 (a) shows the input-output voltage characteristics ($|\Delta V_{OUT}|$ vs. $|\Delta V_{IN}|$) of the a-ITZO TFT C-APS circuit. The device dimensions and driving scheme were shown in Table 7.3. μ_{eff} of the a-ITZO TFTs is 31.2 cm^2/Vs.

As shown in Equation 1.21, the voltage gain (A_V) measures the ratio between output and input voltage signal. In this study, $A_V = |\Delta V_{OUT}/\Delta V_{IN}| = 1.53$ can be extracted from the slope of the curve in Figure 7.6 (a). In comparison to the CMOS V-APS circuit based on the source follower circuitry ($A_V < 1$), A_V greater than 1 can be achieved using the C-APS circuit. The voltage gain is equivalent to a conversion gain of qA_V/C_{PIX} = 1.75 μV/e^- without further signal amplification.

Figure 7.6 (b) shows the absolute value of output charge (i.e., $\Delta Q_{OUT} = Q_{OUT}(I_{ph}) - Q_{OUT}(I_{ph}=0) = \Delta V_{OUT}\ C_{FB}$) as a function of input charge (i.e., $\Delta Q_{IN} = Q_{IN}(I_{ph}) - Q_{IN}(I_{ph}=0) = \Delta I_{ph}\ t_{INT}$).

As shown in Equation 1.20, The charge gain (G) measures the ratio between output and input charge signal. In this study, $G = |\Delta Q_{OUT}/\Delta Q_{IN}| = 1084$ can be obtained as the derivative of the curve in Figure 7.6 (b). The extracted charge gain is consistent with the expression $G = A_V\ C_{FB}/C_{PIX} \approx 1100$. A large charge gain is important for on-pixel signal amplification to reduce the electronic noise, especially the readout circuit noise.

When I_{ph} is greater than around 7.8 pA, ΔQ_{OUT} will reach the maximum value of Q_{max} = 822 pC. The corresponding saturated ΔQ_{IN}, also known as full well capacity (FW) for CMOS APS, is around FW = 4.7×10^6 e^-. Such FW value is greater than that of the DynAMITe CMOS APS detector (FW = 2.8×10^5 e^-) with the same pixel pitch

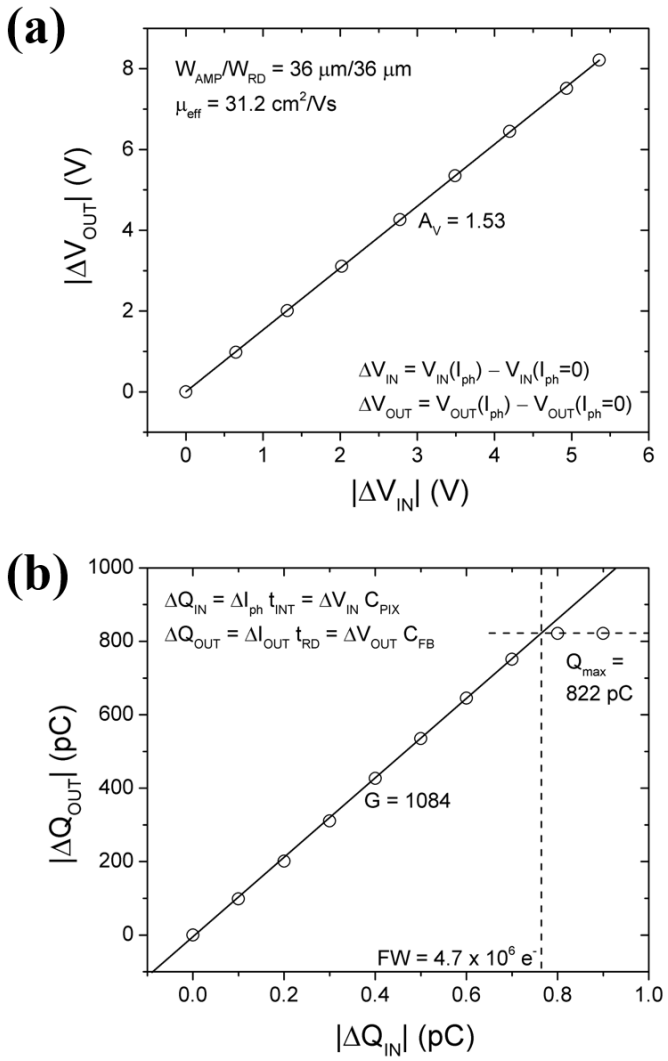

Figure 7.6 Absolute value of (a) ΔV_{OUT} versus ΔV_{IN} and (b) ΔQ_{OUT} versus ΔQ_{IN} for I_{ph} ranging from 0 to 9 pA. The voltage and charge gains can be extracted from the slope of these curves.

(50 μm). A large FW is critical to realize a wide detector dynamic range and sufficient digital levels for projection digital images.

7.5.2 Signal linearity

For the indirect a-ITZO TFT C-APS x-ray detector, the signal conversion can be summarized as: (a) x-ray quanta to optical photon in the scintillator, (b) optical photon to electron in the a-Si:H photodiode, (c) electron to V_{IN} on C_{PIX}, (d) V_{IN} to I_{OUT} by T_{AMP} and (e) I_{OUT} to V_{OUT} on C_{FB}. Each of these conversions may introduce signal nonlinearity. For the C-APS system, we consider the dominant term to be (d) V_{IN} to I_{OUT}

nonlinearity. In this section, the V_{IN} to I_{OUT} nonlinearity is discussed, while the other nonlinearity factors are ignored.

The nonlinearity between I_{OUT} and V_{IN} was described by Karim *et al*. [75]. The condition to realize a linear circuit response is given by [75]

$$\Delta V_{GS} \ll 2(V_{GS} - V_T), \tag{7.2}$$

where V_{GS} is the gate-to-source voltage of T_{AMP}. From the SPICE simulation, the probed V_{GS} values at I_{ph} = 0 and 7 pA (a high photocurrent) are 6.65 and 3.56 V, respectively. Therefore ΔV_{GS} is 3.09 V, which is smaller than $2(V_{GS} - V_T)$ =2×(6.65 + 0.93) =15.16 V. Therefore, the condition for achieving a linear circuit response is validated. As shown in Figure 7.6, the C-APS circuit demonstrates a good linearity for ΔV_{OUT} vs. ΔV_{IN} with a Pearson's correlation coefficient of 0.99998 [225].

7.5.3 Impact of field-effect mobility

To amplify the signal and reduce the electronic noise, high A_V and G are needed for C-APS x-ray detectors. Equation 1.20 and 1.21 indicate that both A_V and G are proportional to the T_{AMP} transconductance (g_m) and thus the TFT field-effect mobility (μ_{eff}). At the same time, a larger T_{AMP} device dimension (W_{AMP}/L) could also increase APS gains. However, the TFT device dimension is limited by the small APS pixel pitch (50 μm). Also, the conversion gains can be degraded by a nonnegligible T_{RD} on-resistance (R_{ON}) and data line series resistance (R_{DATA}). Among all the factors, μ_{eff} is deterministic and has the most significant impact on A_V and G.

To evaluate the impact of μ_{eff} on A_V and G, we varied the TFT band mobility (MUBAND in Table 7.1) from 50 to 20 and 1 cm^2/Vs. The μ_{eff} values are 31.2, 12.5 and 0.6 cm^2/Vs corresponding to those of a-ITZO, a-IGZO and a-Si:H TFTs, respectively. Figure 7.7 shows the extract input-output voltage characteristics for the C-APS using TFTs (T_{RS}, T_{AMP} and T_{RD}) with μ_{eff} of 31.2, 12.5 and 0.6 cm^2/Vs. The extract A_V values are 1.53, 0.62 and 0.03, respectively. It is demonstrated that the voltage gain is proportional to the TFT field-effect mobility. This observation is consistent with Equation 1.21. Therefore, to realize high gain C-APS circuits, the TFT mobility must be optimized. The proposed high mobility a-ITZO TFTs are very promising among other TFT technologies.

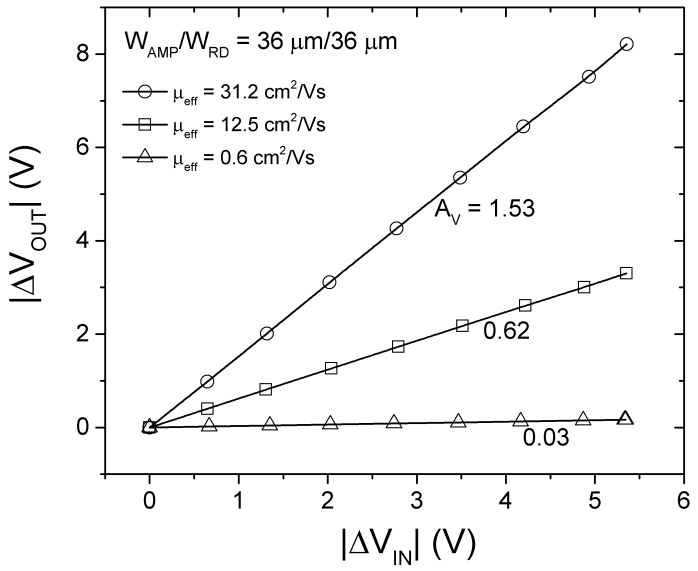

Figure 7.7 Absolute value of ΔV_{OUT} versus ΔV_{IN} and for I_{ph} ranging from 0 to 9 pA using TFT μ_{eff} of 31.2, 12.5 and 0.6 cm^2/Vs.

The impact of μ_{eff} on the charge gain follows the same trend for A_V. Extracted G values for μ_{eff} of 31.2, 12.5 and 0.6 cm^2/Vs are 1084, 434 and 21, respectively. As discussed later in Section 7.8, a large charge gain is required to reduce the post-amplifying noise ($\sigma_{post\text{-}AMP}$) dominated by the op-amp noise (σ_{amp}).

7.5.4 Impact of a-ITZO TFT threshold voltage shift

It was shown that TFTs under long-term operation suffer from threshold voltage shifts (ΔV_T) [97], [99], [194], [202], which may influence the TFT-based circuit performance. Hence, it is necessary to investigate the impact of ΔV_T on the C-APS performance. Duty ratios for T_{RS} and T_{RD}, operated in linear region as switches, are all below 0.1% which are not expected to produce high ΔV_T. On the other hand, since T_{AMP} is used to amplify photo-induced signals during the readout stage, any ΔV_T of this transistor will affect the circuit performance. During readout time, T_{AMP} is positively biased (V_{GS} >0) with a very small duty cycle of around 0.02%. During reset and integration period, T_{AMP} is negatively biased ($V_{GS} \leq 0$), since $V_{DS} \approx 0$ and $V_{IN} \leq V_{DD}$. The duty cycle for T_{AMP} under negative bias is very close to 1. Therefore, a negative ΔV_T is expected for T_{AMP} after a long-time usage.

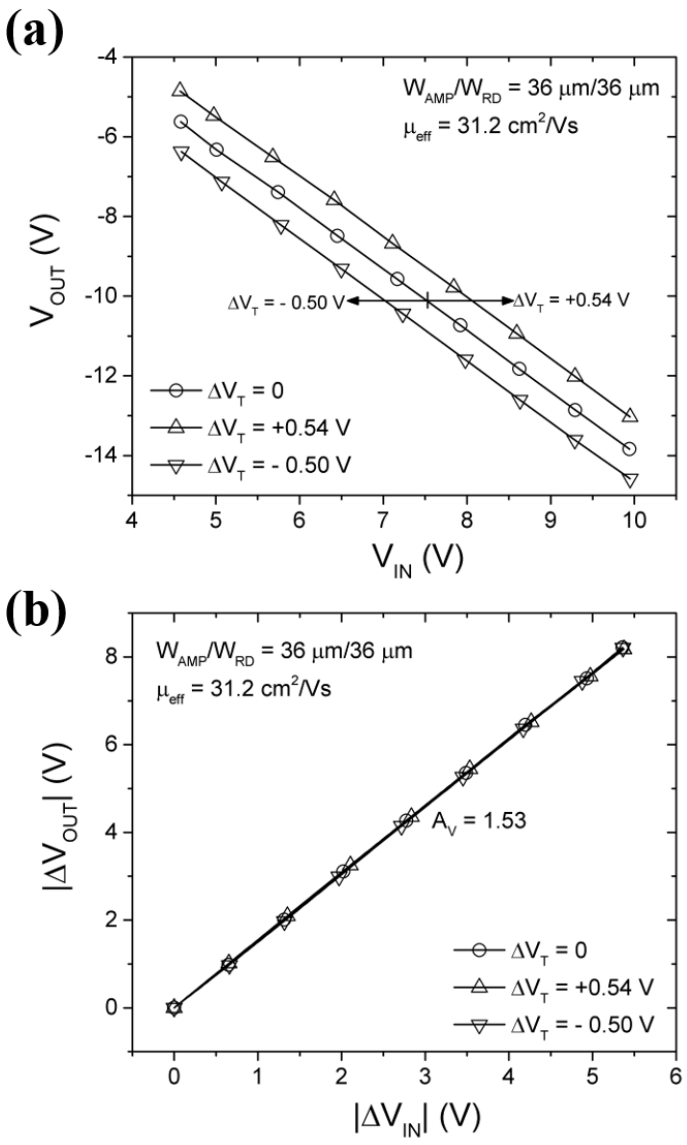

Figure 7.8 Extracted (a) V_{IN} and V_{OUT}, and (b) ΔV_{IN} and ΔV_{OUT} for C-APS with ΔV_T of 0, +0.54 and -0.5 V applied to T_{AMP}.

In this study, the impact of both positive and negative ΔV_T is evaluated. The dc gate bias-induced positive and negative a-ITZO TFT ΔV_T was observed to be +0.54 V and -0.5 V, respectively [97]. The ΔV_T for a-ITZO TFTs can be included in the SPICE simulation by shifting both the VTO and VFB parameters by +0.54 or -0.5 V at the same time.

The extracted V_{IN} and V_{OUT} for ΔV_T of 0, +0.54 and -0.5 V are shown in Figure 7.8 (a). It is observed that a positive ΔV_T leads to a smaller I_{OUT} for T_{AMP}. Hence a reduced $|V_{OUT}|$ is expected (note: V_{OUT} is negative). On the contrary, a negative ΔV_T gives an

increased $|V_{OUT}|$ (i.e., a more negative V_{OUT}). In comparison to the case without V_T shift, V_{OUT} changes by 0.81 and -0.74 V for ΔV_T of +0.54 and -0.5 V, respectively. Nevertheless, since V_{OUT} also shifts at $I_{ph} = 0$ ($V_{IN} \approx 10$ V), $\Delta V_{OUT}/\Delta V_{IN}$ (i.e., the voltage gain) does not change with ΔV_T as shown in Figure 7.8 (b). The extracted A_V values are constant ($A_V = 1.53$) with V_T shift. Therefore, it is expected that the V_T instability should not affect the circuit performance as measured by A_V.

7.5.5 Impact of W_{AMP} / W_{RD} ratio

To optimize the electrical performance of the proposed C-APS circuit, the device dimensions should be optimized. Considering a 50 μm pixel pitch and a critical dimension (channel length) $L = 3$ μm, a total channel width for T_{AMP} and T_{RD} ($W_{AMP} + W_{RD}$) of 72 μm can be obtained. We varied the ratio of W_{AMP}/W_{RD} from 63 μm / 9 μm to 9 μm / 63 μm, while keeping $W_{AMP} + W_{RD} = 72$ μm and $\mu_{eff} = 31.2$ cm^2/Vs. Figure 7.9 shows the extracted voltage gains using various W_{AMP}/W_{RD} ratios. A narrow W_{AMP}/W_{RD} ratio range (0.5 to 1.2) allows a high voltage gain greater than 1.5. The accepted W_{AMP}/W_{RD} dimensions are 36 μm / 36 μm and 27 μm / 45 μm. Eventually, W_{AMP}/W_{RD} = 36 μm / 36 μm ($A_V = 1.53$), which favors the pixel layout design, was selected for the pixel layout for a 50 μm pixel pitch C-APS as discussed in Section 7.6.

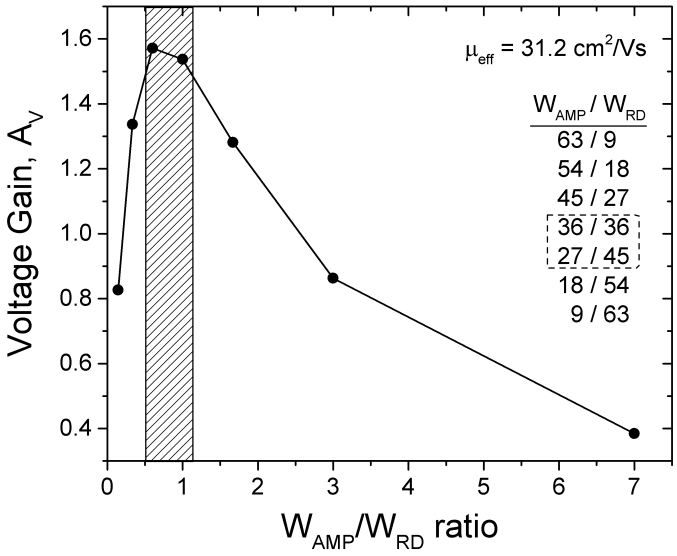

Figure 7.9 Extracted voltage gains for various W_{AMP}/W_{RD} ratio ranging from 63/9 to 9/63. TFT field-effect mobility of 31.2 cm^2/Vs was used.

7.6 Proposed 50 µm Pixel Circuit Layout and Fabrication Process

Figure 7.10 proposes a 50 µm pixel pitch layout for the a-ITZO TFT C-APS. Considering the TFT layout, the half-Corbino TFT structure with the inner-drain configuration is adopted to acquire higher operation current (I_{OUT}) for T_{AMP} [99]. On the other hand, the outer-drain bias condition is used for T_{RD} to reduce the gate-to-source capacitance [99], [226], [227] and data line parasitic capacitance to be described in Section 7.7. The TFT sizes are the same as those listed in Table 7.3, and the critical dimension (minimum width) of metal lines is 3 µm.

We propose the following 10-mask processing steps for the a-ITZO TFT [97], [220] and the a-Si:H photodiode [222] fabrication.

First, metal #1 (Mo, for gate electrodes of T_{RS}, T_{AMP}, and T_{RD}, and V_{RS} and V_{RD} lines) is formed by DC sputtering on glass substrate. The standard photolithography is used for metal definition (**mask #1**). Next, a 470-nm amorphous silicon oxide (a-SiO_x) as the gate insulator is deposited using PECVD. Then, a 30-nm a-ITZO films DC sputtered using the optimized O_2 flow ratio of 5%, subsequently patterned into active islands by a wet etching process (**mask #2**) and annealed at 300 °C. The gate contact VIA is defined (**mask #3**) to connect V_{IN} and the gate of T_{AMP} using the reactive-ion etching (RIE). At the same time, contact VIAs for V_{RS} and V_{RD} pads are created. Afterward, metal #2 (Mo, for S/D electrodes of T_{RS}, T_{AMP}, and T_{RD} and V_{DD} and V_M lines) are deposited by sputtering and patterned using the back channel etch process (**mask #4**). A 3 µm a-SiO_x passivation layer (PSV #1) is deposited over the fabricated a-ITZO TFTs. A contact VIA is generated using RIE (**mask #5**) to electrically connect the source electrode of T_{RS} / the gate electrode of T_{AMP} to the patterned bottom Mo electrode (cathode) of the a-Si:H photodiode (**mask #6**). Also, VIAs for the four contact pads (V_{RS}, V_{RD}, V_M, and V_{DD}) are etched using mask #5. The opaque bottom electrode of a-Si:H photodiode also serves as a light shield for a-ITZO TFTs. Using PECVD, a 50-nm n^+ layer, a 1-µm thick undoped/intrinsic a-Si:H layer, and a 50-nm p^+ layer are sequentially deposited and patterned by photolithography (**mask #7**). A second passivation layer (PSV #2) can be deposited on top of the p^+ layer. Next, the photodiode

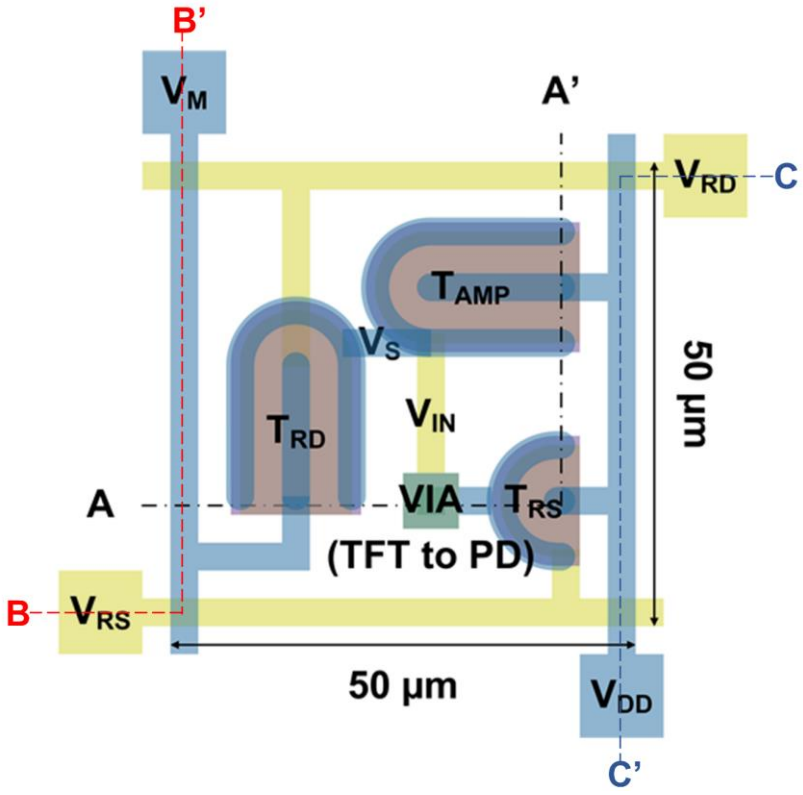

Figure 7.10 A 50-µm pixel pitch layout for the proposed a-ITZO TFT C-APS. A critical dimension of 3 µm was used for the layout design. The VIA is used to connect the photodiode bottom electrode to T_{AMP} gate and T_{RS} source. V_M is the data line output voltage connected to the negative input node of the op-amp.

top electrode area and VIAs for all four contact pads are defined (**mask #8**). A transparent indium-tin oxide (ITO) layer is deposited as the top electrode of the a-Si:H photodiode. Then, the a-Si:H photodiode is annealed at 150 °C to suppress the excess current coming from extrinsic defect generation. The ITO layer is patterned out of the active-matrix array as the top conductive layer for four contact pads (**mask #9**). After etching ITO, the ITO needs to be thermally annealed at around 230 °C [228]. A third passivation layer (PSV #3) is deposited to protect the entire structure. Finally, contact VIAs for pads V_{RS}, V_{RD}, V_M, V_{DD} and V_{PD} are defined out of the active-matrix array by etching the PSV #3 (**mask #10**).

A 150-µm CsI:Tl scintillator can be directly deposited (or attached using a FOP) on top of the passivated a-Si:H photodiode layer to complete the detector fabrication.

Figure 7.11 illustrates the lithography process steps and cross-sectional views (A to

A') of the C-APS pixel referring to the layout in Figure 7.10. Figure 7.12 shows the final cross-sectional view (B to B') of the data line, V_{RS} and V_M pads after the entire process. The cross-sectional view (C to C') of the V_{DD} and V_{RD} pads (not shown) is the same as Figure 7.12 by replacing V_{RS} with V_{RD} and V_M with V_{DD}.

It should be noted that the a-Si:H photodiode bottom electrode is also used as a light shield for a-ITZO TFTs. At the same time, since the photodiode bottom electrode voltage is the same as the gate voltage of T_{AMP}, T_{AMP} behaves like a dual-gate TFT with top and bottom gates biased together. It was reported by Baek *et al*. that increased operational current can be achieved especially in the saturation region, when the dual-gate TFT structure is used [194]. The increased I_{OUT} can lead to higher A_V and G, which is favorable. Since the top and bottom gates are biased together, instead of having different V_{GS}, it is expected that the threshold voltage of T_{AMP} will not be affected.

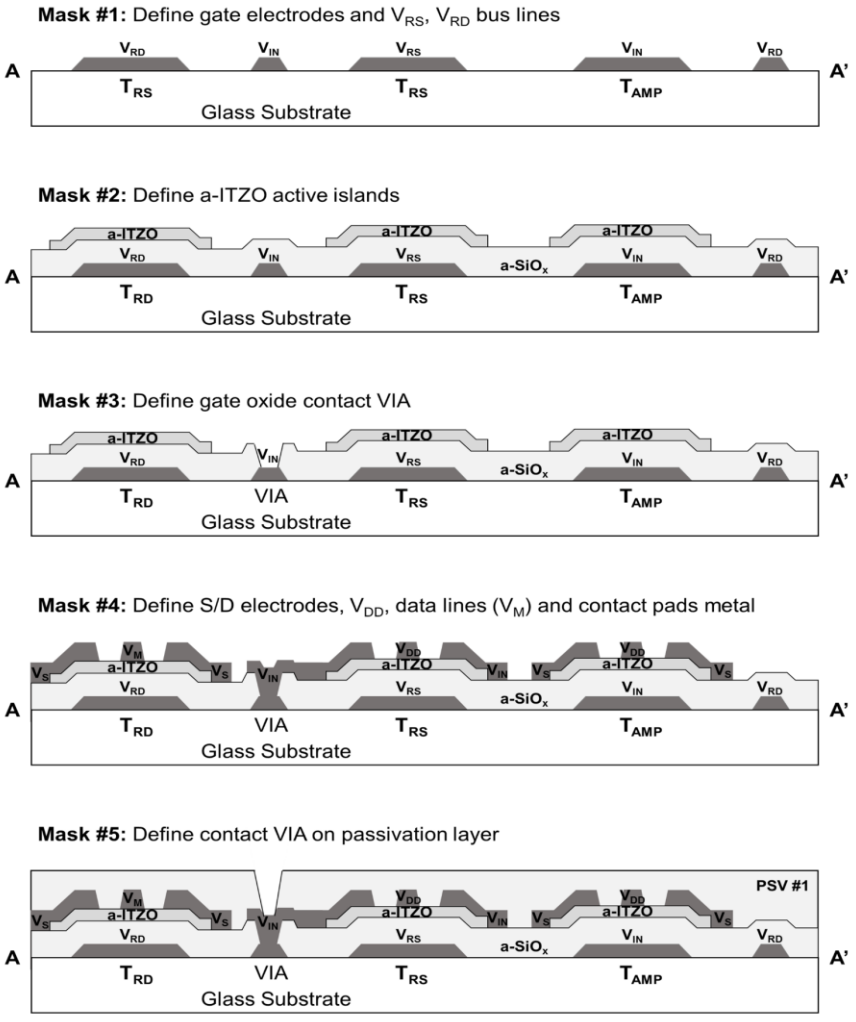

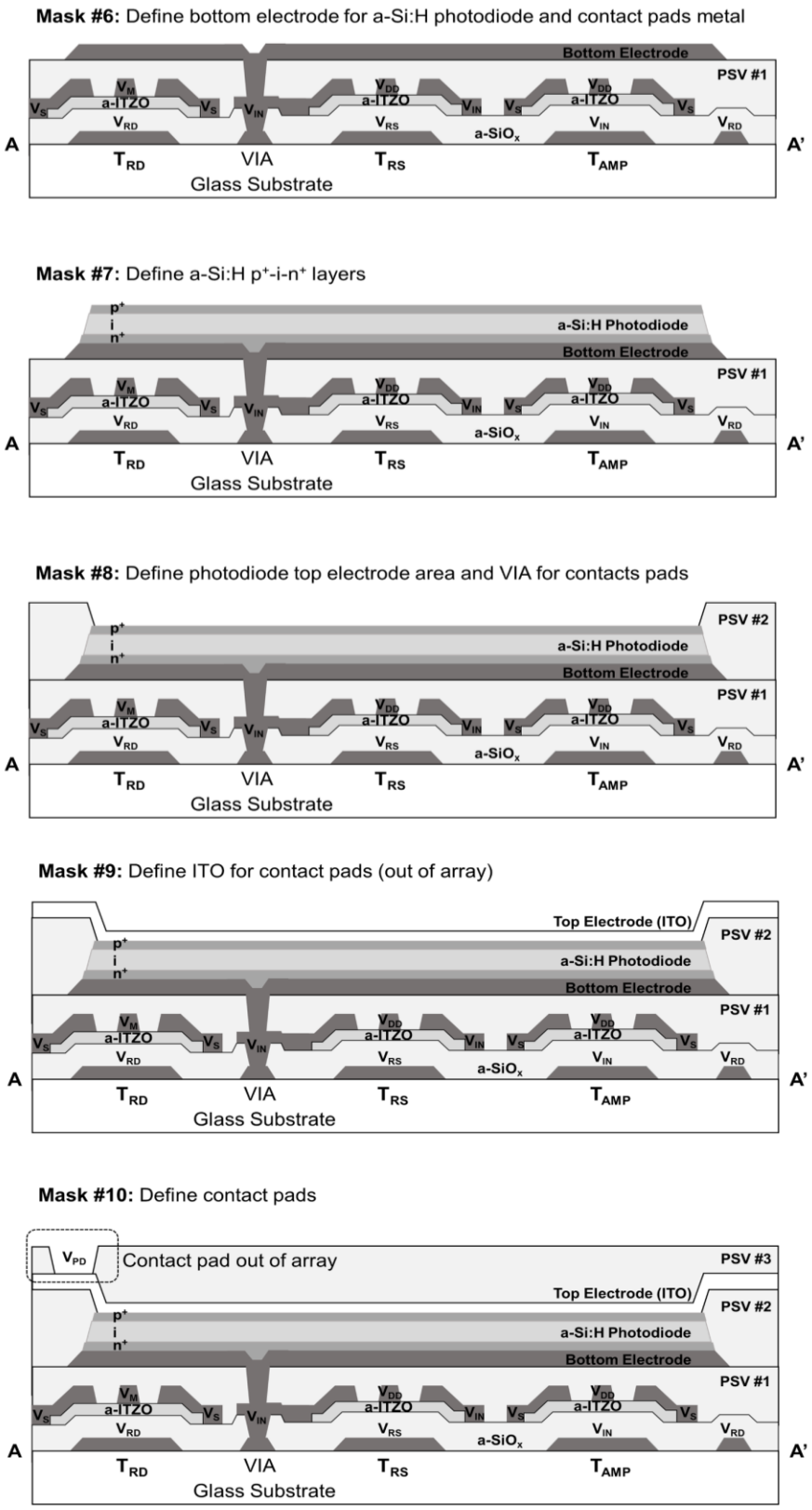

Figure 7.11 Cross-sectional view (A to A') of a-Si:H photodiode / a-ITZO TFT C-APS and illustration of photolithography steps (10 mask steps).

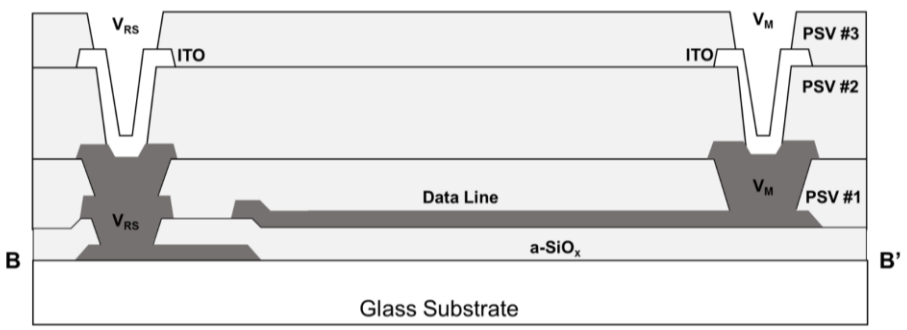

Figure 7.12 Cross-sectional view (B to B') of the fabricated data line, V_{RS} and V_M pads after mask #10. Cross-section view from C to C' shows the same structure.

7.7 Impact of Data Line Resistance and Parasitic Capacitance

For active-matrix arrays, the data line (V_M) series resistance (R_{DATA}) and parasitic capacitance (C_{DATA}), could cause problems such as degenerated conversion gains, feedthrough voltages when gates are pulsed, an increase in readout electronic noise, output signal delays, and pixel crosstalk due to capacitive coupling [229]. When R_{DATA} and C_{DATA} are taken into consideration for the a-ITZO TFT C-APS, it can be predicted that I_{OUT} and both A_V and G will be affected.

R_{DATA} is associated with the Mo data line with a resistivity of 53.4×10^{-9} Ω·m.

As shown in Figure 7.13, based on the layout described in Section 7.6, C_{DATA} consists of the gate-to-source overlapping capacitance (C_{GS}) of T_{RD}, the overlapping capacitance (C_{RD}) between the data line and V_{RD}, the overlapping capacitance (C_{RS}) between the data line and V_{RS}, and the overlapping capacitance (C_{PSV}) between the data line and the a-Si:H photodiode bottom electrode. Hence, C_{DATA} can be estimated by

$$C_{DATA} = N(C_{GS} + C_{RD} + C_{RS} + C_{PSV}) = N\left[C_{ox}(L_S L + 2L^2) + C_{ox,PSV}(a_{pix} L)\right], \quad (7.3)$$

where N is the number of pixels on a data line, L is the both process critical dimension and line width (3 μm), L_S is the length of the T_{RD} source electrode (~15 μm), a_{pix} is the pixel pitch (50 μm), C_{ox} is the gate oxide (470 nm a-SiO_x) capacitance (7.34 nF/cm^2), $C_{ox,PSV}$ is the passivation layer (e.g., 3 μm a-SiO_x) capacitance (1.15 nF/cm^2).

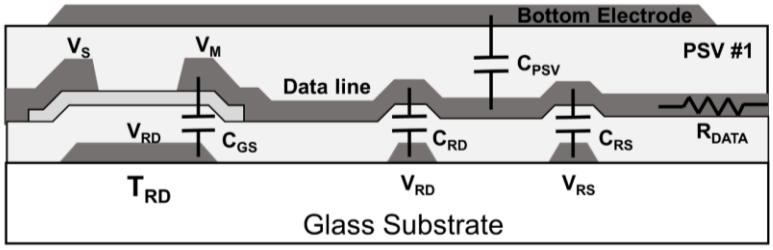

Figure 7.13 Cross-sectional schematic of T_{RD} and the data line series resistance (R_{DATA}) and parasitic capacitances (C_{DATA}). To simplify the drawing, the regular TFT structure is shown.

Considering a large-area x-ray detector featuring a 4k-resolution (N = 4000) with a data line metal thickness of 200 nm and a pixel pitch of 50 μm, R_{DATA} is estimated to be 17.8 kΩ. Using a metal with a lower resistivity such as Al or Cu, R_{DATA} is expected to be reduced.

The estimated C_{DATA} is around 25.3 pF ($N{\cdot}C_{GS}$ = 13.2 pF, $N{\cdot}C_{RS}$ = $N{\cdot}C_{RD}$ = 2.6 pF, $N{\cdot}C_{PSV}$ = 6.9 pF). The dominant parasitic capacitance is C_{GS} of T_{RD} ($N{\cdot}C_{GS}$ = 13.2 pF). Patterning gate electrodes (gate-to-source overlapping width of 0.2 μm) is helpful to minimize the overlapping capacitance to further diminish C_{GS} of the half-Corbino T_{RD} [227]. The reduced total C_{GS} is expected to be about 1.8 pF, and the total C_{DATA} can be drastically decreased to 13.9 pF. Also, self-aligned [230] or coplanar homojunction [231] TFT structures could be used to further reduce C_{DATA}. In addition, patterning the bus line intersections could also help reduce C_{RS} and C_{RD}.

To study the data line loading impact on the performance of the proposed a-ITZO TFT C-APS, SPICE simulation involving R_{DATA} = 17.8 kΩ and C_{DATA} = 25.3 pF was conducted. Figure 7.14 presents the extracted input-output (a) voltage and (b) charge characteristics for C-APS circuit with and without R_{DATA} and C_{DATA}. Both the extracted A_V and G reduced by around 21% to A_V = 1.21 and G = 855 with data line loadings. The corresponding APS conversion gain also drops from 1.75 to 1.37 μV/e^-.

As shown in Equation 1.20 and 1.21, this reduction is due to the source follower degeneration with additional R_{DATA} in combination with R_{ON} of T_{RD}. Since additional voltage ($I_{OUT}R_{DATA}$) is dropped on R_{DATA}, it is expected that both I_{OUT} and the circuit gains will be degraded. At the same time, the maximum output charge is also reduced from Q_{max} = 822 to 652 pC due to both the reduced G and loss of charges stored on

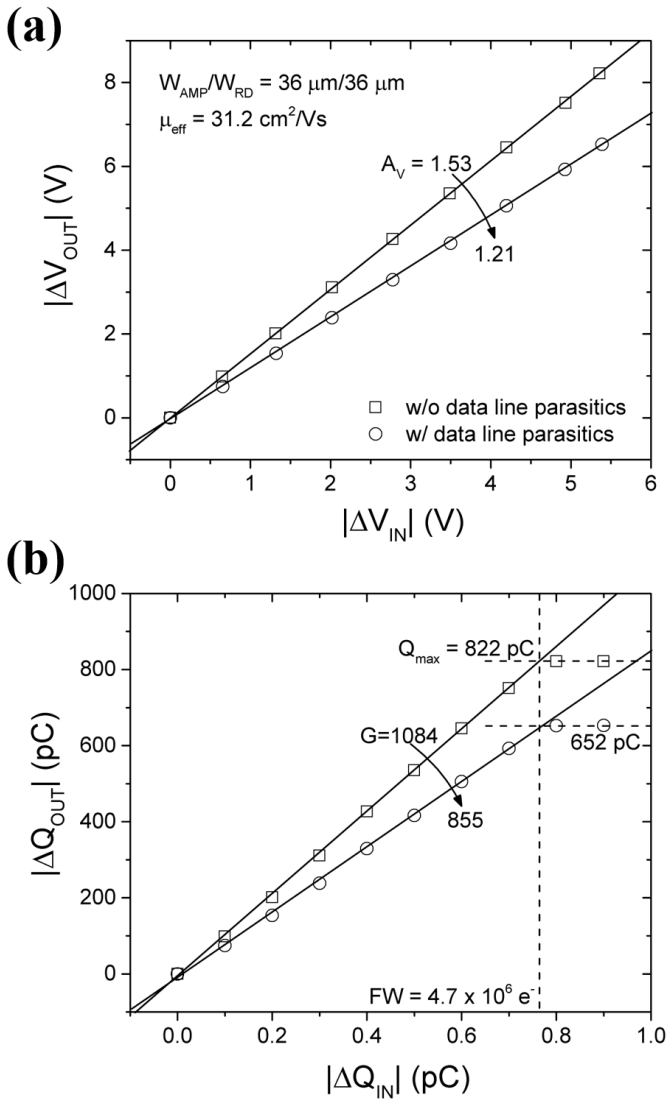

Figure 7.14 Extracted input-output (a) voltage and (b) charge characteristics for C-APS with and without data line loadings. I_{ph} is ranging from 0 to 9 pA.

C_{DATA} instead of C_{FB}. As expected, the data line loading does not affect V_{IN} or Q_{IN}.

The simulation results with data line loading is used to calculate the electronic noise for C-APS as discussed in Section 7.8.

7.8 Noise Analysis

Each electronic noise element is modeled and calculated based on the reported

C-APS noise model developed by Karim *et al* [53]. First, the a-Si:H photodiode dark current shot noise is given by [232]

$$\sigma_{\text{PD,shot}} = \sqrt{I_{\text{dark}} t_{\text{frame}} / q}, \tag{7.4}$$

where I_{dark} (~ 3.7×10^{-16} A) is the dark current of a-Si:H photodiode and t_{frame} is the frame time (100.2 ms).

Similarly, the T_{RS} leakage current shot noise is given by

$$\sigma_{\text{TFT,shot}} = \sqrt{I_{\text{off}} t_{\text{frame}} / q}, \tag{7.5}$$

where I_{off} (~ 1.5×10^{-14} A) is the TFT leakage current (off-current) of T_{RS}.

If uncorrelated double sampling is applied, the reset noise for APS is given by [232]

$$\sigma_{\text{reset}} = \sqrt{2kTC_{\text{pix}}} / q, \tag{7.6}$$

where k is the Boltzmann constant, T is the Kelvin temperature, and C_{pix} (~ 0.139 pF) is the input pixel capacitance, which is dominated by photodiode capacitance of 0.12 pF.

The input referred pre-amplifying pixel noise, which cannot be removed by APS, is given by

$$\sigma_{\text{pre-AMP}} = \sqrt{\sigma_{\text{PD,shot}}^{\ 2} + \sigma_{\text{TFT,shot}}^{\ 2} + \sigma_{\text{reset}}^{\ 2}}. \tag{7.7}$$

In this work, since T_{AMP} and T_{RD} operate in the saturation and linear region, respectively, the noise power spectral density of thermal noise for T_{AMP} and T_{RD} are given by [195]

$$\begin{aligned} S_{\text{th, AMP}} &= \frac{2}{3} \cdot 4kT\mu_{\text{eff}} C_{\text{ox}} \left(W_{\text{AMP}} / L\right)\left(V_{\text{GS,AMP}} - V_{\text{T}}\right), \quad \text{(saturation region)} \\ S_{\text{th, RD}} &= 4kT\mu_{\text{eff}} C_{\text{ox}} \left(W_{\text{RD}} / L\right)\left(V_{\text{GS,RD}} - V_{\text{T}}\right). \qquad \text{(linear region)} \end{aligned} \tag{7.8}$$

All the device and driving parameters can be extracted from the SPICE simulation. The corresponding thermal noise equivalent electrons of T_{AMP} and T_{RD} ($\sigma_{\text{th,AMP}}$ and $\sigma_{\text{th,RD}}$) can be calculated by integrating the noise power spectral density over the noise bandwidth of a first-order low-pass filtering circuit using the method and equations developed by Karim *et al* [53].

The noise power spectral density of the flicker noise for T_{AMP} and T_{RD} are [195]

$$S_{\mathrm{fl,AMP}} = \frac{\alpha_{\mathrm{H}} q \mu_{\mathrm{eff}} C_{\mathrm{ox}} W_{\mathrm{AMP}} (V_{\mathrm{GS,AMP}} - V_{\mathrm{T}})^3}{2 f L^3}, \qquad \text{(saturation region)}$$
$$S_{\mathrm{fl,RD}} = \frac{\alpha_{\mathrm{H}} q \mu_{\mathrm{eff}} C_{\mathrm{ox}} W_{\mathrm{RD}} (V_{\mathrm{GS,RD}} - V_{\mathrm{T}}) V_{\mathrm{DS}}^2}{f L^3}. \qquad \text{(linear region)} \tag{7.9}$$

where α_{H} is the Hooge's parameter and f is the circuit frequency. We used the measured α_{H} value (~ 1.5×10^{-3}) for a-IGZO TFTs for the flicker noise calculation. A similar (or even smaller) α_{H} parameter is expected for a-ITZO TFTs. The flicker noise equivalent electrons $\sigma_{\mathrm{fl,AMP}}$ and $\sigma_{\mathrm{fl,RD}}$ can be calculated by integrating the noise spectral density over frequency adopted from the model developed by Karim *et al* [53].

The external readout circuit noise (σ_{amp}) is mainly generated by the switched integrator. The readout circuit noise can be modeled as having a fixed noise component of the amplifier (σ_{amp0}) in addition to capacitance dependent component ($\gamma_{\mathrm{amp}} C_{DATA}$) previously shown in Equation 1.5.

$$\sigma_{amp} = \sigma_{amp0} + \gamma_{amp} C_{DATA}, \tag{1.5}$$

where σ_{amp} and γ_{amp} are an amplifier's characteristic constants. C_{DATA} is the capacitance loading at the amplifier's input node. For the specific low-noise amplifier, σ_{amp0} and γ_{amp} are found to be 250 electrons and as 15 electrons/pF, respectively [224].

The output referred post-amplifying pixel noise is given by

$$\sigma_{\mathrm{post\text{-}AMP,out}} = \sqrt{\sigma_{\mathrm{th,AMP}}^2 + \sigma_{\mathrm{th,READ}}^2 + \sigma_{\mathrm{fl,AMP}}^2 + \sigma_{\mathrm{fl,READ}}^2 + \sigma_{\mathrm{amp}}^2}. \tag{7.10}$$

The input referred post-amplifying pixel noise, which can be significantly reduced by the C-APS, is given by output referred post-amplifying pixel noise divided by the APS charge gain of 855 ($\sigma_{\mathrm{post\text{-}AMP,in}} = \sigma_{\mathrm{post\text{-}AMP,out}} / G$). Finally, the total input referred noise (σ_{total}) is given by the square root of the quadratic sum of the input referred pre-amplifying and post-amplifying noise.

$$\sigma_{total} = \sqrt{\sigma_{pre-AMP,in}^2 + \sigma_{post-AMP,in}^2} = \sqrt{\sigma_{pre-AMP,in}^2 + \sigma_{post-AMP,out}^2 / G^2} \tag{7.11}$$

Table 7.4 lists all the calculated input referred electronic noise components for the proposed a-ITZO TFT C-APS. It is shown that all the post-amplifying noise, especially the op-amp noise, can be minimized by the high APS charge gain of 855. Similar to CMOS V-APS (Section 3.2.5), the dominant noise component is the reset noise σ_{reset} of 212 e^-, which cannot be minimized by APS.

In the ideal case, the total input referred electronic noise of the a-ITZO TFT C-APS circuit is around 239 e^-, which is comparable to that of CMOS V-APS detector (150 e^-) and much smaller in comparison to a-Si:H PPS detectors (>1000 e^-). As discussed in Chapter 5 (Section 5.4.2), such a low electronic noise (below 300 e^-) is not expected to significantly degrade the x-ray imager detectability for subtle features such as microcalcifications. Hence, we believe that the indirect a-ITZO TFT C-APS in combination with an a-Si:H photodiode could be considered as a promising candidate for the next generation x-ray imager to replace the old a-Si:H PPS technology suffering from a much higher electronic noise. The integration between a-Si:H photodiode and a-ITZO TFT arrays must be resolved at the manufacturing level.

Parameter	Description	Value (e^-)
$\sigma_{PD,shot}$	PD dark current shot noise	15
$\sigma_{TFT,shot}$	T_{RS} leakage current shot noise	97
σ_{reset}	Reset noise	212
$\sigma_{th,AMP}$	Input referred T_{AMP} thermal noise	3
$\sigma_{th,RD}$	Input referred T_{RD} thermal noise	3
$\sigma_{fl,AMP}$	Input referred T_{AMP} flicker noise	46
$\sigma_{fl,RD}$	Input referred T_{RD} flicker noise	14
σ_{amp}	Input referred op-amp noise	1
$\sigma_{pre\text{-}AMP}$	Input referred pre-amplifying noise	234
$\sigma_{post\text{-}AMP,in}$	Input referred post-amplifying noise	48
σ_{total}	Total input referred noise	239

Table 7.4 Input referred electronic noise of a-ITZO TFT C-APS.

7.9 Summary

In this chapter, we proposed the a-ITZO TFT C-APS circuit for DBT. The C-APS circuit electrical properties were evaluated using SPICE simulation. A 50 μm pixel layout was designed with corresponding fabrication process suggested. With data line parasitics considered, a high charge gain of around 855 is expected. The estimated electronic noise of the a-ITZO TFT C-APS is about 239 e^-. The high charge gain and

low electronic noise are both favorable for DBT. Active-matrix arrays based on the proposed a-ITZO TFT C-APS technology still need to be fabricated and evaluated for DBT.

Chapter 8
Conclusions and Proposed Future Work

8.1 Conclusions of Dissertation

In this dissertation, we have evaluated high-resolution large area CMOS APS x-ray detectors (Dexela 2923 MAM and DynAMITe) and proposed a novel a-ITZO TFT-based C-APS for DBT application.

Both the Dexela and DynAMITe CMOS APS x-ray detectors have achieved superior 2D x-ray imaging performance as measured by the 2D MTF, NPS and DQE parameters. The 75 μm pixel pitch Dexela 2923 MAM CMOS APS detector demonstrates a high DQE of 0.2 to 0.65 at a very low air kerma of 1.69 μGy (using a broadband x-ray radiation at 28 kVp). The detector performance can be further improved, if monochromatic synchrotron radiation is used. The Nyquist frequency achieved is limited at 6.67 mm^{-1} according to a pixel pitch of 75 μm. To further improve the detector resolution, we evaluated a 50 μm pixel pitch DynAMITe CMOS APS detector. The DynAMITe detector achieves even higher Nyquist frequency of 10 mm^{-1} and very low electronic noise of around 150 e^-. The maximum DQE of around 0.55 has been demonstrated at a low DBT K_a below 10 μGy.

In addition, we have developed a 2D cascaded system analysis model to simulate both the 2D x-ray imaging performance and detector electrical properties for CMOS APS x-ray detectors. The validated 2D model has been extended to 3D spatial frequency space to evaluate the 3D imaging performance of the DynAMITe detector. We have first measured and modeled the angle-dependent 2D MTF, NNPS and DQE parameters at projection angles up to 30°. The experimental and simulation results demonstrate that a

wider incident projection angle will degrade the MTF and DQE in the high spatial frequency range, while the NNPS is not affected. The impacts of acquisition geometry, dose and detector parameters were investigated using the 3D cascaded system analysis in combination with the FBP reconstruction method to calculated 3D MTF, NNPS and DQE parameters. It is shown that a wider projection angle range (e.g. 30°) will prevent image information loss at low spatial frequencies, which is suitable for large, low contrast objects (such as masses) detection. Low MGD (0.5 mGy) does not affect the CMOS APS detector response (in-plane DQE) due to the low electronic noise. We found that the dominant factors limiting the investigated CMOS APS detector 3D imaging performance include the focal spot size and the scintillator blurring effect. Specifically, a large focal spot size will remarkably decrease both the in-plane MTF, and DQE. To achieve satisfactory image quality for DBT, a focal spot size of smaller than 0.3 mm should be used. A remarkable improvement on the in-plane MTF and DQE are achieved when the pixelated scintillator is used to reduce its blurring effect. Although the scintillator pixel fill factor can reduce the x-ray photon capture when 50 μm pixel pitch is used, we believe that a thicker pixelated scintillator in combination with the CMOS APS detector can be used to address this issue.

To evaluate the DBT image quality using the advanced 50 μm pixel pitch CMOS APS x-ray detector, we presented a task-based modeling framework to simulate the imaging performance for a high resolution medical imaging system that contains both a 50 μm pixel pitch DynAMITe detector and a 165 μm high definition medical imaging. Detectability index and AUC characteristics for detecting small, high contrast and large, low contrast objects were evaluated. The simulation results show that to optimize the AUCs for microcalcification detection, a display pixel pitch of 165 μm or smaller and zoom factor of greater than 10 should be used. Detector electronic noise of smaller than 300 e^- is promising to distinguish small size microcalcifications (<150 μm). On the other hand, to detect large, low contrast masses, 12 bits or higher display gray levels would be desirable. Also, image display gray level magnification of greater than 2 can increase the AUC. To further enhance the detectability for large, low contrast objects, a wider projection angle range of more than ±30° should be used, especially when the anatomical background noise is high. Finally, a display with a high maximum

luminance (>1000 cd/m^2) at a low ambient luminance (<5 cd/m^2) should be considered to realize good image quality as measured by AUC. The task-based simulation demonstrates reasonable results for various conditions. The results could help guide the hardware design for prototype high-resolution APS x-ray detectors and medical imaging displays.

Another candidate for large area DBT APS x-ray detectors is the amorphous oxide semiconductor TFT C-APS. First, we studied the electrical properties of a-ITZO TFTs fabricated using shadow masks. The device shows a V_T of 1.6 V, a high μ_{eff} of 30.6 cm^2/Vs, and a *SS* of 0.38 V/dec. We have established that μ_{eff} is gate voltage dependent. To take this into account, we used both the least square error linear fitting (Method 1) and second derivative methods (Method 2) to extract parameters such as V_T, γ and K with high consistency to experimental data. Method 1 was found to be more precise. In addition, the impacts of a-ITZO channel thickness and O_2 flow ratio on device properties were investigated. We found that effective trap states N_{eff} of a-ITZO reduce with increasing channel thickness, which leads to improved device performance. The variations in device performance at different P_{O2} could be explained by the acceptor-like O^0 or O^- deep states. Besides, the electrical instability under PBTS and NBTS were studied. ΔV_T of +0.54 and -0.50 V were achieved after PBTS and NBTS for 10^3 s, respectively. The V_T shift is smaller in comparison to that of fabricated a-IGZO TFT indicating better electrical stability. We also observed that the electrical instability during PBTS is highly oxygen-related. The origins of electrical instability during PBTS and NBTS can be explained by the increased acceptor-like O^0 or O^- deep states and enhanced H-doping to the a-ITZO channel. Considering both device electrical performance and stability, the optimized a-ITZO film thickness and O_2 flow ratio are 50 nm and 5%, respectively.

Based on the experimental results on a-ITZO TFTs, the a-ITZO TFT C-APS circuit in combination with an a-Si:H p^+-i-n^+ photodiode was proposed for DBT. We developed SPICE models for both the a-ITZO TFTs and the a-Si:H photodiode. The extracted parameters were used for the C-APS pixel circuit SPICE simulation. Circuit characteristics such as voltage and charge gains were extracted from the simulation results. It was established that the circuit gains are proportional to TFT field-effect

mobility while invariant with the TFT threshold voltage shift. The device dimensions W_{AMP}/W_{RD} were optimized to be around 1. Next, we have proposed a 50 μm pitch C-APS pixel circuit layout and a 10-mask photolithography fabrication process steps. Based on the pixel layout, the data line series resistance and parasitic capacitance were estimated and included in the SPICE simulation. The C-APS circuit with data line loadings demonstrates both high A_V and G of 1.21 and 855. The high charge gain is sufficient to minimize the post-amplifying noise, especially the op-amp noise. The proposed C-APS circuit demonstrates a low total electronic noise of around 239 e^-. These properties are very promising for the next generation x-ray detectors for DBT. At the same time, the proposed fabrication process for a-ITZO TFT C-APS is reliable for large area photolithography process on a glass substrate.

8.2 Recommendations for Future Work

Three directions are recommended for future research:

- Virtual clinical trial and observer studies for CMOS APS x-ray detectors:

To study the DBT image quality, virtual clinical evaluations are suggested. A numerical model can be developed to model the x-ray spectrum, x-ray ray tracing and scattering in a simulated breast phantom to generate idealized 2D images at each DBT projection angles. The developed 2D cascaded system analysis model for CMOS APS x-ray detectors can be used to blur and add noise to the idealized images. Next image reconstruction can be applied to obtain simulated DBT images. Observer studies can be done to evaluate the image quality and compared with the results demonstrated using the task-based model [170].

- Direct conversion CMOS APS x-ray detectors:

The 2D and 3D cascaded system analysis model can be modified by replacing the CsI:Tl scintillator, FOP and a-Si:H photodiode by an direct conversion detector such as a-Se or HgI_2. The direct conversion CMOS APS detector is expected to achieve superior image resolution in comparison to indirect conversion detectors whose MTF is limited

by the scintillator blurring. The direct conversion detector ensures high image resolution, while the CMOS APS backplane achieves ultra-low electronic noise at the same time. 2D/3D cascaded system analysis and task-based modeling for direct conversion detectors are suggested.

- Fabrication and evaluation of a-ITZO TFT C-APS circuits:

We have proposed a pixel layout and fabrication process for the a-Si:H p^+-i-n^+ photodiode / a-ITZO TFT C-APS. For future research, we recommend to fabricate the a-ITZO TFT C-APS circuit and small size array to evaluate the electrical performance such as voltage and charge gains of the proposed circuits. The measured results can be compared with the SPICE simulation results presented in this dissertation. In combination with a scintillator, the pixel performance under x-ray exposure can be also evaluated.

BIBLIOGRAPHY

[1] E. A. Rafferty, “Digital Mammography: Novel Applications,” *Radiol. Clin. North Am.*, vol. 45, no. 5, pp. 831–843, 2007.

[2] L. T. Niklason, B. T. Christian, L. E. Niklason, D. B. Kopans, D. E. Castleberry, B. H. Opsahl-Ong, C. E. Landberg, P. J. Slanetz, a a Giardino, R. Moore, D. Albagli, M. C. DeJule, P. F. Fitzgerald, D. F. Fobare, B. W. Giambattista, R. F. Kwasnick, J. Liu, S. J. Lubowski, G. E. Possin, J. F. Richotte, C. Y. Wei, and R. F. Wirth, “Digital tomosynthesis in breast imaging.,” *Radiology*, vol. 205, no. 2, pp. 399–406, 1997.

[3] D. B. Kopans, “Digital breast tomosynthesis from concept to clinical care,” *Am. J. Roentgenol.*, vol. 202, no. 2, pp. 299–308, 2014.

[4] I. Sechopoulos, “A review of breast tomosynthesis. Part I. The image acquisition process.,” *Med. Phys.*, vol. 40, no. 1, p. 14301, 2013.

[5] J. A. Baker and J. Y. Lo, “Breast tomosynthesis. State-of-the-art and review of the literature,” *Acad. Radiol.*, vol. 18, no. 10, pp. 1298–1310, 2011.

[6] S. J. Glick, “Breast CT.,” *Annu. Rev. Biomed. Eng.*, vol. 9, pp. 501–26, 2007.

[7] J. M. Boone, A. L. C. Kwan, K. Yang, G. W. Burkett, K. K. Lindfors, and T. R. Nelson, “Computed tomography for imaging the breast,” *J. Mammary Gland Biol. Neoplasia*, vol. 11, no. 2, pp. 103–111, 2006.

[8] J. M. Boone, T. R. Nelson, K. K. Lindfors, and J. A. Seibert, “Dedicated Breast CT: Radiation Dose and Image Quality Evaluation,” *Radiology*, vol. 221, no. 3, pp. 657–667, 2001.

[9] N. D. Prionas, K. K. Lindfors, S. Ray, S.-Y. Huang, L. a Beckett, W. L. Monsky, and J. M. Boone, “Contrast-enhanced dedicated breast CT: initial clinical experience.,” *Radiology*, vol. 256, no. 3, pp. 714–723, 2010.

[10] I. Sechopoulos, S. S. J. Feng, and C. J. D'Orsi, "Dosimetric characterization of a dedicated breast computed tomography clinical prototype.," *Med. Phys.*, vol. 37, no. 8, pp. 4110–4120, 2010.

[11] M. A. Helvie, "Digital Mammography Imaging: Breast Tomosynthesis and Advanced Applications," *Radiol. Clin. North Am.*, vol. 48, no. 5, pp. 917–929, 2010.

[12] D. Gur, G. S. Abrams, D. M. Chough, M. A. Ganott, C. M. Hakim, R. L. Perrin, G. Y. Rathfon, J. H. Sumkin, M. L. Zuley, and A. I. Bandos, "Digital breast tomosynthesis: Observer performance study," *Am. J. Roentgenol.*, vol. 193, no. 2, pp. 586–591, 2009.

[13] D. Gur, M. L. Zuley, M. I. Anello, G. Y. Rathfon, D. M. Chough, M. A. Ganott, C. M. Hakim, L. Wallace, A. Lu, and A. I. Bandos, "Dose Reduction in Digital Breast Tomosynthesis (DBT) Screening using Synthetically Reconstructed Projection Images. An Observer Performance Study.," *Acad. Radiol.*, vol. 19, no. 2, pp. 166–171, 2012.

[14] Y. Lu, H.-P. Chan, J. Wei, M. Goodsitt, P. L. Carson, L. Hadjiiski, A. Schmitz, J. W. Eberhard, and B. E. H. Claus, "Image quality of microcalcifications in digital breast tomosynthesis: effects of projection-view distributions.," *Med. Phys.*, vol. 38, no. 10, pp. 5703–12, 2011.

[15] M. M. Goodsitt, H.-P. Chan, A. Schmitz, S. Zelakiewicz, S. Telang, L. Hadjiiski, K. Watcharotone, M. a Helvie, C. Paramagul, C. Neal, E. Christodoulou, S. C. Larson, and P. L. Carson, "Digital breast tomosynthesis: studies of the effects of acquisition geometry on contrast-to-noise ratio and observer preference of low-contrast objects in breast phantom images.," *Phys. Med. Biol.*, vol. 59, no. 19, pp. 5883–902, 2014.

[16] H.-P. Chan, M. M. Goodsitt, M. a. Helvie, S. Zelakiewicz, A. Schmitz, M. Noroozian, C. Paramagul, M. a. Roubidoux, A. V. Nees, C. H. Neal, P. Carson, Y. Lu, L. Hadjiiski, and J. Wei, "Digital breast tomosynthesis: observer performance of clustered microcalcification detection on breast phantom images acquired with an experimental system using variable scan angles, angular increments, and number of projection views.," *Radiology*, vol. 273, no. 3, pp. 675–85, Dec. 2014.

[17] Y.-H. Hu and W. Zhao, “The effect of angular dose distribution on the detection of microcalcifications in digital breast tomosynthesis.,” *Med. Phys.*, vol. 38, no. 5, pp. 2455–2466, 2011.

[18] Y.-H. Hu, B. Zhao, and W. Zhao, “Image artifacts in digital breast tomosynthesis: investigation of the effects of system geometry and reconstruction parameters using a linear system approach.,” *Med. Phys.*, vol. 35, no. 2008, pp. 5242–5252, 2008.

[19] Y. Zhang, H.-P. Chan, B. Sahiner, Y.-T. Wu, C. Zhou, J. Ge, J. Wei, and L. M. Hadjiiski, “Application of boundary detection information in breast tomosynthesis reconstruction.,” *Med. Phys.*, vol. 34, no. 9, pp. 3603–13, 2007.

[20] T. Wu, R. H. Moore, E. a Rafferty, and D. B. Kopans, “A comparison of reconstruction algorithms for breast tomosynthesis.,” *Med. Phys.*, vol. 31, no. 9, pp. 2636–2647, 2004.

[21] E. Y. Sidky, X. Pan, I. S. Reiser, R. M. Nishikawa, R. H. Moore, and D. B. Kopans, “Enhanced imaging of microcalcifications in digital breast tomosynthesis through improved image-reconstruction algorithms.,” *Med. Phys.*, vol. 36, no. 11, pp. 4920–32, 2009.

[22] J. Zheng, J. A. Fessler, and H.-P. Chan, “Digital breast tomosynthesis reconstruction using spatially weighted non-convex regularization,” vol. 9783, p. 978369, 2016.

[23] I. Andersson, D. M. Ikeda, S. Zackrisson, M. Ruschin, T. Svahn, P. Timberg, and A. Tingberg, “Breast tomosynthesis and digital mammography: A comparison of breast cancer visibility and BIRADS classification in a population of cancers with subtle mammographic findings,” *Eur. Radiol.*, vol. 18, no. 12, pp. 2817–2825, 2008.

[24] E. a Rafferty, J. M. Park, L. E. Philpotts, S. P. Poplack, and J. H. Sumkin, “Digital Mammography and Breast Tomosynthesis Compared with Digital Mammography Alone : Results of a Multicenter, multireader trial,” *Radiology*, vol. 266, no. 1, pp. 104–113, 2013.

[25] P. Skaane, A. I. Bandos, R. Gullien, E. B. Eben, U. Ekseth, U. Haakenaasen, M. Izadi, I. N. Jebsen, G. Jahr, M. Krager, L. T. Niklason, S. Hofvind, and D. Gur,

"Comparison of Digital Mammography Alone and Digital Mammography Plus Tomosynthesis in a Population-based Screening Program," *Radiology*, vol. 267, no. 1, pp. 47–56, 2013.

[26] C. Ghetti, A. Borrini, O. Ortenzia, R. Rossi, and P. L. Ordóñez, "Physical characteristics of GE Senographe Essential and DS digital mammography detectors.," *Med. Phys.*, vol. 35, no. 2, pp. 456–463, 2008.

[27] S. S. J. Feng and I. Sechopoulos, "Clinical Digital Breast Tomosynthesis System: Dosimetric Characterization," *Radiology*, vol. 263, no. 1, pp. 35–42, 2012.

[28] B. Zhao and W. Zhao, "Imaging performance of an amorphous selenium digital mammography detector in a breast tomosynthesis system.," *Med. Phys.*, vol. 35, no. 5, pp. 1978–87, 2008.

[29] M. Spahn, "Flat detectors and their clinical applications," *Eur. Radiol.*, vol. 15, no. 9, pp. 1934–1947, 2005.

[30] NHSBSP Equipment Report, "Routine quality control tests for breast tomosynthesis (physicists) NHS Breast Screening Programme Equipment Report 1407," London, 2015.

[31] R. J. Acciavatti and A. D. A. Maidment, "Observation of super-resolution in digital breast tomosynthesis," *Med. Phys.*, vol. 39, no. 12, pp. 7518–7539, Nov. 2012.

[32] R. J. Acciavatti and A. D. A. Maidment, "Oblique reconstructions in tomosynthesis. II. Super-resolution," *Med. Phys.*, vol. 40, no. 11, p. 111912, Oct. 2013.

[33] J. T. Dobbins, "Tomosynthesis imaging: at a translational crossroads.," *Med. Phys.*, vol. 36, no. 6, pp. 1956–1967, 2009.

[34] E. Shaheen, N. Marshall, and H. Bosmans, "Investigation of the effect of tube motion in breast tomosynthesis: continuous or step and shoot?," in *Proceedings of SPIE 7961; Medical Imaging 2011: Physics of Medical Imaging*, 2011, vol. 7961, no. November 2015, p. 79611E.

[35] S. Kasap, J. B. Frey, G. Belev, O. Tousignant, H. Mani, J. Greenspan, L. Laperriere, O. Bubon, A. Reznik, G. DeCrescenzo, K. S. Karim, and J. A. Rowlands, "Amorphous and polycrystalline photoconductors for direct

conversion flat panel x-ray image sensors," *Sensors*, vol. 11, no. 5, pp. 5112–5157, 2011.

[36] M. J. Yaffe and J. A. Rowlands, "X-ray detectors for digital radiography," *Phys Med Biol*, vol. 42, no. 1, pp. 1–39, 1997.

[37] B. Zhao and W. Zhao, "Three-dimensional linear system analysis for breast tomosynthesis.," *Med. Phys.*, vol. 35, no. 12, pp. 5219–5232, 2008.

[38] B. Zhao, J. Zhou, Y.-H. Hu, T. Mertelmeier, J. Ludwig, and W. Zhao, "Experimental validation of a three-dimensional linear system model for breast tomosynthesis," *Med. Phys.*, vol. 36, no. 1, pp. 240–251, 2009.

[39] Y. Zhang, H.-P. Chan, B. Sahiner, J. Wei, M. M. Goodsitt, L. M. Hadjiiski, J. Ge, and C. Zhou, "A comparative study of limited-angle cone-beam reconstruction methods for breast tomosynthesis.," *Med. Phys.*, vol. 33, no. 10, pp. 3781–3795, 2006.

[40] R. L. Weisfield and N. R. Bennett, "E : 01234," vol. 4320, pp. 209–218, 2001.

[41] W. Zhao and J. A. Rowlands, "X-ray imaging using amorphous selenium: Feasibility of a flat panel self-scanned detector for digital radiology," *Med. Phys.*, vol. 22, no. 10, pp. 1595–1604, 1995.

[42] J. Yorkston and J. a Rowlands, "Flat Panel Detectors for Digital Radiography," in *Handbook of Medical Imaging*, J. Beutel, H. L. Kundel, and R. L. V. Mett, Eds. SPIE PRESS, 2000, pp. 225–328.

[43] C. Haugen, S. O. Kasap, and J. Rowlands, "Charge transport and electron-hole-pair creation energy in stabilized a-Se x-ray photoconductors," *J. Phys. D. Appl. Phys.*, vol. 32, no. 3, pp. 200–207, 1999.

[44] G. Belev and S. O. Kasap, "Amorphous selenium as an X-ray photoconductor," *J. Non. Cryst. Solids*, vol. 345–346, pp. 484–488, 2004.

[45] S. O. Kasap, "X-ray sensitivity of photoconductors: application to stabilized a-Se," *J. Phys. D. Appl. Phys.*, vol. 33, no. 21, pp. 2853–2865, 2000.

[46] Y. El-Mohri, L. E. Antonuk, Q. Zhao, Y. Wang, Y. Li, H. Du, and A. Sawant, "Performance of a high fill factor, indirect detection prototype flat-panel imager for mammography," *Med Phys*, vol. 34, no. 1, pp. 315–327, 2007.

[47] J. H. Siewerdsen, L. E. Antonuk, Y. el-Mohri, J. Yorkston, W. Huang, J. M.

Boudry, I. A. Cunningham, Y. ElMohri, J. Yorkston, W. Huang, J. M. Boudry, I. A. Cunningham, and Y. el-Mohri, “Empirical and theoretical investigation of the noise performance of indirect detection, active matrix flat-panel imagers (AMFPIs) for diagnostic radiology,” *Med. Phys.*, vol. 24, no. 1, pp. 71–89, 1997.

[48] S. Vedantham, A. Karellas, S. Suryanarayanan, D. Albagli, S. Han, E. J. Tkaczyk, C. E. Landberg, B. Opsahl-Ong, P. R. Granfors, I. Levis, C. J. D’Orsi, and R. E. Hendrick, “Full breast digital mammography with an amorphous silicon-based flat panel detector: physical characteristics of a clinical prototype.,” *Med. Phys.*, vol. 27, no. 3, pp. 558–567, 2000.

[49] C. Ronda, Ed., *Luminescence*. Weinheim, Germany: Wiley-VCH Verlag GmbH & Co. KGaA, 2007.

[50] W. Yen, S. Shionoya, and H. Yamamoto, Eds., *Phosphor Handbook*. CRC Press, 2006.

[51] B. K. Cha, J. H. Bae, C. h. Lee, H. Jeon, H. Kim, S. Chang, B. S. Kang, and G. Cho, “Improvement of the sensitivity and spatial resolution of pixelated CsI:Tl scintillator with reflective coating,” *Nucl. Instruments Methods Phys. Res. Sect. A Accel. Spectrometers, Detect. Assoc. Equip.*, vol. 607, no. 1, pp. 145–149, 2009.

[52] H. K. Kim, S. M. Yun, J. S. Ko, G. Cho, and T. Graeve, “Cascade modeling of pixelated scintillator detectors for X-ray imaging,” *IEEE Trans. Nucl. Sci.*, vol. 55, no. 3, pp. 1357–1366, 2008.

[53] K. S. Karim, A. Nathan, S. Member, and J. A. Rowlands, “Amorphous Silicon Active Pixel Sensor Readout Circuit for Digital Imaging,” *IEEE Trans. Electron Devices*, vol. 50, no. 1, pp. 200–208, 2003.

[54] E. R. Fossum, “CMOS image sensors: electronic camera-on-a-chip,” *IEEE Trans. Electron Devices*, vol. 44, no. 10, pp. 1689–1698, 1997.

[55] A. El Gamal and H. Eltoukhy, “CMOS Image Sensors,” *Circuits Devices Mag. IEEE*, vol. 21, no. 3, pp. 6–20, 2005.

[56] S. E. Bohndiek, A. Blue, J. Cabello, A. T. Clark, N. Guerrini, P. M. Evans, E. J. Harris, A. Konstantinidis, D. Maneuski, J. Osmond, V. O’Shea, R. D. Speller, R. Turchetta, K. Wells, H. Zin, and N. M. Allinson, “Characterization and Testing of LAS: A Prototype ‘Large Area Sensor’ With Performance Characteristics Suitable

for Medical Imaging Applications," *Nucl. Sci. IEEE Trans.*, vol. 56, no. 5, pp. 2938–2946, 2009.

[57] M. Esposito, T. Anaxagoras, A. Fant, K. Wells, A. Konstantinidis, J. P. F. Osmond, P. M. Evans, R. D. Speller, and N. M. Allinson, "DynAMITe: a wafer scale sensor for biomedical applications," *J. Instrum.*, vol. 6, no. 12, pp. C12064–C12064, 2011.

[58] M. Esposito, T. Anaxagoras, A. C. Konstantinidis, Y. Zheng, R. D. Speller, P. M. Evans, N. M. Allinson, and K. Wells, "Performance of a novel wafer scale CMOS active pixel sensor for bio-medical imaging.," *Phys. Med. Biol.*, vol. 59, no. 13, pp. 3533–54, Jul. 2014.

[59] A. C. Konstantinidis, M. B. Szafraniec, L. Rigon, G. Tromba, D. Dreossi, N. Sodini, P. F. Liaparinos, S. Naday, S. Gunn, A. McArthur, R. D. Speller, and A. Olivo, "X-ray performance evaluation of the dexela cmos aps x-ray detector using monochromatic synchrotron radiation in the mammographic energy range," *IEEE Trans. Nucl. Sci.*, vol. 60, no. 5, pp. 3969–3980, 2013.

[60] G. Zentai, "Comparison of CMOS and a-Si flat panel imagers for X-ray imaging," *2011 IEEE Int. Conf. Imaging Syst. Tech. IST 2011 - Proc.*, pp. 194–200, 2011.

[61] J.-G. Choi, H.-S. Park, Y. Kim, Y.-W. Choi, T.-H. Ham, and H.-J. Kim, "Characterization of prototype full-field breast tomosynthesis by using a CMOS array coupled with a columnar CsI(Tl) scintillator," *J. Korean Phys. Soc.*, vol. 60, no. 3, pp. 521–526, 2012.

[62] A. C. Konstantinidis, M. B. Szafraniec, R. D. Speller, and A. Olivo, "The Dexela 2923 CMOS X-ray detector: A flat panel detector based on CMOS active pixel sensors for medical imaging applications," *Nucl. Instruments Methods Phys. Res. Sect. A Accel. Spectrometers, Detect. Assoc. Equip.*, vol. 689, pp. 12–21, 2012.

[63] T. Patel, K. Klanian, Z. Gong, and M. B. Williams, "Detective quantum efficiency of a CsI-CMOS x-ray detector for breast tomosynthesis operating in high dynamic range and high sensitivity modes," in *International Workshop on Digital Mammography*, Springer Berlin Heidelberg, 2012, pp. 80–87.

[64] S. Naday, E. F. Bullard, S. Gunn, J. E. Brodrick, E. O. O'Tuairisg, A. McArthur, H. Amin, M. B. Williams, P. G. Judy, and A. Konstantinidis, "Optimised Breast

Tomosynthesis with a Novel CMOS Flat Panel Detector," in *International Workshop on Digital Mammography*, Springer Berlin Heidelberg, 2010, pp. 428–435.

[65] F. W. Wheeler, A. G. A. Perera, B. E. Claus, S. L. Muller, G. Peters, and J. P. Kaufhold, "Micro-calcification detection in digital tomosynthesis mammography," *Med. Imaging 2006 Image Process.*, vol. 6144, p. 614420+, 2006.

[66] H. S. Park, Y. S. Kim, H. J. Kim, Y. W. Choi, and J. G. Choi, "Optimization of configuration parameters in a newly developed digital breast tomosynthesis system," *J. Radiat. Res.*, vol. 55, no. 3, pp. 589–599, 2014.

[67] A. C. Konstantinidis, Y. Zheng, A. Olivo, K. Bliznakova, M. Yip, T. Anaxagoras, K. Wells, N. Allinson, and R. D. Speller, "Evaluation of a novel wafer-scale CMOS APS X-ray detector for use in mammography," *IEEE Nucl. Sci. Symp. Conf. Rec.*, pp. 3254–3260, 2012.

[68] C. Zhao, J. Kanicki, A. C. Konstantinidis, and T. Patel, "Large area CMOS active pixel sensor x-ray imager for digital breast tomosynthesis: Analysis, modeling, and characterization," *Med. Phys.*, vol. 42, no. 11, pp. 6294–6308, 2015.

[69] C. Zhao, A. C. Konstantinidis, Y. Zheng, T. Anaxagoras, R. D. Speller, and J. Kanicki, "50 μ m pixel pitch wafer-scale CMOS active pixel sensor x-ray detector for digital breast tomosynthesis," *Phys. Med. Biol.*, vol. 60, no. 23, pp. 8977–9001, Dec. 2015.

[70] J. Ohta, *Smart CMOS Image Sensors and Applications*, vol. 20073131. CRC Press, 2007.

[71] S. M. Sze and K. K. Ng, *Physics of Semiconductor Devices*. Hoboken, NJ, USA: John Wiley & Sons, Inc., 2006.

[72] K. Salama and A. E. Gamal, "Analysis of active pixel sensor readout circuit," *IEEE Trans. Circuits Syst. I Fundam. Theory Appl.*, vol. 50, no. 7, pp. 941–944, Jul. 2003.

[73] K. S. Karim and A. Nathan, "Readout circuit in active pixel sensors in amorphous silicon technology," *IEEE Electron Device Lett.*, vol. 22, no. 10, pp. 469–471, 2001.

[74] K. S. Karim, A. Nathan, and J. a. Rowlands, "Active pixel sensor architectures in

a-SiH for medical imaging," *J. Vac. Sci. Technol. A Vacuum, Surfaces, Film.*, vol. 20, no. 3, p. 1095, 2002.

[75] K. S. Karim, "Pixel Architectures for Digital Imaging using amorphous silicon technology," University of Waterloo, 2002.

[76] F. De Roose, S. Steudel, P. E. Malinowski, K. Myny, and A. Xhakoni, "Active Pixel Concepts for High-Resolution Large Area Imagers," pp. 139–141, 2015.

[77] K. S. Karim, A. Nathan, and J. A. Rowlands, "Active pixel sensor architectures for large area medical imaging," *J. Non. Cryst. Solids*, vol. 299–302, pp. 1250–1255, 2002.

[78] Y. El-Mohri, L. E. Antonuk, M. Koniczek, Q. Zhao, Y. Li, R. A. Street, and J. P. Lu, "Active pixel imagers incorporating pixel-level amplifiers based on polycrystalline-silicon thin-film transistors," *Med Phys*, vol. 36, no. 7, pp. 3340–3355, 2009.

[79] M. Koniczek, Y. El-Mohri, L. E. Antonuk, A. Liang, Q. Zhao, and H. Jiang, "Noise performance limits of advanced x-ray imagers employing poly-Si-based active pixel architectures," *Physics (College. Park. Md).*, vol. 7961, p. 79610P–79610P–10, 2011.

[80] L. E. Antonuk, Y. El-Mohri, Q. Zhao, M. Koniczek, A. Liang, H. Jiang, J. McDonald, R. a. Street, and J.-P. Lu, "Performance analysis of several generations of flat-panel x-ray imagers based on polycrystalline silicon TFTs," vol. 8668, p. 86680A, 2013.

[81] L. E. Antonuk, Y. El-Mohri, Q. Zhao, M. Koniczek, J. McDonald, M. Yeakey, Y. Wang, M. Behravan, R. a. Street, and J. Lu, "Exploration of the potential performance of polycrystalline silicon-based active matrix flat-panel imagers incorporating active pixel sensor architectures," *Proc. SPIE*, vol. 6913, p. 69130I–69130I–13, 2008.

[82] L. E. Antonuk, "Investigation of strategies to achieve optimal DQE performance from indirect-detection active-matrix flat-panel imagers (AMFPIs) through novel pixel amplification architectures (Invited Paper)," *Proc. SPIE*, vol. 5745, pp. 18–31, 2005.

[83] R. Zhang, L. Bie, T.-C. Fung, E. K.-H. Yu, C. Zhao, and J. Kanicki, "High

performance amorphous metal-oxide semiconductors thin-film passive and active pixel sensors," in *2013 IEEE International Electron Devices Meeting*, 2013, p. 27.3.1-27.3.4.

[84] C. Zhao and J. Kanicki, "Amorphous In-Ga-Zn-O thin-film transistor active pixel sensor x-ray imager for digital breast tomosynthesis.," *Med. Phys.*, vol. 41, no. 9, p. 91902, 2014.

[85] M. Cheng, C. Zhao, C. Huang, H. Kim, M. Nakata, and J. Kanicki, "Amorphous InSnZnO thin-film transistor voltage-mode active pixel sensor circuits for indirect x-ray imagers," *IEEE Trans. Electron Devices*, vol. 63, no. 12, pp. 4802–4810, Dec. 2016.

[86] S. Lee, J. H. Park, K. Jeon, S. Kim, Y. Jeon, D. H. Kim, D. M. Kim, J. C. Park, and C. J. Kim, "Modeling and characterization of metal-semiconductor-metal-based source-drain contacts in amorphous InGaZnO thin film transistors," *Appl. Phys. Lett.*, vol. 96, no. 11, pp. 2008–2011, 2010.

[87] T. C. Fung, K. Abe, H. Kumomi, and J. Kanicki, "Electrical instability of rf sputter amorphous In-Ga-Zn-O thin-film transistors," *IEEE/OSA J. Disp. Technol.*, vol. 5, no. 12, pp. 452–461, 2009.

[88] K. Nomura, H. Ohta, A. Takagi, T. Kamiya, M. Hirano, and H. Hosono, "Room-temperature fabrication of transparent flexible thin-film transistors using amorphous oxide semiconductors.," *Nature*, vol. 432, no. 7016, pp. 488–492, 2004.

[89] T. Arai, "Oxide-TFT technologies for next-generation AMOLED displays," *J. Soc. Inf. Disp.*, vol. 20, no. 3, p. 156, 2012.

[90] Y. Lee, E. K. Yu, D. Shim, H. Kong, L. Bie, and J. Kanicki, "Oxygen flow effects on electrical properties, stability, and density of states of amorphous In–Ga–Zn–O thin-film transistors," *Jpn. J. Appl. Phys.*, vol. 53, no. 12, p. 121101, 2014.

[91] K. Jang, J. Raja, Y. J. Lee, D. Kim, and J. Yi, "Effects of carrier concentration, indium content, and crystallinity on the electrical properties of indium-tin-zinc-oxide thin-film transistors," *IEEE Electron Device Lett.*, vol. 34, no. 9, pp. 1151–1153, 2013.

[92] J. Jang, D. G. Kim, D. M. Kim, S. J. Choi, J. H. Lim, J. H. Lee, Y. S. Kim, B. Du

Ahn, and D. H. Kim, “Investigation on the negative bias illumination stress-induced instability of amorphous indium-tin-zinc-oxide thin film transistors,” *Appl. Phys. Lett.*, vol. 105, no. 15, 2014.

[93] S. Tomai, M. Nishimura, M. Itose, M. Matuura, M. Kasami, S. Matsuzaki, H. Kawashima, F. Utsuno, and K. Yano, “High-Performance Thin Film Transistor with Amorphous In 2O 3-SnO 2-ZnO channel layer,” *Jpn. J. Appl. Phys.*, vol. 51, no. 3 PART 2, 2012.

[94] J. Raja, D. Kim, Y. Lee, J. Yi, J. Kim, and K. Jang, “High field-effect mobility amorphous InSnZnO thin-film transistors with low carrier concentration and oxygen vacancy,” *Electron. Lett.*, vol. 49, no. 16, pp. 1030–1031, 2013.

[95] C. Zhao, N. Vassiljev, A. Konstantinidis, R. Speller, and J. Kanicki, “Three-dimensional cascaded system analysis of a 50 μm pixel pitch wafer-scale CMOS active pixel sensor x-ray detector for digital breast tomosynthesis,” *Phys. Med. Biol.*, vol. 62, pp. 1994–2017, 2017.

[96] C. Zhao and J. Kanicki, “Task-based modeling of a ultra high-resolution medical imaging system for digital breast tomosynthesis,” *IEEE Trans. Med. Imaging* (submitted).

[97] M. Nakata, C. Zhao, and J. Kanicki, “DC sputtered amorphous In–Sn–Zn–O thin-film transistors: Electrical properties and stability,” *Solid-State Electronics*, vol. 116, pp. 22–29, Feb. 2016.

[98] M. Cheng, C. Zhao, and J. Kanicki, “Study of current-mode active pixel sensor circuits using amorphous InSnZnO thin-film transistor for 50-μm pixel-pitch indirect X-ray imagers,” *Solid-State Electronics*, vol. 131, pp. 53–64, May 2017.

[99] C. Zhao, T. C. Fung, and J. Kanicki, “Half-Corbino short-channel amorphous In-Ga-Zn-O thin-film transistors with a-SiOx or a-SiOx/a-SiNx passivation layers,” *Solid-State Electronics*, vol. 120, pp. 25–31, 2016.

[100] J. M. Boone, “Spectral modeling and compilation of quantum fluence in radiography and mammography,” *Med. Imaging ’98*, vol. 3336, no. February, pp. 592–601, 1998.

[101] E. Samei, M. J. Flynn, and D. a Reimann, “A method for measuring the presampled MTF of digital radiographic systems using an edge test device.,” *Med.*

Phys., vol. 25, no. 1, pp. 102–113, 1998.

[102] A. C. Konstantinidis, "Evaluation of digital x-ray detectors for medical imaging applications," University College London, 2011.

[103] A. C. Konstantinidis, A. Olivo, and R. D. Speller, "Technical Note: modification of the standard gain correction algorithm to compensate for the number of used reference flat frames in detector performance studies.," *Med. Phys.*, vol. 38, no. 12, pp. 6683–7, 2011.

[104] IEC 62220-1-2:, *Medical Electrical Equipment: Characteristics of Digital X-ray Imaging Devices. Determination of the Detective Quantum Efficiency--Detectors Used in Mammography*. Geneva: International Electrotechnical Commission, 2007.

[105] B. Pain and B. R. Hancock, "Accurate estimation of conversion gain and quantum efficiency in CMOS imagers," *Proc. SPIE*, vol. 5017, p. 94, 2003.

[106] S. E. Bohndiek, A. Blue, A. T. Clark, M. L. Prydderch, R. Turchetta, G. J. Royle, and R. D. Speller, "Comparison of Methods for Estimating the Conversion Gain of CMOS Active Pixel Sensors," vol. 8, no. 10, pp. 1734–1744, 2008.

[107] I. A. Cunningham and R. Shaw, "Signal-to-noise optimization of medical imaging systems," *J. Opt. Soc. Am. A*, vol. 16, no. 3, p. 621, 1999.

[108] L. E. Antonuk, K. W. Jee, Y. El-Mohri, M. Maolinbay, S. Nassif, X. Rong, Q. Zhao, J. H. Siewerdsen, R. a Street, and K. S. Shah, "Strategies to improve the signal and noise performance of active matrix, flat-panel imagers for diagnostic x-ray applications.," *Med. Phys.*, vol. 27, no. 2, pp. 289–306, 2000.

[109] S. Vedantham, A. Karellas, and S. Suryanarayanan, "Solid-state fluoroscopic imager for high-resolution angiography: Parallel-cascaded linear systems analysis," *Med. Phys.*, vol. 31, no. 5, pp. 1258–1268, 2004.

[110] R. L. Van Metter, J. Beutel, and H. L. Kundel, Eds., *Handbook of Medical Imaging, Volume 1. Physics and Psychophysics*. 1000 20th Street, Bellingham, WA 98227-0010 USA: SPIE, 2000.

[111] P. A. Rodnyi, P. Dorenbos, and C. W. E. van Eijk, "Energy Loss in Inorganic Scintillators," *Phys. Status Solidi*, vol. 187, no. 1, pp. 15–29, 1995.

[112] M. Nikl, "Scintillation detectors for x-rays," *Meas. Sci. Technol.*, vol. 17, no. 4,

pp. R37–R54, 2006.

[113] I. Holl, E. Lorenz, and G. Mageras, “Measurement of the Light Yield of Common Inorganic Scintillators.,” *IEEE Trans. Nucl. Sci.*, vol. 35, no. 1, 1987.

[114] W. Hillen, W. . Eckenbach, P. Quadflieg, and T. T. Zaengel, “Signal-to-noise performance in cesium iodide x-ray fluorescent screens,” in *SPIE Medical Imaging V: Image Physics*, 1991, vol. 1443, pp. 120–131.

[115] W. Zhao, G. Ristic, and J. a Rowlands, “X-ray imaging performance of structured cesium iodide scintillators.,” *Med. Phys.*, vol. 31, no. 9, pp. 2594–2605, 2004.

[116] D. Sharma, A. Badal, and A. Badano, “hybridMANTIS: a CPU-GPU Monte Carlo method for modeling indirect x-ray detectors with columnar scintillators.,” *Phys. Med. Biol.*, vol. 57, no. 8, pp. 2357–72, Apr. 2012.

[117] S. Hejazi and D. P. Trauernicht, “System considerations in CCD-based x-ray imaging for digital chest radiography and digital mammography.,” *Med. Phys.*, vol. 24, no. 2, pp. 287–97, 1997.

[118] A. Jain, D. R. Bednarek, C. Ionita, and S. Rudin, “A theoretical and experimental evaluation of the microangiographic fluoroscope: A high-resolution region-of-interest x-ray imager,” *Med. Phys.*, vol. 38, no. 7, p. 4112, 2011.

[119] D. J. Tward and J. H. Siewerdsen, “Cascaded systems analysis of the 3D noise transfer characteristics of flat-panel cone-beam CT,” *Med. Phys.*, vol. 35, no. 12, p. 5510, 2008.

[120] H. Tian, B. Fowler, and A. El Gamal, “Analysis of temporal noise in CMOS photodiode active pixel sensor,” *IEEE J. Solid-State Circuits*, vol. 36, no. 1, pp. 92–101, 2001.

[121] J. Janesick, J. Pinter, R. Potter, T. Elliott, J. Andrews, J. Tower, M. Grygon, and D. Keller, “Fundamental performance differences between CMOS and CCD imagers, part III,” vol. 7439, p. 77420B–77420B–30, 2010.

[122] I. Sechopoulos, “A review of breast tomosynthesis. Part II. Image reconstruction, processing and analysis, and advanced applications.,” *Med. Phys.*, vol. 40, no. 1, p. 14302, 2013.

[123] Y.-H. Hu and W. Zhao, “The effect of amorphous selenium detector thickness on dual-energy digital breast imaging,” *Med. Phys.*, vol. 41, no. 11, p. 111904, 2014.

[124] J. H. Siewerdsen and D. A. Jaffray, “Three-dimensional NEQ transfer characteristics of volume CT using direct- and indirect-detection flat-panel imagers,” *SPIE Med. Imaging 2003*, vol. 5030, pp. 92–102, 2003.

[125] G. J. Gang, J. Lee, J. W. Stayman, D. J. Tward, W. Zbijewski, J. L. Prince, and J. H. Siewerdsen, “Analysis of Fourier-domain task-based detectability index in tomosynthesis and cone-beam CT in relation to human observer performance.,” *Med. Phys.*, vol. 38, no. 4, pp. 1754–1768, 2011.

[126] J. G. Mainprize, A. K. Bloomquist, M. P. Kempston, and M. J. Yaffe, “Resolution at oblique incidence angles of a flat panel imager for breast tomosynthesis.,” *Med. Phys.*, vol. 33, no. 9, pp. 3159–3164, 2006.

[127] J. Zhou, B. Zhao, and W. Zhao, “A computer simulation platform for the optimization of a breast tomosynthesis system.,” *Med. Phys.*, vol. 34, no. January, pp. 1098–1109, 2007.

[128] J. M. Boone, “Normalized glandular dose (DgN) coefficients for arbitrary X-ray spectra in mammography: computer-fit values of Monte Carlo derived data.,” *Med. Phys.*, vol. 29, no. 5, pp. 869–875, 2002.

[129] X. Wu, E. L. Gingold, G. T. Barnes, and D. M. Tucker, “Normalized average glandular dose in molybdenum target-rhodium filter and rhodium target-rhodium filter mammography.,” *Radiology*, vol. 193, pp. 83–89, 1994.

[130] D. R. Dance, C. L. Skinner, K. C. Young, J. R. Beckett, and C. J. Kotre, “Additional factors for the estimation of mean glandular breast dose using the UK mammography dosimetry protocol.,” *Phys. Med. Biol.*, vol. 45, no. 11, pp. 3225–3240, 2000.

[131] D. R. Dance, “Monte Carlo calculation of conversion factors for the estimation of mean glandular breast dose.,” *Phys. Med. Biol.*, vol. 35, no. 9, pp. 1211–1219, 1990.

[132] I. Sechopoulos, S. Suryanarayanan, S. Vedantham, C. D’Orsi, and A. Karellas, “Computation of the glandular radiation dose in digital tomosynthesis of the breast.,” *Med. Phys.*, vol. 34, no. 2007, pp. 221–232, 2007.

[133] D. Scheffer, “A Wafer scale active pixel CMOS image sensor for generic x-ray radiology,” *Proc. SPIE*, vol. 6510, p. 65100O–65100O–9, 2007.

[134] A. Konstantinidis, T. Anaxagoras, M. Esposito, N. Allinson, and R. Speller, “DynAMITe: a prototype large area CMOS APS for breast cancer diagnosis using x-ray diffraction measurements,” in *Proc. SPIE*, 2012, vol. 8313, p. 83135H.

[135] O. Yadid-Pecht and R. Etienne-Cummings, Eds., *CMOS Imagers*. Boston: Kluwer Academic Publishers, 2004.

[136] E. S. Eid, T. Y. Chan, E. R. Fossum, R. H. Tsai, R. Spagnuolo, J. Deily, W. B. Byers, and J. C. Peden, “Design and characterization of ionizing radiation-tolerant CMOS APS image sensors up to 30 Mrd (Si) total dose,” *IEEE Trans. Nucl. Sci.*, vol. 48, no. 6 I, pp. 1796–1806, 2001.

[137] R. C. Lacoe, “Improving Integrated Circuit Performance Through the Application of Hardness-by-Design Methodology,” *IEEE Trans. Nucl. Sci.*, vol. 55, no. 4, pp. 1903–1925, Aug. 2008.

[138] M. Esposito, T. Anaxagoras, O. Diaz, K. Wells, and N. M. Allinson, “Radiation hardness of a large area CMOS active pixel sensor for bio-medical applications,” in *2012 IEEE Nuclear Science Symposium and Medical Imaging Conference Record (NSS/MIC)*, 2012, vol. N14, pp. 1300–1304.

[139] J. H. Siewerdsen, A. M. Waese, D. J. Moseley, S. Richard, and D. a Jaffray, “Spektr: A computational tool for x-ray spectral analysis and imaging system optimization,” *Med. Phys.*, vol. 31, no. 11, pp. 3057–3067, 2004.

[140] M. Bissonnette, M. Hansroul, E. Masson, S. Savard, S. Cadieux, P. Warmoes, D. Gravel, J. Agopan, B. Polischuk, W. Haerer, T. Mertelmeier, J. Y. Lo, Y. Chen, J. T. Dobbins III, J. L. Jesneck, and S. Singh, “Digital breast tomosynthesis using an amorphous selenium flat panel detector,” *SPIE Med. Imaging Phys. Med. Imaging*, vol. 5745, pp. 529–540, 2005.

[141] H. Tian, B. Fowler, and A. El Gamal, “Analysis of temporal noise in CMOS APS,” *Proc. SPIE IS&T Electron. Imaging*, vol. 3649, no. 1, pp. 177–185, 1999.

[142] A. Parsafar, C. C. Scott, A. El-Falou, P. M. Levine, and K. S. Karim, “Direct-conversion CMOS X-ray imager with with 5.6 μm × 6.25 μm pixels,” *IEEE Electron Device Lett.*, vol. 36, no. 5, pp. 481–483, 2015.

[143] H. Tian and A. El Gamal, “Analysis of 1 / f noise in CMOS APS,” in *Proc. SPIE*, 2000, vol. 3965, no. 1, pp. 1–9.

[144] T. Lulé, S. Benthien, H. Keller, F. Mütze, P. Rieve, K. Seibel, M. Sommer, and M. Böhm, “Sensitivity of CMOS based imagers and scaling perspectives,” *IEEE Trans. Electron Devices*, vol. 47, no. 11, pp. 2110–2122, 2000.

[145] R. Guidash, T. Lee, P. P. K. Lee, D. H. Sackett, C. I. Drowley, M. S. Swenson, L. Arbaugh, R. Hollstein, F. Shapiro, and S. Domer, “A 0.6 μm CMOS pinned photodiode color imager technology,” *Int. Electron Devices Meet. IEDM Tech. Dig.*, vol. 3019, no. 1996, pp. 927–929, 1997.

[146] G. J. Gang, W. Zbijewski, J. Webster Stayman, and J. H. Siewerdsen, “Cascaded systems analysis of noise and detectability in dual-energy cone-beam CT,” *Med. Phys.*, vol. 39, no. 8, p. 5145, 2012.

[147] G. Hajdok and I. A. Cunningham, “Penalty on the detective quantum efficiency from off-axis incident x rays,” in *SPIE Medical Imaging*, 2004, vol. 5368, p. 109.

[148] H. Fujita, D.-Y. Tsai, T. Itoh, K. Doi, J. Morishita, K. Ueda, and A. Ohtsuka, “A simple method for determining the modulation transfer function in digital radiography,” *IEEE Trans. Med. Imaging*, vol. 11, no. 1, pp. 34–39, 1992.

[149] C. R. Crawford, “CT filtration aliasing artifacts,” *IEEE Trans. Med. Imaging*, vol. 10, no. 1, pp. 99–102, 1991.

[150] I. Sechopoulos, J. M. Sabol, J. Berglund, W. E. Bolch, L. Brateman, E. Christodoulou, M. Flynn, W. Geiser, M. Goodsitt, a K. Jones, J. Y. Lo, A. D. a Maidment, K. Nishino, A. Nosratieh, B. Ren, W. P. Segars, and M. Von Tiedemann, “Radiation dosimetry in digital breast tomosynthesis: report of AAPM Tomosynthesis Subcommittee Task Group 223.,” *Med. Phys.*, vol. 41, no. 9, p. 91501, 2014.

[151] B. Ren, C. Ruth, J. Stein, A. Smith, I. Shaw, and Z. Jing, “Design and performance of the prototype full field breast tomosynthesis system with selenium based flat panel detector,” *Proc. SPIE Med. Imaging*, vol. 5745, pp. 550–561, 2005.

[152] V. V. Nagarkar, S. V. Tipnis, V. B. Gaysinskiy, S. R. Miller, A. Karellas, and S. Vedantham, “New design of a structured CsI(Tl) screen for digital mammography,” in *Medical Imaging 2003: Physics of Medical Imaging*, 2003, vol. 5030, p. 541.

[153] S. R. Miller, V. Gaysinskiy, I. Shestakova, and V. V. Nagarkar, “Recent Advances in Columnar CsI(Tl) Scintillator Screens,” *Proc. SPIE*, vol. 5923, p. 59230F1-59230F10, 2005.

[154] H. K. Kim, I. A. Cunningham, Z. Yin, and G. Cho, “On the Development of Digital Radiography Detectors : A Review,” *Precis. Eng.*, vol. 9, no. 4, pp. 86–100, 2008.

[155] B. K. Cha, B.-J. Kim, G. Cho, S. C. Jeon, J. H. Bae, Y. K. Chi, G.-H. Lim, and Y.-H. Kim, “A Pixelated CsI (Tl) Scintillator for CMOS-based X-ray Image Sensor,” in *2006 IEEE Nuclear Science Symposium Conference Record*, 2006, pp. 1139–1143.

[156] B. K. Cha, J. H. Bae, B. J. Kim, H. Jeon, and G. Cho, “Performance studies of a monolithic scintillator-CMOS image sensor for X-ray application,” *Nucl. Instruments Methods Phys. Res. Sect. A Accel. Spectrometers, Detect. Assoc. Equip.*, vol. 591, no. 1, pp. 113–116, 2008.

[157] M. Simon, K. J. Engel, B. Menser, X. Badel, and J. Linnros, “X-ray imaging performance of scintillator-filled silicon pore arrays,” *Med Phys*, vol. 35, no. 3, pp. 968–981, 2008.

[158] C. C. Scott, S. Abbaszadeh, S. Ghanbarzadeh, G. Allan, M. Farrier, I. a. Cunningham, and K. S. Karim, “Amorphous selenium direct detection CMOS digital x-ray imager with 25 micron pixel pitch,” in *Proc.SPIE Medical Imaging*, 2014, vol. 9033, no. February, p. 90331G.

[159] J. H. Siewerdsen and D. A. Jaffray, “Optimization of x-ray imaging geometry (with specific application to flat-panel cone-beam computed tomography),” *Med. Phys.*, vol. 27, no. 8, p. 1903, 2000.

[160] S. Richard, J. H. Siewerdsen, D. A. Jaffray, D. J. Moseley, and B. Bakhtiar, “Generalized DQE analysis of dual-energy imaging using flat-panel detectors,” *Med Phys*, vol. 5745, no. 5, pp. 1397–1413, 2005.

[161] Y.-S. Kim, H.-S. Park, S.-J. Park, S. Choi, H. Lee, D. Lee, Y.-W. Choi, and H.-J. Kim, “Characterizing X-ray detectors for prototype digital breast tomosynthesis systems,” *J. Instrum.*, vol. 11, no. 3, pp. P03022–P03022, Mar. 2016.

[162] H. H. Barrett, J. Yao, J. Rolland, and K. . Myers, “Model observers for

assessment of image quality," in *National Academy of Sciences USA*, 1993, vol. 90, pp. 9758–9765.

[163] H. H. Barrett, C. K. Abbey, and E. Clarkson, "Objective assessment of image quality III . ROC and likelihood-generating functions," *J. Opt. Soc. Am. A*, vol. 15, no. 6, pp. 1520–1535, 1998.

[164] A. E. Burgess, X. Li, and C. K. Abbey, "Visual signal detectability with two noise components: anomalous masking effects," *J. Opt. Soc. Am. A*, vol. 14, no. 9, p. 2420, Sep. 1997.

[165] I. Reiser and R. M. Nishikawa, "Task-based assessment of breast tomosynthesis: effect of acquisition parameters and quantum noise.," *Med. Phys.*, vol. 37, no. 4, pp. 1591–600, 2010.

[166] E. Samei and S. Richard, "Assessment of the dose reduction potential of a model-based iterative reconstruction algorithm using a task-based performance metrology," *Med. Phys.*, vol. 42, no. 1, pp. 314–323, 2015.

[167] L. C. Ikejimba, N. Kiarashi, S. V. Ghate, E. Samei, and J. Y. Lo, "Task-based strategy for optimized contrast enhanced breast imaging: analysis of six imaging techniques for mammography and tomosynthesis.," *Med. Phys.*, vol. 41, no. 6, p. 61908, 2014.

[168] J. Xu, A. Sisniega, W. Zbijewski, H. Dang, J. W. Stayman, X. Wang, D. H. Foos, N. Aygun, V. E. Koliatsos, and J. H. Siewerdsen, "Modeling and design of a cone-beam CT head scanner using task-based imaging performance optimization," *Phys. Med. Biol.*, vol. 61, no. 8, pp. 3180–3207, 2016.

[169] S. Richard and J. H. Siewerdsen, "Comparison of model and human observer performance for detection and discrimination tasks using dual-energy x-ray images.," *Med. Phys.*, vol. 35, no. 11, pp. 5043–5053, 2008.

[170] S. Young, P. R. Bakic, K. J. Myers, R. J. Jennings, and S. Park, "A virtual trial framework for quantifying the detectability of masses in breast tomosynthesis projection data.," *Med. Phys.*, vol. 40, no. 5, p. 51914, 2013.

[171] S. Park, G. Zhang, and K. J. Myers, "Comparison of Channel Methods and Observer Models for the Task-Based Assessment of Multi-Projection Imaging in the Presence of Structured Anatomical Noise," *IEEE Trans. Med. Imaging*, vol.

35, no. 6, pp. 1431–1442, 2016.

[172] K. Michielsen, J. Nuyts, L. Cockmartin, N. Marshall, and H. Bosmans, “Design of a model observer to evaluate calcification detectability in breast tomosynthesis and application to smoothing prior optimization,” *Med. Phys.*, vol. 43, no. 12, pp. 6577–6587, 2016.

[173] A. S. Chawla, J. Y. Lo, J. A. Baker, and E. Samei, “Optimized image acquisition for breast tomosynthesis in projection and reconstruction space.,” *Med. Phys.*, vol. 36, no. 11, pp. 4859–69, 2009.

[174] L. Cockmartin, N. W. Marshall, and H. Bosmans, “Comparison of SNDR, NPWE model and human observer results for spherical densities and microcalcifications in real patient backgrounds for 2D digital mammography and breast tomosynthesis,” *Lect. Notes Comput. Sci. (including Subser. Lect. Notes Artif. Intell. Lect. Notes Bioinformatics)*, vol. 8539 LNCS, pp. 134–141, 2014.

[175] I. Diaz, P. Timberg, S. Zhang, C. K. Abbey, F. R. Verdun, and F. O. Bochud, “Development of model observers applied to 3D breast tomosynthesis microcalcifications and masses,” *SPIE Med. Imaging Image Perception, Obs. Performance, Technol. Assess.*, vol. 7966, p. 79660F, 2011.

[176] L. Korthout, D. Verbugt, J. Timpert, a Mierop, W. de Haan, W. Maes, J. de Meulmeester, W. Muhammad, B. Dillen, H. Stoldt, Others, W. De Haan, J. De Meulmeester, I. Peters, and E. Fox, “A wafer-scale CMOS APS imager for medical X-ray applications,” *Proc. 2009 Int. Image Sens. Work. Pap.*, vol. 70, pp. 22–28, 2009.

[177] P. G. J. Barten, “Formula for the contrast sensitivity of the human eye,” *Conf. Image Qual. Syst. Perform.*, vol. 5294, pp. 231–238, 2004.

[178] S. Richard and J. H. Siewerdsen, “Optimization of dual-energy imaging systems using generalized NEQ and imaging task,” *Med. Phys.*, vol. 34, no. 1, pp. 127–139, 2007.

[179] DICOM Standard, “DICOM PS3.14 2016c - Grayscale Standard Display Function,” 2016.

[180] A. Burgess, “Mammographic structure: Data preparation and spatial statistics analysis,” *Proc. SPIE*, vol. 3661, no. February, pp. 642–653, 1999.

[181] G. J. Gang, D. J. Tward, J. Lee, and J. H. Siewerdsen, “Anatomical background and generalized detectability in tomosynthesis and cone-beam CT,” *Med. Phys.*, vol. 37, no. 5, pp. 1948–1965, 2010.

[182] P. G. J. Barten, “Physical model for the contrast sensitivity of the human eye,” 1992, vol. 1666, p. 57.

[183] P. G. J. Barten, “Spatiotemporal model for the contrast sensitivity of the human eye and its temporal aspects,” 1993, vol. 2, no. 4, pp. 2–14.

[184] J. H. Hubbel and S. M. Seltzer, “Tables of x-ray mass attenuation coefficient and mass energy-absorption coefficients 1 keV to 20 MeV for elements Z=1 to 92 and 48 additional substances of dosimetric interest,” 1995.

[185] H. Jiang, Q. Zhao, L. E. Antonuk, Y. El-Mohri, and T. Gupta, “Development of active matrix flat panel imagers incorporating thin layers of polycrystalline HgI(2) for mammographic x-ray imaging.,” *Phys. Med. Biol.*, vol. 58, no. 3, pp. 703–714, 2013.

[186] M. J. Michell, A. Iqbal, R. K. Wasan, D. R. Evans, C. Peacock, C. P. Lawinski, A. Douiri, R. Wilson, and P. Whelehan, “A comparison of the accuracy of film-screen mammography, full-field digital mammography, and digital breast tomosynthesis,” *Clin. Radiol.*, vol. 67, no. 10, pp. 976–981, 2012.

[187] C. Michail, I. Valais, I. Seferis, N. Kalyvas, G. Fountos, and I. Kandarakis, “Experimental measurement of a high resolution CMOS detector coupled to CsI scintillators under X-ray radiation,” *Radiat. Meas.*, vol. 74, pp. 39–46, 2015.

[188] I. M. Peters, C. Smit, J. J. Miller, and A. Lomako, “High dynamic range CMOS-based mammography detector for FFDM and DBT,” in *SPIE Medical Imaging. International Society for Optics and Photonics*, 2016, vol. 9783, p. 978316.

[189] A. E. Burgess, F. L. Jacobson, and P. F. Judy, “Human observer detection experiments with mammograms and power-law noise,” *Med. Phys.*, vol. 28, no. 4, pp. 419–437, 2001.

[190] P. C. Johns and M. J. Yaffe, “X-ray characterisation of normal and neoplastic breast tissues,” *Phys. Med. Biol.*, vol. 32, no. 6, pp. 675–695, Jun. 1987.

[191] B. J. Pollard, E. Samei, A. S. Chawla, C. Beam, L. E. Heyneman, L. M. H.

Koweek, S. Martinez-Jimenez, L. Washington, N. Hashimoto, and H. P. McAdams, “The Effects of Ambient Lighting in Chest Radiology Reading Rooms,” *J. Digit. Imaging*, vol. 25, no. 4, pp. 520–526, Aug. 2012.

[192] N. Perry, M. Broeders, C. de Wolf, S. Törnberg, R. Holland, and L. von Karsa, *European guidelines for quality assurance in breast cancer screening and diagnosis.*, vol. 19, no. 4. 2008.

[193] R. A. Street, “Hydrogenated amorphous silicon,” *Cambridge Univ. Press*, no. 2, pp. 62–91, 1991.

[194] G. Baek, K. Abe, A. Kuo, H. Kumomi, and J. Kanicki, “Electrical properties and stability of dual-gate coplanar homojunction DC sputtered amorphous indium-gallium-zinc-oxide thin-film transistors and its application to AM-OLEDs,” *IEEE Trans. Electron Devices*, vol. 58, no. 12, pp. 4344–4353, 2011.

[195] T. C. Fung, G. Baek, and J. Kanicki, “Low frequency noise in long channel amorphous In-Ga-Zn-O thin film transistors,” *J. Appl. Phys.*, vol. 108, no. 7, pp. 1–10, 2010.

[196] J. S. Park, T. W. Kim, D. Stryakhilev, J. S. Lee, S. G. An, Y. S. Pyo, D. B. Lee, Y. G. Mo, D. U. Jin, and H. K. Chung, “Flexible full color organic light-emitting diode display on polyimide plastic substrate driven by amorphous indium gallium zinc oxide thin-film transistors,” *Appl. Phys. Lett.*, vol. 95, no. 1, 2009.

[197] J. K. Jeong, H. Won Yang, J. H. Jeong, Y. G. Mo, and H. D. Kim, “Origin of threshold voltage instability in indium-gallium-zinc oxide thin film transistors,” *Appl. Phys. Lett.*, vol. 93, no. 12, pp. 1–4, 2008.

[198] S. C. Kim, Y. S. Kim, E. K.-H. Yu, and J. Kanicki, “Short channel amorphous In–Ga–Zn–O thin-film transistor arrays for ultra-high definition active matrix liquid crystal displays: Electrical properties and stability,” *Solid. State. Electron.*, vol. 111, pp. 67–75, 2015.

[199] T. C. Fung, C. S. Chuang, C. Chen, K. Abe, R. Cottle, M. Townsend, H. Kumomi, and J. Kanicki, “Two-dimensional numerical simulation of radio frequency sputter amorphous In-Ga-Zn-O thin-film transistors,” *J. Appl. Phys.*, vol. 106, no. 8, 2009.

[200] K. Abe, A. Sato, K. Takahashi, H. Kumomi, T. Kamiya, and H. Hosono, “Mobility- and temperature-dependent device model for amorphous In-Ga-Zn-O thin-film transistors,” *Thin Solid Films*, vol. 559, pp. 40–43, 2014.

[201] M. Mativenga, S. H. Ha, D. Geng, D. H. Kang, R. K. Mruthyunjaya, G. N. Heiler, T. J. Tredwell, and J. Jang, “Infinite output resistance of corbino thin-film transistors with an amorphous-In ga znO active layer for large-area AMOLED displays,” *IEEE Trans. Electron Devices*, vol. 61, no. 9, pp. 3199–3205, 2014.

[202] K. Nomura, T. Kamiya, M. Hirano, and H. Hosono, “Origins of threshold voltage shifts in room-temperature deposited and annealed a-In-Ga-Zn-O thin-film transistors,” *Appl. Phys. Lett.*, vol. 95, no. 1, pp. 2007–2010, 2009.

[203] T. Arai and T. Sasaoka, “49.1: Invited Paper: Emergent Oxide TFT Technologies for Next-Generation AM-OLED Displays,” *SID Symp. Dig. Tech. Pap.*, vol. 42, no. 1, pp. 710–713, 2011.

[204] T. Arai and Y. Shiraishi, “56.1: Invited Paper : Manufacturing Issues for Oxide TFT Technologies for Large-Sized AMOLED Displays,” *SID Symp. Dig. Tech. Pap.*, vol. 43, no. 1, pp. 756–759, 2012.

[205] T. Shih, H. Ting, P. Lin, C. Chen, L. Tsai, C. Chen, L. Lin, C. Liu, C. Chen, H. Lin, L. Chang, Y. Lin, and H. Hong, “Development of Oxide-TFT OLED-TV Technologies,” pp. 766–769, 2014.

[206] E. Fukumoto, T. Arai, N. Morosawa, K. Tokunaga, Y. Terai, T. Fujimori, and T. Sasaoka, “High-mobility oxide TFT for circuit integration of AMOLEDs,” *J. Soc. Inf. Disp.*, vol. 19, p. 867, 2011.

[207] R. A. Lujan and R. A. Street, “Flexible X-ray detector array fabricated with oxide thin-film transistors,” *IEEE Electron Device Lett.*, vol. 33, no. 5, pp. 688–690, 2012.

[208] D. Wang, C. Li, M. Furuta, S. Tomai, M. Sunagawa, M. Nishimura, E. Kawashima, M. Kasami, and K. Yano, “Influence of Active Layer Thickness on Performance and Reliability of InSnZnO Thin-Film Transistors,” in *19th International Workshop on AM-FPD*, 2012, pp. 159–162.

[209] W.-H. Tseng, S.-W. Fang, C.-Y. Lu, H.-Y. Chuang, F.-W. Chang, G.-Y. Lin, T.-W. Chen, K.-H. Ma, H.-S. Chen, T.-K. Chen, Y.-H. Chen, J.-Y. Lee, T.-H. Shih, H.-C.

Ting, C.-Y. Chen, Y.-H. Lin, and H.-J. Hong, “The effect of nitrous oxide plasma treatment on the bias temperature stress of metal oxide thin film transistors with high mobility,” *Solid. State. Electron.*, vol. 103, pp. 5–9, 2014.

[210] M. K. Ryu, S. Yang, S. H. K. Park, C. S. Hwang, and J. K. Jeong, “High performance thin film transistor with cosputtered amorphous Zn-In-Sn-O channel: Combinatorial approach,” *Appl. Phys. Lett.*, vol. 95, no. 7, pp. 1–4, 2009.

[211] M. K. Ryu, S. Yang, S. H. K. Park, C. S. Hwang, and J. K. Jeong, “Impact of Sn/Zn ratio on the gate bias and temperature-induced instability of Zn-In-Sn-O thin film transistors,” *Appl. Phys. Lett.*, vol. 95, no. 17, pp. 7–10, 2009.

[212] J.-Y. Noh, H. Kim, H.-H. Nahm, Y.-S. Kim, D. Hwan Kim, B.-D. Ahn, J.-H. Lim, G. Hee Kim, J.-H. Lee, and J. Song, “Cation composition effects on electronic structures of In-Sn-Zn-O amorphous semiconductors,” *J. Appl. Phys.*, vol. 113, no. 18, p. 183706, 2013.

[213] C. Hyun, M. S. Shur, M. Hack, Z. Yaniv, and V. Cannella, “Above threshold characteristics of amorphous silicon alloy thin-film transistors,” *Appl. Phys. Lett.*, vol. 45, no. 11, pp. 1202–1203, 1984.

[214] A. Kuo, T. K. Won, and J. Kanicki, “Advanced Multilayer Amorphous Silicon Thin-Film Transistor Structure: Film Thickness Effect on Its Electrical Performance and Contact Resistance,” *Jpn. J. Appl. Phys.*, vol. 47, no. 5, pp. 3362–3367, 2008.

[215] A. Rolland, “Electrical Properties of Amorphous Silicon Transistors and MIS-Devices: Comparative Study of Top Nitride and Bottom Nitride Configurations,” *J. Electrochem. Soc.*, vol. 140, no. 12, p. 3679, 1993.

[216] C. R. Kagan and P. Andry, Eds., *Thin-film transistors*. CRC Press, 2003.

[217] T. Kamiya, K. Nomura, and H. Hosono, “Origins of High Mobility and Low Operation Voltage of Amorphous Oxide TFTs: Electronic Structure, Electron Transport, Defects and Doping*,” *J. Disp. Technol.*, vol. 5, no. 7, pp. 273–288, 2009.

[218] S.-K. Jeong, M.-H. Kim, S.-Y. Lee, H. Seo, and D.-K. Choi, “Dual active layer a-IGZO TFT via homogeneous conductive layer formation by photochemical H-doping.,” *Nanoscale Res. Lett.*, vol. 9, no. 1, p. 619, 2014.

[219] K. Ide, Y. Kikuchi, K. Nomura, M. Kimura, T. Kamiya, and H. Hosono, “Effects of excess oxygen on operation characteristics of amorphous In-Ga-Zn-O thin-film transistors,” *Appl. Phys. Lett.*, vol. 99, no. 9, pp. 2009–2012, 2011.

[220] M. Nakata, G. Motomura, Y. Nakajima, T. Takei, H. Tsuji, H. Fukagawa, T. Shimizu, T. Tsuzuki, Y. Fujisaki, and T. Yamamoto, “Development of flexible displays using back-channel-etched In-Sn-Zn-O thin-film transistors and air-stable inverted organic light-emitting diodes,” *J. Soc. Inf. Disp.*, vol. 24, no. 1, pp. 3–11, 2016.

[221] R. L. Weisfield, W. Yao, T. Speaker, K. Zhou, R. E. Colbeth, and C. Proano, “Performance analysis of a 127-micron pixel large-area TFT/photodiode array with boosted fill factor,” *Proc. SPIE 5368, Med. Imaging 2004 Phys. Med. Imaging*, vol. 5368, pp. 338–348, 2004.

[222] R. A. Street, “Thermal generation currents in hydrogenated amorphous silicon p-i-n structures,” *Appl. Phys. Lett.*, vol. 57, no. 13, pp. 1334–1336, 1990.

[223] M. S. Shur, “SPICE Models for Amorphous Silicon and Polysilicon Thin Film Transistors,” *J. Electrochem. Soc.*, vol. 144, no. 8, p. 2833, 1997.

[224] “ACF2101 PSpice model,” *Tools and software, (Texas Instruments, Oct. 2000)*. [Online]. Available: http://www.ti.com/product/acf2101.

[225] K. Pearson, “Mathematical Contributions to the Theory of Evolution . III . Regression , Heredity , and Panmixia,” *Philos. Trans. R. Soc. London . Ser. A , Contain. Pap. a Math. or Phys. C*, vol. 187, no. 1896, pp. 253–318, 1896.

[226] H. Lee, J. Yoo, C. Kim, I. Chung, J. Kanicki, and S. Member, “Asymmetric Electrical Properties of Corbino a-Si : H TFT and Concepts of Its Application to Flat Panel Displays,” *IEEE Trans. Electron Devices*, vol. 54, no. 4, pp. 654–662, 2007.

[227] H. Lee, C. H. Liu, and J. Kanicki, “Asymmetric electrical properties of half corbino hydrogenated amorphous silicon thin-film transistor and its applications to flat panel displays,” *Jpn. J. Appl. Phys.*, vol. 50, no. 7 PART 1, pp. 1–8, 2011.

[228] J.-H. Lan and J. Kanicki, “Atomic Hydrogen Effects on the Optical and Electrical Properties of Transparent Conducting Oxides For a-Si:H TFT-LCDs,” *MRS Proc.*, vol. 424, p. 347, Jan. 1996.

[229] M. Mulato, J. P. Lu, and R. A. Street, “Simulated and measured data-line parasitic capacitance of amorphous silicon large-area image sensor arrays,” *J. Appl. Phys.*, vol. 89, no. 1, pp. 638–647, 2001.

[230] F. De Roose, K. Myny, S. Steudel, M. Willigems, S. Smout, T. Piessens, J. Genoe, and W. Dehaene, “16.5 A flexible thin-film pixel array with a charge-to-current gain of 59μA/pC and 0.33% nonlinearity and a cost effective readout circuit for large-area X-ray imaging,” in *2016 IEEE International Solid-State Circuits Conference (ISSCC)*, 2016, pp. 296–297.

[231] G. Baek, K. Abe, H. Kumomi, and Kanicki, “Scaling of Coplanar Homojunction Amorphous In–Ga–Zn–O Thin-Film Transistors,” *Jpn. J. Appl. Phys.*, vol. 52, no. 3S, p. 03BB05, Mar. 2013.

[232] M. H. Izadi, K. S. Karim, A. Nathan, and J. a. Rowlands, “Low-noise pixel architecture for advanced diagnostic medical x-ray imaging applications,” *Proc. SPIE*, vol. 6142, p. 61420T–61420T–11, 2006.